



**Department of Electrical and Computational
Engineering**



CPEE 2021

**Warsaw University
of Technology**



**22th International Conference
"Computational Problems of Electrical Engineering"**

Information for the Participants

The conference will be held online via Google Meet.



<https://meet.google.com/chd-mjvc-fnu>

Information for the Presenters

Online presentations are 10 minutes long and must include a brief introduction to the topic and a description of the work itself. The presentation is followed by a 5-minute discussion.

Program of the conference

Thursday, September 16, 2021

08:30 – 09:00	Opening Ceremony of the Conference CPEE 2021
09:00 – 09:30	Plenary Lecture Chairman: Ivo Doležel <i>Modeling of heat transfer and shape of surfaces obtained by additive technique</i> Václav Kotlan, Iveta Petrášová, Roman Hamar, Ivo Doležel
09:30 – 11:30	Oral Session 1 – “Industrial Applications” Chairman: Ivo Doležel, Jacek Starzyński
09:30 – 09:45	<i>Influence of the static compensator current on the average power flow</i> Jacek Korytkowski, Kazimierz Mikolajuk, Krzysztof Siwek and Andrzej Tobola
09:45 – 10:00	<i>Models and Methods of Research of Series Reactive Power Compensation of Induction Motors in Phase Coordinates</i> Vasyl Malyar, Orest Hamola, Volodymyr Maday and Ivanna Vasylychshyn
10:00 – 10:15	<i>An Excitation Control of an Autonomous Synchronous Generator with a Current-Compounding Loop</i> Andriy Kutsyk, Mykola Semeniuk and Valeriy Misiurenko
10:15 – 10:30	<i>Mathematical model of analysis of wave electromagnetic processes in three-winding transformers</i> Mykhailo Seheda, Petro Gogoluyk and Yurii Blyznak
10:30 – 10:45	<i>Thermal image processing for segmentation of photovoltaic panels</i> Jacek Starzyński
10:45 – 11:00	<i>System for the support of the intravenous infusion process continuity</i> Adam Jósko and Wojciech Romanik
11:00 – 11:15	<i>Non-contact Electromagnetic Actuator for a Ball Valve</i> David Šmucr, Martin Vitek, František Mach and Karel Pospíšil
11:15 – 11:30	<i>Simulation of heat transfer and air flow inside the switchboard cabinet</i> Jan Kohout and Lenka Sroubova

11:30 – 13:00	Break
13:00 – 15:00	Oral Session 2 – “Software Engineering” Chairman: Václav Kotlan, Ladislav Janoušek
13:00 – 13:15	<i>Distributed event queue management system</i> Patryk Nowacki, Radosław Roszczyk and Artur Krupa
13:15 – 13:30	<i>Analysis of the sound for recognition of keyboard operations</i> Jurczak Marcin and Marcin Kolodziej
13:30 – 13:45	<i>Practical studies of local HTTP cache security</i> Janusz Sawicki, Paweł Zych and Bartosz Sawicki
13:45 – 14:00	<i>Computational Problems in Forecasting in Complex Dynamical Systems</i> Bohdan Melnyk, Petro Stakhiv, Nataliya Melnyk and Stepan Trokhaniak
14:00 – 14:15	<i>Coilgun Design by Simulation</i> Krzysztof Korytkowski and Jacek Starzyński
14:15 – 14:30	<i>Peculiarities of the LPTV circuits optimization in the MATLAB software environment</i> Yuriy Shapovalov, Dariya Bachyk and Ksenia Detsyk
14:30 – 14:45	<i>Machine learning algorithms usage for satellites simulation and control</i> Natalya Shakhovska, Yurii Bobalo and Bohdan Mytnyk
14:45 – 15:00	<i>U-Net training models for efficient brain tumour segmentation on multi-modality CT and PET images</i> Esterka Kot, Zuzanna Krawczyk, Krzysztof Siwek, Kacper Pleska, Jakub Rogalski and Piotr Czwarnowski
15:00– 15:15	Break
15:15 – 17:00	Oral Session 3 – “Computer Modeling” Chairman: Petr Kropík, Milan Smetana
15:15 – 15:30	<i>Design of bioamplifier for educational purposes</i> Michal Labuda, Tadeas Bednar and Marek Jarkovsky
15:30 – 15:45	<i>Numerical Integrators on Electrical Circuits' Transient Calculation</i> Volodymyr Moroz and Anastasiia Vakarchuk
15:45 – 16:00	<i>Optimization Material Characteristics for Electroheat Model Based on Calibration Material Properties</i> Iveta Petrášová, Pavel Karban, Václav Kotlan and Ivo Doležel
16:00 – 16:15	<i>Face detection in a real-time videostream on Raspberry Pi</i> Jaroslav Podestát, Petr Kropík and Jan Beneš
16:15 – 16:30	<i>Sweep frequency eddy current testing: numerical simulation of various probe types</i> Filip Vaverka, Milan Smetana, Daniela Gombarska and Ladislav Janousek
16:30 – 16:45	<i>Cell-centered, geometric multigrid field solver for Particle-in-Cell simulations</i> Bartosz Chaber
16:45 – 17:00	<i>Parallel implementation of a Particle-in-Cell code in Julia programming language</i> Wiktor Łodyga and Bartosz Chaber

Friday, September 17, 2021

08:30 – 10:30	Oral Session 4 – “High Frequency Applications” Chairman: David Pánek, Zuzana Pšeňáková
08:30 – 08:45	<i>Real-time Mobile-Based Platform for Determining Level and Location of Radiation Background</i> <i>Roman Diachok, Halyna Klym and Ivanna Vasylchyshyn</i>
08:45 – 09:00	<i>Prediction of GNSS Horizontal Navigation System Error (HNSE) using Artificial Neural Networks</i> <i>Krzysztof Paczuski, Mikołaj Kowalczewski and Karolina Krzykowska-Piotrowska</i>
09:00 – 09:15	<i>Impact of thermal shielding on heating efficiency of SiC in single mode microwave resonant cavity</i> <i>Stanislav Cichon and Jan Machac</i>
09:15 – 09:30	<i>Human exposure to mobile phone EMF inside shielded space</i> <i>Mariana Benova, Milan Smetana and Andrea Cirkaiova</i>
09:30 – 09:45	<i>Simulations of electromagnetic exposure system for irradiation of biological cultures: comparison of CST Studio Suite and COMSOL Multiphysics</i> <i>Zuzana Judáková, Ladislav Janoušek, Dominika Oreničová and Lucia Čarnecká</i>
09:45 – 10:00	<i>Modeling and simulation of biological structures exposition to 5G network</i> <i>Zuzana Pšeňáková, Daniela Gombárska, Milan Smetana and Miroslav Janovčík</i>
10:00 – 10:15	<i>Modeling and simulation of high frequency electromagnetic field influence to tumor tissue</i> <i>Zuzana Pšeňáková, Daniela Gombárska, Zuzana Judáková, Lucia Čarnecká and Frederika Bačová</i>
10:15 – 10:30	<i>Amplitude synthesis of linear antenna array by Taguchi method</i> <i>Deubauh Cedrick Gnawa and Pavel Karban</i>
<hr/>	
10:30– 10:45	Break
<hr/>	
10:45 – 12:00	Oral Session 5 – “Electromechanical Systems” Chairman: Pavel Karban, Robert Szmurlo
10:45 – 11:00	<i>Kinematics of the movement of the pilot of a paraglider simulator</i> <i>Petr Stašek, Pavel Karban and Petr Kropík</i>
11:00 – 11:15	<i>Deep CNN ensemble for recognition of face images</i> <i>Robert Szmurlo and Stanislaw Osowski</i>
11:15 – 11:30	<i>Definition System of Human Body Position in Virtual Reality</i> <i>Roman Diachok, Halyna Klym, Ivanna Vasylchyshyn and Ivan Karbovnyk</i>
11:30 – 11:45	<i>CNN-based character recognition for a contextless text input system in immersive VR</i> <i>Szymon Kuś and Robert Szmurlo</i>
11:45 – 12:00	<i>Advanced paraglider simulator control system</i> <i>Richard Sivera, Petr Stašek, Jakub Vorlíček, Petr Kropík and Pavel Karban</i>
<hr/>	
12:00– 12:15	Closing Ceremony of the Conference CPEE 2021
<hr/>	

SESSION 1 - INDUSTRIAL APPLICATIONS

Influence of the static compensator current on the average power flow

Jacek Korytkowski
Warsaw University of Technology,
Faculty of Electrical Engineering,
ul. Koszykowa 75,
00-662 Warszawa, Poland,

Krzysztof Siwek
Warsaw University of Technology,
Faculty of Electrical Engineering,
ul. Koszykowa 75,
00-662 Warszawa, Poland,
<https://orcid.org/0000-0003-2642-2319>

Kazimierz Mikołajuk
Warsaw University of Technology,
Faculty of Electrical Engineering,
ul. Koszykowa 75,
00-662 Warszawa, Poland,

Andrzej Tobiła
Warsaw University of Technology,
Faculty of Electrical Engineering,
ul. Koszykowa 75,
00-662 Warszawa, Poland,

Abstract—The shunt static compensator with the iterative control is presented. The compensator generates reactive current computed in the real time with the use of the iterative method. The RMS value of grid voltage is chosen as the compensator aim. Analytical and simulation results show the influence of the compensator current on the average power drawn from the energy sources. The multiport representation of the grid is presented.

Keywords—static compensator, iterative control, power flow

I. INTRODUCTION

Power flow studies are important in designing and in determining the best operation of existing systems. Electric utility companies use very elaborate programs for power flow studies to obtain information concerning the system design and operation. Very advanced arrangements are installed in order to control power flow in a electric grid [1]. The possibility of generating or absorbing controllable reactive power with various power electronic switching converters has long been recognized [2]. These converters do not use capacitor or reactor banks to produce reactive power. They operate as alternating voltage or current sources.

The development of the power theory of electrical circuits and systems has long history with great variety of different. In general, p-q theory can be used for both harmonic and reactive power compensation and it works effectively even under unbalanced conditions [3]. For balanced three-phase systems d-q transformation enables to transform the system to the stationary frame.

The local system weaknesses such as low voltages or over-voltages can be reduced by electronic power compensators. The STATCOM regulates voltage at its terminal by controlling the amount of reactive power injected into the power system. Such arrangements can be controlled by the local node voltage. The improving of the power system flexibility is specially needed for the power system with a large share or renewable energy sources [4]. The considered compensator is oriented only on the fundamental harmonic, higher harmonics are beyond the scope of this paper. Assuming that harmonic contents in the voltage is small the control can be based on the RMS value. The complex RMS values are denoted by capital letters U and I , vertical bars describe modules of these

complex values $|U|$ and $|I|$. The control signal is achieved with the use of the iterative algorithm. Such approach is classified as the repetitive method.

II. RELATION BETWEEN 2-PORT AND THEVENIN 1-PORT MODEL

Let the 2-port be terminated with the independent sinusoidal voltage source U_2 as shown in Fig. 1. It is assumed that the 2-port does not contain independent sources in box, it is linear and considered in the steady state. It means that the voltage source can be represented by complex RMS value U_2 and the circuit elements can be represented by their complex impedances and admittances.

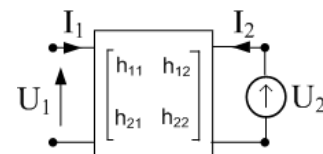


Fig.1. 2-port terminated with the voltage source

It is assumed that the 2-port does not contain independent sources in box, it is linear and considered in the steady state. It means that the voltage source can be represented by complex rms value U_2 and the circuit elements can be represented by their complex impedances and admittances.

The hybrid equations of the 2-port can be written as

$$U_1 = h_{11}I_1 + h_{12}U_2 \quad (1)$$

$$I_2 = h_{21}I_1 + h_{22}U_2 \quad (2)$$

The circuit shown in Fig 1 can be reduced to Thevenin 1-port shown in Fig.2.

Putting $I_1 = 0$ in (1) the equivalent Thevenin voltage $U_T = U_1$ is obtained

$$U_T = h_{12}U_2 \quad (3)$$

Putting $U_2 = 0$ in (1) the equivalent impedance $Z_T = \frac{U_1}{I_1}$ is obtained

$$Z_T = h_{11} \quad (4)$$

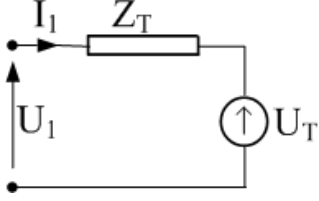


Fig. 2. Thevenin representation of the circuit from Fig. 1

Voltage U_1 and current I_1 are the same in 2-port and 1-port. But after reduction of 2-port to 1-port source U_2 vanishes. The power drawn from this source cannot be computed on the 1-port ground. The power at port remain the same in both models. The second port is expose when the 1-port seen Fig. 2 is unfolded to the 2-port seen Fig. 1. Such packing and unpacking can be done for n-port structures.

III. 2-PORT WITH THE STATIC COMPENSATOR CONNECTED

Assume that the compensator modelled by current source is connected to the 2-port as shown in Fig. 3.

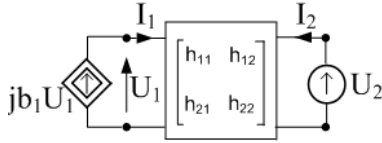


Fig. 3. 2-port with the independent voltage source and controlled current source

For the further investigation it is assumed that the 2-port does not contain independent sources inside the box, so it is reciprocal. The current source $I_1 = j b_1 U_1$ is controlled by voltage U_1 of port 1. The gain $j b_1$ is imaginary number. It means that current I_1 is shifted to voltage U_1 by $\pi/2$. Real coefficient b_1 is slowly time-varying and computed in the control process.

For the circuit in Fig. 3 equations (1) and (2) lead to the relation between two voltages

$$U_1 = \frac{h_{12}}{1 - j b_1 h_{11}} U_2 \quad (5)$$

and

$$I_2 = \left(\frac{-j b_1 h_{12} h_{21}}{1 - j b_1 h_{11}} + h_{22} \right) U_2 \quad (6)$$

For the reciprocal 2-port $h_{21} = h_{12}$. Current component

$$\frac{-j b_1 h_{12} h_{21}}{1 - j b_1 h_{11}} U_2$$

flowing in source U_2 is caused by the compensator, as it is equal to zero for $b_1 = 0$. The additional average power drawn from source U_2 can be expressed as

$$P_a = \text{real} \left(\frac{-j b_1 h_{12} h_{21}}{1 - j b_1 h_{11}} |U_2|^2 \right) \quad (7)$$

Average power (7) depends on control parameter b_1 . Power P_2 cannot be computed from Thevenin equivalent 1-port seen in Fig. 2. However, voltage U_1 in Fig. 2 and U_1 in Fig. 1 is the same. If current source $j b_1 U_1$ is connected to the circuit shown in Fig. 2, then

$$U_1 = Z_T j b_1 U_1 + U_T \quad (8)$$

Putting (3) and (4) to (8) gives the expression identical to (5). It means that from the nodes of the compensator connection the Thevenin model is equivalent to the 2-port model. The influence of the compensator on the average power drawn from the energy source is illustrated in the next section.

IV. SIMULATION ILLUSTRATING THE POWER FLOW

The simulation presented in this section shows how the power drawn from the voltage source changes within the compensation process. The iterative control of the compensator is described in [5]. This control method is formulated as the optimization problem formulated as follows. Find compensator parameter b_1 such that grid voltage $|U_1|$ at the compensator port is close to desirable value U_d .

The iterative algorithm based on the secant method can be comprised in the following steps.

Step 0. Measure voltage $|U_0|$ for zero compensator current

$$b_0 = 0 \quad (7)$$

Step 1. Measure voltage $|U_1|$ for optional chosen nonzero compensator parameter b_1 such that $|I_1| = |b_1| |U_0| < I_{\max}$, where I_{\max} the maximum value of the compensator current.

Step k. Measure voltage $|U_k|$ and compute parameter b_k

$$b_k = \frac{|U_0| - U_d}{|U_0| - |U_{k-1}|} b_{k-1} \quad (8)$$

for $k = 2, \dots, K$, where final index K is such that condition $(\|U_K| - U_d|) < U_{\min}$ is fulfilled.

A shunt compensator operates as a current source controlled by the grid voltage waveform. This current source is obtained from DC/AC voltage inverter with the additional series inductor which reactance is denoted as X . The modified algorithm uses new control parameter w defined as

$$w = 1 - bX \quad (9)$$

In the new algorithm reactance X does not appear, so the knowledge of reactance value is not demanded. The new algorithm is formulated as follows
Step 0.

$$w_0 = 1 \quad (10)$$

Step 1. Optionally chosen $w_1 \neq 1$, such that

$$|I_1| = \frac{|w_1 - 1|}{X_L} |U_1| \leq I_{\max} \quad (11)$$

where I_{\max} is the rating compensator current and X estimated grid reactance.
Step 2.

$$w_2 = 1 - \frac{|U_0| - U_d}{|U_0| - |U_1|} (1 - w_1) \quad (12)$$

Step k.

$$w_k = 1 - \frac{|U_0| - U_d}{|U_0| - |U_{k-1}|} (1 - w_{k-1}) \quad (13)$$

The set w_k for $k = 0, 1, 2, \dots, K$ determines the set of voltage phasors

$$U_{ack} = w_k U_{k-1} \quad (14)$$

Obtained parameters w_k are real, so voltages U_{ac} and U are in phase. Power angle δ should be introduced in order to maintain the DC capacitor voltage. Instead of angle δ the properly chosen time delay of the control signal can be used.

Presented simulation was obtained with the use of PLECS program.

The PLECS block model of the inverter and grid is shown in Fig. 4.

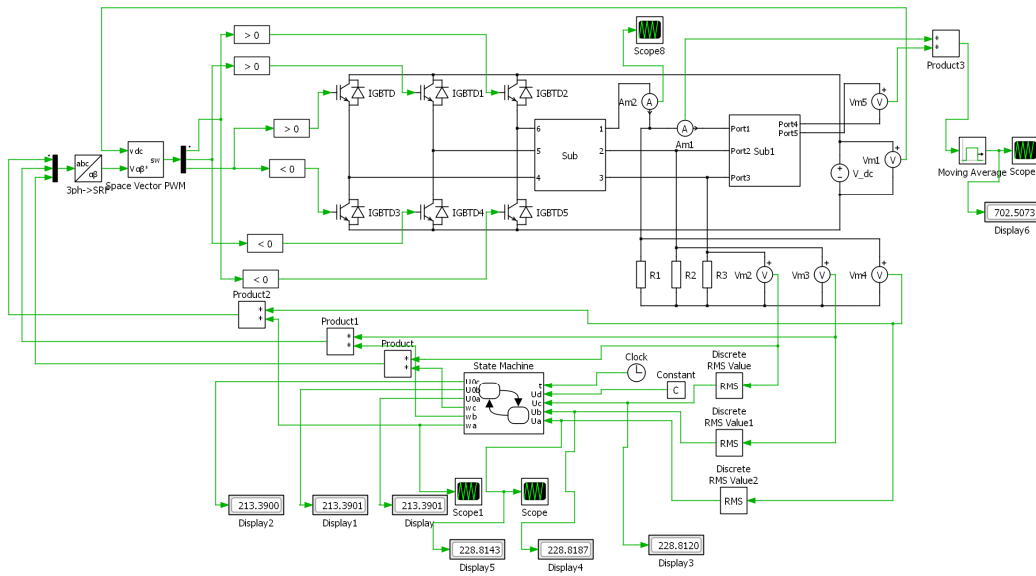


Fig. 4. PLECS model of the inverter and grid

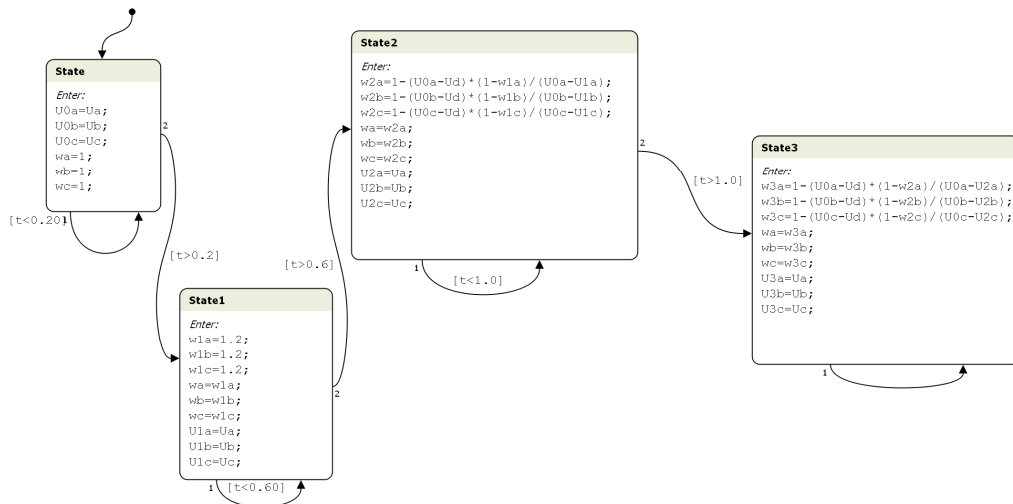


Fig. 5. State machine

State machine shown in Fig. 5 executes the algorithm presented in equations (13), (14). This machine contains 4

state boxes. Each state responds to one algorithm step. Transitions are represented by curved arrows from one state

to another. The time intervals are defined by the condition trigger written for each transition.

PLECS model shown in Fig. 4 contains three product blocs. These blocks realize in time domain the equation (14) written in the phasor form.

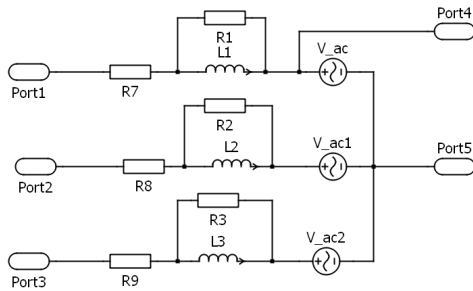


Fig. 6. Grid model

Fig. 6 shows the unfolded subsystem Sub1, this circuit is balanced with parameters: $R_7 = 1\Omega$, $R_1 = 500\Omega$, $L_1 = 0.004$ H, amplitude of source voltage $V_{ac} = 305$ V. In order to avoid inductive cutsets the resistors are parallelly connected to the inductors. The star connected resistances seen in Fig. 4, in PLECS model $R_1 = R_2 = R_3 = 100\Omega$.

Figs. 7 to 10 show the simulation results.

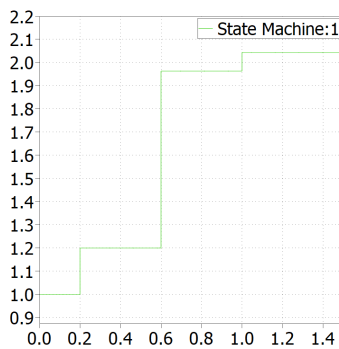


Fig. 7. Control parameter w_a

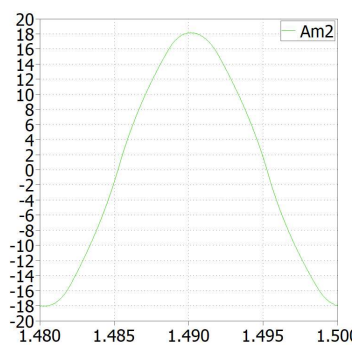


Fig. 8. The last period of the compensator current, amperes

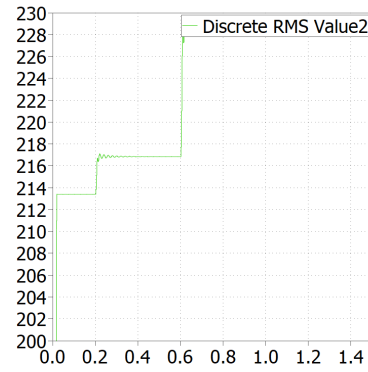


Fig. 9. RMS voltage $|U_a|$, volts

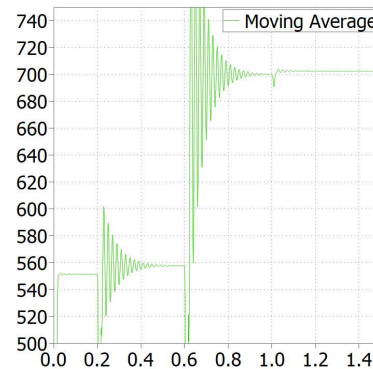


Fig. 10. Moving average power P_a , wats

The waveform presented in Figs. 7 to 10 are presented for time interval equal 1.5 second which includes four steps of the iterative algorithm. In Fig. 8 the time interval is equal to one period of grid voltage.

Fig. 10 shows how the average power delivered by the voltage source changes as a result of the compensation. This power changes from 551W before compensation to 702W after compensation. The main reason of such result follows from the circuit topology of the considered model. The voltage increases at the nodes with the resistors connected to them. In the real grid the consumed power less depends on the grid voltage.

REFERENCES

- [1] Kannan S., Shesha J., Salama M.M., Real and Reactive Power Coordination for a Unifird Power Flow Contoller, IEEE Power Systems Trans. Vol. 16, No. 3, August 2004, 1454-1461.
- [2] Schauder C., Gernhardt M., Stacey E., Lemak T., Gyugyi L., Development of a ± 100 MVAR Static Condenser for Voltage Control of Transmission Systems, IEEE Trans. on Power Del., Vol. 10, No. 3, July 1995, 1486-1496.
- [3] Cheepati K. R., Maddala N. R. Munagala S. K., Johnson B., Pike G.E., A Novel Reference Current Extraction Technique with Multi-Functional Capability for Shunt Active Filter, Journal of Electrical Engineering Technology, February (2020).
- [4] Raczkowski R., Robak S., System magazynowania energii elektrycznej jako środek poprawy elastyczności systemu elektroenergetycznego z dużym udziałem energii OZE, Przegląd Elektrotechniczny, 3'2021 pp.1-8.
- [5] Mikołajuk K., Siwek K., Toboła A., Iterative control of the static compensator, Przegląd Elektrotechniczny 5'2021, pp. 134-139.

Models and Methods of Research of Series Reactive Power Compensation of Induction Motors in Phase Coordinates

Vasyl Malyar
Institute of Power Engineering and
Control Systems
Lviv Polytechnic National University
Lviv, Ukraine
vasyl.s.maliar@lpnu.ua

Orest Hamola
Institute of Power Engineering and
Control Systems
Lviv Polytechnic National University
Lviv, Ukraine
orest.y.hamola@lpnu.ua

Volodymyr Maday
Institute of Power Engineering and
Control Systems
Lviv Polytechnic National University
Lviv, Ukraine
volodymyr.s.madai@lpnu.ua

Ivanna Vasylychshyn
Institute of Power Engineering and
Control Systems
Lviv Polytechnic National University
Lviv, Ukraine
ivanna.i.vasylychshyn@lpnu.ua

Abstract – This paper proposes mathematical models and algorithms for calculating the processes and characteristics of induction motors in series compensation reactive power. The developed algorithms are based on a mathematical model of the induction motor in phase coordinates. A complete system of differential equations of electromechanical equilibrium of stator and rotor circuits is used for transient analysis. The algorithm for calculating static characteristics is based on the projection method for solving the boundary value problem for system equations of electrical equilibrium.

Keywords – induction motor, reactive power, series compensation, transient process, boundary problem, static characteristics.

I. INTRODUCTION

Induction motors (IM) are consumers of reactive power, and its transmission from the generator to the place of consumption causes additional loading of the line with reactive currents. [1, 2]. The problem of reactive power compensation is always relevant. It must be solved separately for each electric drive because it should not worsen the economic performance of the power supply system as a whole. One way to compensate for reactive power is to install capacitor devices in the electrical distribution networks connected in parallel to the consumers or series. In addition, compensation can be group or individual [3, 4]. The peculiarity of series compensation is that a load current flows through the capacitors, which at any time can vary widely. Hence, the reactive power of series-connected capacitors is also a variable. The capacitance of the capacitors must be continuously adjusted to maintain the power factor ($\cos \varphi$) at a given level [5]. Such control can occur either manually or automatically [6], but for microprocessor control, it is necessary to have programs for calculating processes in real-time.

Most electric drives use direct starting of IM with a squirrel-cage rotor, at which the starting current can reach eight times the value. This current value is not dangerous for the motor, but in the case of prolonged, frequent starts, the temperature of the motor windings may exceed the permissible limits. In addition, when starting powerful motors, the starting current can cause a significant reduction in mains voltage, impairing or completely disrupting other consumers'

regular operation. Therefore, there is a need to research the start-up process of the electric drive system on a mathematical model [5 – 7] to develop a control system for the start-up process, which reduces the start-up time or the amount of current.

The capacitor capacity choice based on simplified mathematical models of IM can be unreliable. Its unsuccessful choice can lead to overloading of IM, the appearance of self-excitation [8, 9], or non-starting. However, using dynamic mathematical models of IM of a high level of adequacy requires appropriate high-efficiency calculation methods.

An essential task of mathematical modeling of processes in the IM with capacitors in the phases of the stator winding is the choice of coordinate system. In particular, phase voltages are converted to orthogonal coordinate axes in automatic control systems. However, their use is not always effective because it is impossible to adequately describe processes in transformed coordinates. Using mathematical models in phase coordinates, we can increase the accuracy of regulating and expanding the range of problems. The developed algorithms must have a high-speed operation that allows real-time control of the process.

The purpose of the article is to present the methods and algorithms of mathematical modeling of three-phase IM with series-connected capacitors developed based on the mathematical model of IM in phase coordinates. They make it possible to determine capacitance capacitors, which compensate for reactive power depending on the mode of operation.

II. ELECTRICAL EQUILIBRIUM EQUATION

The mathematical models of IM developed based on the theory of circuits in three-phase physical coordinates give the chance to consider various factors that define the behavior of the electric drive system. However, the differential equations (DE) of the electrical equilibrium of the IM in three-phase physical coordinates due to the rotor rotation have periodic coefficients, which significantly complicates their solution and makes it almost impossible to calculate static characteristics. The algorithms of numerical analysis of processes in IM with capacitors connected in series to the stator winding are developed in fixed three-phase axes [11],

which are actual physical for stator windings and fixed three-phase for rotor phases. The rotor phase axis α coincides with the stator phase axis A. The electrical circuit of the motor loops is shown in Fig. 1.

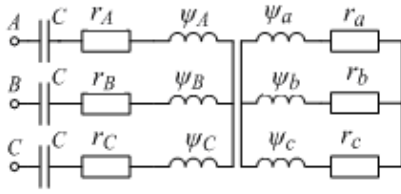


Fig. 1. The electrical circuit of the IM with capacitors of capacity C

The system of electrical equilibrium equations, which describes the dynamic mode of the IM, has the form

$$\begin{aligned} \frac{d\psi_A}{dt} - \frac{d\psi_B}{dt} &= -r_A i_A + r_B i_B - u_{kA} + u_{kB} + u_{AB}; \\ \frac{d\psi_B}{dt} - \frac{d\psi_C}{dt} &= -r_B i_B + r_C i_C - u_{kB} + u_{kC} + u_{BC}; \\ i_A + i_B + i_C &= 0; \\ \frac{d\psi_a}{dt} - \frac{d\psi_b}{dt} &= -r_a i_a + r_b i_b - \omega(\psi_b - 2\psi_c + \psi_a) / \sqrt{3}; \\ \frac{d\psi_b}{dt} - \frac{d\psi_c}{dt} &= -r_b i_b + r_c i_c - \omega(\psi_c - 2\psi_a + \psi_b) / \sqrt{3}; \\ i_a + i_b + i_c &= 0; \\ \frac{du_{kA}}{dt} &= \frac{i_A}{C}, \quad \frac{du_{kB}}{dt} = \frac{i_B}{C}, \quad \frac{du_{kC}}{dt} = \frac{i_C}{C}, \end{aligned} \quad (1)$$

where ψ_η , i_η , r_η – flux linkage, currents, and resistances of contours ($\eta = A, B, C, a, b, c$); u_{AB}, u_{BC} – corresponding line voltages; u_{kA}, u_{kB}, u_{kC} – voltage on capacitors with capacitance C ; $\omega = \omega_0(1-s)$ – angular speed of rotation of the rotor, expressed in electric radians per second; s – slip; ω_0 – mains voltage frequency.

The equation describes the dynamics of rotor motion

$$d\omega/dt = p_0(M_e - M_c)/J, \quad (2)$$

where M_e – electromagnetic torque of IM in phase coordinates [11]; M_c – the moment of loading on a motor shaft; J – the equivalent moment of inertia of the electric drive system; p_0 – the number of pole pairs of IM.

From finite equations of system (1), we can move to differential ones, and therefore we assume that electromechanical processes are described by a nonlinear system DE, which consists of equations (1), (2). As a result of its numerical integration, it is possible to obtain the dependences of circuit currents and rotor speed on time and research the influence of any coordinate (capacitor capacity,

moment of inertia, load moment) included in this system on the transient process. The following are examples of time dependences of stator phase currents and rotor speed during motor start 4A80B2Y3 ($P=2,2$ kW, $U = 220$ V, $I = 4,7$ A).

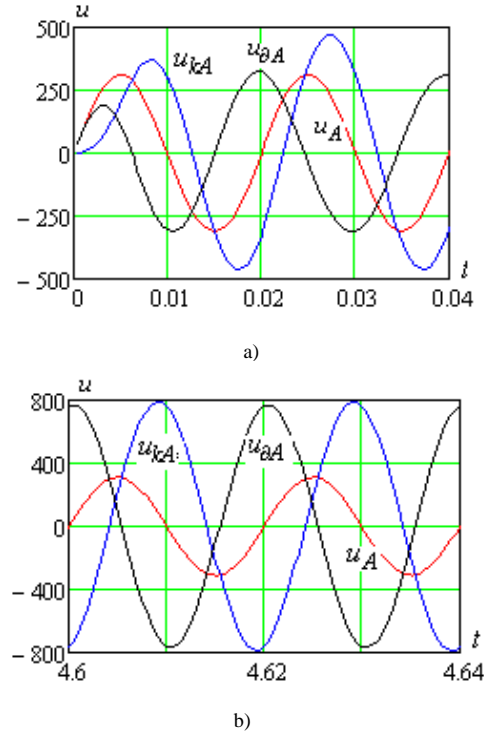


Fig. 2. Dependences on time of voltages of IM without loading with the capacitors with capacity connected in series $300 \mu F$: supply of stator phase A (u_A), capacitor (u_{kA}) and on the motor (u_{0A}) during start-up (a) and after the end of the transient process (b)

As can be seen from the fig. 2, during start-up, the voltage on the motor exceeds the supply voltage, which reduces the start-up time. However, starting at some values of the capacitance of the capacitors may occur in resonant mode (Fig. 3). Therefore, voltages and currents at the same time considerably exceed nominal values.

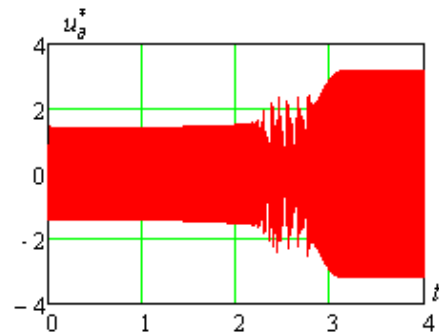


Fig. 3. Time dependences of the relative value of the voltage on the motor during the start of the motor with rated load and capacitors capacity $300 \mu F$

To avoid overvoltage and the current overload of the IM sometime after start-up, it necessary to reduce the capacitance of the capacitors. An example of the transient process calculation that occurs during start-up with a capacitor of capacity $300 \mu F$ followed by a reduction to $100 \mu F$ is shown in Fig.4.

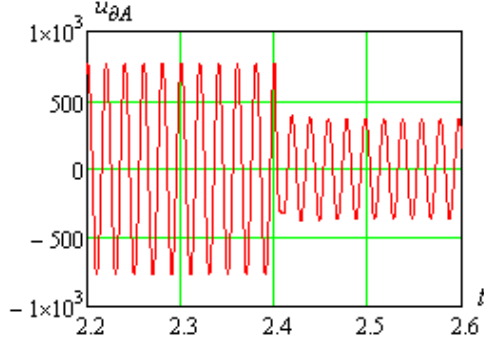


Fig. 4. Dependences on the voltage-time on the motor during start-up with rated load

III. STATIC CHARACTERISTICS

The start-up process is transient, but its analysis can be performed using static characteristics. They are considered a sequence of appropriate steady-state modes of operation of the IM at different slips. Under the condition of constant slip due to periodic perturbation (supply voltage), the DE system (1) describes a steady-state mode in which the flux linkage and currents, as well as the coordinates that depend on them, change according to the periodic law with period $T=1/f$, where f - supply voltage frequency. The calculation of the periodic mode in mathematical terms is a boundary value problem for a system of nonlinear DE (1) of the first order with periodic boundary conditions. The result of its solution is the dependence of the coordinates \mathbf{v} during the period T .

Consider the algorithm for calculating static characteristics. To do this, we write the system DE (1) of the electrical equilibrium of the contours of the IM will be written in the form of a vector equation

$$\frac{d \vec{y}(\vec{x}, t)}{dt} = \vec{z}(\vec{y}, \vec{x}, t) + \vec{u}(t), \quad (3)$$

where

$$\vec{y} = (\vec{\psi}, \vec{u}_k)^*; \vec{x} = (\vec{i}, \vec{u}_k)^*; \vec{u}(t)$$

– T -periodic time vector functions in which:

$$\vec{\psi} = (\psi_A, \psi_B, \psi_C, \psi_a, \psi_b, \psi_c)^*; \vec{u}_k = (u_{kA}, u_{kB}, u_{kC})^*;$$

$$\vec{i} = (i_A, i_B, i_C, i_a, i_b, i_c)^*; \vec{u}(t) = (u_{AB}(t), u_{BC}(t), 0, \dots, 0)^* -$$

a given vector function of a periodic perturbation.

Since the system of equations (3) includes the time coordinate t , each slip value s corresponds to a periodic dependence

$$\vec{x}(t) = \vec{x}(t+T),$$

which describes the change of coordinates during the period. Thus, the essence of the boundary value problem is not determining the coordinates at the one-time point but determining the functional dependences of the coordinates during the period T .

The simplest method of determining these dependences is the numerical integration of equation (3) to the steady-state process. However, this method is not acceptable for the

calculation of static characteristics. Periodic functional dependences of coordinates can be obtained without resorting to the analysis of the transient process if we consider the problem as a boundary.

Forming a boundary value problem requires algebraization of the DE system (1) over a period, namely, creating its discrete analog. The calculation algorithms developed by us are based on the algebraization of DE (3) using the approximation of state variables by cubic splines [9]. The properties of which allow us to perform calculations with a minimum amount of calculations. The solution of the received system allows finding the approximate solution in numerical values of state variables on a grid of nodes of the period T .

The calculation of the required to compensate the reactive power of the capacitor capacitance and the laws of its regulation in specific modes can be done by calculating the multidimensional static characteristic as the dependence of the set of nodal coordinates of the mode on the value of capacitor capacitance for each slip s . Consider the method of obtaining it.

IV. ALGORITHM FOR SOLVING A BOUNDARY VALUE PROBLEM

Carrying out a spline approximation of coordinates on the grid $N+1$ nodes of the period by splines of the third-order by what was stated in [10], we obtain a discrete analog of the system DE (4) m -th order in the form of a nonlinear algebraic equation of order Nm

$$H\vec{Y} + B\vec{Z} = -B\vec{U}, \quad (4)$$

where H, B – block-diagonal matrices of spline coefficients, the elements of which are determined by a grid of nodes;

$$\vec{Y} = (\vec{y}_1, \vec{y}_N)^*; \vec{Z} = (\vec{z}_1, \vec{z}_N)^*; \vec{U} = (\vec{u}_1, \vec{u}_N)^*$$

– vectors, each of which consists of N vectors of nodal values of the corresponding variables. In system (4), there is an unknown vector $\vec{X} = (\vec{x}_1, \vec{x}_N)^*$.

System (4) is solved by the continuation method with iterative refinement by Newton's method. The elements of the Jacobi matrix are the resistances, capacitors capacitances, and the differential inductances of the IM circuits, which are determined for each j -th node of the grid $j = (\overline{1, N})$ according to [11].

The coordinates' research depends on the capacitance of the capacitor for a given value of slip at constant voltage is carried out by the differential method [10]. To do this, we differentiate the algebraic equation (4) by C . As a result, we obtain the DE system of argument C , in which the Jacobi matrix is the same as in (6), and the right-hand sides are the vector $\partial \vec{Z} / \partial C$.

For example, fig. 5 shows the static characteristics calculation results in the form of dependences on the capacitance of the capacitors, RMS voltage on the stator phase A capacitor, and the relative value of the electromagnetic torque the motor 4A80B2Y3 during slip $s=1,0$. As can be seen from the figure, these curves have clearly expressed maxima corresponding to different capacitor capacitance values.

The results of calculating the dependence of current and active and reactive power in relative units on capacitance capacitors are shown in Fig. 6.

As can be seen from Fig. 6, at the capacitance of the capacitors 600, μF there is a total compensation of the reactive power of the IM. There is overcompensation in the case of its increase (reactive power changes the sign to negative).

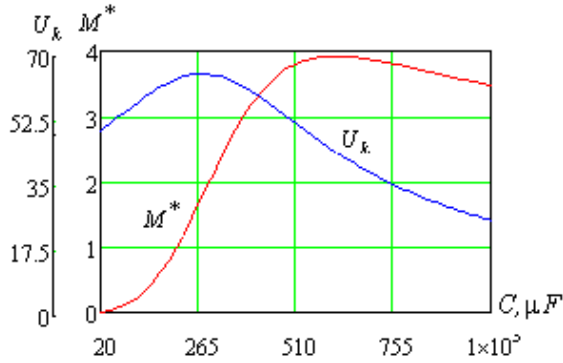


Fig. 5. Dependences on the capacitance of capacitors of RMS voltage on capacitors (U_k) and relative value of the electromagnetic torque (M^*) at slip $s = 1,0$

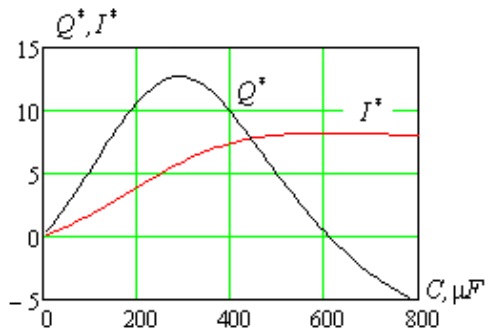


Fig. 6. Dependences of relative values of current (I^*) and reactive powers (Q^*) on the capacitance (C) of capacitors

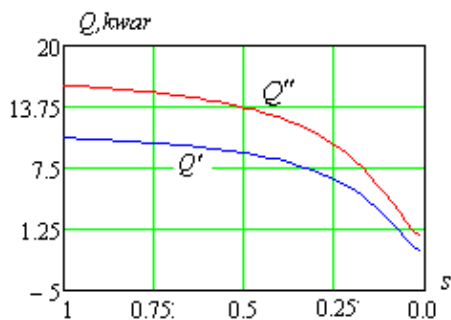


Fig. 7. Dependence on the slip of reactive power at the input of the electric drive system (Q') and the input of the motor (Q'') with series-connected capacitors $C=300 \mu F$

From those shown in Fig. 7, dependences offer how much the reactive power consumed by the electric drive

system changes due to the connection of capacitors in series to the IM.

V. CONCLUSION

1. Mathematical models for numerical analysis of dynamic modes and static characteristics of IM with series compensation of reactive power based on the system of differential equations of electromechanical equilibrium written in three-phase fixed coordinates are developed. Based on them, calculation algorithms have been developed, and computer models have been created to research the influence of capacitance on the dynamics of IM start-up and its static characteristics.

2. The calculation of static characteristics is based on the projection method for solving the boundary value problem for the DE system of electric equilibrium of the IM circuits, the essential functions of cubic splines, and the method of parametric differentiation. The result of the calculation is the periodic dependence of the coordinates. The projection method makes it possible to obtain them in the timeless domain, and the method of parametric differentiation - to investigate the effect of changing any parameter on the nature of the change of coordinates during the period.

REFERENCES

- [1] Yu.S. Zhelezko, Energy losses. Reactive power. Power quality M.:ENAS, 2009. (Russian)
- [2] V.N. Radkevych, M.Yu. Tarasova, "Assessment of the degree of reduction of active power losses in transmission lines with reactive power compensation," Energy. Izv. vyssh. ucheb. zavedenij i energetich. Ob'edinenij SNG, 2016, vol.59, no. 1, pp.5-13. (Russian)
- [3] O.Yu. Davydov, O.V. Bialobrzhesky, 'Analysis of reactive power compensation in electrical systems," Visnyk Kremenchutskoho DU im. M. Ostrohradskoho, 2010 (62), issue 3, p.1. pp.132-136. (Ukrainian)
- [4] K.S. Yolkin, A.D. Kolosov, S. A. Nebogin, "Application of series-capacitive compensation units to increase the useful power factor. Modern technologies. System analysis. Modeling," 2018, vol. 57, no. 1, pp. 23-30. doi: 10.26731/1813-9108.2018.1(57).23. (Russian)
- [5] V.S. Malyar, O.Ye. Hamola, V.S. Maday, I.I. Vasylychshyn, "Mathematical modeling of starting modes of induction motors with squirrel-cage rotor," Electrical Engineering & Electromechanics, 2021, no. 2, pp. 9-15. doi: <https://doi.org/10.20998/2074-272X.2021.2.02>
- [6] A.N. Besarab, V.N. Nevol'nichenko, M.Yu. SHabovta, "Research of transients during individual reactive power compensation of an induction motor," Electrical engineering and electrical equipment, 2007, issue 68, pp.39-44. (Russian)
- [7] V. Malyar, O. Hamola, V. Maday, I. Vasylychshyn, "Static characteristics of asynchronous motors with series reactive power compensation," 9th International conference on advanced computer information technologies: conference proceedings, June 5-7, 2019, Ceske Budejovice, Czech Republic, 2019, pp. 141-144.
- [8] V.H. Rudnytskyi, V.V. Bondarenko, "Analysis of the occurrence of self-excitation of induction motors with series switching on the capacitor in the device for voltage and reactive power control," Electrical engineering and electrical equipment, 2006, issue. 66, pp. 232-233. (Ukrainian)
- [9] V.S. Malyar, O.Ye. Hamola, V.S. Maday, "Calculation of capacitors for starting up a three-phase asynchronous motor fed by single-phase power supply," Computational problems of electrical engineering: proceedings of 17th International Conference, 8 November 2016, pp. 1-4.
- [10] V.S. Maliar, A.V. Maliar, "Mathematical modeling of periodic modes of operation of electrical devices," Electronic modeling, 2005, vol. 27, no. 3, pp. 39-53. (Russian)
- [11] R.V. Filts, Mathematical foundations of the theory of electromechanical transducers, K: Naukova dumka, 1979. (Russian)

An Excitation Control of an Autonomous Synchronous Generator with a Current-Compounding Loop

Andriy Kutsyk^{1,2}, Mykola Semeniuk², Valeriy Misiurenko²

¹ University of Science and Technology, Bydgoszcz, Poland

² Lviv Polytechnic National University, Lviv, Ukraine

Andrii.S.Kutsyk@lpnu.ua, Mykola.B.Semeniuk@lpnu.ua, Valerii.O.Misiurenko@lpnu.ua

Abstract— the article deals with autonomous synchronous generator, which is used to supply electric power to remote and isolated areas where power grid is absent. There are three types of excitation regulation: closing control, disturbance-compensating control and combined approach of excitation control. An error-closing control of excitation system is realized by an automatic voltage regulator. A disturbance-compensating control is realized by a current-compounding loop. The voltage control quality of autonomous synchronous generator with three type of excitation regulation under sharp load variations, investigation of an influence of compound-loop parameters on voltage control quality is analyzed.

Keywords— *compounding excitation system; autonomous synchronous generator; voltage control*

I. INTRODUCTION

The autonomous synchronous generators (ASG) are used widely to supply electric power to remote and isolated areas where power grid is absent. The main task of the ASG excitation system is providing a required quality of terminal-voltage regulation [1,2].

There are three types of ASG excitation regulation approaches: error-closing control, disturbance-compensating control and combined approach of excitation control[1]. An error-closing control of excitation system is realized by an Automatic Voltage Regulator (AVR) [3,4]. Thus, a disturbance-compensating control is realized by a compounding loop [5,6,7].

The compound loops of disturbance-compensating control of the excitation are used in two types: current compound excitation systems [5,6] and phase-compounding excitation systems [7,8,9,10]. The feature of phase-compounding excitation systems is that these systems improve the voltage control quality under sharp load variations, and under short circuit on generator output [11,12].

The electromechanical system with ASG and error-closing excitation control is shown in Figure 1. The field current of ASG is formed by controlled rectifier (Rectifier 1), which is connected to the Power voltage transformer (Power PT). The input of voltage transformer is connected to the terminals of ASG. The terminal voltage regulation of ASG is regulated by AVR.

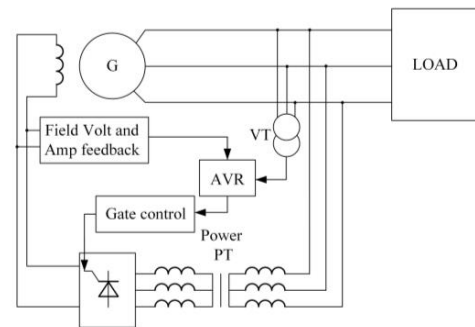


Fig. 1. Bloc diagram of electromechanical system with autonomous synchronous generator and controlled rectifier (error-closing control)

The electromechanical system with ASG and disturbance-compensating excitation control is shown in Figure 2. The field current of ASG in such system is sum of non-controlled rectifier (Rectifier 1) current and non-controlled rectifier (Rectifier 2) current which is proportional to the ASG stator current. The terminal voltage regulation of ASG is regulated by current-compounding loop which consist of non-controlled rectifier (Rectifier 2) and Power current transformer (Power CT).

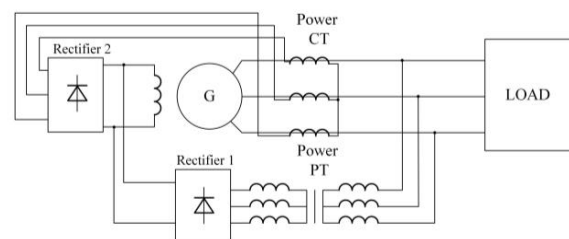


Fig. 2. Bloc diagram of electromechanical system with autonomous synchronous generator and non-controlled rectifier and current-compounding loop (disturbance-compensating control)

The ASG field current in system with combined approach of excitation control is sum of controlled rectifier (Rectifier 1) current and non-controlled rectifier (Rectifier 2) current which is proportional to the ASG stator current (Figure 3). The ASG terminal voltage regulation is regulated by AVR and current-compounding loop.

AVR is used in electromechanical system with error-closing control and combined approach of ASG excitation control and realizes PI control technique.

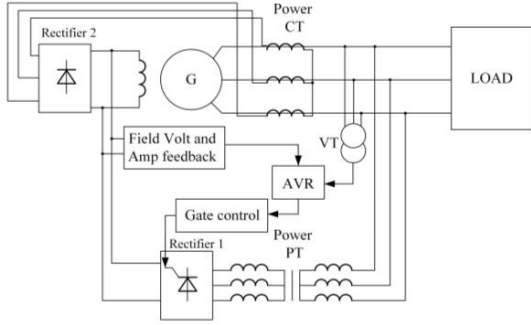


Fig. 3. Bloc diagram of electromechanical system with autonomous synchronous generator and controlled rectifier and current-compounding loop (combined approach of excitation control)

The main task of the article is analyzed of the voltage control quality of autonomous synchronous generator with three types of ASG excitation control: error-closing control, disturbance-compensating control and combined approach of excitation control.

II. MATHEMATICAL MODEL AND ANALYTICAL EXPLANATION

The mathematical model of electromechanical system with ASG and current-compounding loop is based on the method of average voltages in the integration step. The mathematical model of the ASG is developed in phase coordinates and takes into consideration the non-linearity of the magnetic circuit characteristics and the influence of the rotor damper system [13].

According to power-circuit calculation scheme (Figure 4) mathematical model of the electromechanical system with ASG consist of the ASG and Controlled Rectifier, RL-branches, Power Network and resistance-inductive Load. Current-compounding loop is represented as current source and diode, which is connected in parallel to the field winding of ASG as shown in Figure 4. Power-network voltage is proportional to terminal voltage of ASG (self-excitation system).

Mathematical model of current source is represented according to follow equation:

$$I_{\text{Rect}2} = \frac{g_A}{k_{CT}} i_A + \frac{g_B}{k_{CT}} i_B + \frac{g_C}{k_{CT}} i_C, \quad (1)$$

where g_A, g_B, g_C – A, B, C phase conductance's of the non-controlled rectifier 2, k_{CT} – ratio of the power current transformer, i_A, i_B, i_C – ASG stator currents.

The field current of ASG with compounding loop increases non-proportional to increase of the current of the non-controlled rectifier 2 (current of the current source), because the rectifier 1 current (current of the voltage source) is reduced. Such currents' redistribution of ASG excitation system in steady mode is determined by the following equations according to [8]:

$$\Delta I_f = \frac{k_u \Delta U_g + k_i \cdot \Delta I_g}{\left(1 + \frac{R_f}{R_w}\right)}, \quad \Delta I_{\text{Rect}1} = \frac{k_u \Delta U_g - k_i \Delta I_g}{\left(1 + \frac{R_w}{R_f}\right)}. \quad (2)$$

where $\Delta I_{\text{Rect}1}$ – increment of the current at the output of the Rectifier 1, k_i – coefficient, which takes into account transformer ratio of current transformer and coefficient of the non-controlled Rectifier 2, ΔU_g – increment of terminal voltage of ASG, ΔI_g – increment of stator current of ASG, k_u – coefficient, which takes into account transformer ratio of voltage transformer and coefficient of the rectifier 1, R_f – resistance of the field winding, R_w – internal resistance of excitation voltage source of ASG.

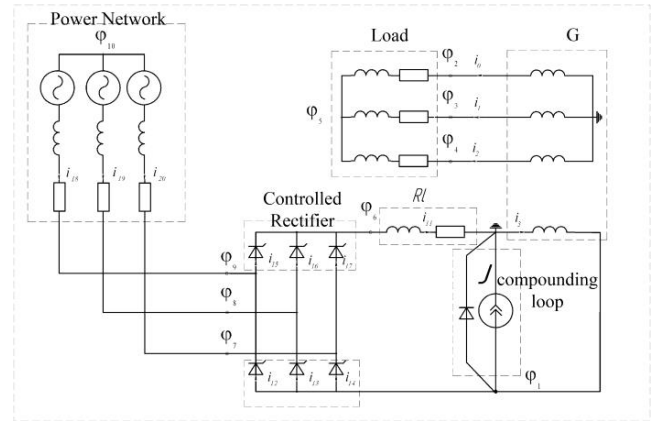


Fig. 4. Power-circuit calculation scheme of the electromechanical system with ASG and current-compounding loop

According to equations (2) the influence of the stator current ΔI_g on the excitation current I_f depends on the internal resistance of the excitation voltage source. The increasing of internal resistance will lead to a decrease in the drain of current at the output of the voltage source $\Delta I_{\text{Rect}1}$ and increase the field current of ASG.

III. EXPERIMENTAL RESULTS AND MODEL VERIFICATION

The physical experimental unit of ASG with compounding loop (Figure 3, combined approach of excitation control, $k_{CT}=2,0$) has been developed to proof adequacy of the model. Experimental and simulation results are shown in Figure 6 – Figure 10 in case using controlled Rectifier 1 without AVR.

Experimental static characteristics of ASG with compounding loop (Figure 5) proof that the compounding loop provides enough terminal-voltage control quality for wide range of the stator current changes without using AVR.

Static characteristics of ASG with compounding loop are corresponded to the equations (2).

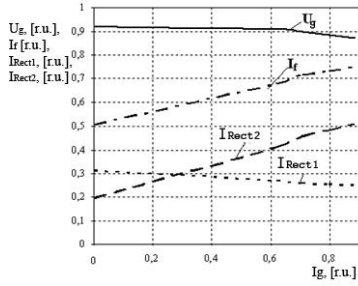


Fig. 5. Experimental static characteristics of ASG with compounding loop

The ASG with compounding loop provides sufficient accuracy of the terminal-voltage control (static error - 5%, Figure 6) without AVR in the case of a sharp load changing of ASG in a wide range (up to 80% of nominal value). An increase of field current (Figure 7) in this mode is provided by increasing current on at the output of the non-controlled rectifier 2 (compounding current).

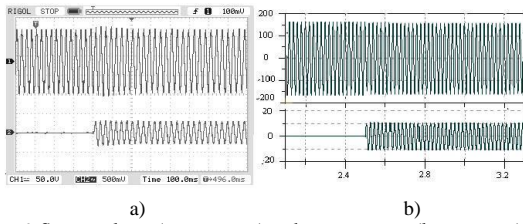


Fig. 6. Stator voltage (upper curve) and stator current (lower curve) of ASG in generator's loading mode by using compounding loop and controlled rectifier without AVR: a – experimental results (100 V/scale, 20 A/scale), b – simulation results

The increasing of the compound current provides a decrease of the current at the output of the controlled rectifier 1 (Figure 8) according to question (2).

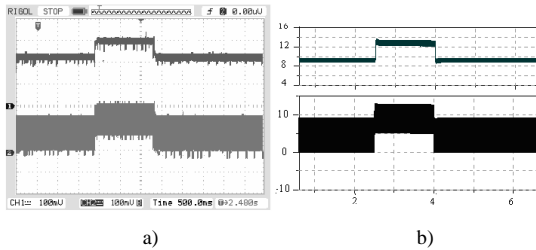


Fig. 7. Field current (upper curve) and compounding current (lower curve) of ASG in generator's loading mode by using compounding loop and controlled rectifier without AVR: a – experimental results (4.5 A/scale, 6 A/scale), b – simulation results

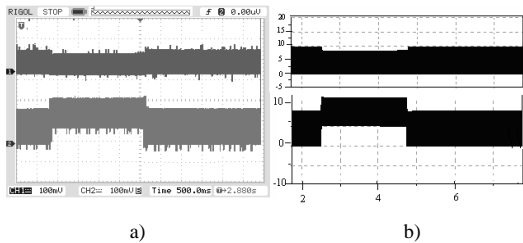


Fig. 8. Rectifier 1 current (upper curve) and compounding current (lower curve) of ASG in generator's loading mode by using compounding loop and controlled rectifier without AVR: a – experimental results (4.5 A/scale, 6 A/scale), b – simulation results

The field current of ASG decreases to zero not instantly in de-excitation mode (Figure 9). This is explained that field current of ASG flows through the diodes of non-controlled rectifier 2. The rate of the stator-voltage decrease in de-excitation mode is determined by the ASG field current and damping system (Figure 10).

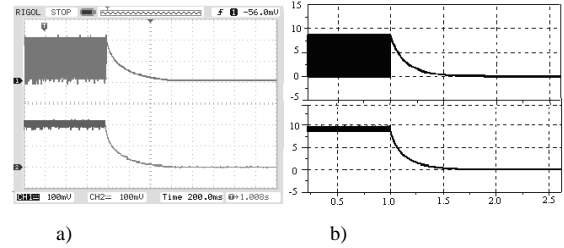


Fig. 9. Compounding current (upper curve) and field current (lower curve) of ASG in de-excitation mode by using compounding loop and controlled rectifier without AVR: a – experimental results (4.5 A/scale, 4.5 A/scale), b – simulation results

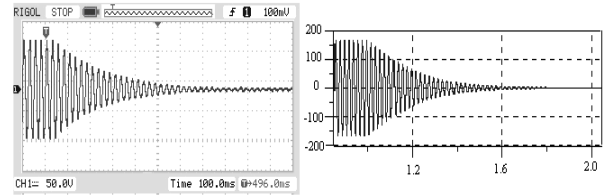


Fig. 10. Stator voltage of ASG in the de-excitation mode by using compounding loop and controlled rectifier without AVR: a – experimental results (100 V/scale), b – simulation results

IV. SIMULATION RESULTS

Simulation results of electromagnetic process in ASG with error-closing control (Figure 1), disturbance-compensating control (Figure 2) and combined approach of excitation control (Figure 3) in initial-excitation mode and ASG loading mode are shown in Figure 11- Figure 14. The resistance-inductive loading of ASG provides in 0,5 s.

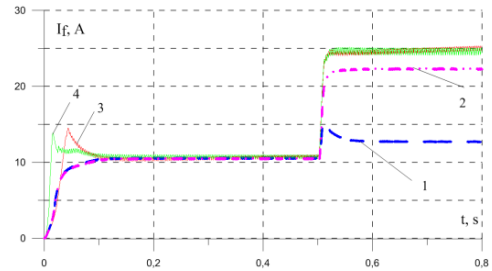


Fig. 11. ASG field current in case disturbance-compensating control (curve 1 for $k_{CT}=2,0$ and curve 2 for $k_{CT}=1,0$), error-closing control (curve 3) combined approach of excitation control (curve 4 for $k_{CT}=2,0$)

The ASG disturbance-compensating control provides sufficient accuracy of the stator voltage control (static error - 20% for $k_{CT}=2,0$ and static error - 4,4 % for $k_{CT}=1,0$) in ASG loading mode (Figure 12, a).

The ASG error-closing control and combined approach of excitation control provides high accuracy of the stator voltage control (static error is absent, Figure 12, b).

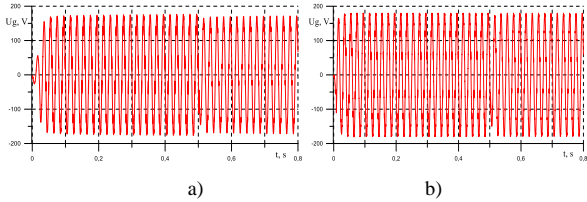


Fig. 12. ASG stator voltage in case disturbance-compensating control for $k_{CT}=1,0$ (a), combined approach of excitation control for $k_{CT}=2,0$ (b)

The ASG disturbance-compensating control keeps an increase of field current (Figure 11, curve 2) in ASG loading mode due to increase of stator current and respectively current at the output of non-controlled rectifier 2 (compounding current, Figure 14, a). There's current drop at the output of rectifier 1 (Figure 13, a) according to equation (2).

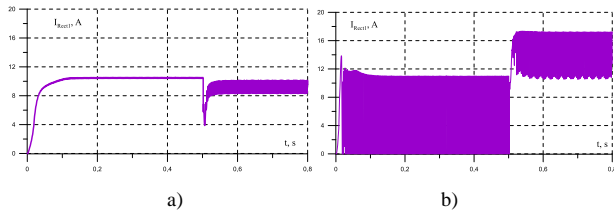


Fig. 13. Current at the output of the rectifier 1 in case disturbance-compensating control for $k_{CT}=1,0$ (a), combined approach of excitation control for $k_{CT}=2,0$ (b)

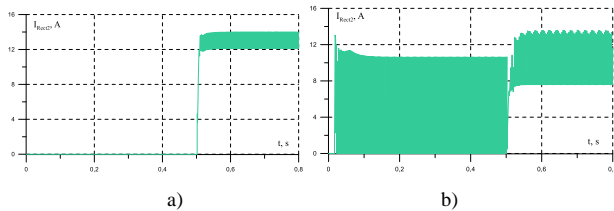


Fig. 14. Compounding current in case disturbance-compensating control for $k_{CT}=1,0$ (a), combined approach of excitation control for $k_{CT}=2,0$ (b)

The combined approach of ASG excitation control keeps an increase of field current (Figure 11, curve 4) in ASG loading mode due to increase of stator current and respectively current at the output of non-controlled rectifier 2 (compounding current, Figure 14, b). AVR provides current increase at the output of rectifier 1 (Figure 13, b) in order to ensure minimal static error of the ASG voltage regulation.

CONCLUSIONS

The ASG error-closing control (Figure 1) provides high accuracy of the stator voltage control in generator loading (static error is zero). The synthesis of such excitation system consists in calculation of AVR parameters.

The ASG disturbance-compensating control (Figure 2) provides sufficient accuracy of the stator voltage control in generator loading (static error is less than 5%). The synthesis of such excitation system consists in calculation of compounding-loop parameters.

The ASG combined approach of excitation control (Figure 3) provides high accuracy of the stator voltage control

in generator loading (static error is zero). The synthesis of such excitation system consists in calculation of AVR parameters and compounding-loop parameters.

APPENDIX

ASG: ratings $P_n = 4,5$ kW, $U_n = 220$ V, $I_n = 11,3$ A, no-load excitation current $I_{f0} = 11,5$ A, rated excitation current $I_{fn} = 25$ A, windings resistances $R_f = 2,0$ Ω , number of pole pairs $p = 2$, Inductances: $L_d = 0.042$ H, $L_{ad} = 0.039$ H, $L_q = 0.035$ H, $L_{aq} = 0.033$ H, $L_{of} = 0.01$ H.

Load resistance $R = 9.2$ Ω . Load inductance $L = 0.02$ H.

REFERENCES

- [1] P. M. Anderson and A. A. Fouad, Power system control and stability, IEEE Press, Piscataway, NJ, USA, 2003.
- [2] R. Seliga, E. Ernest, K. Paciura and N. L. Brown, "Operation of sine-wave voltage source inverter in hybrid genset based autonomous power system," *7th IET International Conference on Power Electronics, Machines and Drives (PEMD 2014)*, 2014, pp. 1-5.
- [3] S. Park, J. Yu, S. Lee, S. Lee and C. Won, "Output voltage control of synchronous generator for ships using a PMG type digital AVR," *2009 IEEE Energy Conversion Congress and Exposition*, 2009, pp. 417-421, doi: 10.1109/ECCE.2009.5316195.
- [4] M. Babescu, R. Boraci, O. Gana and C. Koch-Ciobotaru, "The control of the Diesel-synchronous generator electro-energetic system," *2010 International Joint Conference on Computational Cybernetics and Technical Informatics*, Timisoara, 2010, pp. 581-584.
- [5] J. Meng, H. Lan, T. Lin and F. Liu, "Robust L2 Control Design for Controllable Phase Compounding Excitation System of Marine Diesel Engine Generator," *2012 Asia-Pacific Power and Energy Engineering Conference*, Shanghai, 2012, pp. 1-4.
- [6] S.-H. Park, S.-K. Lee, S.-W. Lee, J.-S. Yu, S.-S. Lee, C.-Y. Won, "Output Voltage Control of a Synchronous Generator for Ships Using Compound Type Digital AVR," in *31st Int. Telecommunications Energy Conf.*, 2009, INTELEC 2009, Oct. 18–22, 2009, pp. 1–6.
- [7] Erceg, G., Tesnjak, S., & Erceg, R. "Modelling and simulation of diesel electrical aggregate voltage controller with current sink," in *Industrial Technology*, 1996.(ICIT'96), Proceedings of The IEEE International Conference on pp. 875-879.
- [8] A. Kutsyk, M. Semeniuk, V. Tutka and T. Galiyanti, "A Pulse-Width Regulation of a Compound Excitation System for a Synchronous Generator," *2018 IEEE 3rd International Conference on Intelligent Energy and Power Systems (IEPS)*, Kharkiv, 2018, pp. 97-100.
- [9] A. Kutsyk, M. Semeniuk, M. Khai and T. Galantiy, "An Experimental Study of a Voltage Control Quality of a Diesel-Engine Synchronous Generator with a Phase-Compounding Excitation System," *2020 IEEE Problems of Automated Electrodrive. Theory and Practice (PAEP)*, 2020, pp. 1-4, doi: 10.1109/PAEP49887.2020.9240899.
- [10] R. Jordan, R. Schaefer, J. Estes and M. Dube "Selecting the excitation system for the additional turbine generator at the Port Wentworth pulp mill," *2004 Ann. Pulp and Paper Industry Techn. Conf.*, 2004, pp. 102-110. doi: 10.1109/PAPCON.2004.1338370/
- [11] Xianlin Liu and C. Q. Liu, "Analysis on oscillations between two generators in a hydro power plant and development of math model for a compound excitation system," *Proceedings. International Conference on Power System Technology*, Kunming, China, 2002, pp. 1254-1258 vol.2.
- [12] A. Kutsyk, M. Semeniuk and O. Kuznyetsov, "An application of fuzzy voltage regulator to a static excitation system of a phase compound synchronous generator," *2017 IEEE International Young Scientists Forum on Applied Physics and Engineering*, Lviv, 2017, pp. 46-49.
- [13] Plakhtyna, O.; Kutsyk, A.; Semeniuk, M. Real-Time Models of Electromechanical Power Systems, Based on the Method of Average Voltages in Integration Step and Their Computer Application. *Energies* **2020**, *13*, 2263.

Mathematical model of analysis of wave electromagnetic processes in three-winding transformers

Mykhailo Seheda

Institute of Power Engineering and Control Systems

Lviv Polytechnic National University,

Lviv, Ukraine

mykhailo.s.seheda@lpnu.ua

Petro Gogoluyk

Institute of Power Engineering and Control Systems

Lviv Polytechnic National University,

Lviv, Ukraine

petro.f.hoholiuk@lpnu.ua

Yurii Blyznak

Institute of Power Engineering and Control Systems

Lviv Polytechnic National University,

Lviv, Ukraine

yurii.v.blyznak@lpnu.ua

Abstract – A mathematical model for the research of wave processes in three-winding transformers, with adequate considering of electromagnetic connections between windings and turns of windings, is created.

Index Terms – wave process, mathematical model, transformer, partial differential equation, initial and boundary conditions.

I. INTRODUCTION

The need to consider the electromagnetic connections between the winding and turns of the winding of three-winding transformers, taking into account the main magnetic flux, ensures the proper adequacy of the results of mathematical modeling. The development of mathematical models for the research of wave processes in transformers, consider these factors, is relevant. The action of pulsed overvoltage on the insulation of transformers is crucial and depends on the proper coordination of insulation.

For a long time, the research of wave processes in the windings of transformers, without taking into account the electromagnetic connection between the windings and the connection between the turns of the windings, was carried out according to the substitution scheme of one winding [1 - 5]. At present, the methods of analysis of wave processes in the windings of transformers, consider the electromagnetic relationships between the windings and turns of the windings of three-winding transformers, are aimed at developing mathematical models [6 - 8]. Modeling by the «white box» method requires the formation of mathematical models of the elements of the electric power system (EPS), consider all the parameters of the substitution scheme of the element, which allows researching its internal transients [9 - 10].

II. EASE OF USE

A. Mathematical model for the research of wave processes in three-winding transformers

The purpose of the article is to create a mathematical model for the research of wave processes in three-winding transformers, taking into account the electromagnetic connections between the windings and the turns of the windings.

The mathematical model of the three-winding transformers is created based on the substitution scheme in fig. 1.

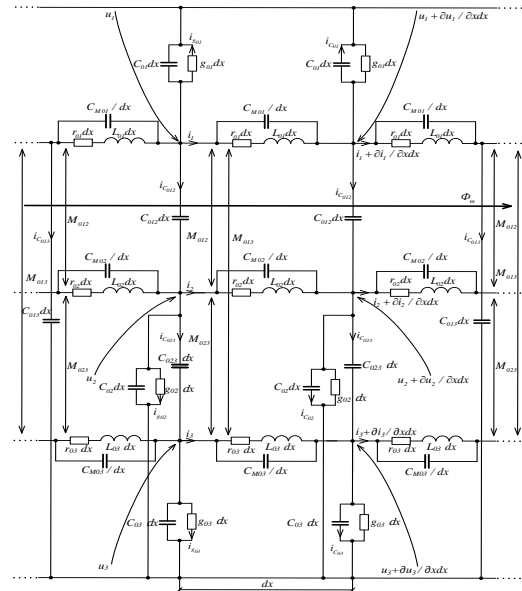


Fig. 1. Substitution scheme of the longitudinal element of a three-winding transformer.

The equation of change of currents flowing through the windings is written basing on Kirchhoff's current law (1 st law).

$$-\frac{\partial i_1(x,t)}{\partial x} = g_{01}u_1(x,t) + (C_{012} + C_{013} + C_{01}) \frac{\partial u_1(x,t)}{\partial t} - C_{012} \frac{\partial u_2(x,t)}{\partial t} - C_{013} \frac{\partial u_3(x,t)}{\partial t} - C_{M01} \frac{\partial^3 u_1(x,t)}{\partial x^2 \partial t}; \quad (1)$$

$$-\frac{\partial i_2(x,t)}{\partial x} = g_{02}u_2(x,t) - C_{012} \frac{\partial u_1(x,t)}{\partial t} + (C_{012} + C_{023} + C_{02}) \frac{\partial u_2(x,t)}{\partial t} - C_{023} \frac{\partial u_3(x,t)}{\partial t} - C_{M02} \frac{\partial^3 u_2(x,t)}{\partial x^2 \partial t}; \quad (2)$$

$$-\frac{\partial i_3(x,t)}{\partial x} = g_{03}u_3(x,t) - C_{013} \frac{\partial u_1(x,t)}{\partial t} - C_{023} \frac{\partial u_2(x,t)}{\partial t} + (C_{013} + C_{023} + C_{03}) \frac{\partial u_3(x,t)}{\partial t} - C_{M03} \frac{\partial^3 u_3(x,t)}{\partial x^2 \partial t}. \quad (3)$$

where $i_1, i_2, i_3, u_1, u_2, u_3$ – respectively, the currents and voltages of the transformer windings; $g_{01}, g_{02}, g_{03}, C_{01}, C_{01}, C_{03}$ – conductivity and own capacities of transformer windings per unit of their length; $C_{012}, C_{013}, C_{023}$ – mutual capacities of transformer windings per unit of their length; $C_{M01}, C_{M02}, C_{M03}$ – inter-turn capacitance of windings along the axis per unit of its length.

To increase the adequacy and efficiency of the mathematical model of wave processes, the second group of equations of the electromagnetic state of the transformer was improved by taking into account the main magnetic flux ϕ_m , eigenvalues, and mutual inter-turn, mutual inter-turn scattering fluxes.

The equation of voltage fall per unit length of windings is written basing on Kirchhoff's voltage law (2st law).

$$-\frac{\partial u_1(x,t)}{\partial x} = r_{01}i_1(x,t) + L_{01}\frac{\partial i_1(x,t)}{\partial t} + M_{012}\frac{\partial i_2(x,t)}{\partial t} + M_{013}\frac{\partial i_3(x,t)}{\partial t} + \frac{\partial \Psi_{\sigma 1}(x,t)}{\partial t}; \quad (4)$$

$$-\frac{\partial u_2(x,t)}{\partial x} = r_{02}i_2(x,t) + L_{02}\frac{\partial i_2(x,t)}{\partial t} + M_{012}\frac{\partial i_1(x,t)}{\partial t} + M_{023}\frac{\partial i_3(x,t)}{\partial t} + \frac{\partial \Psi_{\sigma 2}(x,t)}{\partial t}; \quad (5)$$

$$-\frac{\partial u_3(x,t)}{\partial x} = r_{03}i_3(x,t) + L_{03}\frac{\partial i_3(x,t)}{\partial t} + M_{013}\frac{\partial i_1(x,t)}{\partial t} + M_{023}\frac{\partial i_2(x,t)}{\partial t} + \frac{\partial \Psi_{\sigma 3}(x,t)}{\partial t}, \quad (6)$$

where $L_{01} = L_{\mu 0} + L_{\sigma 01}$; $L_{02} = \frac{L_{\mu 0}}{k_{12}^2} + L_{\sigma 02}$; $L_{03} = \frac{L_{\mu 0}}{k_{13}^2} + L_{\sigma 03}$;

$M_{012} = \frac{L_{\mu 0}}{k_{12}} + M_{\sigma 012}$; $M_{013} = \frac{L_{\mu 0}}{k_{13}} + M_{\sigma 013}$; $M_{230} = \frac{L_{\mu 0}}{k_{12}k_{13}} + M_{\sigma 230}$;

$L_{\sigma 01}, L_{\sigma 02}, L_{\sigma 03}, M_{\sigma 012}, M_{\sigma 013}, M_{\sigma 023}$ – own and mutual inductances of scattering of elements of windings; $\Psi_{\sigma 1}, \Psi_{\sigma 2}, \Psi_{\sigma 3}$ – flux coupling of elements of length from own and mutual inter-turn inductance of scattering of windings; $L_{\mu 0}$ – inductance of the magnetic system of the transformer, k_{12}, k_{13} – transformer transformation ratio between windings.

Expressions for finding derivatives of flux couplings are found as follows

$$\frac{\partial \Psi_{\sigma 1}}{\partial t} = \sum_{0,x}^{x,l} (M_{\sigma 1}(x,s)\frac{\partial i_1}{\partial t} + M_{\sigma 12}(x,s)\frac{\partial i_2}{\partial t} + M_{\sigma 13}(x,s)\frac{\partial i_3}{\partial t}) ds; \quad (7)$$

$$\frac{\partial \Psi_{\sigma 2}}{\partial t} = \sum_{0,x}^{x,l} (M_{\sigma 2}(x,s)\frac{\partial i_2}{\partial t} + M_{\sigma 12}(x,s)\frac{\partial i_1}{\partial t} + M_{\sigma 23}(x,s)\frac{\partial i_3}{\partial t}) ds; \quad (8)$$

$$\frac{\partial \Psi_{\sigma 3}}{\partial t} = \sum_{0,x}^{x,l} (M_{\sigma 3}(x,s)\frac{\partial i_3}{\partial t} + M_{\sigma 13}(x,s)\frac{\partial i_1}{\partial t} + M_{\sigma 23}(x,s)\frac{\partial i_2}{\partial t}) ds, \quad (9)$$

where $M_{\sigma 1}(x,s), M_{\sigma 2}(x,s), M_{\sigma 3}(x,s), M_{\sigma 12}(x,s), M_{\sigma 13}(x,s), M_{\sigma 23}(x,s)$ – self and mutual inter-turn inductances of scattering of primary, secondary and tertiary windings; l – windings length, x – instant longitudinal coordinate, s – the instant coordinate, which determines the distance from place x to the coordinate of any other place on the axis of the winding.

Equations (1) - (3) are differentiated by t

$$-\frac{\partial^2 i_1(x,t)}{\partial x \partial t} = g_{01}\frac{\partial u_1(x,t)}{\partial t} + (C_{012} + C_{013} + C_{01})\frac{\partial^2 u_1(x,t)}{\partial t^2} - C_{012}\frac{\partial^2 u_2(x,t)}{\partial t^2} - C_{013}\frac{\partial^2 u_3(x,t)}{\partial t^2} - C_{M01}\frac{\partial^4 u_1(x,t)}{\partial x^2 \partial t^2}; \quad (10)$$

$$-\frac{\partial^2 i_2(x,t)}{\partial x \partial t} = g_{02}\frac{\partial u_2(x,t)}{\partial t} - C_{012}\frac{\partial^2 u_1(x,t)}{\partial t^2} + (C_{012} + C_{023} + C_{01})\frac{\partial^2 u_2(x,t)}{\partial t^2} - C_{023}\frac{\partial^2 u_3(x,t)}{\partial t^2} - C_{M02}\frac{\partial^4 u_2(x,t)}{\partial x^2 \partial t^2}; \quad (11)$$

$$-\frac{\partial^2 i_3(x,t)}{\partial x \partial t} = g_{03}\frac{\partial u_3(x,t)}{\partial t} - C_{013}\frac{\partial^2 u_1(x,t)}{\partial t^2} - C_{023}\frac{\partial^2 u_2(x,t)}{\partial t^2} + (C_{013} + C_{023} + C_{03})\frac{\partial^2 u_3(x,t)}{\partial t^2} - C_{M03}\frac{\partial^4 u_3(x,t)}{\partial x^2 \partial t^2}. \quad (12)$$

Equation (4) - (6) is differentiated by x , obtain

$$-\frac{\partial^2 u_1(x,t)}{\partial x^2} = r_{01}\frac{\partial i_1(x,t)}{\partial x} + L_{01}\frac{\partial^2 i_1(x,t)}{\partial t \partial x} + M_{012}\frac{\partial^2 i_2(x,t)}{\partial t \partial x} + M_{013}\frac{\partial^2 i_3(x,t)}{\partial t \partial x} + \frac{\partial^2 \Psi_{\sigma 1}(x,t)}{\partial x \partial t}; \quad (13)$$

$$-\frac{\partial^2 u_2(x,t)}{\partial x} = r_{02}\frac{\partial i_2(x,t)}{\partial x} + L_{02}\frac{\partial^2 i_2(x,t)}{\partial t \partial x} + M_{012}\frac{\partial^2 i_1(x,t)}{\partial t \partial x} + M_{023}\frac{\partial^2 i_3(x,t)}{\partial t \partial x} + \frac{\partial^2 \Psi_{\sigma 2}(x,t)}{\partial t \partial x}; \quad (14)$$

$$-\frac{\partial^2 u_3(x,t)}{\partial x^2} = r_{03}\frac{\partial i_3(x,t)}{\partial x} + L_{03}\frac{\partial^2 i_3(x,t)}{\partial t \partial x} + M_{013}\frac{\partial^2 i_1(x,t)}{\partial t \partial x} + M_{230}\frac{\partial^2 i_2(x,t)}{\partial t \partial x} + \frac{\partial^2 \Psi_{\sigma 3}(x,t)}{\partial t \partial x}. \quad (15)$$

Equations (1) - (3) and (10) - (12) are substituted in (13) - (15), respectively, as a result obtain

$$\begin{aligned}
& -\frac{\partial^2 u_1(x,t)}{\partial x^2} = r_{01}(-g_{01}u_1(x,t) - (C_{012} + C_{013} + C_{01})\frac{\partial u_1(x,t)}{\partial t} + \\
& + C_{012}\frac{\partial u_2(x,t)}{\partial t} + C_{013}\frac{\partial u_3(x,t)}{\partial t} + C_{M01}\frac{\partial^3 u_1(x,t)}{\partial x^2 \partial t}) + \\
& + L_{01}(-g_{01}\frac{\partial u_1(x,t)}{\partial t} - (C_{012} + C_{013} + C_{01})\frac{\partial^2 u_1(x,t)}{\partial t^2} + \\
& + C_{012}\frac{\partial^2 u_2(x,t)}{\partial t^2} + C_{013}\frac{\partial^2 u_3(x,t)}{\partial t^2} + C_{M01}\frac{\partial^4 u_1(x,t)}{\partial x^2 \partial t^2}) + \\
& + M_{012}(-g_{02}\frac{\partial u_2(x,t)}{\partial t} + C_{012}\frac{\partial^2 u_1(x,t)}{\partial t^2} - \\
& - (C_{012} + C_{023})\frac{\partial^2 u_2(x,t)}{\partial t^2} + C_{023}\frac{\partial^2 u_3(x,t)}{\partial t^2} + \\
& + C_{M02}\frac{\partial^4 u_2(x,t)}{\partial x^2 \partial t^2}) + M_{013}(-g_{03}\frac{\partial u_3(x,t)}{\partial t} + \\
& + C_{013}\frac{\partial^2 u_1(x,t)}{\partial t^2} + C_{023}\frac{\partial^2 u_2(x,t)}{\partial t^2} - \\
& - (C_{013} + C_{023} + C_{03})\frac{\partial^2 u_3(x,t)}{\partial t^2} + \\
& + C_{M03}\frac{\partial^4 u_3(x,t)}{\partial x^2 \partial t^2}) + \frac{\partial^2 \Psi_{\sigma 1}(x,t)}{\partial t \partial x}; \\
& -\frac{\partial^2 u_2(x,t)}{\partial x} = r_{02}(-g_{02}u_2(x,t) + C_{012}\frac{\partial u_1(x,t)}{\partial t} - \\
& - (C_{012} + C_{023} + C_{02})\frac{\partial u_2(x,t)}{\partial t} + C_{023}\frac{\partial u_3(x,t)}{\partial t} + \\
& + C_{M02}\frac{\partial^3 u_2(x,t)}{\partial x^2 \partial t}) + L_{02}(-g_{02}\frac{\partial u_2(x,t)}{\partial t} + \\
& + C_{012}\frac{\partial^2 u_1(x,t)}{\partial t^2} - (C_{012} + C_{023} + C_{02})\frac{\partial^2 u_2(x,t)}{\partial t^2} + \\
& + C_{023}\frac{\partial^2 u_3(x,t)}{\partial t^2} + C_{M02}\frac{\partial^4 u_2(x,t)}{\partial x^2 \partial t^2}) + \\
& + M_{012}(-g_{01}\frac{\partial u_1(x,t)}{\partial t} - (C_{012} + C_{013} + C_{01})\frac{\partial^2 u_1(x,t)}{\partial t^2} + \\
& + C_{012}\frac{\partial^2 u_2(x,t)}{\partial t^2} + C_{013}\frac{\partial^2 u_3(x,t)}{\partial t^2} + C_{M01}\frac{\partial^4 u_1(x,t)}{\partial x^2 \partial t^2}) + \\
& + M_{023}(-g_{03}\frac{\partial u_3(x,t)}{\partial t} + C_{013}\frac{\partial^2 u_1(x,t)}{\partial t^2} + \\
& + C_{023}\frac{\partial^2 u_2(x,t)}{\partial t^2} - (C_{013} + C_{023} + C_{03})\frac{\partial^2 u_3(x,t)}{\partial t^2} + \\
& + C_{M03}\frac{\partial^4 u_3(x,t)}{\partial x^2 \partial t^2}) + \frac{\partial^2 \Psi_{\sigma 2}(x,t)}{\partial x \partial t}; \\
& -\frac{\partial^2 u_3(x,t)}{\partial x^2} = r_{03}(-g_{03}u_3(x,t) + C_{013}\frac{\partial u_1(x,t)}{\partial t} + \\
& + C_{023}\frac{\partial u_2(x,t)}{\partial t} - (C_{013} + C_{023} + C_{03})\frac{\partial u_3(x,t)}{\partial t} + \\
& + C_{M03}\frac{\partial^3 u_3(x,t)}{\partial x^2 \partial t}) + L_{03}(-g_{03}\frac{\partial u_3(x,t)}{\partial t} + \\
& + C_{013}\frac{\partial^2 u_1(x,t)}{\partial t^2} + C_{023}\frac{\partial^2 u_2(x,t)}{\partial t^2} - \\
& - (C_{013} + C_{023} + C_{03})\frac{\partial^2 u_3(x,t)}{\partial t^2} + C_{M03}\frac{\partial^4 u_3(x,t)}{\partial x^2 \partial t^2}) +
\end{aligned} \tag{16}$$

$$\begin{aligned}
& + M_{013}(-g_{01}\frac{\partial u_1(x,t)}{\partial t} - (C_{012} + C_{013} + C_{01})\frac{\partial^2 u_1(x,t)}{\partial t^2} + \\
& + C_{012}\frac{\partial^2 u_2(x,t)}{\partial t^2} + C_{013}\frac{\partial^2 u_3(x,t)}{\partial t^2} + C_{M01}\frac{\partial^4 u_1(x,t)}{\partial x^2 \partial t^2}) + \\
& + M_{023}(-g_{02}\frac{\partial u_2(x,t)}{\partial t} + C_{012}\frac{\partial^2 u_1(x,t)}{\partial t^2} - \\
& - (C_{012} + C_{023})\frac{\partial^2 u_2(x,t)}{\partial t^2} + C_{023}\frac{\partial^2 u_3(x,t)}{\partial t^2} + \\
& + C_{M02}\frac{\partial^4 u_2(x,t)}{\partial x^2 \partial t^2}) + \frac{\partial^2 \Psi_{\sigma 3}(x,t)}{\partial x \partial t}.
\end{aligned} \tag{18}$$

Having grouped equation (16), entering the notation

$$\begin{aligned}
a_{11} &= r_{01}g_{01}; b_{11} = r_{01}(C_{01} + C_{012} + C_{013}) + L_{01}g_{01}; \\
c_{11} &= -r_{01}C_{012} + M_{012}g_{02}; d_{11} = -r_{01}C_{013} + M_{013}g_{03}; \\
e_{11} &= L_{01}(C_{01} + C_{012} + C_{013}) - M_{012}C_{012} - M_{013}C_{013}; \\
f_{11} &= -L_{01}C_{012} + M_{012}(C_{02} + C_{012} + C_{023}) - M_{013}C_{023}; \\
g_{11} &= -L_{01}C_{013} - M_{012}C_{023} + M_{013}(C_{03} + C_{013} + C_{023}); \\
h_{11} &= -r_{01}C_{M01}; i_{11} = -L_{01}C_{M01}; j_{11} = -M_{012}C_{M02}; \\
k_{11} &= -M_{013}C_{M03}.
\end{aligned}$$

Equation (16) takes the form

$$\begin{aligned}
\frac{\partial^2 u_1(x,t)}{\partial x^2} &= a_{11}u_1(x,t) + b_{11}\frac{\partial u_1(x,t)}{\partial t} + c_{11}\frac{\partial u_2(x,t)}{\partial t} + \\
d_{11}\frac{\partial u_3(x,t)}{\partial t} &+ e_{11}\frac{\partial^2 u_1(x,t)}{\partial t^2} + f_{11}\frac{\partial^2 u_2(x,t)}{\partial t^2} + \\
+ g_{11}\frac{\partial^2 u_3(x,t)}{\partial t^2} &+ h_{11}\frac{\partial^3 u_1(x,t)}{\partial^2 x \partial t} + i_{11}\frac{\partial^4 u_1(x,t)}{\partial x^2 \partial t^2} + \\
+ j_{11}\frac{\partial^4 u_2(x,t)}{\partial x^2 \partial t^2} &+ k_{11}\frac{\partial^4 u_3(x,t)}{\partial x^2 \partial t^2} + \frac{\partial^2 \Psi_{\sigma 1}(x,t)}{\partial x \partial t}.
\end{aligned} \tag{19}$$

Having grouped equation (17), entering the notation

$$\begin{aligned}
a_{21} &= r_{02}g_{02}; b_{21} = -r_{02}C_{01} + M_{012}g_{01}; \\
c_{21} &= r_{02}(C_{02} + C_{012} + C_{023}) + L_{02}g_{02}; \\
d_{21} &= -r_{02}C_{023} + M_{023}g_{02}; \\
e_{21} &= -L_{02}C_{012} + M_{012}(C_{01} + C_{012} + C_{013}) - M_{023}C_{013}; \\
f_{21} &= L_{02}(C_{02} + C_{012} + C_{023}) - M_{012}C_{012} - M_{023}C_{023}; \\
g_{21} &= -L_{02}C_{023} - M_{012}C_{013} + M_{023}(C_{03} + C_{013} + C_{023}); \\
h_{21} &= -r_{02}C_{M02}; i_{21} = -L_{02}C_{M02}; j_{11} = -M_{012}C_{M01}; \\
k_{21} &= -M_{023}C_{M03}.
\end{aligned}$$

Equation (17) takes the form

$$\begin{aligned}
\frac{\partial^2 u_2(x,t)}{\partial x^2} &= a_{21}u_2(x,t) + b_{21}\frac{\partial u_1(x,t)}{\partial t} + c_{21}\frac{\partial u_2(x,t)}{\partial t} + \\
d_{21}\frac{\partial u_3(x,t)}{\partial t} &+ e_{21}\frac{\partial^2 u_1(x,t)}{\partial t^2} + f_{21}\frac{\partial^2 u_2(x,t)}{\partial t^2} +
\end{aligned}$$

$$\begin{aligned}
& + g_{21} \frac{\partial^2 u_3(x,t)}{\partial t^2} + h_{21} \frac{\partial^3 u_2(x,t)}{\partial^2 x \partial t} + i_{21} \frac{\partial^4 u_2(x,t)}{\partial x^2 \partial t^2} + \\
& + j_{21} \frac{\partial^4 u_1(x,t)}{\partial x^2 \partial t^2} + k_{21} \frac{\partial^4 u_3(x,t)}{\partial x^2 \partial t^2} + \frac{\partial^2 \Psi_{\sigma_2}(x,t)}{\partial x \partial t}.
\end{aligned} \quad (20)$$

Having grouped equation (18), entering the notation

$$\begin{aligned}
a_{31} &= r_{03} g_{03}; b_{31} = -r_{03} C_{013} + M_{013} g_{01}; \\
c_{31} &= -r_{03} C_{023} + M_{023} g_{02}; \\
d_{31} &= r_{03} (C_{03} + C_{013} + C_{023}) + L_{03} g_{03}; \\
e_{31} &= -L_{03} C_{013} + M_{013} (C_{01} + C_{012} + C_{013}) - M_{023} C_{013}; \\
f_{31} &= -L_{03} C_{023} - M_{013} C_{012} + M_{023} (C_{02} + C_{012} + C_{023}); \\
g_{31} &= +L_{03} (C_{03} + C_{013} + C_{023}) - M_{013} C_{013} - M_{023} C_{023}; \\
h_{31} &= -r_{03} C_{M03}; i_{31} = -L_{03} C_{M03}; j_{31} = -M_{013} C_{M01}; \\
k_{31} &= -M_{023} C_{M02}.
\end{aligned}$$

Equation (18) takes the form

$$\begin{aligned}
\frac{\partial^2 u_3(x,t)}{\partial x^2} &= a_{31} u_3(x,t) + b_{31} \frac{\partial u_1(x,t)}{\partial t} + c_{31} \frac{\partial u_2(x,t)}{\partial t} + \\
d_{31} \frac{\partial u_3(x,t)}{\partial t} &+ e_{31} \frac{\partial^2 u_1(x,t)}{\partial t^2} + f_{31} \frac{\partial^2 u_2(x,t)}{\partial t^2} + \\
+ g_{31} \frac{\partial^2 u_3(x,t)}{\partial t^2} &+ h_{31} \frac{\partial^3 u_2(x,t)}{\partial^2 x \partial t} + i_{31} \frac{\partial^4 u_2(x,t)}{\partial x^2 \partial t^2} + \\
+ j_{31} \frac{\partial^4 u_1(x,t)}{\partial x^2 \partial t^2} &+ k_{31} \frac{\partial^4 u_3(x,t)}{\partial x^2 \partial t^2} + \frac{\partial^2 \Psi_{\sigma_3}(x,t)}{\partial x \partial t}.
\end{aligned} \quad (21)$$

Initial conditions

$$\begin{aligned}
u_1(x,t)|_{t=0} &= u_1(x) = U_{m1} - k_1 x; \\
\frac{\partial u_1(x,t)}{\partial t} \Big|_{t=0} &= du_1(x) = 0;
\end{aligned} \quad (22)$$

$$\begin{aligned}
u_2(x,t)|_{t=0} &= u_2(x) = U_{m2} - k_2 x; \\
\frac{\partial u_2(x,t)}{\partial t} \Big|_{t=0} &= du_2(x) = 0,
\end{aligned} \quad (23)$$

$$\begin{aligned}
u_3(x,t)|_{t=0} &= u_3(x) = U_{m3} - k_3 x; \\
\frac{\partial u_3(x,t)}{\partial t} \Big|_{t=0} &= du_3(x) = 0; x \in (0;l),
\end{aligned} \quad (24)$$

where U_{m1} , U_{m2} , U_{m3} – respectively, the amplitude values of the voltage of the primary, secondary and tertiary winding of the steady-state; k_1 , k_2 , k_3 – the coefficient of the rate of change of voltage along the windings for the moment of time $t=0$.

Boundary conditions

$$u_1(x,t)|_{x=0} = f_{10}(t) = e_{im}(t); u_1(x,t)|_{x=l} = f_{1l}(t) = 0; \quad (25)$$

$$u_2(x,t)|_{x=0} = f_{20}(t) = 0; u_2(x,t)|_{x=l} = f_{2l}(t) = 0; \quad (26)$$

$$u_3(x,t)|_{x=0} = f_{30}(t) = 0; u_3(x,t)|_{x=l} = f_{3l}(t) = 0. \quad (27)$$

CONCLUSION

The improved mathematical model for analyzing wave processes in power three-winding transformers, with adequate consideration of the transverse electromagnetic connections between the windings and the longitudinal connections between the turns of the windings, the initial and boundary conditions, is created. The model allows the calculation of the high-speed transients of the transformer windings and to develop means of protection against high-frequency overvoltage, coordinate winding isolation, is proposed.

REFERENCES

- [1] L.V. Bewley, *Traveling Waves on Transmission Systems*, John Wiley and Sons, NY, USA, 1951. – p. 288.
- [2] B. Heller, and A. Veverka, Impulse processes in electrical machines, М., Энергия, 1973. – p. 440. (in USSR).
- [3] Isaev Y.N., Startseva E.V., Schekotuev A.V. Investigation of wave processes of transformer windings as electric circuit with distributed parameters. *Izvestiya Tomskogo Politechnicheskogo universiteta. Inzhiniering energoresursov*. 2015. Vol. 326. No 8. P. 29 - 35. (Rus)
- [4] Mikulović J. Č., Šekara T. B. The Numerical Method of Inverse Laplace Transform for Calculation of Overvoltages in Power Transformers and Test Results. *Serbian Journal of Electrical Engineering*. Vol. 11, No. 2. June 2014. P. 243-256.
- [5] Bontidean S. G., Badic M., Iordache M., Galan N. Simulations and experimental tests on the distribution of overvoltage within transformer windings. *U.P.B. Sci. Bull. Series C*, Vol. 77. Iss. 3, 2015.
- [6] Sehedá M. S., Cheremnykh Y. V., Chimjk I.V., Mazur T. A., Kurylyshyn O.M. Mathematical modelling of stress distribution along the winding transformers under impulse surges. *Tekhnichna Elektrodynamika*. 2015. No 6. Pp. 8 – 11.
- [7] Mykhailo Sehedá, Oksana Hoholyuk, Petro Gogolyuk, Yurii Blyznak Mathematical Model of Periodic Wave Processes of the Windings of High-Frequency Power Sources. *15 International Conference "Advanced trends in Radioelectronics, Telecommunications and Computer Engineering"*, 2020, Slavske-Lviv, Ukraine.
- [8] Sehedá M. S., Cheremnykh Y. V., Gogolyuk P.F., Blyznak Y.V. Mathematical model of wave processes in two-winding transformers // *Tekhnichna Elektrodynamika*. – 2020. No 6.– Pp. 63 – 67.
- [9] CIGRE Brochure 577A, Electrical Transient Interaction between Transformers and the Power System. Part 1: Expertise. Joint Working Group A2/C4.39. – CIGRE, April 2014, 176 p. http://www.http://xmlopez.webs.uvigo.es/Html/Info/2014_Electrical_Transients_Part1_Expertise.pdf.
- [10] CIGRE Brochure 577B, Electrical Transient Interaction between Transformers and the Power System. Part 2: Expertise. Case Studies. Joint Working Group A2/C4.39. – CIGRE, April 2014, 124 p. http://www.http://xmlopez.webs.uvigo.es/Html/Info/2014_Electrical_Transients_Part2_Expertise.pdf.

Thermal Image Processing for Segmentation of Photovoltaic Panels

Jacek Starzyński
SENSE Software Sp. z o.o.
ul. Obrzeźna 1F/6U9
Warszawa, Poland
js@sensesoft.eu

Artur Siepietowski
Faculty of Electrical Engineering
Warsaw University of Technology
Warszawa, Poland
01148032@pw.edu.pl

Artur Maj
Faculty of Electrical Engineering
Warsaw University of Technology
Warszawa, Poland
01148023@pw.edu.pl

Abstract—Automatic diagnostics of photovoltaic farms can easily be carried out using unmanned aerial vehicles equipped with thermal imaging cameras. However, this approach requires automatic processing of the obtained images. A lot of research is currently being conducted to find and train suitable machine learning-based software for automatic detection and fault location of photovoltaic devices. However, this approach requires the preparation of a large amount of training data. This can be done manually, but the use of appropriately selected image processing algorithms can speed up and facilitate this tedious task.

This paper presents a selection of classical image processing algorithms that form a pipeline for fast, semi-automatic segmentation of photovoltaic panels based on thermal images.

Index Terms—photovoltaic farms, thermovision, image processing, automatic diagnostics

I. INTRODUCTION

Automated detection and localisation of faults in photovoltaic equipment on large farms can be accelerated by using unmanned aerial vehicles equipped with thermal imaging cameras. The large number of images obtained by such an approach can be efficiently processed using deep neural networks such as YOLO [1], UNET [2] and similar, but the preparation of such tools requires a huge amount of training data. To date, no such datasets exist and the current efforts of the authors of this paper are aimed at creating tools which can help to speed up the process of database creation.

Using commercial software such as SENSE Reporting [3] or free tool as labelImg [4] or cocoAnnotator [5], it is possible to label individual photovoltaic tables or modules. Depending on the interface of the tool used it may be possible to connect labels to rectangular bounding boxes or to more precise polygon regions.

The disadvantage of hand-held tools is the very labour-intensive nature of the module marking process, which means that each image takes at least several minutes to process (depending on the number of visible modules).

Figure 1 shows graphical user interface (GUI) of labelImg with photovoltaic modules labelled with bounding box technique. Even for the presented picture orientation of thermographic image use of rectangular bounding box is acceptable for a few panels only. If the image would be rotated by 45 degrees, the bounding boxes are not useful at all and manual

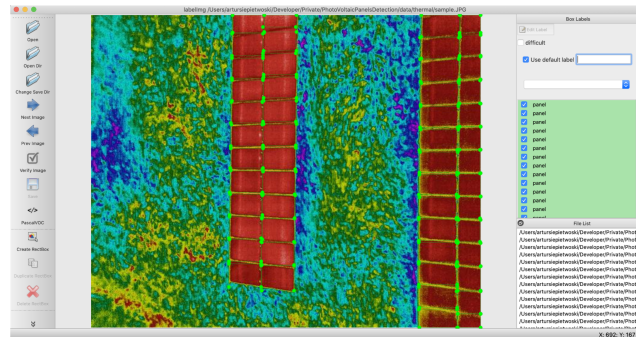


Fig. 1. User interfaced of labelImg with labeled thermographic image.

creation of dozens of polygons will make the time of the processing of each image unacceptably long.

The following sections of the paper presents an approach to speed up the human supervised labelling process by semi-automated creation of polygons bounding the modules. As it will be shown, the approach based on image processing algorithms if not error-free. It will produce relatively big amount of false positive polygons, but for the human operator selecting and removing the bad selections is much faster, than manual creation of good polygons.

The weak point of “classical” image processing algorithms is the need to select optimal, or at least appropriate, parameters that allow the algorithm to be “tuned” to a given class of images. It is no different in the case described here. Therefore, we decided to present the algorithm by describing the processing pipeline so that the reader becomes familiar with the most important, in our opinion, of these parameters. The whole process of creating a suitable set of algorithms is based on heuristics and experiments. This is certainly not a correct approach from a theoretical point of view, but in practice it gives satisfactory results.

II. THE DATA

All data (thermographic images) used in this paper are properties on SENSE Software Sp. z o.o.. They were collected within the realisation of project no. POIR.01.01.01-00-0491/20-00 “An intelligent system for defect recognition

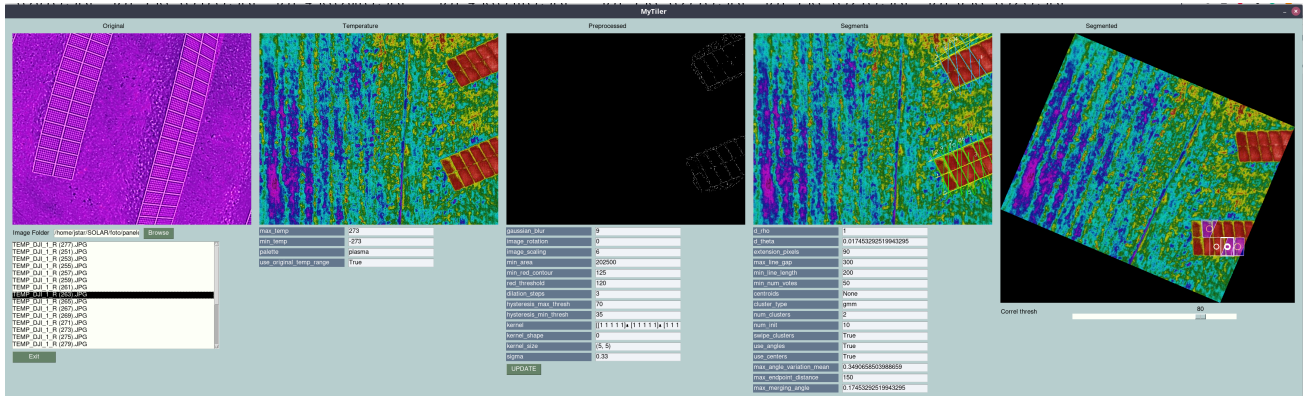


Fig. 2. GUI of the semiautomatic segmentation tool.

in photovoltaic modules using thermal imaging” financed by the Polish National Centre for Research and Development (NCBR) under the Intelligent Development Operational Programme. The images were taken by Artur Pawelec on various photovoltaic farms in Poland.

III. THE ALGORITHM

The proposed algorithm can be summarized as follows:

- 1) Image reprocessing;
- 2) Edge detection;
- 3) Line detection with Hough transformation;
- 4) Line clustering;
- 5) Finding intersection points of lines;
- 6) Creating quadrilaterals.

In this section the enumerated stages will be successively described and the most important parameters of each stage will be presented. The pipeline is experimentally implemented in Python with OpenCV [6]. The GUI allows to change the current values of parameters, adjusting the algorithm to given image. The general view of GUI is shown in Fig. 2.

IV. THE PITFALLS

CONCLUSION

This paper presents an image processing pipeline for semi-automatic segmentation of photovoltaic panels on thermal images. Based on several tests, an optimised choice of algorithms is proposed. The pipeline starts with the extraction of temperature data from a thermal image, the overlay of an appropriate colour map, image preprocessing and finally a set of algorithms for edge, segment and polygon extraction. The final tool, implemented in Python with the OpenCV library, requires human intervention but reduces image processing time by more than 90 % compared to manual segmentation.

The presented tool is useful for preparing datasets used for training and testing machine learning-based algorithms in automated diagnostics.

REFERENCES

- [1] J. Redmon and A. Farhadi, “Yolov3: An incremental improvement,” 2018.
- [2] H. Zhang, X. Hong, S. Zhou, and Q. Wang, *Infrared Image Segmentation for Photovoltaic Panels Based on Res-UNet*. Springer, 10 2019, pp. 611–622.
- [3] S. Soft, “Sense reporting,” ul. Obrzeźna 1F/6U9,02-691 Warszawa, Poland, 2021. [Online]. Available: <https://sensesof.eu>
- [4] Tzatalin, “Labeling. git code.” 2015. [Online]. Available: <https://github.com/tzatalin/labellmg>
- [5] P. Wspanialy, J. Brooks, and M. Moussa, “An image labeling tool and agricultural dataset for deep learning,” 2020.
- [6] G. Bradski, “The OpenCV Library,” *Dr. Dobb's Journal of Software Tools*, 2000.

System for the support of the intravenous infusion process continuity

Adam JÓSKO

*Institute of Theory of Electrical Engineering, Measurement and Information Systems,
Faculty of Electrical Engineering
Warsaw University of Technology.
Warsaw, Poland*
<https://orcid.org/0000-0003-4093-6252>

Wojciech ROMANIK

*II Department Of Anaesthesiology And Intensive Care
Medical University of Warsaw
Warsaw, Poland*
wojciech.romanik@wum.edu.pl

Abstract— The work presents the concept of a system for monitoring the decrease in the level of infusion fluid. The task of this system is to inform the medical staff about the low level of infusion fluid in the container. This is to allow the (almost) empty infusion fluid container to be replaced with a new, full one before the drip chamber and drain connected to the venflon on the patient's body are emptied. In the latter case, replenishment of the fluid requires additional filling with a drip chamber and a drain. In clinical practice, this is often a nuisance. Therefore, the basic task of the proposed measuring system is to warn against complete emptying of the infusion system. Thanks to this, it is possible to replace the fluid container efficiently and without additional annoyance and complications, maintaining in principle an uninterrupted process of intravenous fluid administration.

Keywords — *medical treatment, infusion process, microcontroller system, mass measurement*

I. INTRODUCTION

In everyday anaesthesiological practice a physician and a nurse create a team that takes care and safety measures during surgery. Anaesthetic work requires constant attention focused on the administration of anesthesia, observation of the operating field and the patient's vital signs, and the appropriate response to events that occur in the dynamic process of the surgery. The senses that are most involved in the anaesthetic work are sight, hearing and touch. Visual and sound signals from a cardiac monitor, anesthesia machine and surgical devices, verbal communication with the surgeon, blood vessel cannulation, the whole range of regional anesthesia procedures, parenteral administration of drugs - these are just a few of the areas that remain at the anaesthesiologist's disposal and contribute to the effective management of the patient through a stressful situation of surgery. Thus, properly set visual and audible alarms are the elements that significantly improve patient safety, notifying the anaesthesiological staff about the situation beyond the set norms.

Patient condition monitoring during anesthesia includes, among other measurements of the blood pressure, heart rate, ECG, saturation, the level of exhaled carbon dioxide, concentrations of medical gases and inhaled anesthetic, pressures in the respiratory tract, the degree of muscle relaxation. Each of the parameters requires the attention of a physician or a nurse. The emerging alarm focuses their attention on the parameter, a deviation may turn out to be critical at the given moment. The anaesthetic team is particularly sensitive to the sound signal from the measurement of saturation. Its rhythm and pitch, which constantly accompanies the anaesthesia, are one of the most important information about the patient for the anaesthesiologist.

During the preop-meeting, the anaesthesiologist asks the patient about their diseases, medicines, and the patient's medical history. They are interested in patient's laboratory and imaging studies. They have to know about all the potential patient's abnormalities. Although the anaesthesia affects almost all human body organs, it is mainly realized by influencing respiratory and cardiovascular systems. Each patient must have an intravenous cannula. Through a cannula, the anaesthesiologist administers drugs, medical fluids and, if necessary, blood products. Intravenous cannula insertion is a basic element of patient safety. It enables the immediate administration of drugs or fluids, and allows them to work immediately.

Apart from intravenous drugs, special fluids are administered during anesthesia. These are electrolyte solutions, hydroxyethyl starches or gelatins. These fluids are administered as a supplement to the lost fluids during surgery. During anesthesia, the anesthetist gives many different drugs and fluids in 50 to 1000 milliliter containers, which must be changed quite often. They use an IV kit consisting of:

- a drain with a drip chamber, i.e. a several centimeter long widening in the form of a cylinder,
- a movable clamp on the drain,
- end 1 - hammered into a container with a liquid, in the form of a pointed tube,
- end 2 - end of the drain with a thread, screwed on a cannula.

The container with the liquid is always placed about 1-1.5 meters above the lying patient. This allows gravity to flow into the venous system, where the pressure is lower than that exerted by the liquid column in the reservoir and drain. The fluid flows down until the pressure is equal with the patient's venous pressure. During the complete drainage of the fluid from the container through the tubing into the cannula and the patient's venous system, fluid usually stops in the drain. Starting the next fluid bottle outflow would cause air to enter the patient's venous system. It may create a very dangerous complication called "venous air embolism" (VAE), which could lead to arrhythmias and cardiac arrest. For this reason, it is required to remove the rest air from the drain. Then a drain requires filling with the new fluid and then starting the drip infusion.

There are several possibilities for the staff to empty the drain from the air. Some of them require action and it is possible to contact blood or dirty the set. Using a clamp on the drain, the personnel prevents the drain from emptying completely and then connects another fluid bottle. It is possible when the proper moment is noticed by the anaesthesia team. However, in everyday practice, among many other activities the moment is sometimes missed. Especially during anesthesia that requires extraordinary

activities from the physician and the nurse, which engage their special attention.

There are infusion pumps and drop counting devices used for regulated administration of intravenous drugs during surgery. However, fluid therapy on an operation theater requires a constant attentiveness of the staff. This emerges a need of an alerting device that alarms the ending of fluid in the container.

The hook scale (system for the support of the intravenous infusion process continuity) with an alarm accommodates the need. The scale is hung on the operation stand. The fluid container is attached to the scale.

The user sets on the scale the desired weight of the fluid bottle associated with an alarm. Then, the infusion can be started. When the bottle weight decreases to the set level, the scale alarm beeps. The user has some time to stop the fluid using the clamp on the drain. The scale does not cause any other problems. It does not interfere with the infusion, it has no contact with the patient, it is completely safe. In the case of the device failure or unnoticed alarm, anaesthesiological procedures remain the same as previously.

As explained above the design of a device to monitor the process of intravenous administration of drugs is dictated by the need to maintain the continuity of this process. During medical procedures or intensive care, there is a need for long-term and at the same time continuous administration of intravenous drugs. At this point, the long-term nature means the need to replenish the infusion fluid. The gravity fluid feeding system consists of a fluid container, a drain with a drip chamber (Fig. 1) and ends with a venflon attached to the patient's vein.



Fig 1. Sample of the fluid container and drain with a drip chamber.

In medical practice, it is important that the fluid container is replaced at the right time before it is completely emptied. Then the task basically boils down to substituting the fluid container itself. Otherwise, the fluid will leave the tray, then the drip chamber and the next part of the drain where it will stop in a certain part of it, in which, according to the laws of physics, the pressures will become balanced. Unfortunately, this happens every day in clinical practice. Thanks to the scale with alarm function and fluid retention while still in the drip chamber, one does not need to replace the drain or push the fluid up into the drip chamber. One can connect another fluid container immediately after the previous one, without a combination with an empty drain. The problem is described in the literature [1,2,3] as there is a significant need to monitor the process. There are different ways to achieve this including reflection (infrared or ultrasonic detectors) and impedance measurement. The paper presents another possibility based on the mass measurement. The aim of the work is to propose simple, reliable and of course not too expensive method supporting medical treatment.

II. MEASUREMENT SYSTEM

The proposed system shall take the form of an electronic scale which continuously measures the mass of the infusion system and generates alarm information (sound) when its mass reaches a certain minimum level associated with the emptying of the liquid container. The scale was made as a battery-powered microcontroller system, with a strain gauge and a warning sound source. At the heart of the measuring and control system there is the Arduino UNO board with AVR ATmega 328 microcontroller [4,5], extended with a standard display with keyboard for device control and menu operation [6]. A tensometric beam of a range covering the available capacities of infusion fluid storage units (100 to 2000ml) was used to measure the mass [7]. A typical buzzer was used as a sound source (Fig. 2).



Fig. 2. Electronic components of the scale (from the top: Arduino UNO board, LCD Keypad Shield, tensometric beam with signal conditioning and buzzer at the left lower corner).

III. FUNCTIONALITY

The device is designed to monitor the level of infusion fluids by measuring the mass of typical infusion fluid containers in the range of 100 to 2000 ml. By empirical means, net mass, gross and tare values were determined. The alarm level can be set in the range of 5-20% of the initial net mass of the fluid, depending on the type of packaging. Each time one turns on the device (fig 3.), it can be calibrated.

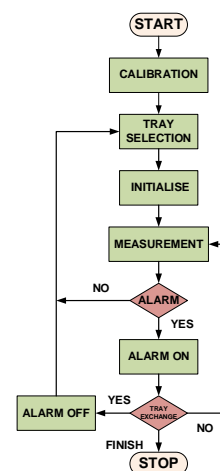


Fig 3. Basic diagram of the scale algorithm.

Next, selection the size of the container is to be completed, after which one can start monitoring the level of the fluid. The process is being continued until the level of the fluid becomes alarmingly low.

When the alarm level is reached, a beep sound is activated reminding one to replace the container. As it is done, one sets the capacity of the new container and the monitoring procedure can be started again. The developed concept of the measurement device is presented in the fig. 4.



Fig. 4. The developed concept of the infusion fluid level monitoring system.

IV. MEASUREMENT SYSTEM EVALUATION

The aim of the project was to create a device that will allow to notice the moment just before the drip chamber is completely empty. The “scale with alarm” prototype was subjected to clinical trials. The scale was suspended on a stand with a rubber band. The drip tube was connected to a cannula in the patient's peripheral vein. Then, in some cases, the tube was attached to the patient's skin at a distance of approx. 20 cm from the cannula for protection from additional forces. The scale was handled as instructed after each additional bottle of liquid was suspended. The fluid container was observed during the infusion and the fluid flow rate was controlled as clinically needed.

The alarm was triggered at the expected moment after reaching the mass set point. It was observed that in each case fluid was still present in the container as expected. The alarm signal let control the flow of the fluid in such a way that it does not leave the drip chamber. This control took about 1-3 minutes. When an alarm occurs, the user should have no more than about 10 seconds to react. Filling the drip chamber is a key element to achieve the aim.

Initial intermittent beep (warning 1) changed into continuous beep (warning 2) after several beeps. The sound of the scale alarm was a new one for the staff as intended not to be mistaken with other, standard ones. The device has been calibrated for 100, 250, 500 and 1000 ml liquid containers. Such settings are also available in the menu.

The device was tested in an operating room. This description reflects the facts and expectations regarding the designed device in these circumstances. Finally, it is worth noting that adding a wireless module (Bluetooth, WIFI) to a device can help nurses work in hospital wards. The alarm in the smartphone application will allow better control of intravenous infusions at patients' beds.

V. SUMMARY

The scale design is a response to the idea presented by physicians and is due to the problems encountered during daily activities in medical procedures. The monitoring system has undergone an initial phase of engineering testing resulted in satisfactory outcomes. The phase was followed by the clinician tests. Though they revealed some weaknesses concerning the dimensions of the scale prototype, duration and sound properties of the alarms, time aspects of the generated alarms and finally the need of the more complex scale operation menu (alarm postponement and clearing, different possibilities of the fluid containers interchange support, etc.) in general at the presented stage of scale development the clinician tests ended up with positive outcomes. So it is reasonable to apply necessary modifications making the device fulfilling the demands of the qualified personnel. Adding a wireless modules (Bluetooth, Wi-Fi) to a device can help nurses work in hospital wards. The alarm in the smartphone application will allow better control of intravenous infusions at patients' beds. Authors also keep in mind that the mass measurement method is sensitive to any movement, so the system is to be handled steady. The tests performed in the hospital conditions pointed the sensitivity of this aspect and it is planned to involve other mentioned methods to be used even in parallel if needed.

REFERENCES

- [1] A. Cataldo, G. Cannazza, N. Giaquinto, A. Trotta and G. Andria, "Development of a remote system for real-time control of intravenous drip infusions," *2011 IEEE International Symposium on Medical Measurements and Applications*, 2011, pp. 234-237, doi: 10.1109/MeMeA.2011.5966738.
- [2] C. Jianwen and Z. Han, "Design of intravenous infusion monitoring and alarm system based on wireless communication technology," *2011 IEEE International Conference on Mechatronics and Automation*, 2011, pp. 130-134, doi: 10.1109/ICMA.2011.5985644.
- [3] H. Ogawa, H. Maki, S. Tsukamoto, Y. Yonezawa, H. Amano and W. M. Caldwell, "A new drip infusion solution monitoring system with a free-flow detection function," *2010 Annual International Conference of the IEEE Engineering in Medicine and Biology*, 2010, pp. 1214-1217, doi: 10.1109/IEMBS.2010.5626449.
- [4] 8-Bit Atmel AVR Microcontroller data sheet.
- [5] <https://www.arduino.cc/>
- [6] https://www.dfrobot.com/index.php?route=product/product&product_id=51&search=DFR0009&description=true&category_id=48
- [7] HX711 24-Bit Analog-to-Digital Converter (ADC) for Weight Scales

Non-contact Electromagnetic Actuator for a Ball Valve

David Šmucr*, Martin Vitek†, František Mach‡ and Karel Pospíšil§

Department of Electrical and Computational Engineering

Faculty of Electrical Engineering

University of West Bohemia

Pilsen, Czech Republic

{*smucr, †martinv, ‡fmach, §pospisik}@fel.zcu.cz

Abstract—The article deals with the issue of a fully electromagnetic non-contact actuator for a ball valve - a valve controlled by a purely electromagnetic field (direct drive) created by coils (electromagnets) placed outside the operating part of the valve.

Index Terms—actuator, ball valve, direct drive, electromagnetic field, mathematical model, prototype

I. INTRODUCTION AND MOTIVATION

Ball valves can be encountered quite often in everyday life. They are used from households (garden water valve) to complex industrial applications (liquid flow control). In some applications, such as in the rocket industry, there is a need for fast and accurate control of the valves. Here a valve with a non-contact actuator could find use. Figure 1 shows a cross section of a simple ball valve.

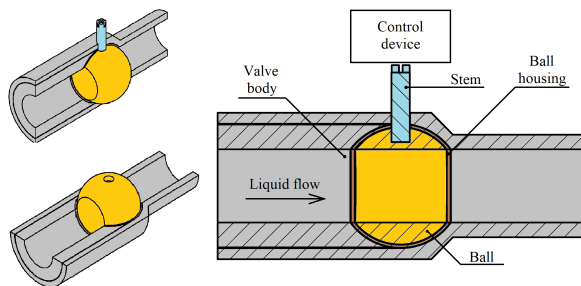


Fig. 1. Ball valve easy sketch

It is clear from the Figure 1 that conventional ball valves consist of the following basic parts: valve body, ball, ball housing, stem and control device. The control device can be of various types from manual handles to electric motors. [1]

At this point can be mentioned the main motivation of this project - the removal of external control device with the stem and control the ball directly by the electromagnetic field. This could result in the following benefits:

This research has been supported in part by the Technology Agency of the Czech Republic under the project Electromagnetic valves with high degree of embedded intelligence (TH04010270) and in part by the University of West Bohemia under the project Development of system order reduction techniques in electrical applications (SGS-2021-011).

- Absence of any openings through which the medium could leak.
- Suitability for high pressure applications.
- Direct control by electric (magnetic) field - fast response to demand.
- Full ball rotation - a function similar to a reluctance motor.
- Elimination of mechanical inner components related to the external control device.

Unfortunately, the current test prototype also has many shortcomings, including:

- Complicated installation of the channel for the medium - the solution could be to route the channel through one pair of the coils.
- Unknown fixation of the axis of rotation without the use of a stem - the solution could be a ball with protruding parts.
- In use, a constant electric current is required to hold ball at position, which leads to permanent power consumption - permanent magnets can be a solution.
- Generally complicated design.

The following chapters will explain the basic principle of the device, give an introduction to the procedure for designing the valve actuator prototype and show the results of individual tests.

II. PROBLEM DESCRIPTION

In the previous chapter, the basic possibilities of ball valve control and its typical construction were already mentioned. One of the parts of the valve is a ball, an element which regulates the flow of medium through the valve. In our case, stainless steel was chosen, which is resistant to various media. However, this stainless steel must also be ferromagnetic in order to be able to position the valve by the electromagnetic field. In the event that it would be necessary to increase the applied torque, it would be appropriate to insert permanent magnets into the ball, which, however, have the disadvantage of clogging the valve with dirt.

The actuator principle of this valve is then quite simple and can be compared to the principle of a reluctance motor.

The ferromagnetic ball is the rotor of the "motor" and its position is controlled by switching the individual coil pairs along its perimeter. When the individual coils are powered, the ball rotates in the direction in which it has the lowest magnetic resistance to the powered coils (principle of minimum energy) as can be seen in Figure 2.

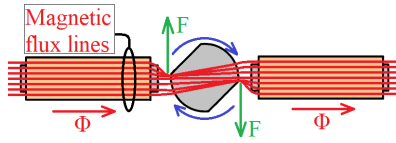


Fig. 2. Basic principle of function

In the Figure 3 it is possible to see 8 coils distributed around the circumference of the ball forming 4 pairs which are placed opposite of each other. 8 coils is the minimum to rotate a ball. The advantage of a multi-coil design could be the achievability of more valve positions and thus better fluid flow control.

By switching these pairs of coils (connected in series), a change of the valve's position is achieved, as shown in Figure 3. By cyclic switching, it is then possible to keep the ball in rotation like the already mentioned switched reluctance motor.

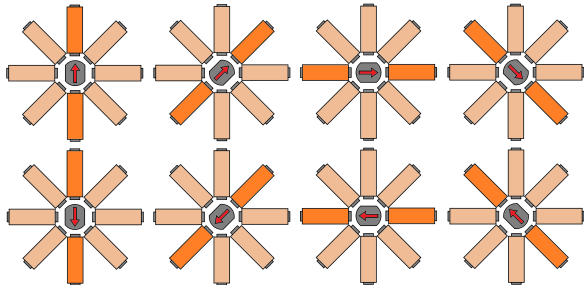


Fig. 3. Function description

A mathematical model is also derived from this construction, which will be further discussed below. The aim is to optimize the function of the actuator as much as possible in terms of the magnitude of the force, the course of the torque and, last but not least, the energy consumption.

III. DEVELOPMENT STEP BY STEP

During the development, 3 test prototypes have been created so far, which were used for basic verification of the idea. Countless other imaginary prototypes in the form of mathematical models have been created and are still being created to make the actuator as efficient as possible. In the following text, these test prototypes will be outlined together with the results of individual experiments. More about the creation, experiments and mathematical models of the first two test prototypes can be found in [2].

A. Permanent magnet positioning

The test prototype is shown in Figure 4. This design was created for the purpose of positioning the ball by an external

magnetic field created by a permanent magnet. The result of the experiment was that the ball can be positioned by applying an external magnetic field. The picture also shows a barrier (purple), which served as a path for moving the neodymium permanent magnet.

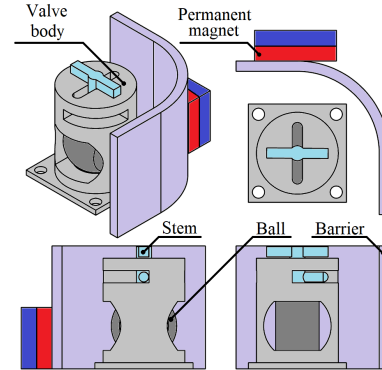


Fig. 4. Permanent magnet positioning test prototype

B. Replacement of the permanent magnet with a coil

After verifying the principle of valve control, it was necessary to replace the permanent magnet with an electrically controlled element forming a magnetic field - a coil (Figure 5). The coils (or electromagnets) consist of a ferromagnetic core, a plastic body and a winding.

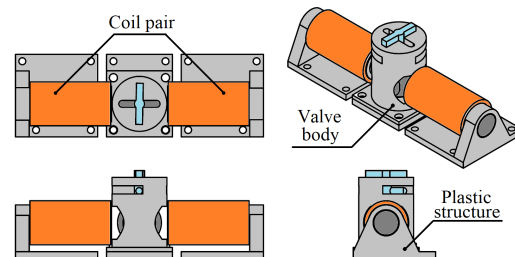


Fig. 5. Replacing a magnet with a pair of coils

In this particular test prototype, two coils (one pair) were used to move the valve to only one position. However, many experiments were performed on this test prototype and its mathematical model was also created.

1) *Definition of a mathematical model:* The mathematical model of this simple arrangement serves in particular to determine the force / torque acting on the ball depending on the parameters of the coils, such as current, number of turns, etc. The mathematical model was created in COMSOL Multiphysics.

It contains only the "electromagnetically active" parts of the test prototype - the coil and the ferromagnetic ball, as can be seen in Figure 6 together with an explanation of the position of the ball for better understanding of the results later.

The basic equation for describing a mathematical model is Ampère's circuital law in the form

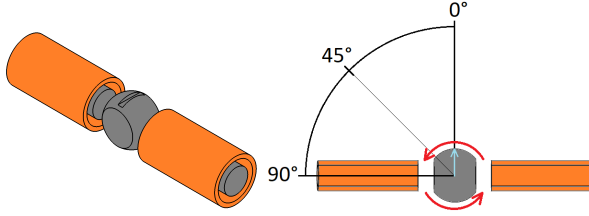


Fig. 6. Mathematical model of a test prototype

$$\text{curl} \left(\frac{1}{\mu(|\mathbf{B}|)} \cdot \text{curl}(\mathbf{A} - \mathbf{B}_r) \right) = \mathbf{J}_{\text{ext}}, \quad (1)$$

where $\mu(|\mathbf{B}|)$ denotes the magnetic permeability depending on magnetic induction, \mathbf{A} stands for magnetic vector potential, symbol \mathbf{B}_r stands for the remanent magnetization of potential permanent magnets and \mathbf{J}_{ext} stands for the density of the field current.

In this particular case, the most significant result is the force and torque acting on the ball, which is based on the equations

$$\mathbf{F}_m = \int_{\partial\Omega} \mathbf{n} \cdot \mathbf{T} dS \quad (2)$$

and

$$\mathbf{M}_m = \int_{\partial\Omega} (\mathbf{r} - \mathbf{r}_0) \times (\mathbf{n} \cdot \mathbf{T}) dS, \quad (3)$$

where \mathbf{n} represents normal vector, \mathbf{T} stands for Maxwell's tensor and the quantities in the first parenthesis of Equation (3) represent the dimension of the arm.

As mentioned, thanks to the results of this model, it was easier to design the necessary parameters of the coils. The approximate values of the magnetic induction on the surface of the ball needed to change the position of the valve were already known from the *permanent magnet positioning test*.

Another result was the torque characteristic of the torque acting on the ball depending on the angle of rotation of the ball, which was described in Figure 6. The torque characteristic is then shown in Figure 7.

From the torque characteristic it can be read that the highest torque acting on the ball is in the vicinity of the angle of rotation from 30° to 45°. At the same time, it can be seen that in the positions when the angle of rotation of the ball is nearly 0°, the applied torque is very small. This knowledge will play a role later in conducting the experiment.

2) *Experiment and motion study*: The mechanical model of this arrangement was then subjected to an experiment in which an effort was made to rotate the ball (change the position of the valve) by powering a single pair of coils. As already mentioned, due to the small force acting at 0° (in fact 0 Nm), it was not possible to turn the ball from a 0° position by a single pair of coils. For this reason, the ball was rotated to a position of approximately 6° at the beginning of the experiment.

After successfully testing the concept, a movement study was performed. The coils of this test prototype each have 60 turns and are supplied with a current of approximately

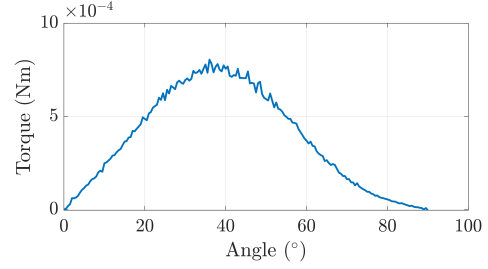


Fig. 7. Torque characteristic for one pair of coils

7.5 A. During the experiment, the movement of the ball in the valve body was recorded with a high-speed camera and this recording was then analyzed. Figure 8 shows a graph of the position of the ball as a function of time together with an image depicting the motion analysis in the Tracker Video Analysis and Modeling Tool [3]. From this, the speed of rotation of the ball to the 90° position itself can be deduced - approximately 220 ms. However, as can be seen, the ball bounced in the final position due to a mechanical stop in the stem bushing area.

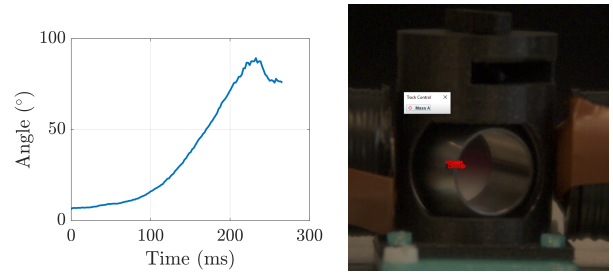


Fig. 8. Motion study

C. Test prototype of an 8-coil actuator.

The design of the current valve actuator test prototype is shown in Figure 9. Important note: the test prototype does not yet contain a channel for the passage of liquids! So far, only the possibility of positioning the valve is solved. It is basically an extension of the previous concept by another 6 coils. This ensures that the valve's ball can be fully rotated by cyclically switching the individual pairs of coils.

From Figure 9 it is also possible to notice the stem, which still fixes the axis of rotation of the ball. At this moment, an attempt is being made to devise another possible solution to this problem, since the removal of this mechanical component is the fundamental advantage of this device.

1) *Definition of a mathematical model*: The mathematical model of this arrangement is very similar to the previous solution, the only difference is that another 6 coils are inserted into it - once again. In this case, it was already possible to determine the torque characteristic at full rotation of the ball by 360° by suitable switching of the coils during the analysis.

The description of the mathematical model is then based on the same equations as in the case of one pair of coils. The

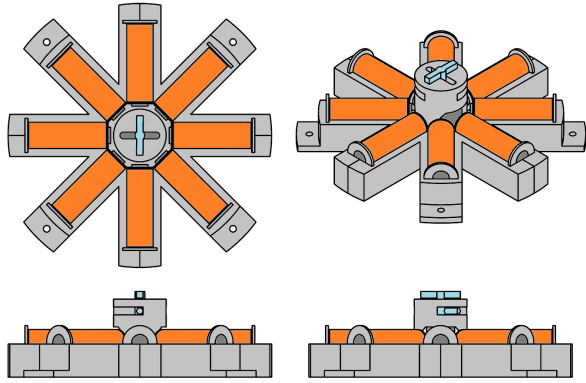


Fig. 9. Test prototype design

magnetic field distribution together with the torque characteristic is shown in Figure 10.

For a better understanding of the torque characteristic, the figure is supplemented by a color model, where the degrees of rotation of the ball can be seen together with the color designation of individual pairs of coils corresponding to the colors of the torque characteristic sections.

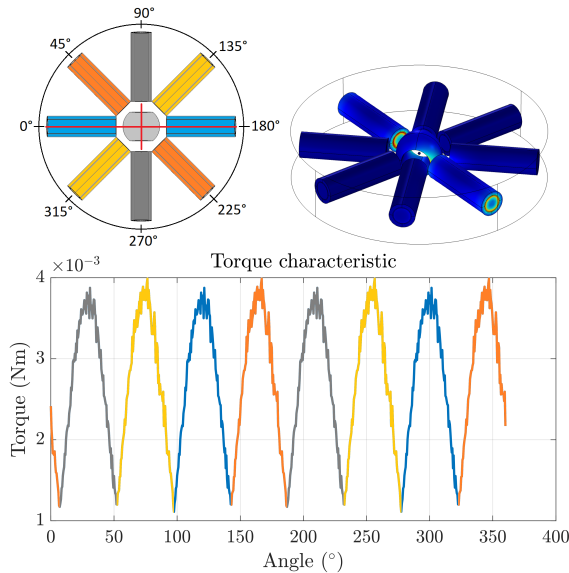


Fig. 10. Results of mathematical model

2) *Solution for switching coil pairs:* In the mechanical experimental model, the switching of individual pairs of coils is solved using the Arduino Uno control circuit with the appropriate relay shield. It is planned for the future to design new electronics for this specific device.

3) *Experiment and motion study:* This test prototype was then also tested, both in valve mode (90 ° rotation) and in "motor" mode (full 360 ° rotation), at 150 rpm. The real form of the test prototype is shown in Figure 11.

The coils of this test prototype each have 165 turns and are supplied with a current of approximately 5 A. However, the



Fig. 11. Current test prototype together with valve body and ball itself

magnitude of the current through one pair of coils depends on the number of simultaneously powered pairs - experimentation has also been made with overlapping switching times.

Furthermore, as with the prototype with one pair of coils, a motion study was performed to ensure the speed of rotation. During the rotation of the ball, a point on the surface of the stem was spotted and from this the course of rotation in one 360 ° revolution was analyzed in the Tracker Video Analysis and Modeling Tool [3]. The result of the motion study is visible in Figure 12.

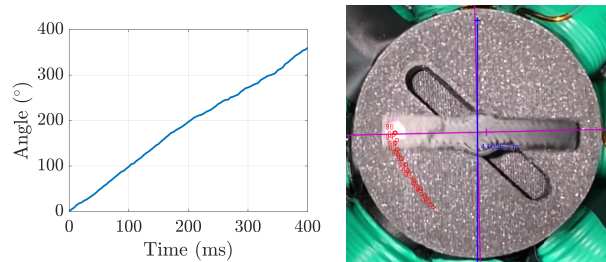


Fig. 12. Motion study of the current test prototype

IV. SUMMARY

The article introduced the basic concept of a non-contact actuator for a ball valve. From the results of mathematical models and performed experiments it is clear that the functionality of this concept has been verified. However, a lot of work is still needed to create a fully functional prototype.

In the next steps, it is necessary to optimize the actuator to create the highest possible torque at the cost of the lowest possible current. Furthermore, also remove the stem and create a pass-through channel for the media, which will occur in the coming months.

REFERENCES

- [1] B. NESBITT, *Handbook of Valves and Actuators*, ser. Valves Manual International. Elsevier Science & Technology Books, 2007, vol. 546.
- [2] D. ŠMUCR, "Fully electromagnetic ball valve," Bachelor thesis, Faculty of Electrical Engineering at University of West Bohemia, Pilsen, Czech republic, 2020.
- [3] Tracker video analysis and modeling tool. [Online]. Available: <https://physlets.org/tracker/>

Simulation of heat transfer and air flow inside the switchboard cabinet

1st Jan Kohout

*Department of electrical and computational engineering
University of West Bohemia
Pilsen, Czech Republic
kohoutj@students.zcu.cz*

2nd Lenka Šroubová

*Department of electrical and computational engineering
University of West Bohemia
Pilsen, Czech Republic
lsroubov@fel.zcu.cz*

Abstract—The purpose of this paper is to model and simulation of the heat transfer and airflow inside the switchboard cabinet. For simulations, the program COMSOL Multiphysics was used. Additionally, this paper deals with the measurement of temperature inside the switchboard cabinet. Final results from simulations are compared with values obtained from measurement.

Index Terms—switchboard cabinet, air flow simulation, heat transfer simulation

I. INTRODUCTION

In the last few months, work has been in progress on new and simplified versions of a paraglider simulator. This project of a paragliding simulator arose due to increase the safety and reduce the risks of paraglider pilot's injuries. Using our simulator we are able to simulate the conditions, which can be difficult to handle by the pilots. This simulator, obviously, requires a special switchboard. For the easier use of a paragliding simulator, it is necessary to reduce its size and also the size of the switchboard cabinet. With the smaller switchboard cabinet's dimensions, high-temperature problems can occur inside the switchboard cabinet caused by semiconductor converters and a DC power supply. The main aim of this paper is to simulate the heat transfer inside the switchboard cabinet and be able to predict the behavior of internal temperature. Another problem that this article solves is the flow of air inside the switchboard cabinet during forced cooling. The forced cooling is triggered by the external ventilator.

II. MATHEMATICAL MODEL OF HEAT TRANSFER

The mathematical model for calculation of heat transfer inside the switchboard cabinet is described by Fourier-Kirchhoff's partial differential equation [1], which is shown below (1).

$$-div \lambda \cdot grad T + \rho \cdot c_p \left(\frac{\partial T}{\partial t} + v \cdot grad T \right) = p, \quad (1)$$

where λ is a thermal conductivity, T is the temperature, ρ is a specific weight of the material, c_p is a thermal capacity, v is a velocity and p represents external the heat sources.

III. MATHEMATICAL MODEL OF AIRFLOW

This airflow in the switchboard cabinet is described by the Navier-Stokes's partial differential equation (2).

$$\rho \frac{\delta \vec{u}}{\delta t} - \eta \cdot \nabla^2 \vec{u} + \rho (\vec{u} \cdot \nabla) \vec{u} + \nabla p = \vec{F}, \quad (2)$$

$$\nabla \cdot \vec{u} = 0.$$

where ρ is density, η is dynamic viscosity, \vec{u} is field of the velocities, p is a pressure and \vec{F} is a force field intensity.

IV. SIMULATION

The computer model was solved in the COMSOL Multiphysics software [2] and consists of two coupled physical fields. The temperature distribution in the switchboard is influenced by the air flow and the heat transfer depends on the flow of the surrounding air.

The main heat sources are converters, which task is to control the servo motors. The main task of converters, which causes the most heat, is to control servo motors. The servo motors are located on the construction of the simulator, and they are used for moving with the pilot in the glider. There are also the smaller sources of heat and those are two direct voltage sources. They are used for supplying microcontrollers with electric energy. The heat, that arises due to microcontrollers, is in simulations neglected. 2D geometry models were created in ProgeCAD and 3D geometry models in SOLIDWORKS according the datasheet [4]. The solution must not contain too much fine details, because of the compromise of the reliability of the final design. Firstly is necessary to import geometry to the COMSOL from CAD software. Next step is to choose the physics and time dependence. In the case of time dependence, for heat transfer simulation the time-dependent simulation was used, on the other hand for simulation of airflow, stationary simulation was used due to high computing power requirements. The information from stationary simulation of airflow is, for our purposes, sufficient, though. Physics which were used for our simulation was Heat transfer in solid and fluids and Laminar flow.

For correct results we need to set up the appropriate materials. The materials, which we are using are from COMSOL's library. The usual cabinet material is sheet steel. Settings of

boundary conditions follow. Boundary condition for thermal insulation, boundary condition of heat flow, conditions of internal blown walls inside the switchboard cabinet and for walls of switchboard cabinet have to be determined. The last step before simulation itself, the mesh has to be set and generated. The mesh was very detailed and refined on the edges and corners of the components inside the switchboard cabinet. The convergence of results was carefully tested on the mesh density.

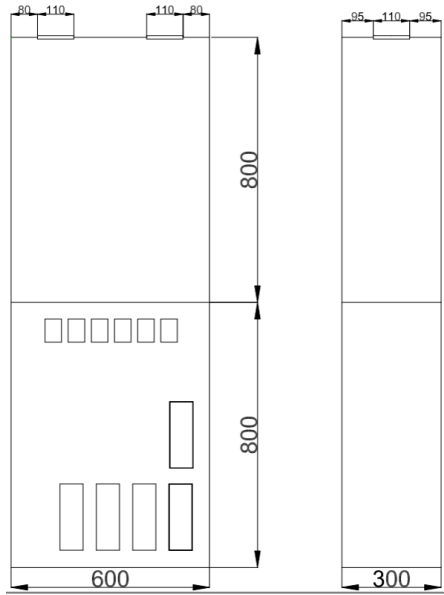


Fig. 1. Dimensions of the switchboard cabinet

V. ILLUSTRATIVE EXAMPLES

The first switchboard cabinet is currently in use. The switchboard cabinet consists of two main parts. In the bottom part, converters, control circuits for controlling servo motors, are situated. In the upper part are located voltage sources, circuit breakers, and other protective elements. The dimensions of one part of the switchboard cabinet are 800 x 600 x 300 mm, Fig.1. A construction and calculations of heat transfer in this switchboard cabinet are described in detail in [3], there are also measurements, which verify the correctness of simulations. Figures with a comparison of measurement and simulation are below. Fig.2 shows temperature inside the switchboard cabinet without forced cooling. The heat transfer coefficient $\alpha = 20 \text{ W}\cdot\text{m}^{-2}\cdot\text{K}^{-1}$ represents natural cooling.

Fig. 3 depicts temperature inside the switchboard cabinet with forced cooling. During the simulation the value of the heat transfer coefficient $\alpha = 150 \text{ W}\cdot\text{m}^{-2}\cdot\text{K}^{-1}$ was used.

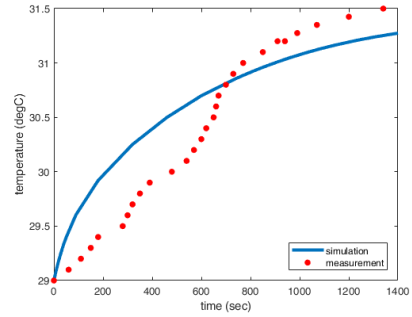


Fig. 2. Temperature inside the switchboard cabinet without forced

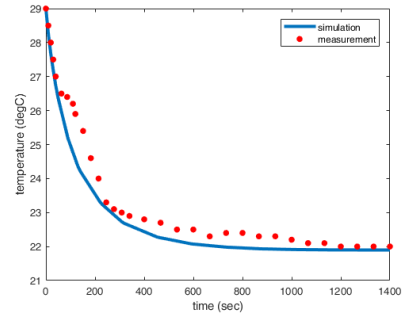


Fig. 3. Temperature inside the switchboard cabinet with forced

In this paper, the simulation of the airflow inside the mentioned switchboard cabinet is shown. In this example are two ventilators, which blow the air through the switchboard cabinet. We are used ventilators Maglev Vapo with incoming electric power of 5 W, the supply voltage is 24 V and rotation speed is 3100 RPM. The airflow through the ventilators is, according to the datasheet, 108.20 CFM/183.83 m³/h. In Fig. 4 is shown the airflow through the switchboard cabinet.

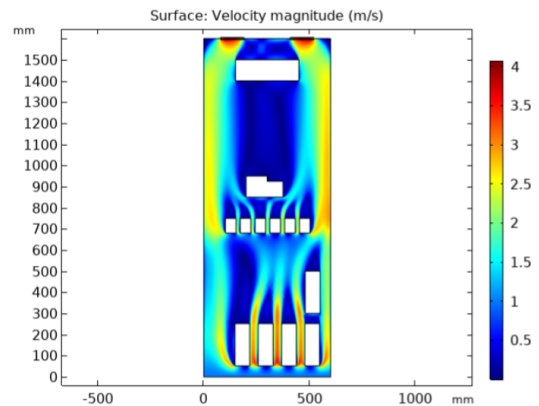


Fig. 4. The simulation of airflow inside the switchboard cabinet obtained by 2D simulation

From Fig. 4 is evident, that maximum speed of airflow is approximately 4 m/s. A similar simulation was made in 3D too, which is shown in the following Fig. 5.

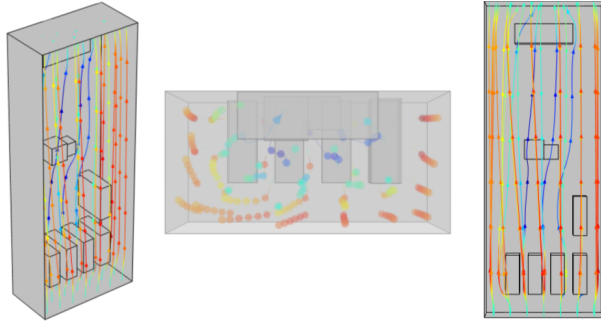


Fig. 5. The simulation of airflow inside the switchboard cabinet obtained by 3D simulation

From the results, obtained by simulation, it can be stated, that in the middle of the top of the switchboard cabinet is the velocity of air, pretty slowly. So the best location for the ventilators is on the edges of the upper part of the switchboard cabinet.

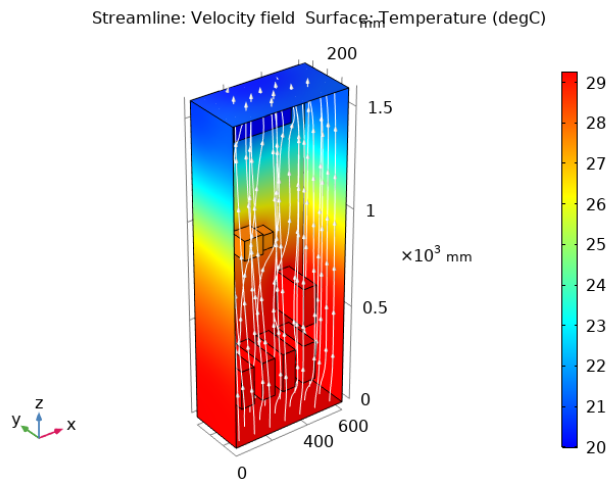


Fig. 6. Heat transfer and airflow simulation in the switchboard cabinet

Fig. 6 shows two associated physics in one simulation (heating simulation and simulation of airflow).

The second example is about a smaller switchboard cabinet, which is used for a less complex version of the paragliding simulator. The switchboard cabinet consists of a steel frame, too. Inside, the converters, DC voltage source, protective and securing elements are situated. The ventilator is located at the bottom of the switchboard cabinet and is supplied by a DC power supply. Inside the switchboard cabinet are also located control circuits and microcontrollers, but the heating contribution, which they are producing, is negligible. Hence they are not shown in the figure and also they are not included in simulations. The switchboard cabinet model is shown in the following figure 7. In figure 7 the principle of the cooling system is shown as well. The dimensions of the switchboard cabinet are, according to the datasheet 400 x 400 x 200 mm.

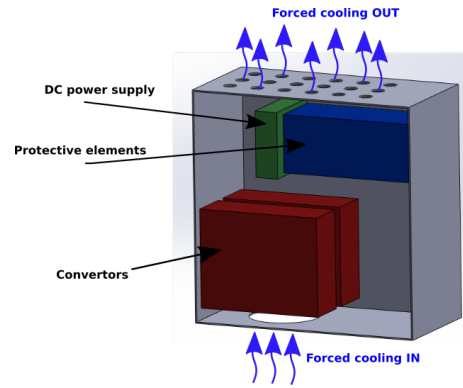


Fig. 7. Model of switchboard cabinet

Before anything else, the heat sources in COMSOL Multiphysics were set up. As being said, the main sources are converters and DC voltage source. The confined space between the individual components must, of course, be taken into account. The cramped space between the individual components is represented in the simulation by the heat transfer coefficient $\alpha = 15 \text{ W}\cdot\text{m}^{-2}\cdot\text{K}^{-1}$.

The result, obtained from simulation is shown in following figure 8.

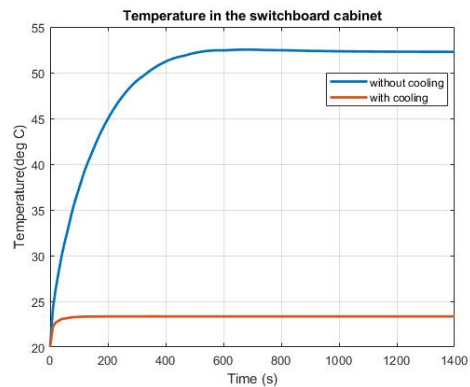


Fig. 8. Graph of temperature in the switchboard cabinet

It is evident from the figure that the maximum temperature is around 53°C. In the figure 8, is also shown the process of the temperature inside the switchboard cabinet, during forced cooling. For simulation of forced cooling, we were set the heat transfer coefficient to the $\alpha = 150 \text{ W}\cdot\text{m}^{-2}\cdot\text{K}^{-1}$. According the figure 8 we can see, that the temperature inside the switchboard cabinet, during forced cooling, is maximum something about 23 °C. So it is certainly advantageous for a long-term operation to operate the switchboard with active cooling.

Forced cooling was obtained by the same type of ventilator as in the previous example. For the small switchboard cabinet is one ventilator sufficient. The first simulation is shown in the following figure. Results are obtained from 2D simulation. The simulation was performed from the front side of the switchboard and also from a lateral side of the switchboard

cabinet. As being said, the results are shown in the following figure 9.

From the figure, we can see, that maximum velocity magnitude is 3 km/h. In simulation from the lateral side of the switchboard cabinet is evident, that the air flow rapidly between drivers and cool them, as being presumed.

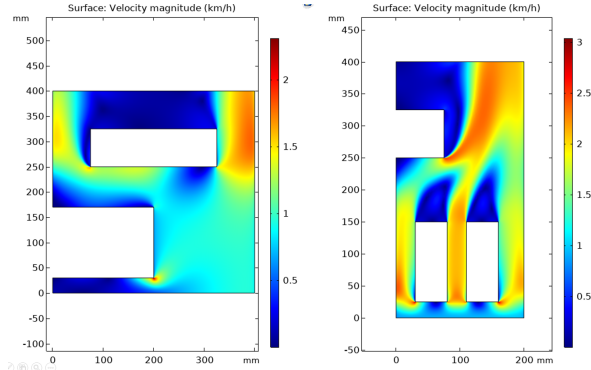


Fig. 9. The simulation of airflow inside the switchboard cabinet in 2D

Another presented simulation is a simulation of airflow in 3D. For this simulation, the same geometry, shown in figure 7, is used. We also used the same parameters as in 2D simulations. The result is shown in the following figure 10.

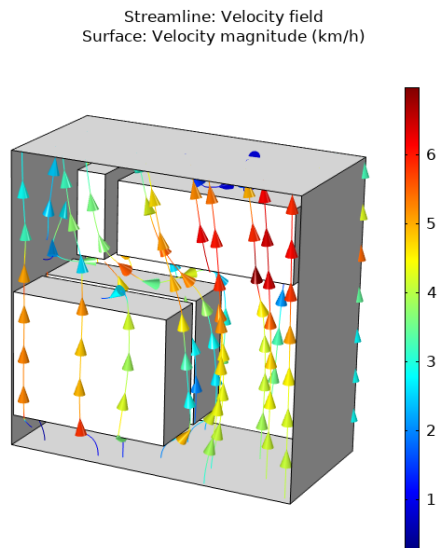


Fig. 10. The simulation of airflow inside the switchboard cabinet in 3D

The figure shows the velocity of the airflow simulation inside the switchboard cabinet. As you can see, the magnitude of the velocity of the airflow reaches 6 km per hour, which is two times bigger than the maximum velocity which was obtained from 2D simulations. The reason why this situation occurs is, that in 2D we are not able to represent every condition and behavior as in 3D modeling. The tax for this fact is computation power requirements.

VI. CONCLUSION

In this paper, we obtained results from simulations of heat transfer and airflow inside the switchboard cabinet. Two examples of switchboard cabinets were shown. These two instances are in operation on the FlyOnVision project [5].

From simulations and models, we are able to model and predict the behavior of heat transfer inside the switchboard with forced cooling and without forced cooling. The prediction of progression of the heat transfer was verified from measurement in another article. The results of heat transfer simulation can be used for other examples of other types of switchboard cabinets.

The results from laminar flow, which we are obtained from the simulation show the trajectory and magnitude of velocity inside the switchboard cabinets. From those results, we are able to determine the best spot for the ventilator and its application which is suction or blowing.

The most significant result is, that we are able to put those algorithms to varied types of switchboard cabinets and predict heat transfer and airflow inside them. The only parameters that we need for simulations are geometry, used materials, cooling system, and approximate shape of components inside switchboard cabinets.

ACKNOWLEDGMENT

This research has been supported by the project of the Technology Agency of the Czech Republic with number FW01010257: Paragliding Flight Simulator and internal project of UWB and University Students Project SGS-2021-011


REFERENCES


- [1] J. P. Holman., "Heat Transfer," in McGraw-Hill, New York, 2002.
- [2] COMSOL Multiphysics Reference Manual [cit. 10. 8. 2021]. Available on <https://www.comsol.com>
- [3] J. Kohout, L. Šroubová, Modeling of the heat transfer in the switchboard cabinet, XIX International UIE Congress on Evolution and New Trends in Electrothermal Processes, Pilsen, August 2021.
- [4] Schrack technik. Datasheet for WST8060300. [online], [cit. 14. 8. 2021]. Available on: <https://www.schrack.cz/eshop/rozvadec-wst-ip66-800x600x300mm-1kridle-dvere-vcetne-md-wst8060300.html>
- [5] University of West Bohemia – Fly on Vison team (FEL KEP), "FlyOnVision", [online], UWB, 2020, [cit. 10. 8. 2021]. Available on <https://flyonvision.com/>.

SESSION 2 - SOFTWARE ENGINEERING

Distributed event queue management system

Patryk Nowacki
Warsaw, Poland
p.g.nowacki@protonmail.com

Radosław Roszczyk  Member, IEEE,
Warsaw University of Technology
Warsaw, Poland

Artur Krupa 
Warsaw University of Life Sciences
Warsaw, Poland

Abstract—This document describes innovative ways of storing events in queues and the working principle of the event queue management system. The paper also includes a description of methods preventing accidents of the event queue management system. The work also presents example scenarios of using the proposed system.

Index Terms—distributed system, events, queue system

I. INTRODUCTION

Management of continuously growing data in digital systems has a severe matter of effectiveness and its functionality. Network communication requires fast and dynamic data transfer regardless of media issues, possible delay, or trace routing of packages. Waiting over a defined time for incoming information is unacceptable and requires transmission repetition. A great example of a nearly perfectly implemented data split solution among multiple nodes and optimized transfer is TCP/IP Protocol. It maximizes the capabilities of the transmission system and minimizes current issues nearly to zero. Use of buffering data packets, implementation of the definition of packet existence (Time-To-Live parameter), redirection through the network to find the best route are precisely implemented solutions that pass the exam.

The problem occurs when it is necessary to accomplish data transmission away from the direct network protocol - in monolith-based systems, or integrated circuits/systems. This is why Queue Management System is desirable in this situation. Algorithms that describe well-working solutions are not widely used. Most of them are already described as patented or waiting to be patented in public documentation and can not be cited. Among these definitions, there is a generally available mechanism that all of them use - called AQM (Active Queue Management) [1], that is based on RED (Random Early Detection) scheme [2] with its modifications taking account of the sensitivity parameter.

Interesting is also defined an AQM implementation with Linear Quadratic Regulator (LQR) method in [3] combined with PID controller that realizes "responsiveness and minimum steady-state error means stable queue length." Finally, the implementation of the idea of Queue Management was described in [4], which was proposed as a real-time service based on IoT devices (Arduino platform supported with WebRTC technology).

This article presents an innovative model of a Queue Management System that allows for effective and reliable managing resources connected to a queue system. It contains an introduction to the fundamentals of the system, information

that describes each of the types of queuing, and a description of typical scenarios associated with the designed Queue Management System. The article was summarized with the advantages and disadvantages of the system.

II. MANAGEMENT SYSTEM

The Queue Management Service proposed here is connected with managing data stored in queues. Data defined here are called "messages." The idea is based on RabbitMQ idea. Each message is processed by Queue Manager, which defines the importance of each message and creates a properly defined queue. Each queue contains zero or more messages, and messages can be stored or taken from the queue. The message itself contains binary data that can be decoded for further processing in a queuing system. Message processing can be considered finished if the sender has processed no further existing relation or last delivery confirmation. For more efficient processing, each message in the system has its own identifier (ID).

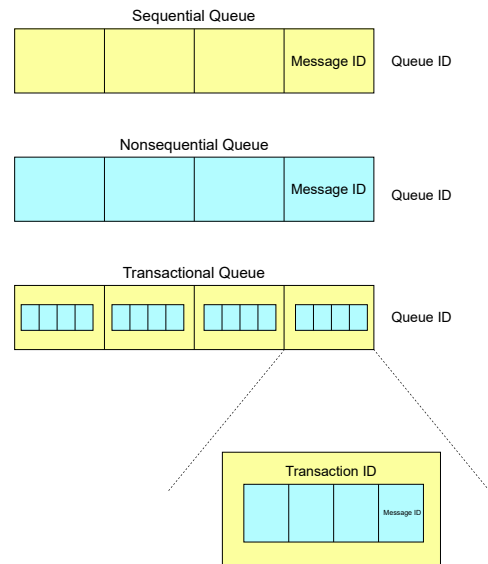


Fig. 1. Three types of Queues structure

Each message has three possible states: ready, processing, removed. The "ready" state defines the message as "put into a system and wait for the system queue". The "processing" state defines the message as "taken from the queue" but not admitted yet, so the process does not finish the task now. The

”removed” state declares that the message has been processed and confirmed.

III. TYPES OF QUEUING

There are widely known three types of queuing systems - nonsequential, sequential, and transactional. Each of these systems was designed to meet the requirements of queue processing models.

To explain the distributed event management system, we have to show how each of the queuing is operating.

The first type of queuing is Nonsequential Queue, which is connected with no sequential actions - the next message is taken from the queue regardless of success or failure in processing the previous one. Each message ready to be processed is taken from the queue and consumed consecutively without acknowledging the status. Based on the presented scheme Fig.2 two messages have been processed and probably finished with success.

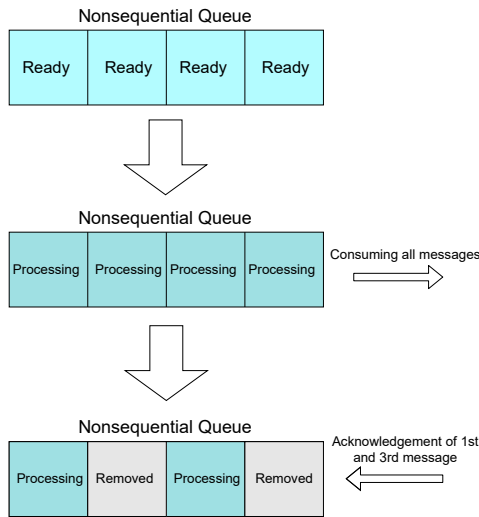


Fig. 2. Nonsequential Queue structure

The second type of queuing is Sequential Queues connected directly with sequential actions, which forces the system to take the next message from the queue only on the previous success state. As presented in Fig.3 all messages at the beginning are in a ready state after this queue system takes the first message and consumes it to a processing state. After the message status returns to the queue (or not, after the declared time), the next message can be consumed from the queue to a processing state.

The last queuing system is Transactional Queue, a hybrid of the Nonsequential Queue and the Sequential Queues. All messages sent to a queuing system are divided into more significant messages containing submessages only related to their parent. More significant messages are consumed in a processing state in Sequential Queues. The next block is consumed after taking information about the previous one processed with success or failure. Each larger message contains

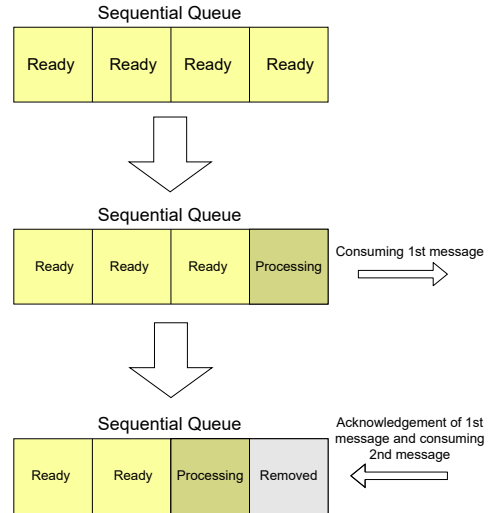


Fig. 3. Sequential Queue structure

a set of submessages consumed in one transaction without the necessity of waiting for a single message. Success in the processing of a transaction were set after all messages in transaction were processed. The processing diagram has been presented in Fig.4.

IV. DISTRIBUTED ARCHITECTURE

The designed queue management system is a type of distributed architecture and consists of sectors and modules. A sector is a group of modules that provide the same functionality. Distribution is that modules interact with each other by using network protocols, and each sector can be developed regardless of the other sectors, but according to its functionality.

Designed and presented in this article, the queue management system consists of the following modules:

- Producer - initialized queues in the queue service puts messages into queues for further jobs. After that, Queue Manager sends the queue ID to an instance of Job Manager. Job Manager starts to take messages from a queue with the given ID, despite this queue type.
- Job Manager - takes messages from the queue specified by the queue ID and sends them to an instance of the worker. Job Manager also processes feedback from Ack Manager whether the message is processed correctly and returns a success or failure message. It manages the message state to "removed" or "processing again" in case of an issue.
- Worker - processing message provided by Job Manager. After successful processing, the worker has to confirm success or failure by informing Ack Manager.
- Ack Manager - waiting to the end of processing the specified message by any instance of worker. After the end, the worker informs the Ack Manager about the success or failure of the message. Next, Ack Manager

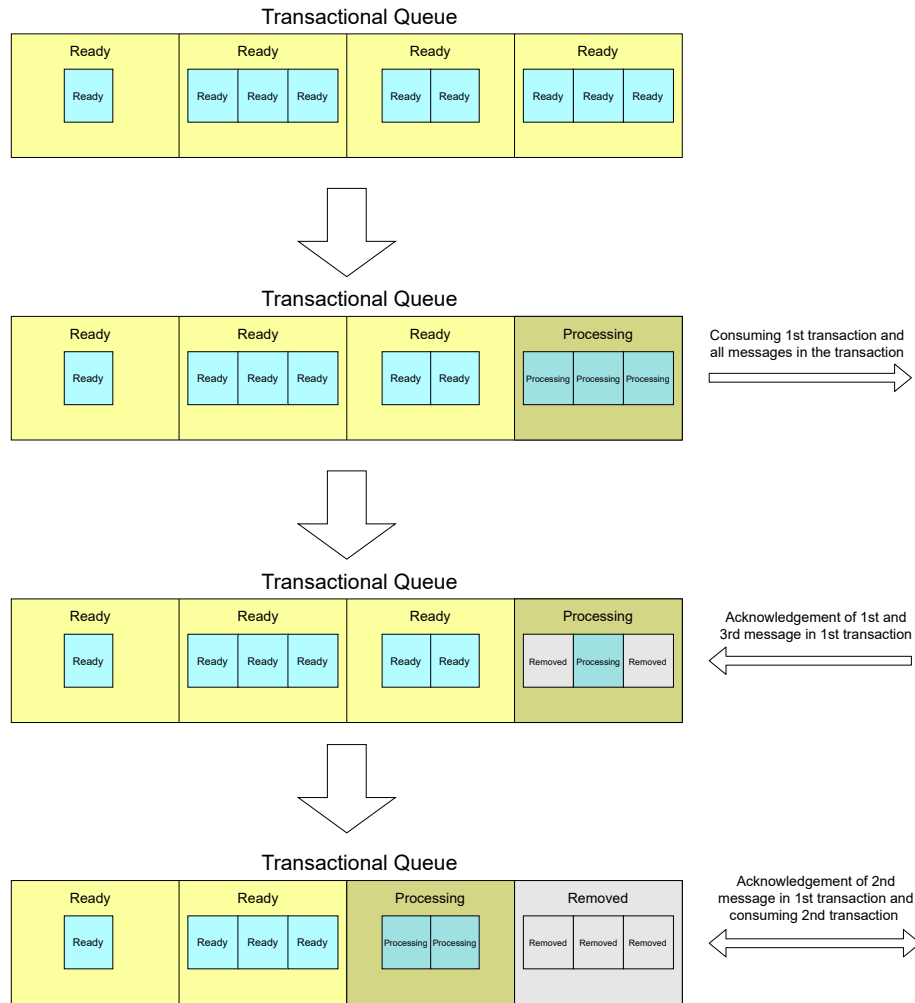


Fig. 4. Transactional Queue structure

is sending information to the Job Manager about the end of the message processing.

- Database - contain crucial information about the message management process and modules responsible for supervision and job execution. These are:
 - Job Manager ID - indicates which instance of Job Manager received a specified message from a queue.
 - Worker ID - indicates which instance of the worker is processing a specified message.
 - Queue ID - indicates to which queue in Queue Service the processed message is related.
 - Transaction ID - indicates to which transaction the processed message is related. If the queue with Queue ID is not the Transactional Queue, then Transaction ID receives a special value.
 - Message ID - indicates which message is processed in the queue.

V. DESCRIPTION OF FUNCTIONALITY

To better understand the processing system, the system and the steps must be described in the process. At first, the producer puts messages into the queue with QueueID. Next, Queue Manager sends Queue ID to any instance of Job Manager. After that, the Job Manager starts consuming the queue with the given Queue ID. The consumption process depends on the queue type and is connected to making a copy of a message for further processing. Then, the Job Manager starts a new instance of a worker, updates the database with a new record associated with the processing message, and sends the message to the worker and the unique ID (Job Manager ID). Subsequently, Worker registers itself in AckManager, processes the message, and after the end of that process, Worker informs Ack Manager about it and passes the Job Manager ID to Worker ID and it. Hence, Ack Manager informs Job Manager specified by Job Manager ID about the acknowledging the message processed by Worker, specified by Worker ID. Finally, the Job Manager deletes the

record associated with the processed message and removes the message from Queue Service.

There is a probability that an accident can occur for some module, i.e., lost connection with the system or a technical problem. The designed queue management system is resistant to those situations. For the introduced management queue system, some following methods prevent undesirable situations:

- Security strategy of Job Manager - related to two situations. The first is taking a copy of a message from a queue, passing it to the worker. The second is receiving information from an instance of Ack Manager and removing a message from the queue.

To prevent the effects of the first case, the Job Manager creates a checkpoint after receiving the Queue ID from Queue Manager. The checkpoint lasts until Job Managers pass a message along with an instance of a worker. When the accident happens in that period, the emergency part of the Job Manager will make a rollback discarding all changes committed after the checkpoint. After that, the new instance of Job Manager starts and gains control of the controller's queue by the lost Job Manager.

To avoid the second situation, we do repetitive signals from the Ack Manager instance and create a checkpoint. The checkpoint is created after the signal of the Ack Manager. It lasts until the Job Manager removes a message from the queue. When an instance of Job Manager loses connection with the system, the emergency part of the Job Manager will make a rollback discarding all changes committed after the checkpoint. Then, Ack Manager is informing the other instance of Job Manager about acknowledging the message as long as the instance of Job Manager gives Ack Manager a return callback to stop it.

- Security Strategy of Worker - is simple and relies on creating a new worker instance. The instance of the worker takes over processing a message that the lost worker processed before losing his connection to the system. When the accident happens, Ack Manager handles the connection error associated with the worker and sends information to Job Manager about the accident. Then Job Manager checks the database to determine which message was processed before the accident. Later that, the message is recopied from the queue. After that, the processing message is targeted at the new instance of the worker.
- Security Strategy of Ack Manager - relies on repetitive signals from the instance of workers. If an accident of Ack Manager happens, Worker informs the other instance of Ack Manager about the end of the processing message. If Ack Manager sends the message to Job Manager successfully, Ack Manager sends a return callback to Worker to stop signalling.

VI. EXAMPLE - BASIC SCENARIO

Producer initializes two queues: Sequential Queue (q1) and Nonsequential Queue (q2). The producer puts two messages (m1 and m2) into q1 and two other messages (m3 and m4)

into q2. There are two instances of Job Manager (jm1 and jm2). Queue Manager gives the ID of q1 to jm1 and the ID of q2 to jm2. Next, some activities happen simultaneously:

- jm1 takes m1 from q1, changes the state of m1 from the ready state to the processing state, and gives m1 to an instance of Worker (w1). Jm1 also stores the IDs of jm1, q1, m1, and w1. After the end of processing m1, w1 informs an Ack Manager (a1) instance about it. Hence, a1 informs jm1 about the acknowledgement of processing m1. Then, jm1 removes data from the database associated with IDs of the process and changes the state of m1 from processing to removal. In the next step, jm1 does take m2 from q1. The processing of m2 will be analogous to the processing of m1 with the existence of the Worker (w2).
- jm2 takes m3 from q2, changes the state of m3 from ready to processing, and gives m3 to an instance of Worker (w3). Jm2 also stores the IDs of jm2, q2, m3, and w3. Next, whatever would happen to m3, jm2 takes m4 from q2, changes the state of m4 from ready to processing, and gives m4 to an instance of Worker (w4). Hence, jm2 stores the IDs of jm2, q2, m4, and w4. When any of the worker instances processes m3 or m4, w3 or w4 informs about Ack Manager's instance (a1). The a1 informs jm2 about the acknowledgement of processing m3 or m4. Then, jm2 removes data from the database associated with IDs of the process and changes the state of m3 or m4 from processing to removal.

VII. CONCLUSIONS

Commonly known architectures of distributed event queue management systems are different than presented here. This has some important advantages:

- provides full control and verification of processing messages from queues,
- provides quite failure-free work.

The designed queue management system contains mechanisms that allow for full control of message processing execution. Entering Ack Management Sector into the queue management system provides verification and proper reaction to message processing.

Modules of the designed queue management system define signalling mechanisms to prevent unpredictable events associated with connection loss or hardware failures. Each receiving module has to confirm its actions by giving a return callback to the sending module.

REFERENCES

- [1] S. S. Kunniyur and R. Srikant, "An Adaptive Virtual Queue (AVQ) algorithm for Active Queue Management," *IEEE/ACM Transactions on Networking*, vol. 12, no. 2, pp. 286–299, 2004.
- [2] V. Firoiu and M. Borden, "Study of active queue management for congestion control," *Proceedings - IEEE INFOCOM*, vol. 3, no. c, pp. 1435–1445, 2000.
- [3] D. Agrawal and F. Granelli, "Redesigning an active queue management system," *GLOBECOM - IEEE Global Telecommunications Conference*, vol. 2, pp. 702–706, 2004.
- [4] M. Ghazal, R. Hamouda, and S. Ali, "An IoT smart queue management system with real-time queue tracking," *Proceedings - 2015 5th International Conference on e-Learning, ECONF 2015*, pp. 257–262, 2016.

Analysis of the sound for recognition of keyboard operations

Marcin Jurczak, Marcin Kołodziej

Warsaw Univeristy of Technology

The Institute of the Theory of Electrical Engineering, Measurement and Information Systems

Warsaw, Poland

marcin.jurczak.dokt@pw.edu.pl

Abstract—The paper presents the problem of identifying the pressed buttons of a typical computer keyboard using audio signals. During the experiments, signals were recorded by a digital recorder while pressing A, M, P, Backspace, and Space keyboard keys. For identification, there were used feature extraction methods and classifiers. The key recognition efficiency for the random forests method was equal 97.5%. There were also implemented disturbance software to prevent proper classification. The conducted research confirms that the developed solution effectively prevents acoustic cryptanalysis.

Index Terms—sound analysis, classification, signal processing, feature extraction, acoustic cryptanalysis

I. INTRODUCTION

The sound is called an auditory sensation caused by acoustic vibrations evoked by an acoustic wave reaching the ear [1]. Sound can be described by many parameters - among them are frequency and intensity. While some sounds (such as human speech) are easy to recognize, others (such as sounds of keyboard keys) are much more difficult for us and our hearing. It turns out that the acoustic signal can be used for acoustic cryptanalysis.

The acoustic cryptanalysis topic has been described in many scientific articles [2]–[6]. Topic similar to this paper research is included in the article [2]. The researchers' aim was to identify the computer keyboard pressed key based on its sound. For this purpose, they created recordings of 30 different keys recorded by computer and a parabolic microphone - only neural networks were used for classification. As training data, they chose 8-10ms window Fast Fourier Transform values. Experiments have shown that the recognition efficiency was 79% (with 300 test sounds), but it turns out that changing the keyboard position reduced efficiency to about 50%.

The article [3] was about an experiment conducted to check it is possible to decipher sounds generated by the computer keyboard during talking via Skype. Three laptop types were analyzed, and key sounds were recorded by microphones built into these laptops. The training dataset contained ten sounds for each of 26 analyzed keyboard keys. The 32 features (mel-frequency cepstral coefficients and coefficients of fast Fourier transform) were selected for training. There were used a lot of classification methods, but the best were linear regression and SVM - recognition efficiency was about 90% then. Lower results were achieved by choosing the k-NN algorithm.

Based on the literature, it turned out that there is also the possibility to „eavesdrop” on data typed on the mobile device touchscreen. This issue was discussed in the article [4]. The built-in microphones of tested devices were used to record the sounds. Researchers conducted 20 attempts consisting of decrypting of 4 digit PIN code from a base of 200 codes. Recognition efficiency was 61%, and the model was not trained with attack victim data. An interesting type of attack, called dictionary attack was discussed in the article [5]. The conclusions from the research showed that long passwords are easier to guess. The authors suggest 7-8 characters as a safe password length. The article [6] presents creating of a more complex model, allowing to increase a proper classification of keyboard keys from 10 minutes recording up to 96%. There were used a computer microphone for recording key sounds. The model consisted of many components responsible for feature extraction, grammatic correction of predicting phrases, and classification. Researchers were used hidden Markov model, linear classifier, and neural networks.

The aim of our research was to identify selected keys of a typical computer keyboard based on recorded audio signals. In the next stage, the authors developed an algorithm that allows to effectively limit the recognition efficiency and thwarting an acoustic attack.

The first research step was to create a selected keys recordings database. During collecting data, there were also needed proper sound processing - adjusting the duration of a single keypress to other keys. In research, authors focused on five keyboard keys - A, P, M, Space, and Backspace.

The next step was a feature extraction. From each sound represented in discrete digital form (samples), we are able to calculate some numerical features using mathematical operations. The features used in our research are the energy of a signal, zero-crossing rate, mel-frequency cepstral coefficients, spectral centroid, spectral roll-off, spectral flux, and pitches.

After each sound feature extraction process, a stage of training the selected classifiers and the neural network was performed - based on extracted features. The data were previously divided into training and testing datasets.

The next step was testing the trained classifiers and neural network with the testing dataset and to draw conclusions from the conducted research.

II. MATERIALS

The sound recording position was located in a quiet room. It consisted of a keyboard, digital recorder, and a tripod which allows choosing a proper recorder position in relation to the keyboard. All recording sounds needed to be recorded in the same recorder - keyboard position. This approach lets us obtain correct training and testing data. Tascam DR-05 digital recorder was chosen for the keyboard sounds recording process. It is equipped with a pair of omnidirectional microphones arranged in the A-B technique. The digital recorder was placed on a tripod and facing it to record sounds generated by the mechanical keyboard.

The tripod was placed in the middle of the alphanumeric key block. The way the recorder was set up made that sounds generated by keys on a right side of a keyboard (keys P, M, Backspace) reached the recorder's left microphone better and a keys on the left side (key A) - right microphone. The sound generated by the Space key reached both microphones similarly.

Approximately 30 various lengths of recordings of sounds generated by keyboard keys during pressing were recorded at the workstation. Each recording contained 10-30 single key pressing sounds, but not all the recordings were used for the training process. Some of the recordings were created with other digital recorder position. This was to test later how digital recorder position affected learning results. The sounds of a single keystroke had to be selected from each recording. Audacity software was used for this purpose. The authors decided that the duration of A, P, M, and Backspace key sounds would be 300 milliseconds. Sound of Space keystroke duration time was longer (due to higher volume) and equaled 350 milliseconds. Forty recordings of each key (200 total) were selected for the training and testing process. Additionally, there were also selected ten recordings of each key, recorded in improper digital recorder position - for testing process. The authors recorded ten sounds of each key during the working of disturbance software. A total of 300 recordings of single keystrokes were used for research - a summary of the sounds can be seen in table I.

TABLE I
SUMMARY OF THE NUMBER OF RECORDINGS FOR EACH ATTEMPT.

	<i>A</i>	<i>Backspace</i>	<i>M</i>	<i>P</i>	<i>Space</i>
Proper recorder position	40	40	40	40	40
Changed recorder position	10	10	10	10	10
Interference software	10	10	10	10	10

Figure 1 presents an example of a recorded audio signal of a keystroke. We can observe there amplitude fluctuations caused by key pressing and release.

III. METHODS

A. Feature extraction

The feature extraction process allowed for the mathematical description of the signal, which enabled model training.

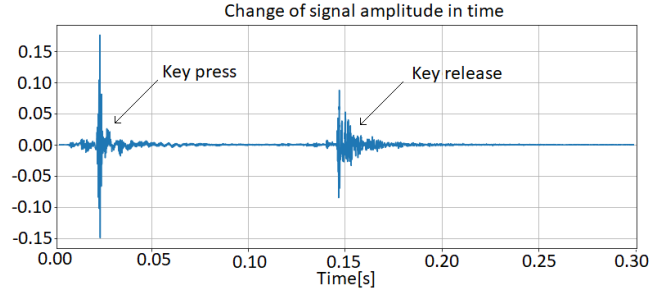


Fig. 1. Graph of amplitude fluctuations caused by key pressing and release.

Sounds were loaded as monophonic to reduce the number of features. Most of the features extracted from sounds have been described in [7] and were related to Short Time Fourier Transform (STFT). These were spectral centroid, roll-off, flux, and twenty mel-frequency cepstral coefficients. Other features extracted from signals were the energy of a signal, root mean square energy (RMSE), zero-crossing rate, and pitches. Some of the extracted features were based on the time form of the signal and were determined only with time-varying amplitude - for example, zero-crossing rate or energy of a signal. Features like spectral roll-off (which informs us about the frequency below which a certain part of the total energy of the signal is concentrated) or spectral flux (which describes changes in the dynamics of the spectrum) required the use of time-frequency analysis.

B. Classification

Decision trees, random forests and neural networks models were used for classification process [8], [9]. A decision tree is a tree-like structure (drawn with a root up). It consists of a root, nodes, edges, and leaves. The decision tree represents the various possible decision paths, and the consequences of choosing each path [8].

Because of overfitting decision trees to the training data, a technique called random forests can be used. It involves creating many decision trees and letting them choose how to classify input data by voting. Instead of training each tree on all training dataset samples, we can train them on a subset of this dataset (bootstrap aggregation). Additionally, random forests provide a selection of the most important features during classifier building.

Neural networks are another models that allow data classification [9]. After conducting many experiments, it was decided for the four-layer network, which contained 18, 18, 18, and 5 neurons. The last layer, because of five classes (analysis of five different keyboard keys), had five outputs. „Relu” activation function was applied for each layer, except the output layer - there „Softmax” activation function was chosen.

C. Assessing the effectiveness of classification

The authors used a confusion matrix to assess the effectiveness of classification [10]. Metric, which allows measuring the effectiveness, is called an accuracy [10]. The accuracy

value depends on the number of input data and the correctness of their classification. As described earlier, there were used 200 recordings (5 keyboard keys, each sound recorded 40 times) for training and testing classification models. Feature extraction was applied, and extracted 30 different features from each recording. The recorded signals were randomly divided for training and testing in an 80 to 20 ratio (160 recordings for training and 40 for testing).

IV. RESULTS

A. Classification results

The decision tree model was the first classification method. Analyzing the results, we can observe a significant number of classification errors, even though the training process was successful. Classification accuracy was equal 82.5%. Despite seven prediction errors, the accuracy was at a satisfactory level. However, this confirms the tendency of decision trees for overfitting.

As a comparison to the earlier model - decision trees, a random forests method (with a selection of best features and without it) will be presented. Obtained accuracy for no best features selection was equal 92.5%, but a selection of the most important features let achieved 97.5% - confusion matrix for this case is shown in the figure 2.

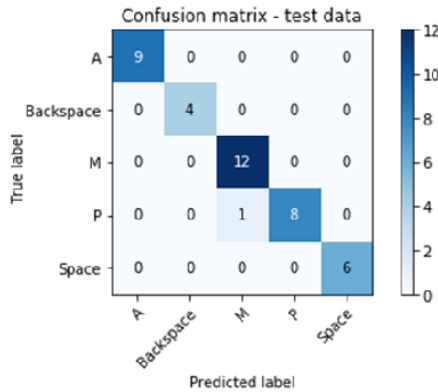


Fig. 2. Prediction results for random forest with the best feature selection.

The prediction results of neural networks depend on the number of training epochs - it should be selected not to overfit the model. Many trials have been conducted, however, the best results were obtained for 5000 training epochs. Classification accuracy for this case was equal 87.5%, but training time was about 30 seconds.

The last described classification model was combining two methods - neural networks and random forests. The idea of using this combination is to select the best features with random forest first and then start the neural network training stage with selected features only. In this case, for 5000 training epochs, obtained accuracy was 97.5%, and training time was about 30 seconds. While analyzing the results, it was noted that for a limited number of features there was an increase of classification accuracy (for similar calculation time).

Table II summarizes averaged classification accuracies obtained during 10 trials for analyzed models.

TABLE II
AVERAGED CLASSIFICATION ACCURACY FOR EACH OF ANALYZED MODELS DURING 10 TRIALS.

Classifier	Accuracy
Decision tree	0.89
Random forest	0.95
Random forest with the best features selection	0.97
Neural network	0.88
Neural network with the best features selection	0.89

B. Disturbance software to prevent a key-pressing eavesdropping

Sounds generated by mechanical keyboard keys during typing can be recorded and classified by trained classifiers. To prevent key-pressing eavesdropping, the authors implemented a disturbance software. Its purpose was to prevent the proper recording of sounds and their correct classification. It causes (just after key pressing) playback interference sound (noise) from the computer speaker, preventing proper recording. Sound recorded while Space key pressing (turning on an interference sound) is shown in the figure 3. The initial phase (key pressing) is clearly visible, but releasing phase has been successfully masked by the playback noise. Duration of interference noise lasts 30 seconds after key pressed - so next sounds of keys pressing and releasing are effectively drowned out.

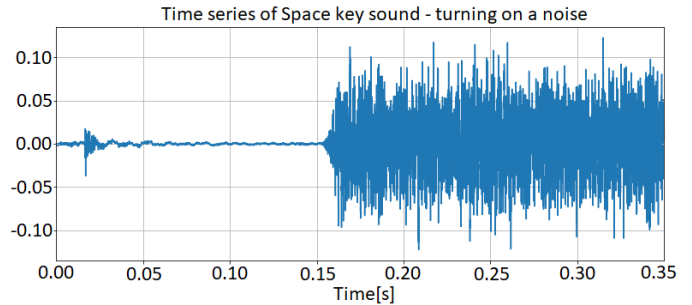


Fig. 3. The recorded sound of a key that turning on noise playback.

Table III presents a summary of accuracy reached by analyzed models during the running of disturbance software.

The conducted experiments show that none of the trained and described classification models are resistant to interfering sounds.

V. DISCUSSION

Analyzing the results, we can observe that the best classification accuracy was reached by standard random forest and random forest with the best feature selection. Random forest training was quick (it took about 40 milliseconds), and classification accuracy was very high. In the case of neural networks,

TABLE III
CLASSIFICATION ACCURACY REACHED BY ANALYZED MODELS DURING
THE RUNNING OF DISTURBANCE SOFTWARE.

Classifier	Accuracy
Decision tree	0.18
Random forest	0.18
Random forest with the best features selection	0.20
Neural network	0.20
Neural network with the best features selection	0.20

training took much more time - it shows the superiority of other models. The neural networks were determined to give the best results for 5000 training epochs, but they showed relatively low classification accuracy (comparable to decision trees). The decision trees proved vulnerable for overfitting - too much fit to the training data caused problems with proper classification of test data.

The authors determined a threshold that enabled choosing the best feature subset. Only features with weights above the threshold were used in further analysis. During the research, the threshold value was set to 0.02, which caused choosing 16 most important features. As a result of this procedure, the unnecessary features were removed from input data while keeping the most important. Features selected to further analysis are presented in table IV.

TABLE IV
FEATURES SELECTED BY RANDOM FOREST.

Number of feature	Feature
1	Change sign
2	Energy value
3	Spectral flux
4	Normalized force
5	Pitches average
6	MFCC 1
7	MFCC 2
8	MFCC 3
9	MFCC 4
10	MFCC 5
11	MFCC 7
12	MFCC 8
13	MFCC 14
14	MFCC 15
15	MFCC 17
16	MFCC 19

Another observation is the relatively small number of analyzing mechanical keyboard keys and keyboard in general. A frequently noted classification error was the classification of „P” key as a „M” key and vice versa. These keyboard keys are situated on the same keyboard side, so it could be a reason of mistakes. The „Space” key was the loudest one, so its classification usually did not cause any problems. Another keyboard should also be checked.

A very important conclusion is related to a digital recorder position while recording the sounds of keystrokes. The test has shown that classifiers trained with recordings recorded in proper position (the tripod was placed in the middle of the

alphanumeric key block, facing the keyboard) and tested with different position recordings caused classification errors. This means that the digital recorder’s position is very important. Therefore, training and testing records must be recorded in the same recorder position.

A common problem described in articles is a method of protection against acoustic cryptanalysis attacks. The authors implemented software to prevent proper classification by playback interference sound from computer speakers after key pressing. None of the analyzed classifiers achieved a classification accuracy of more than 20%. Each of the keystroke sounds was classified as the loudest keys - „Space” (rarely as a Backspace). This makes it impossible to even classify real „Space” key properly (we are not sure is it a real „Space” key since every sound is classified as a „Space”). A sound signals amplitude has a major influence on a classification result.

VI. CONCLUSION

The research conducted allowed for mechanical keyboard keystroke identification based on sounds generated during pressing and releasing. Feature extraction process and relevant selection of training data provided a proper classification. The best model was a random forest with the best features selection - it achieved classification accuracy equal to 97.5%. It also turned out that the digital recorder position is really important.

In summary, identification of mechanical keyboard keys based on the sounds its generating is possible. However, classification accuracy depends on the chosen classifier.

REFERENCES

- [1] K. Collins, "Studying Sound: A Theory and Practice of Sound Design," in *Studying Sound: A Theory and Practice of Sound Design*, MIT Press, 2020, pp.1-7.
- [2] D. Asonov and R. Agrawal, "Keyboard acoustic emanations," *IEEE Symposium on Security and Privacy*, 2004. Proceedings. 2004, 2004, pp. 3-11, doi: 10.1109/SECPRI.2004.1301311.
- [3] A. Compagno, M. Conti, D. Lain, G. Tsudik, "Don't Skype & Type! Acoustic Eavesdropping in Voice-Over-IP", arXiv:1609.09359v2 [cs.CR] 11 Mar 2017
- [4] A. Compagno, M. Conti, D. Lain, G. Tsudik, "Hearing your touch: A new acoustic side channel on smartphones", arXiv:1903.11137v1 [cs.CR] 26 Mar 2019
- [5] A. Wool, A. Yeredor, "Dictionary attacks using keyboard acoustic emanations", *Conference Paper Proceedings of the 13th ACM Conference on Computer and Communications Security, CCS 2006, Alexandria, VA, USA, Ioctober 30 - November 3, 2006*
- [6] L. Zhuang, F. Zhou, J. D. Tygar, "Keyboard Acoustic Emanations Revisited", *In Proceedings of the 12th ACM Conference on Computer and Communications Security, November 2005*, pp. 373-382
- [7] P. Rao, "Audio Signal Processing", Chapter in "Speech, Audio, Image and Biomedical Signal Processing using Neural Networks", (Eds.) Bhanu Prasad and S. R. Mahadeva Prasanna, Springer-Verlag, 2007
- [8] H. Ahmed; A. K. Nandi, "Decision Trees and Random Forests," in *Condition Monitoring with Vibration Signals: Compressive Sampling and Learning Algorithms for Rotating Machines*, IEEE, 2019, pp.199-224, doi: 10.1002/9781119544678.ch10.
- [9] M. Eremia; Ch. Liu; A. Edris, "Neural Networks," in *Advanced Solutions in Power Systems: HVDC, FACTS, and Artificial Intelligence*, IEEE, 2016, pp.755-783, doi: 10.1002/9781119175391.ch16.
- [10] H. Ahmed; A. K. Nandi, "Classification Algorithm Validation," in *Condition Monitoring with Vibration Signals: Compressive Sampling and Learning Algorithms for Rotating Machines*, IEEE, 2019, pp.307-319, doi: 10.1002/9781119544678.ch15.

Practical studies of local HTTP cache security

Janusz Sawicki
Warsaw University of Technology
email: janusz.sawicki.stud@pw.edu.pl

Paweł Zych
Warsaw University of Technology
email: pawel.zych3.stud@pw.edu.pl

Bartosz Sawicki
Warsaw University of Technology
email: bartosz.sawicki@pw.edu.pl

Abstract—The current security status of the local HTTP cache mechanism has been analysed. We discuss regulating the security of cache mechanism via HTTP headers, study the extent of usage of the headers within the top 100 webpages and their impact on the behaviour of the local cache implementation within six leading web browsers. Finally, we present known attack vectors and propose four practical principles that should be followed to maintain a balance between the security and usability of the local cache mechanism.

I. INTRODUCTION

One of the most important mechanisms that increase the efficiency of HTTP communication is the cache mechanism [1]. In general, the mechanism stores static resources in a location that is more accessible from the perspective of a HTTP client. The improvement of performance is due to the difference in the physical location of the origin server of the resource and the location of cache mechanism, in which the resource is stored. Data stored in cache memory is physically closer than the data residing on the origin server. If the client sends a request to the server for a resource that was previously stored within cache, it will be retrieved from a location that is physically closer, which means that both requests and responses will be routed via a lesser amount of hops. Along with numerous improvements in the context of data availability and reducing network traffic, the widespread use of data caching mechanism introduces security risks that pose a threat to confidentiality, integrity and availability of HTTP data received by Internet users.

Cache mechanism can be divided into two main types: local cache and shared cache. Local cache is a component of a HTTP client, usually a web browser, meaning that it can be used by one user at the time. Shared cache is being implemented by the use of dedicated proxy servers and CDN networks, thus it can be used by multiple users simultaneously.

HTTP cache mechanism analyzes HTTP requests and HTTP responses, sent between the client and the server and stores responses containing static resources so they can be used in response to further requests. Each stored resource has an assigned, unique cache key, on the basis of which the mechanism searches for the requested resource. If, based on the cache key, the resource is found in cache and can be used, it will be loaded. The standard suggests that the cache key should contain the method used in the HTTP request and the URL of requested resource. In practice, the key can only contain a URL of the resource, as vast majority of stored responses result from request that include the GET method [1]. It is worth

noting that, in some cases, manufacturers of web browsers use more complex cache key building methods in order to increase the level of security.

A important part of the data caching mechanism is the concept of freshness of a given resource, i.e. the time during which it can be used without prior communication with the origin server. Stored response becomes stale when the time elapsed since generating the HTTP response exceeds the time of freshness, usually specified via HTTP response headers. The concept is needed as a given resource may change while it is in the cache. If the resource was always fresh then, after a given period of time, the browser would start to load an out-of-date resource. The stale resource is not automatically removed from the cache, but loading it requires its successful validation. Depending on whether the resource has been modified since it was previously downloaded and cached, the HTTP response to the validation request may include information that the resource has not been changed and its saved version can be loaded, or the resource in its modified version. If the resource has not been modified, the origin server will return an HTTP response containing the code `304 Not Modified`. It must be noted that the response may contain information that updates the properties of the stored response, for example, restore its freshness status.

II. ATTACK VECTORS

In this section we present known examples of attack vectors that abuse the local cache mechanism, as well as corresponding proposed mitigation techniques.

A. Unauthorized access to cache data

As the first of three attack vectors, we describe gaining unauthorized access to HTTP cache data in the event of a local attack. The concept of the attack is simple as it consists only of reading the cache data stored on the disk of the victim's workstation and the access to the data itself does not require privileged user rights. In the case of the most popular browsers, reading data directly from the disk is not possible due to the fact that the data is encoded for optimization purposes. Nevertheless, an attacker can read cache entries via the given browser or an external tool, either on the victim's workstation or on their machine, after transferring the data. However, the condition of getting local access to the system by the attacker is difficult to meet. We can indicate two probable scenarios:

- gaining local access through physical access,
- gaining local access through remote code execution.

One of the criteria of attack vector analysis is the evaluation of the potential consequences of their execution. In the event of gaining unauthorized access to the stored local cache, the most serious implication is the loss of confidentiality of sensitive data of a specific user, such as financial or medical data. Such situation can occur when the web application does not define rules that prohibit storing responses containing embedded sensitive data. An example can be an HTML documents that contains details such as victim's bank account number or address in order to display the main dashboard of the application or the order summary. The vulnerability in question is common, thus it is described within a separate CWE-525 category in the Common Weakness Enumeration classification system.

B. Browser cache poisoning

The poisoning of the local cache requires forcing the victim's browser to store a response, that has been altered by the attacker in a way that that loading it by the browser may cause violation safety, which after being generated by the source server has been modified in such way that loading it by the browser may cause a security violation. In order to modify a resource while in transit via HTTPS protocol, an attacker has to break the encryption established between the client and the server. A type of resource which, if used in case of the attack, may pose a serious threat to victim is JavaScript code. The attacker can add malicious code to the script content, thus the payload will be executed in the context of the victim's browser while keeping the script fully functional. This means that potential outcome of the attack can be similar as in the case of the Cross-Site Scripting attack. However, what increases severity of the attack is the fact that the maliciously altered resource is persistently stored in the cache and, if the browser does not use cache partitioning, can be executed in the context of HTML document that the resource is embedded in [2]. As a result, a single script modification could allow an attacker to, for example, steal cookies from web page where a given script has been embedded, and on which cookies are not set with the `HttpOnly` flag.

C. Cache timing attack

The cache timing attack relies on the analysis of the loading time of resources to display a given page. Attack takes advantage of the fact that the loading time of a resource stored in a local cache is noticeable shorter than the time of retrieving the resource from the origin server. Based on the difference in those two times, the attacker can determine whether the victim's browser has recently sent a request for the given resource. An example scenario of the described attack vector is presented below:

- 1) The attacker identifies the URL of the resource.
- 2) The attacker embeds a hyperlink to a resource in the malicious HTML document.
- 3) The attacker embeds a script that monitors resource load times in the malicious page's document.
- 4) The victim visits a malicious website.

- 5) The victim's browser loads the resource and executes the script.
- 6) Based on the loading time of the resource, the attacker determines whether the victim's browser recently received a response containing the resource.

From the attacker's point of view, executing a cache timing attack provides the most useful information when the resource selected by the attacker is unique to the given page. A good example is an image that is embedded only within web pages that can be accessed only by authorised users. In such case, as a result of the described attack, the attacker is able to determine whether the victim has recently authenticated to a given web application [3]. In case of web applications that serve specific content based on geographic location of the user, the attack can allow the attacker to determine victim's physical location [4]. Such information can be used, for example, in order to conduct a social engineering campaign.

III. HTTP HEADERS

Security of the local cache mechanism depends mostly on specific HTTP headers, that may or may not be present within HTTP response. HTTP headers are included in responses based on configuration of the origin server or a proxy server. The authors of the OWASP Web Security Testing Guide recommend verifying the presence of specific headers and directives within HTTP responses during web application security assessments [5]. Therefore, it can be stated that from the point of view of security of the local cache mechanism, HTTP responses should contain the following headers, directives and, in some cases, assigned values:

- `Cache-Control: no-cache`, which informs the cache mechanism that the response must be successfully validated prior to each loading, even if the response remains fresh.
- `Cache-Control: no-store`, which informs the cache mechanism that it is forbidden to store a given response.
- `Cache-Control: must-revalidate`, which informs the cache mechanism that loading a stale response requires its successful validation even if the client specified that it will accept a stale response, for example, by including `Cache-Control: max-stale` header in the request.
- `Cache-Control: max-age` with a value of 0, which informs the cache mechanism should consider a given response as stale immediately after saving it.
- `Pragma: no-cache`, which serves as a backward compatibility mechanism with the HTTP 1.0 protocol. Its meaning is identical to that of the `Cache-Control: no-cache` header.
- `Expires` with an incorrect value or a value that points to a date in the past, which also serves as a backward compatibility mechanism with the HTTP 1.0 protocol and informs the cache mechanism should consider a given response as stale immediately after saving it.

During the study we have examined to what extent appropriate headers, directives and values are included in HTTP responses. We have analyzed HTTP responses containing homepage documents of one hundred web applications that, according to Alexa, were most popular among users living in Poland. Both the data collection and the research were carried out on April 21, 2021.

Figure 1 shows the results of the analysis, The value labeled as Status 200 shows the number of responses containing the 200 OK response code, which indicates that the request has been handled correctly by the server. Remaining values show the number of responses containing the code 200, in which each was included headers and directives. The CC abbreviation seen in the labels stands for the Cache-Control header. The value marked as Set of headers represents the number of correct answers containing all of the aforementioned headers. It should be noted that in each case the value of Expires header was not analyzed because due to the fact that, from point of view, any value that does not represent a future date should be considered appropriate. Only the presence of the header within HTTP responses was the subject of verification.

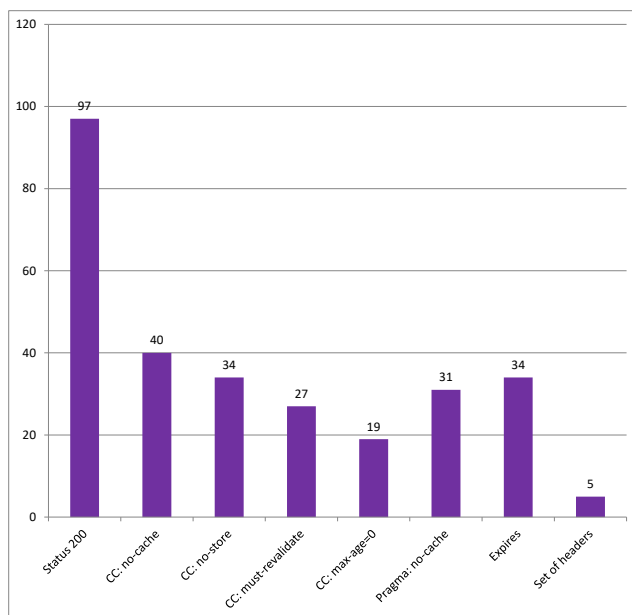


Fig. 1. The occurrence of particular HTTP headers included within HTTP responses containing homepage documents of web applications that are most popular among users living in Poland

Based on the results of the analysis, it can be concluded that the individual headers and directives related improving the security of cache mechanism were included only in about 32% of HTTP responses. The recommended set of headers and directives that disable or significantly restrict cache mechanism was observed only in within five responses.

IV. BROWSER COMPATIBILITY

Another part of study was focused on validating whether browsers respond correctly to headers sent in HTTP responses. Google Chrome, Microsoft Edge, Firefox, Internet Explorer and Opera internet browsers were tested as the most popular web browsers for personal computers [6], excluding Safari. Specialized test environment was built for the purpose of conducting the study. It consisted of an Nginx HTTP server placed in container, Burp Suite HTTP proxy and Windows 10 virtual machine with multiple internet browsers installed. HTTPS was used on both sides of the proxy during testing. Example static web page build of HTML document, CSS style sheet, JS script and PNG image was prepared to be served by HTTP server.

During the testing process various sets of HTTP headers were added to responses by modifying HTTP server configuration file using `add_header` directive. Test cases were:

- TC1 `Cache-Control: max-age=60;`
- TC2 `Cache-Control: no-store;`
- TC3 `Cache-Control: no-cache,`
`Cache-Control: max-age=60;`
- TC4 `Pragma: no-cache;`
- TC5 `Expires: "<date)";`
- TC6 `Cache-Control: max-age=60,`
`Expires: "<date)";`
- TC7 `Expires: "-1",`
`Cache-Control: max-age=60.`

Requests were manually made by clicking a link leading to test page. Request and responses were captured by Burp Suite proxy. Analysis of HTTP history tab in Burp Suite proxy allowed to check if resource was downloaded (status 200 OK), verified (status 304 Not Modified) or assume it was loaded from local cache, when no request was observed.

Almost all internet browsers behaved as expected. Resources were fresh for correct period of time, properly verified or were not cached at all when appropriate HTTP headers were sent. Exception was identified in one case while testing Internet Explorer. Despite sending `Cache-Control: no-cache`, resources were loaded from local cache. This is a violation of section 4 of RFC7234 document. Although header was sent together with `Cache-Control: max-age=60`, restricting caching should have higher priority than allowance for caching.

V. NEED FOR CACHING

In this part of the study we have fetched HTTP traffic from 25 popular webpages in Poland. Then we have analyzed loading times and sizes of resources needed for the browser in order to render the web page. Table II shows the obtained results.

It should be noted that the total times of loading scripts and images presented in the table have been computed assuming that they are requested and loaded in the synchronous manner. In fact, some of these resources are loaded by the browser asynchronously, which shortens the rendering time of page.

TABLE I
THE IMPACT OF HTTP HEADERS ON BEHAVIOR THE LOCAL CACHE MECHANISM

TestCase	Expected	Chrome	Edge	Firefox	Opera	Explorer	Brave
TC1	cached, validated	cached, validated	cached, validated	cached, validated	cached, validated	cached, validated	cached, validated
TC2	not cached	not cached	not cached	not cached	not cached	not cached	not cached
TC3	validated	validated	validated	validated	validated	not validated	validated
TC4	validated	validated	validated	validated	validated	validated	validated
TC5	cached, validated	cached, validated	cached, validated	cached, validated	cached, validated	cached, validated	cached, validated
TC6	max-age priority	max-age priority	max-age priority	max-age priority	max-age priority	max-age priority	max-age priority
TC7	max-age priority	max-age priority	max-age priority	max-age priority	max-age priority	max-age priority	max-age priority

TABLE II
AVERAGE LOADING TIME AND SIZE OF RESOURCES FOR TOP 25 POPULAR WEB APPLICATIONS

	HTML documents	Images	JavaScript scripts
Number of resources per document	1	55	40
Avg. time of loading a single resource [ms]	265	66	76
Avg. size of a single resource [KB]	165	16	36
Total time of loading all resources in a document [ms]	265	3630	3040
Total size of all resources in a document [KB]	165	880	1440

Based on the results, it can be concluded that loading images and scripts requires much more data to be transferred over a longer period of time than loading the HTML document itself. Therefore, from a practical point of view, there is a greater need to cache these types of resources than to cache HTML documents that may contain sensitive data. However, having regard to the attack vectors described in this paper, browser cache poisoning in particular, we believe that only caching of images should be allowed.

VI. FINAL RECOMMENDATIONS

The cache mechanism is a good example of the rule that level of security of a given solution is counter-proportional to its usability. From the security point of view, the best solution is to completely disable the cache mechanism. Obviously, this is the only completely effective way of mitigating the risk associated with usage of the mechanism. However, numerous benefits that it introduces make the risk acceptable. On the other hand, the cache mechanism would be most effective if all restrictions introduced by the described HTTP headers were removed. The desired solution is to find a configuration that provides a great usability of the mechanism, while maintaining the highest possible level of security.

On the basis of presented experiments and studies we have formulated four principles which should be recommended for maintaining high usability and security levels. Note that the fulfillment of the specified principles requires independent actions from different actors of the websecurity theater:

- 1) Protection of HTTP communication through the use of cryptographic mechanisms, implemented by web application developers.
- 2) Correct implementation of security mechanisms within web browsers, carried out by web browser developers.
- 3) Controlling the behaviour of the local cache mechanism, performed by the user.
- 4) Determine the applicable rules for the behaviour of the local cache mechanism depending on type of the resource, implemented by web application developers.

The first principle enforces the encryption of HTTP communication. The use of the encrypted HTTPS protocol ensures the confidentiality of the transmitted data and, which in this case it more relevant, its integrity. Encrypting HTTP communication using strong cryptographic algorithms reduces the risk of performing browser cache poisoning to an acceptable level.

The second principle involves honouring HTTP headers included within responses, as well as the use of available, commonly known defense mechanisms within local cache mechanism implemented by web browsers. An example is cache partitioning [7], [8]. Although this solution significantly increases the redundancy of stored data, we believe that this is an acceptable drawback and the mechanism should be implemented and enforced in all web browsers.

The third principle involves controlling the local cache mechanism works by the user of a given web browser. The level of control is limited, however, some aspects of the mechanism depend on user's preferences. For example, popular web browsers allow the user to delete local cache data, which reduces the risk of gaining unauthorized access to sensitive data by the attacker. Moreover, the user can control behaviour of the local cache mechanism via appropriate web browser extensions and add-ons.

According to the fourth principle, application developers should properly define the caching rules, depending on the type of the resources being returned. Regarding the balance between usability and security, it is appropriate to apply caching only to certain types of resources.

VII. CONCLUSION

Currently used methods of securing the local cache mechanism can potentially reduce the risk posed to confidentiality, integrity and availability of the HTTP data to an acceptable level. In order to achieve that goal, the four aforementioned

Computational Problems in Forecasting in Complex Dynamical Systems

Bohdan Melnyk
dept. Information Systems
of Management
Ivan Franko National University
of Lviv
Lviv, Ukraine
bohdan.melnyk@lnu.edu.ua

Petro Stakhiv
dept. Theoretical and General
Electrical Engineering
Lviv Polytechnic National University
Lviv, Ukraine
petro.h.stakhiv@lpnu.ua

Nataliya Melnyk
dept. Information Systems
of Management
Ivan Franko National University
of Lviv
Lviv, Ukraine
nataliia.melnyk@lnu.edu.ua

Stepan Trokhaniak
dept. Information Systems
of Management
Ivan Franko National University
of Lviv
Lviv, Ukraine
stepan.trokhaniak@lnu.edu.ua

Abstract—The article considers some problems that arise when modeling complex dynamic systems, on the example of the distribution of the computer equipment market. The classic dynamic models used in electrical engineering and electronics are chosen for modeling. It is suggested to use optimization procedures to solve the problems that arise. They make it possible to increase the accuracy of the forecast obtained with the help of a dynamic model. Examples of solving specific optimization problems are considered. Recommendations are given for the application of the proposed approaches for the electrical industry, in particular, the electricity market.

Keywords—dynamic model, optimization procedures, forecast, computer equipment market

I. INTRODUCTION

The concept of Industry 4.0 provides for the development and implementation of intelligent systems in all areas of human life: energy, communications, medicine, science, life, etc. The technical basis for such systems is a variety of computer equipment. It is obvious that the development of this base is closely connected with the existence of a competitive computer equipment market. The larger the market and the more diverse the range of equipment it offers, the faster and more efficient the implementation of computer systems.

Of course, the development of the computer equipment market requires investment. However, before investing their money in a particular business, the investor conducts a comprehensive market research. Such research should be based on scientifically sound methods of modeling and forecasting. In this article, we propose approaches to forecasting the distribution of the computer equipment market in Ukraine.

In Ukraine, the computer equipment market occupies more than 80% of the total domestic market of information technology [1]. Therefore, it is important for the national economy. There are many different sellers in this market. But most of them fall into one of four categories: consumer electronics nets (CEN), specialized computer stores (SCS), mobile communication stores (MCS) and B2B-sector enterprises (B2B) [2]. The computer equipment market is divided into a number of segments: personal computers

(PC), laptops, displays, multifunction devices (MFD), etc. Each category of sellers determines its priorities of presence in a particular segment, which correspond to its trade policy in this market.

We propose to consider the computer equipment market as a complex dynamic system. To model its distribution, it is advisable to use dynamic models, which are borrowed from systems theory [3]. They are often called macromodels [4] and are used in electrical engineering and related fields. In this article, we will look at the challenges of using these models to predict the distribution of the computer equipment market. The proposed approaches to solving these problems can be adapted to the tasks that exist, in particular, in electrical engineering and electronics.

II. GENERAL APPROACHES TO MODELING THE DISTRIBUTION OF THE COMPUTER EQUIPMENT MARKET

The distribution of the computer equipment market over time is changing. To modeling the dynamic of the shares of categories of sellers in different segments of the market, it is proposed [3] to use a classical discrete dynamic model in form:

$$\begin{cases} \vec{x}^{(k+1)} = F \cdot \vec{x}^{(k)} + G \cdot \vec{v}^{(k)} \\ \vec{y}^{(k+1)} = C \cdot \vec{x}^{(k+1)}, k = 0, 1, 2, \dots \end{cases} \quad (1)$$

where $\vec{x}^{(k)}$ – vector of state variables, which characterize the change in the formal state of the market; $\vec{v}^{(k)}$ – vector of input variables that reflect the influence of external factors on the market; $\vec{y}^{(k)}$ – a vector of output variables that reflects the share of market segment held by the category of sellers; k – the moment of time in which the values of the components of the vectors are determined; F, G, C – matrix of formal parameters of the model.

The advantage of this model is that it simultaneously reproduces the dynamics of distribution in all market segments between all categories of sellers. The procedure for its construction does not depend on the number of market segments or the number of categories of sellers.

To identify the parameters of the model (1) are used known in the theory of dynamic systems algorithm of Ho-Kalman [4]. The software implementation of this algorithm in MathCad is presented in [3].

The model in the form (1) can be used to predict the dynamics of distribution of market segments between the categories of sellers, when none of the categories leaves any segment. However, an option is possible when at a certain point in time t_{out} some category ceases to trade a separate type of computer equipment. This means that it ceases to be present in the corresponding market segment. And this market segment will be divided between the categories which continue to sell this particular type of equipment. In order to take into account such changes in the market structure, proposed [3] to use a modified model as:

$$\begin{cases} \bar{x}^{(k+1)} = F \cdot \bar{x}^{(k)} + G \cdot \bar{v}^{(k)} \\ \bar{y}^{(k+1)} = T \cdot C \cdot \bar{x}^{(k+1)}, k = 0, 1, 2, \dots \end{cases}, \quad (2)$$

where T is a diagonal matrix that has the form:

$$T = \begin{pmatrix} f(t_1) & 0 & \dots & 0 \\ 0 & f(t_2) & \dots & 0 \\ \dots & \dots & \dots & \dots \\ \dots & \dots & \dots & \dots \\ 0 & 0 & \dots & f(t_n) \end{pmatrix}, \quad (3)$$

where is the switch function $f(t_j) = \begin{cases} 1, t_j < t_{out} \\ 0, t_j \geq t_{out} \end{cases}$, $j = \overline{1, n}$, n - number of vector components $\bar{y}^{(k)}$ in the model (1).

III. PROBLEMS FOR PREDICTING THE DISTRIBUTION OF MARKET SEGMENTS BETWEEN SELLERS' CATEGORIES

Ho-Kalman algorithm allows you to build a model (1) that accurately reproduces the preliminary distribution of the market. However, when predicting the future distribution, this model gives certain errors. That is why there is a problem of adaptation of the model (1) in order to obtain adequate forecasts.

We are offered such an approach to solving this problem. First we find the forecast of distribution of market segments using the model (1). This forecast is considered as a zero approximation of the final result. Then we analyze the inadequacy of this zero approximation. Based on the analysis, we determine the criteria for achieving an adequate forecast. Taking into account they formulate an appropriate optimization task. At the last stage we solve this task. Its solution will be an adequate result of prediction.

During the use of the model (2) there is another problem. The projected shares of those categories of sellers who remain in a certain segment of the market do not take into account the loss of share by the category that leaves this segment. Obviously, the share lost will be distributed between the categories that remain. To predict this distribution, we propose to apply a separate optimization procedure.

IV. EXAMPLES AND RESULTS OF THE APPLICATION OF OPTIMIZATION PROCEDURES

Consider the example of distribution between categories of sellers of four segments of the computer equipment market ($j = \overline{1, 4}$): PC ($j = 1$), laptops ($j = 2$), displays ($j = 3$), MFD ($j = 4$). Categories of sellers are numbered: CEN ($i = 1$), SCS ($i = 2$), MCS ($i = 3$), B2B ($i = 4$).

To construct a basic model (1) we use statistical data for four periods ($k = \overline{1, 4}$) [3]. With the help of the Ho-Kalman algorithm, the corresponding parameters for this model were identified.

A. Optimization Procedures for Model (1)

Apply the resulting baseline (1) with appropriate parameters to predict the distribution of market segments on the 5th period ($k = 5$). The forecast result is presented in Table 1.

TABLE I. FORECAST OF DISTRIBUTION OF MARKET SEGMENTS IN THE 5TH PERIOD

Categories		Share in market segments, %			
Number	Name	PC	laptops	displays	MFD
1	CEN	34,7	58,0	38,4	56,1
2	SCS	8,2	21,0	23,8	21,2
3	MCS	-1,5	10,7	1,6	5,4
4	B2B	58,6	10,3	36,2	17,3

As can be seen from the table, in the PC segment, the share of MCS matters less than zero that is nonsense. Therefore, the forecast received for all categories w_i^0 ($i = \overline{1, 4}$) will be considered a zero approximation for the final forecast w_i for this segment.

Obviously, the sum of the shares of all categories reaches a maximum at 100%. That is, the objective function for an optimization task has the form

$$\sum_{i=1}^4 w_i \rightarrow \max = 100. \quad (4)$$

The share of any category can not be smaller zero, that is

$$w_i \geq 0, i = \overline{1, 4}. \quad (5)$$

In order to the optimization procedure did not distort the prediction result, which is obtained using a model (1), it is necessary to guarantee the accuracy of this model in a certain neighborhood. To this end, introduce such restrictions for all w_i ($i = \overline{1, 4}$)

$$\left| \frac{w_i - w_i^0}{w_i^0} \right| \leq \varepsilon_i, \quad (6)$$

where $0 \leq \varepsilon_i \leq 1$ are a predetermined errors.

Based on (4) - (6) we formulate an optimization task in general:

$$\begin{cases} w_1 + w_2 + w_3 + w_4 \rightarrow \max \\ \sum_{i=1}^4 w_i = 100 \\ \left| \frac{w_i - w_i^0}{w_i^0} \right| \leq \varepsilon_i \\ w_i \geq 0 \\ 0 \leq \varepsilon_i \leq 1 \\ i = \overline{1,4} \end{cases} \quad (7)$$

The solutions of this task are the final forecast for the 5th period of shares of categories of sellers \tilde{w}_i ($i = \overline{1,4}$) in the PC segment. The forecast that is calculated using the conjugate gradient method is presented in Table 2.

TABLE II. FINAL FORECAST OF THE DISTRIBUTION OF THE PC SEGMENT

Categories	Share in the PC segment, %	Error
CEN	34,0	0,016
SCS	7,8	0,05
MCS	0,1	1,0
B2B	58,1	0,009

As can be seen from Table 2, the magnitude of the predicted MCS share is greater than zero. Comparison of data presented in Tables 1 and 2 shows that the optimization procedure did not distort the distribution trends, which is determined by model (1).

B. Optimization Procedures for Model (2)

Let in the 5th period ($k = 5 = t_{out}$) category MCS refused to trade of displays ($j = 3$). Consequently, when $k = 5$ we have $t_3 = t_{out}$ and accordingly, the switch function $f(t_3) = 0$. For all other $j \neq 3$ the switch function $f(t_j) = 1$. For the category MCS according to (3) matrix T for the model (2) will have the form

$$T = \begin{pmatrix} 1 & 0 & 0 & 0 \\ 0 & 1 & 0 & 0 \\ 0 & 0 & 0 & 0 \\ 0 & 0 & 0 & 1 \end{pmatrix}. \quad (8)$$

For other categories, T is identity matrix.

The Fig. 1 shows the distribution of the segment of the displays, after the use of the model (2) with the corresponding matrices T .

As can be seen from the chart, the category MCS has lost a share, which is equal to 1,6% in segment. Obviously, this share will share those categories that continue to trade displays. To determine the final distribution of the segment, we apply two methods: proportional method and optimization method.

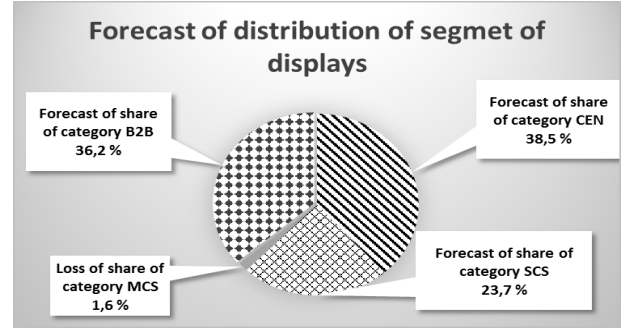


Fig. 1. Forecast of distribution of segment of the displays according to model (2)

1) Proportional method

Under normal conditions, the most likely is proportional distribution of the category MCS shares between categories CEN, SCS and B2B. That is, each category takes the part of the share of the category MCS, which is proportional to their shares in the segment. Namely, category CEN takes 38.5% of 1.6%, category SCS 23.7% and category B2B respectively 36.2%. The Fig. 2 shows the final distribution of the segment.

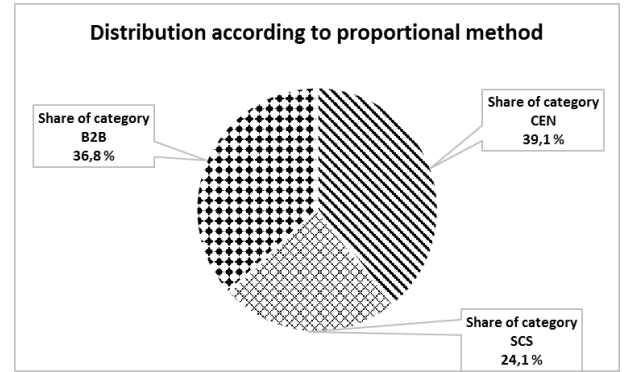


Fig. 2. Forecast of distribution of the segment of the displays by proportional method

2) Optimization method

In many cases, additional conditions must be taken into account when predicted. Therefore, the proportional method should be used at the initial stage of prediction. To take into account the additional conditions we will apply optimization procedures.

a) Optimization procedure 1

Let η_i^0 ($i = \overline{1,2,4}$) is the share of the i -th category according to the forecast received by model (2). As a result of optimization procedure, we obtain a share η_i . Obviously, $\eta_i \geq 0$ and the sum of shares of all categories should be equal to 100% ($\sum_{i=1,2,4} \eta_i = 100$). In addition, none of the categories (CEN, SCS and B2B) can additionally get more than a share which the category MCS has lost, that is 1,6% in the segment. Therefore, restrictions should be performed $|\eta_i - \eta_i^0| \leq 1,6\%$. Consequently, we have an optimization task in the form

$$\begin{cases} \eta_1 + \eta_2 + \eta_4 \rightarrow \max \\ \sum_{i=1,2,4} \eta_i = 100 \\ |\eta_i - \eta_i^0| \leq 1,6 \\ \eta_i \geq 0 \\ i = 1,2,4 \end{cases} \quad (9)$$

The Fig. 3 shows the final forecast of distribution of the segment of the displays by this optimization procedure.

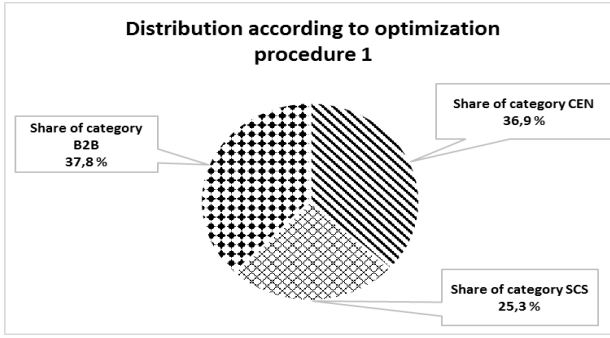


Fig. 3. Forecast of distribution of the segment of the displays by optimization procedure 1

b) Optimization procedure 2

Consider a more difficult situation. Let each of the categories (CEN, SCS and B2B) non plans to increase its share in the segment of the displays more than σ_i . Then in the task (9) must add restrictions $|\eta_i - \eta_i^0| \leq \sigma_i$ ($i = 1,2,4$).

For example, consider a partial case. Let the category SCS ($i = 2$) not plan to increase its share in the segment of the displays more than 0,5%. For this case, the optimization task will have the form

$$\begin{cases} \eta_1 + \eta_2 + \eta_4 \rightarrow \max \\ \sum_{i=1,2,4} \eta_i \rightarrow 100 \\ |\eta_i - \eta_i^0| \leq 1,6 \\ |\eta_2 - \eta_2^0| \leq 0,5 \\ \eta_i \geq 0 \\ i = 1,2,4 \end{cases} \quad (10)$$

The Fig. 4 shows the final forecast of distribution of the segment of the displays by this optimization procedure.

For comparison in Table 3, the results of final forecasts received by different methods and procedures are summarized.

TABLE III. FINAL FORECASTS OF DISTRIBUTION OF THE SEGMENT OF THE DISPLAYS

Categories	Shares according to the final forecast, %		
	Proportional method	Optimization procedure 1	Optimization procedure 2
CEN	39,1	36,9	40,1
SCS	24,1	25,3	23,2
B2B	36,8	37,8	36,7

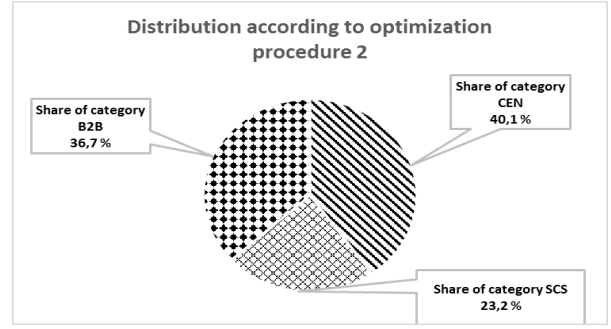


Fig. 4. Forecast of distribution of the segment of the displays by optimization procedure 2

Table 4 shows the difference between forecasts received by different methods and procedures.

TABLE IV. DIFFERENCE BETWEEN FORECASTS

Categories	The difference in predictions between methods, %		
	Proportional method - Optimization procedure 1	Proportional method - Optimization procedure 2	Optimization procedure 1 - Optimization procedure 2
CEN	2,2	-1,0	-3,2
SCS	-1,2	0,9	2,1
B2B	-1,0	0,1	1,1

Let us assume that proportional method specifies the tendency to distribute the share which the category MCS has lost. Based on the analysis of Table 4, it can be concluded that for prediction, the optimization procedure 2 is better than the optimization procedure 1. Smaller differences between predictions obtained by proportional method and according to optimization procedure 2 indicate that. Obviously, the result was influenced by additional restrictions which are in optimization task 2.

V. CONCLUSIONS

Dynamic models in the space of variable states, which are used in various fields, are effective for describing a system with a complex internal structure. However, in the case of constant parameters of such a model, the accuracy of predicting the behavior of the system in the future decreases. Appropriate optimization procedures must be applied to improve accuracy. They make it possible to reduce forecasting errors while maintaining the dynamic characteristics of the system described by the model.

The proposed optimization approaches can be applied in related electrical industries, for example, when forecasting the distribution of electricity production between producers using different generation sources, within a country or region.

REFERENCES

- [1] Information Technology Industry in Ukraine. *Infographic atlas*. 2017. Retrieved from: URL: <http://publications.chamber.ua/2018/IT/the-infographics-report-it-industry-of-ukraine-2017.pdf>.
- [2] GfK Ukraine. Retrieved from: <http://www.gfk.ua>
- [3] N. Melnyk, M. Dyvak, P. Stakhiv, B. Melnyk, Z. Rihova, and M. Vohnoutova, "Modeling the Dynamics of Computer Hardware Market Distribution," in *Advances in Intelligent Systems and Computing V*. CSIT 2020, vol. 1293. Springer, 2021, pp. 823-840.
- [4] P.H. Stakhiv, Y.Y. Kozak, and O.P. Hoholyuk, *Discrete macromodeling in electrical engineering and related fields*, Lviv: Polytechnic Publishing House, 2014 (in Ukrainian).

Coilgun Design by Simulation

Krzysztof Korytkowski

*Faculty of Electrical Engineering
Warsaw University of Technology
Warszawa, Poland*

krzysztof.korytkowski.stud@pw.edu.pl

Jacek Starzyński

*Faculty of Electrical Engineering
Warsaw University of Technology
Warszawa, Poland*

jacek.starzynski@pw.edu.pl

Abstract—Idea of electromagnetic mass driver invariably attracts the attention of both hobbyists in physics, electronics and electrical engineering and people working in these fields at a scientific and research level. Coilguns (aka Gaussian cannons) are one of the most popular devices of this type due to their simplicity and well understood principles of operation. This article describes a computer model of a four-section cannon in which the control of power supply to the solenoids driving the projectile is based on RS switches, electromagnetic tracking of the projectile in the barrel and IGBT transistors switching the power supply to individual solenoids. In order to create the field and circuit models, the ANSYS software environment was used: ANSYS Maxwell2D helped to create a field model of an axisymmetric gun barrel combined with a dynamic model created in ANSYS Simplorer, which solved the circuit and mechanical equations for projectile motion. The aim of authors is to show how much the coupling of the field and circuit models simplify the improvement of the design.

Index Terms—coil gun, computer aided design, coupled modelling

I. INTRODUCTION

The idea of a projectile driven by electrodynamic forces has been of interest to physicists and electrical engineers for years. Numerous applications of such device include not only the weaponry [1] but also testing of objects collisions [2], transport [3], [4] and others. Two fundamental concepts of electrodynamic mass drivers are named railguns and coilguns. The former can be seen as a specialized linear motors in which the conductive projectile form part of a current loop generating the electromagnetic force while the later use typical barrel formed by a coil or a sequence of coils. In this paper we shall concentrate our attention on coilgun, also known as a Gauss rifle or Gauss cannon. Comparing to the railgun it appears to have many advantages, but its design is more complex. Especially for civilian applications coil gun seems to be superior due its non-aggressive operation. Coilguns may in future find widespread use in areas such as transport, space exploration, aircraft engine testing or weapons systems. The EML (Electromagnetic Missile Launcher) developed for the US Navy is one of the most impressive devices based on the principle of operation of the Gauss cannon [5].

The basic idea of a coil gun lies upon a conductive or ferromagnetic object placed on an end of a solenoid excited by a current pulse. Due to the magnetic effect described by Carl Friedrich Gauss this object will be pulled inside the solenoid, by magnetic force trying to place it in the coil centre. The

object will get acceleration, but the force will change the direction once the object passes the coil centre. For that reason the coilgun is usually constructed in form of sequence of coils which are driven by carefully controlled sequence of current pulses.

While some simple coilgun concepts use ferromagnetic projectiles or even permanent magnet projectiles, most advanced designs for high velocities actually incorporate a coil as part of the projectile. In the case of a coil-shaped projectile the magnetic field created by the accelerating solenoids induces a current in the projectile. This current interacts with the field produced by the accelerating solenoid as in an asynchronous machine, creating an accelerating force.

When a current is passed through the driving solenoid, a projectile is drawn into the centre of the solenoid as the system strives for the lowest possible rest energy. When the projectile reaches the centre of the solenoid, the pulling force ceases and a force will appear which will try to slow down the accelerated projectile so that it remains in the centre of the solenoid. Thus, to use a solenoid to accelerate a projectile, the power must be turned off at the moment when the pulling force stops.

Accelerator coils are usually powered from a capacitor bank, what allows a substantial energy to be released in a short time in the form of a high amplitude current pulse. In most classical Gaussian gun designs, each coil is powered by a separate capacitor.

Designing a Gauss cannon involves creating a suitable arrangement of driving coils aligned with an electronic power supply. In the age of CAD, the use of appropriate simulation software can significantly shorten the design process and minimise the number of prototypes. Numerous attempts have been made to optimise the geometry of launcher [7], [8] or the supply/control systems [9]. This paper presents a coil launcher model created in the ANSYS simulation environment. The authors' aim is to show how this complex model, which allows us to consider many aspects of the design, can be used to improve it. We were able to significantly improve the performance of the design by slightly tuning the parameters in the coupled model.

II. CIRCUIT MODEL

A circuit model of the system that supplies and controls the power to the solenoids of the Gauss cannon has been de-

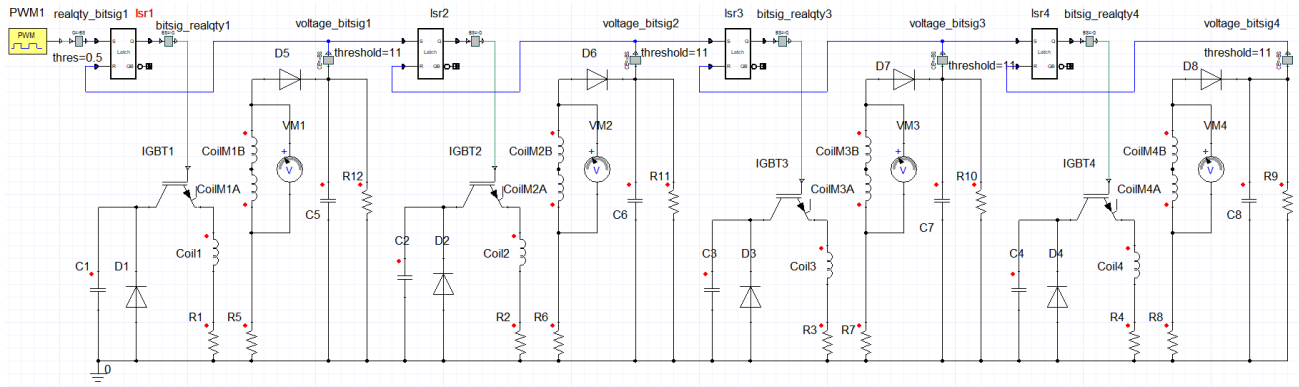


Fig. 1. Conceptual circuit model of the coilgun.

veloped and implemented in ANSYS Simpler. The circuit diagram of the model is shown in Fig. 1.

It should be noticed that Fig. 1 presents not the working model in which the coils are modelled with ANSYS Maxwell, but just the conceptual diagram for explanatory purposes.

The model consists of 4 sections, each supplying single acceleration coil. Each segment includes a power supply part and a control part. View of the single segment is shown in Fig. 2. The reader may easily see the different representation of coils in Fig. 1 and Fig. 2. In the latter each coils is represented just by terminals which couple the circuit and the finite element model (FEM) of the coilgun barrel.

The power supply part consists of a $150 \mu\text{F}$ capacitor charged to 500 V (C2 in Fig. 2), an IGBT transistor that switches the coil power supply circuit, a protective diode, and $1 \text{ m}\Omega$ resistor representing the connecting wires. The measuring part consists of two measuring coils, a rectifying diode, a $1 \mu\text{F}$ (C6) capacitor and a discharge resistor with a resistance of 1Ω . Each section is connected to the respective coils of the field model, represented by ports in the circuit diagram (see Fig. 2, Fig. 3 and Fig. 4).

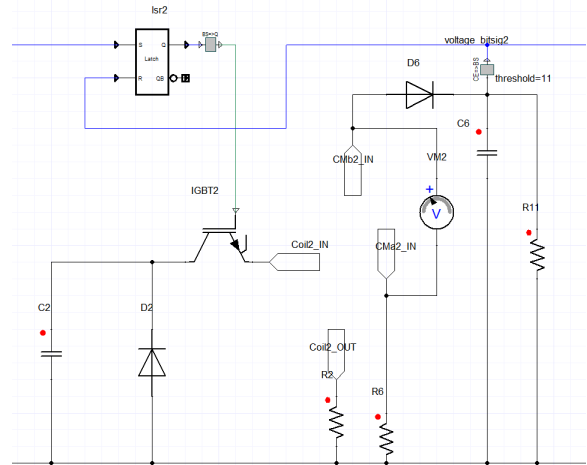


Fig. 2. Single section of the coilgun model. Notice coil terminals coupling the finite element model of the coils.

III. FEM MODEL OF THE PROPULSION SYSTEM

The propulsion system model was modelled using Ansys Maxwell 2D. In order to reduce the computational load, an axisymmetric model was used. Figure 4 shows the most important parts of the finite element model of the cannon. It consists of 4 sections (coils), the projectile and the barrel area in which the projectile moves. In order to allow a realistic distribution of the magnetic field, some external space surrounding the whole model has been added to the model. This external area is not shown in the figure. The materials used for the construction of the model are: copper for the coils, PVC for the supports and 1001 steel for the projectile.

Each section consists of a carcass (green colour) and 3 coils (orange colour). The largest coil is used to accelerate the projectile, while the two small coils in the centre of the case are measuring coils designed to detect when the projectile is just in front of the centre of the coil.

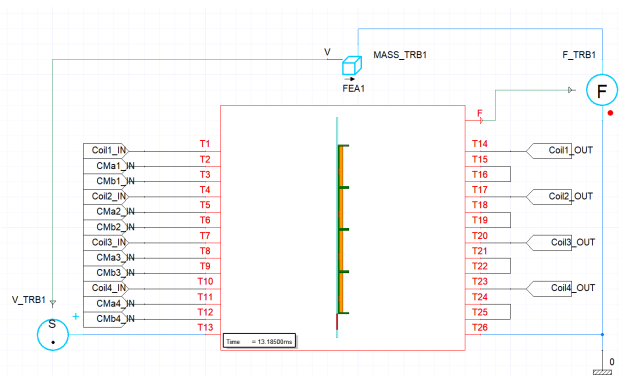


Fig. 3. Combining the circuit model with the field model

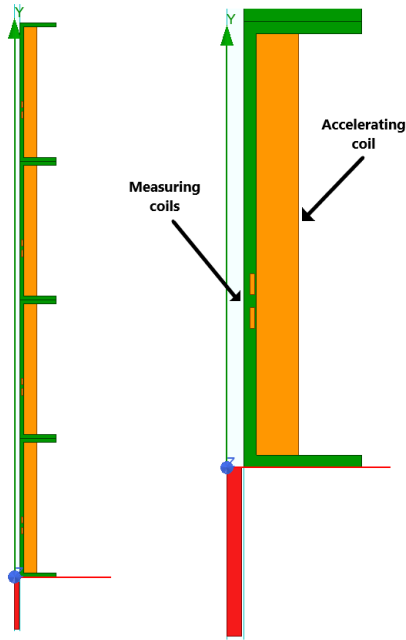


Fig. 4. Propulsion system model (left) and zoom of the first section (right).

Two identical measuring coils from each section are connected in series, but in such a way that the voltage induced in the first measuring coil is subtracted from the voltage induced in the second. Thus, at the terminals of the coils connected in series, the voltage will only appear when a projectile made of ferromagnetic material enters between the measuring coils.

The coils of the model were coupled to corresponding inductors of the circuitual model, presented in the next section.

SIMULATION CYCLE

Set-Reset type latches were used for control of the gun operation. In the first segment one short impulse is sent to the S input of the latch. The pulse comes from a long period, low fill PWM signal source used to trigger the cannon. The pulse sets the Q output of the latch to a high state. A high state is applied to the gate of the first section transistor, which starts conducting. The first coil attracts the projectile (red object in Fig. 4) which starts to move along the barrel. When the projectile enters the measuring coils of the first section, a voltage pulse is induced at the terminals of the connected coils. The voltage pulse is applied to the R input of the first latch and to the S input of the second latch. Thanks to this, at the moment when the projectile is no longer accelerated, and the force changes direction, the power supply to this coil is switched off. The transistor connected to the next accelerating coil begins to conduct and the whole process repeats in the second section, then in the third one ... until the last coil is supplied.

The model includes the components necessary to calculate velocity of projectile, force that acts on it and projectile path.

RESULTS

In Fig. 5 and Fig. 6 show respectively how the velocity of the projectile and the force acting on it are changing as the projectile travels through the barrel of coilgun. Fig. 5 it is shown well how the projectile, as it flies through each segment, accelerates to a certain value and then decelerates slightly. For example, in the first segment, the projectile reaches a maximum velocity of about 31 m/s and then slows down to about 26 m/s. The reason for this slowdown can be found in Fig. 6. The plot of the force acting on the projectile shows well the relatively short peaks of force with large amplitude that slow the projectile down. They always appear after periods of force pulling the projectile into the successive coils. We could say that they occur just before the moment when the power to the acceleration coil in which the projectile is actually located is turned off.

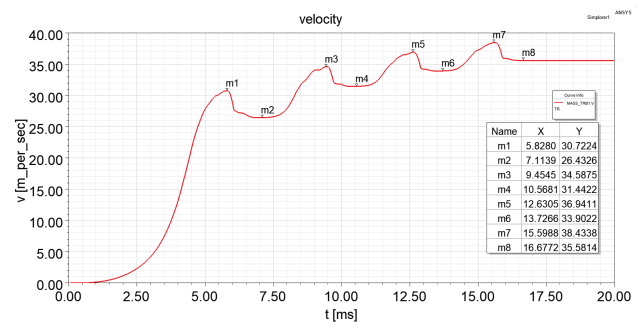


Fig. 5. Projectile velocity as a function of time before model optimization

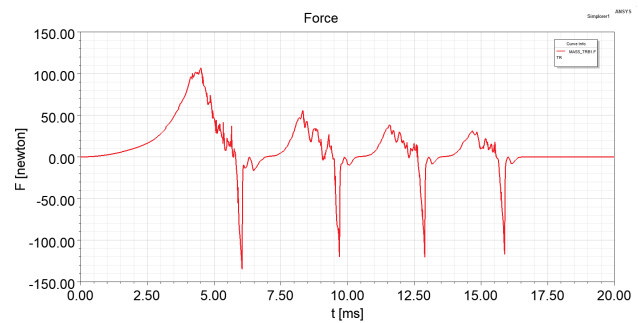


Fig. 6. Projectile acceleration force as a function of time before model optimization

Further analysis of the system performance can be made on the basis of Fig. 7 and Fig. 8. We can see that only the first capacitor is full discharge, while the others are not used effectively (Fig. 7). The cause is observed in Fig. 8 where one can see that currents in the second, third and fourth coils are much smaller than in the first one.

Therefore, in order to minimize the value and duration of these peaks, it was decided to modify the model by moving the measuring coils on the coil former towards the end of the former into which the projectile enters. In the first approach the measuring coils were located in the center of the driving

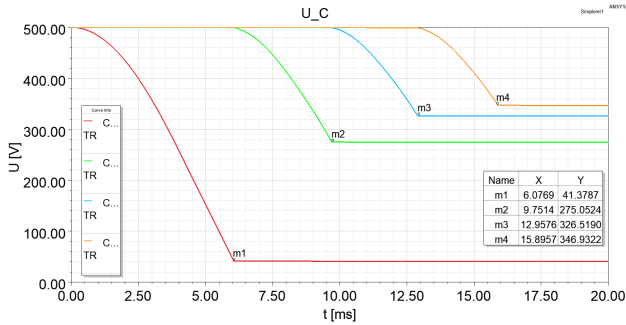


Fig. 7. Voltage across capacitors as a function of time before model optimization

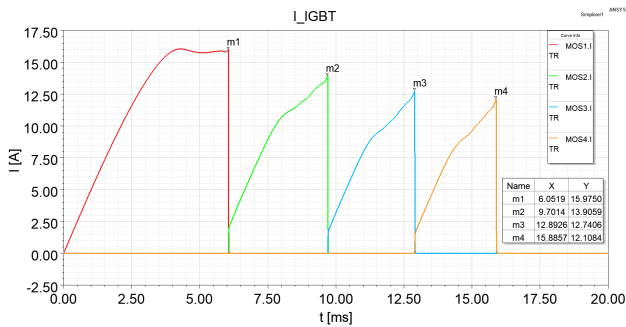


Fig. 8. Emitter currents of IGBT transistors as a function of time before model optimization

coil. Moving the coils slightly down (to the 42.5% from the barrel beginning), we were able to improve substantially the acceleration by reduction of the slowing force peeks. It can be seen by comparing Fig. 6 and Fig. 9.

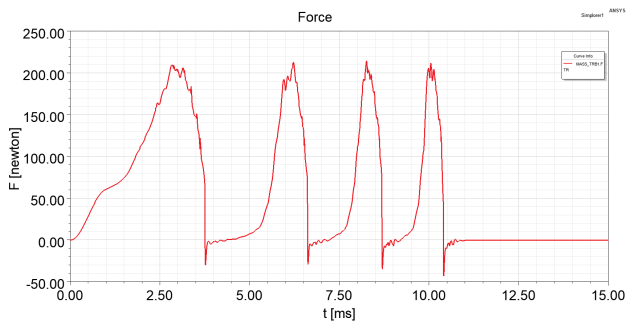


Fig. 9. Projectile acceleration force as a function of time in the improved model

Another modification made after several experiments with the model was increasing the diameter of the winding wire from 1 mm to 2.5 mm. This reduced the number of turns from 1000 to 160, so the resistance and inductance of the coil decreased, while the size of the coil remained the same. Reducing the resistance and inductance allowed to increase the current flowing through the acceleration coils and improve the pulses shape, which can be

seen by comparing Fig. 8 and Fig. 11.

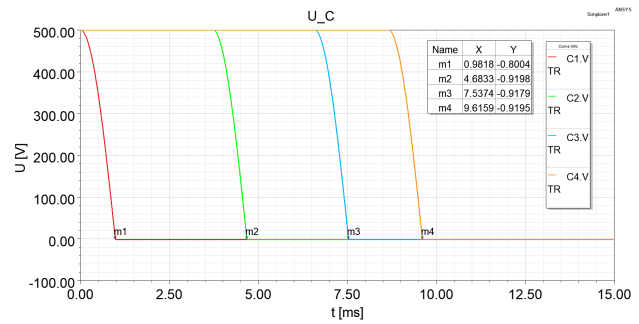


Fig. 10. Voltage across capacitors as a function of time in the improved model

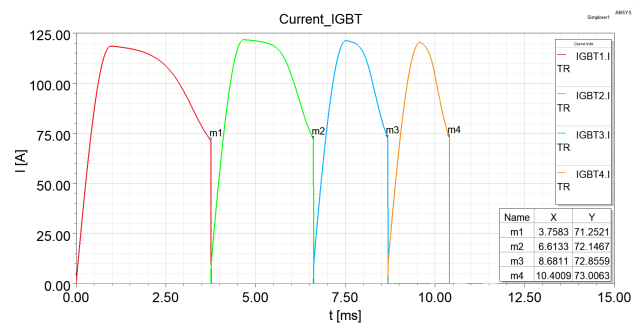


Fig. 11. Emitter currents of IGBT in the improved model

Reducing the resistance and inductance of the acceleration coils also allowed the capacitors to discharge completely during the firing of the Gauss cannon as shown in Fig. 10.

Fig. 12 shows the distance traveled by a projectile over time. The beginning of the plot (up to a time of about 2.5 ms) shows best how the projectile accelerated. This corresponds to the plot of velocity change over time in Fig. 13. It can be seen that the projectile gained 50% of its final velocity by passing through the first coil. It accelerated to about 34 m/s. Each successive coil no longer accelerates the projectile as well as the first. This is most likely due to the fact that the value of the force acting on the projectile does not change much as can be seen in the Fig. 9 but acts on the projectile for a shorter time. Eventually, the projectile is accelerated to a speed of about 68 m/s.

As was written before, in Fig. 10 it can be seen that all capacitors discharge completely when individual transistors are conducting and they do it before the projectile has time to reach the measuring coils, which can be seen if we compare the graphs in Fig. 10 and Fig. 15. Comparing Fig. 11 and Fig. 14 one can conclude that during the time when the capacitor discharges on a given segment according to the resonance phenomenon, the energy stored in it in the electric field flows to the coil and accumulates in the magnetic field (not all of it, of course, considering the resistance loss). The current flows through the RLC circuit, but then doesn't charge the capacitor back up but closes through the diode (Fig. 14).

Peculiarities of the LPTV circuits optimization in the MATLAB software environment

Yuriy Shapovalov
Institute of Telecommunications,
Radioelectronics and Electronic
Engineering
Lviv Polytechnic National University
Lviv, Ukraine
yurii.i.shapovalov@lpnu.ua

Dariya Bachyk
Institute of Telecommunications,
Radioelectronics and Electronic
Engineering
Lviv Polytechnic National University
Lviv, Ukraine
dariia.r.bachyk@lpnu.ua

Ksenia Detsyk
Institute of Telecommunications,
Radioelectronics and Electronic
Engineering
Lviv Polytechnic National University
Lviv, Ukraine
ksenia.o.chaban@lpnu.ua

Abstract— The paper presents the results of applying two optimization functions «patternsearch» and «fmincon» of the MATLAB environment to optimization a single-circuit parametric amplifier. The optimization results showed that the «fmincon» function gave the wrong minimum value, and the «patternsearch» function solved the problem correctly. A similar conclusion was obtained by the developers of MATLAB on their problem. Therefore, in order to obtain adequate results, it is proposed to solve the optimization problem for different starting points and, if necessary, different optimization functions. The objective function is formed on the basis of the symbolic transfer function of the linear periodically time-varying circuit, obtained by the frequency symbol method in the system UDF MAOPCs. Computer experiments performed are described in detail.

Index Terms — circuit analysis computing, linear periodically time-varying circuits, frequency symbolic method, optimization

I. INTRODUCTION

The ability of the linear periodically time-varying (LPTV) circuits (circuits where at least one of the parameters of their elements varies with time at a rate commensurate with the rate of change of applied input signals) to convert the spectrum of input signals and perform parametric amplification of signals at a low noise level has increased its importance in modern radio electronics [1,2,3,4,5]. Over the last decade, interest in the study of LPTV circuits has grown significantly due to the development of high-temperature superconductors and their use in parametric amplifiers, high-quality resonators, filters, long lines, delay lines, etc. [1,2,3,4,5].

As shown in [6,7], the Frequency Symbolic Method (FS method) is one of the most effective tools for modeling and analysis of steady-state LPTV circuits modes in the frequency domain. The method is based on the solution of Zade's equation for a circuit by approximating the conjugate [6] transfer functions $W(x_1, \dots, x_n, s, t)$ of LPTV circuits by a trigonometric Fourier polynomial:

$$W(x_1, \dots, x_n, \Omega, t) = W_{\neq 0}(x_1, \dots, x_n, s) + \sum_{i=1}^k \left[W_{-i}(x_1, \dots, x_n, \omega) \cdot \exp(-ji\Omega t) + W_{+i}(x_1, \dots, x_n, \omega) \cdot \exp(+ji\Omega t) \right], \quad (1)$$

where x_1, \dots, x_n are the symbolic parameters of the elements of the circuit, $s = j\omega$ – is the complex variable, t - time, k - is the number of harmonic components in the polynomial, $\Omega = 2\pi/T$, T – is the period of change of the parameter of the parametric element of the circle under the impact of the pump signal.

In [8,9] the User-Defined Functions (UDF) MAOPCs, is described, which is designed for automated multivariate analysis and optimization of LPTV circuits. The architecture of the system UDF MAOPCs is based on the principles of the MATLAB software environment [10]. The mathematical support of the system UDF MAOPCs is based on the FS method [6,7].

Solving the problem of optimizing LPTV circuits requires following features:

- a) the dependence of the transfer functions and characteristics of the circuit on time;
- b) the necessity of the control of the circle stability when the parameters of its elements are changed.

As it has shown in practice, these features affect the choice of the method for optimizing LPTV circuits, which is a conditional optimization of the function of many variables.

The research paper is devoted to the specified features of LPTV circuits and the choice of the method of their optimization in the MATLAB environment.

II. PECULIARITIES OF LPTV CIRCUITS OPTIMIZATION

As is known [11], the problems of finding the minimum (maximum) of the function $F(x_1, \dots, x_n, s, t)$ that depends on variables x_1, \dots, x_n, s, t with any limits are combined under the common name of *mathematical programming problems* [11, 12]. A function is called an *objective function where the minimum (maximum) value must be calculated (optimality criterion)* [11, 12]. This function evaluates the quality of the optimization performed and assumes the presence of variable parameters x_1, \dots, x_n with values, which change during an optimization and affect the value of the objective function $F(x_1, \dots, x_n, s, t)$ [11, 12]. The solution of the optimization problem is considered to be such finite values of the varied parameters x_1, \dots, x_n that provide the minimum (maximum) value of the objective function $F(x_1, \dots, x_n, s, t)$ under given limits [11,12].

In this paper for optimization of LPTV circuits the general additive criterion of optimality is chosen [11, 12], which is the sum of squares of deviations of initial characteristics from technical requirements. In our case, the objective function $F(x_1, \dots, x_n, s, t)$ (additive optimality criterion) for the selected values of the complex variable $s_i = j\omega_i$ (here $j = \sqrt{-1}$) of the studied frequency range and time values t_j (here $j = 1, 2, \dots$), selected on the period $(0 - 2\pi/\Omega)$ of change of the transfer function, presumably is the following [1, 12]:

$$F(x_1, \dots, x_n, \omega, t) = \sum_{i=1}^p \sum_{j=1}^q \left(M_F(x_1, \dots, x_n, \omega_i, t_j) - M_0(\omega_i, t_j) \right)^2, \quad (2)$$

where $M_0(\omega_i, t_j)$ and $M_F(x_1, \dots, x_n, \omega_i, t_j)$ are the objective function and the characteristic function, respectively. The objective function $M_0(\omega_i, t_j)$ is defined by the researcher using a set of values for the selected variable values ω_i and t_j . The characteristic function $M_F(x_1, \dots, x_n, \omega_i, t_j)$ is defined by the modulus of the parametric transfer function $W(x_1, \dots, x_n, \omega_i, t_j)$ of the LPTV circuit, which, according to the FS method [7,8], is pre-formed as an approximation (1) for the symbolic parameters x_1, \dots, x_n and the current values ω_i, t_j .

As noted above, the peculiarity of the problems of LPTV circuits optimization (mostly parametric amplifiers) is that they require stability control [13,14]. Therefore, the range of change of the varying parameters x_1, \dots, x_n is chosen so that it is inside the stability range of the steady-state mode of the circle in the range of the same variable parameters x_1, \dots, x_n .

The procedure for optimization of a parametric amplifier with two variable parameters of the elements has been considered [12]. The amplifier stability should be evaluated by the denominator $\Delta_G(s, x_1, x_2)$ of the corresponding normal parametric transfer function $G(s, \xi, x_1, x_2)$, which is determined, as well as the conjugate transfer function of the circuit, by the frequency symbolic method [13,14], ξ -moment of supply to the delta pulse circuit.

The result of this evaluation is the area of amplifier stability, the mathematical description of which is a condition for optimization.

The procedure of optimization of the parametric amplifier under the condition of control of its stability is carried out according to the following algorithm:

Step 1. According to the FS-method, the denominator $\Delta_G(s, x_1, x_2)$ of the normal parametric transfer function is formed at the values s, ξ and parameters x_1, x_2 of the given symbols.

Step 2. For each value of x_1 from a number of values of the set range the limit value of x_2 at which stability changes to instability is defined, and dependences $x_{2sp} = f(x_1)$ are formed. As a result the so-called "stability map" in coordinates of parameters x_1 and x_2 is created.

Step 3. The dependences defined in step 2 are approximated, for example, by power polynomials and the stability ranges are determined in the form of inequality $x_2 < f(x_1)$.

Step 4. The objective function $M_0(\omega_i, t_j)$ is formed for the current values of the variables ω_i and t_j .

Step 5. In the form (2) for the current values ω_i and t_j the function of the characteristic $M_F(x_1, x_2, \omega_i, t_j)$ of the

circle with symbolic parameters is determined according to the Frequency Symbolic method.

Step 6. The objective function $F(x_1, x_2)$ is formed as an area in the parameter coordinates x_1, x_2 as (2) for the given values of the variables ω_i and t_j .

Step 7. The minimum value of the objective function, defined by one of the optimization methods when the stability conditions are met as follows $x_2 < f(x_1)$, defines the desired parameter values x_1^* and x_2^* of the parametric amplifier.

The objective and characteristic functions are formed taking into account the considered features of the system UDF MAOPCs. The following optimization of the LPTV circuits is performed using standard MATLAB software tools.

III. OPTIMIZATION IN THE MATLAB SOFTWARE ENVIRONMENT

MATLAB is one of the most powerful systems of computer mathematics, built on the advanced application of matrix calculations [10]. It includes several extension packages such as Simulink, Toolbox, and Blockset, which are focused on a wide variety of tasks that require mathematical calculations, deep analysis, and modeling.

The MATLAB environment Toolbox package includes two packages designed to solve optimization problems: «Toolbox Optimization» and «Toolbox Global Optimization».

The first «Toolbox Optimization» package includes a set of functions that implement methods and algorithms for one-dimensional and multidimensional unconditional and conditional minimization, linear, boolean and quadratic programming, least squares and solving equations, as well as algorithms for multi-criteria optimization.

The functions of the «Global Optimization Toolbox» package are focused on finding a global minimum or multiple minima. It uses direct search, multi-start, and genetic algorithm methods. Also, this package includes the multi-criteria optimization genetic algorithm.

After reviewing and analyzing the optimization functions of the MATLAB software environment, we focused on the two following functions: «patternsearch» [15] from the «Global Optimization Toolbox» package and «fmincon» [16] from the «Optimization Toolbox» package, because they allow conditional optimization of multivariable functions. Let us briefly consider the results of applying the «patternsearch» and «fmincon» functions using a test optimization of a stochastic objective function implemented in the MATLAB software environment [17].

A. Optimization of stochastic objective function [17]

In the example test the developers of MATLAB have used stochastic objective function [17]. It is shown that the «fmincon» function from the «Optimization Toolbox» does not define minimum. As follows from Fig. 1, the function «fmincon» incorrectly defined the minimum of the stochastic objective function [17]. Also In the example test shown that the «patternsearch» function from the «Global Optimization

Toolbox » define minimum of a stochastic objective function. The optimization results are graphically shown in Fig. 1. [17].

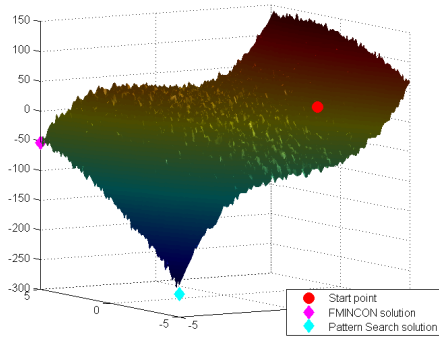


Fig 1. Optimization of a stochastic objective function

According to the results of the test example, the optimization functions in the MATLAB software environment do not always determine the optimal values. The «fmincon» function defined the minimum of the stochastic objective function incorrectly.

Having obtained such results of the test example [17] the task to investigate results that will be obtained when optimizing LPTV circuits, in particular, parametric amplifiers, using the conditional optimization functions «patternsearch» and «fmincon» has been set.

IV. PECULIARITIES OF OPTIMIZATION OF LPTV CIRCUITS IN THE MATLAB SOFTWARE ENVIRONMENT

The single-circuit parametric amplifier from Fig.2 will be optimized in the computer experiment.

Task for the computer experiment. Perform optimization and determine the values c_0^* and m^* , providing a minimum of the objective function $F(c_0, m) = F_{\min}$, which is formed for each frequency point ω_i from the specified range $1.7 \cdot \pi \cdot 10^8 : 0.02 \cdot \pi \cdot 10^8 : 2.5 \cdot \pi \cdot 10^8$ rad/s and for each time point t_j from the specified range $0 : 0.05 \cdot 10^{-9} : 5 \cdot 10^{-9}$ s for the parametric transfer function $Z_1(s, t) = U_1(s, t) / I(s)$ of the single-circuit parametric amplifier from Fig.2 under the condition of its asymptotic stability. The optimization is performed in the MATLAB software environment using the «fmincon» function from the «Optimization Toolbox» package, the «patternsearch» function from the «Global Optimization Toolbox» package, and the system UDF MAOPCs.

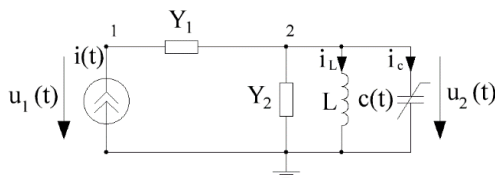


Fig.2. Single-circuit parametric amplifier

$$i(t) = I_m \cdot \cos(\omega_c \cdot t + \varphi), \quad c(t) = c_0 \cdot (1 + m \cdot \cos(\Omega \cdot t)),$$

$$c_0 = 10 \cdot 10^{-12} F, \quad m = 0.05, \quad \Omega = 4 \cdot \pi \cdot 10^8 \text{ rad/s},$$

$$Y_1 = 0.25 S, \quad Y_2 = 0.0004 S, \quad L = 0.2533 \cdot 10^{-6} H,$$

$$s = j\omega_c, \omega_c = 2 \cdot \pi \cdot 10^8 \text{ rad/s}.$$

Performance of the computer experiment According to the optimization procedure for the parametric amplifier,

provided that its stability is controlled, the following steps have been performed :

Step 1. Using the «Stability» function [8,9] of the system UDF MAOPCs, the denominator $\Delta_G(s, m, c_0)$ of the normal parametric transfer function $G(s, \xi)$ for the symbolic parameter values m and c_0 have been calculated.

Step 2. Using the «Stability» function [8,9] of the system UDF MAOPCs and the denominator $\Delta_G(s, m, c_0)$ calculated in Step 1, for each value c_0 the boundary value m is calculated from a number of values in the given range, where stability changes to instability and functional connections $m_{sp} = f(c_0)$ are formed. As a result of such actions, the so-called "stable map" is formed in the coordinates of the parameters m and c_0 .

Step 3. Using the «FunctionOfZoneStability» function [8,9] of the system UDF MAOPCs, the functional connection $m_{sp} = f(c_0)$ calculated in Step 2 was approximated, using a fourth-degree polynomial and find the analytical expression. The resulting inequality is used when using the «patternsearch» and «fmincon» optimization functions.

Step 4. Using the «FSM» function [8,9] of the system UDF MAOPCs, the parametric transfer function $Z_1(s, t)$ was defined, which will be the basis to optimize the amplifier from fig.3. Using the «FormOfFunOfGoal» function [8,9], the objective function $M_0(\omega_i, t_j)$ was defined. In this example, it was formed in such a way that the amplifier from fig.2 is able to implement it, by selecting the value c_0 and m arbitrarily within the physical realizability of their parametric element. These values should be found based on the result of further optimization as c_0^* and m^* , which will indicate that the optimization process is correct. The objective function $M_0(\omega_i, t_j)$ was defined as the modulus of the transfer function of the amplifier $|Z_1(\omega_i, t_j)|$.

Step 5. Using the «FormOfFunCharacteristic» function [8,9] of the system UDF MAOPCs, the characteristic function $M_{Z_1}(c_0, m, \omega_i, t_j)$ of the single-circuit parametric amplifier in the form of the modulus of the transfer function $|Z_1(m, c_0, \omega_i, t_j)|$ has been defined.

Step 6. Using the «FormOfObjectiveFun» function [8,9] of the system UDF MAOPCs, the objective function $F(c_0, m)$ has been defined at the specified values ω_i and t_j : $1.7 \cdot \pi \cdot 10^8 - 2.5 \cdot \pi \cdot 10^8$ rad/s with the step $0.02 \cdot \pi \cdot 10^8$ rad/s and $0 - 5 \cdot 10^{-9}$ s with the step $0.05 \cdot 10^{-9}$ s, respectively, as (2).

Step 7. Using the «patternsearch» and «fmincon» optimization function, provided that the amplifier (3) is stable, we optimize and determine the parameter values c_0 and m , providing the minimum of the objective function $F(c_0, m) = F_{\min}$, which is defined for each frequency point ω_i from the specified range $1.7 \cdot \pi \cdot 10^8 : 0.02 \cdot \pi \cdot 10^8 : 2.5 \cdot \pi \cdot 10^8$ rad/s and for each time point t_j from the specified range $0 : 0.05 \cdot 10^{-9} : 5 \cdot 10^{-9}$ s for

the parametric transfer function $Z_1(s,t)$ of the single-circuit parametric amplifier from fig.2.

Results of the computer experiment. Using the «fmincon» optimization function, provided that the amplifier (3) is stable and the initial values (start point Fig.3) $c_0 = 0.9 \cdot 10^{-11} F$, $m = 0.01$ are random, the value of the objective function has been defined as $F(c_0, m) = 7.151e5$ when $c_0^* = 0.99 \cdot 10^{-11}$ and $m^* = 0.01$ for 15 iterations. This value is not the minimum value of this function. Thus, the «fmincon» optimization function determines the minimum of the function incorrectly. (Fig. 3).

Using the «patternsearch» optimization function, provided that the amplifier (3) is stable and the initial values (start point Fig.3) $c_0 = 0.9 \cdot 10^{-11} F$, $m = 0.01$ are random, the minimum of variable parameters is defined for 7 iterations F_{\min} when $c_0^* = 1 \cdot 10^{-11}$ and $m^* = 0.05$, which is indicated in Fig. 3.

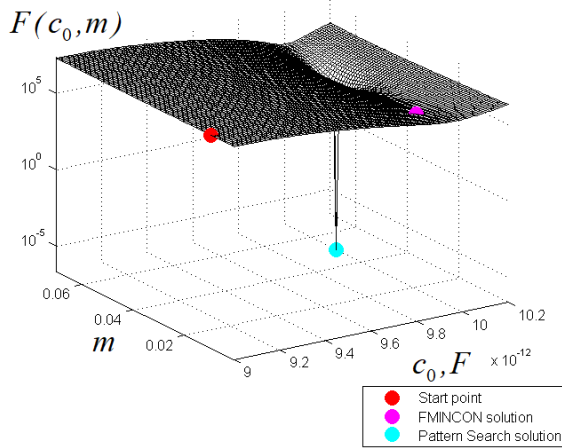


Fig.3. Objective function $F(c_0, m)$ in coordinates c_0 and m .

V. CONCLUSION

1. Symbolic transfer functions of LPTV circuits, formed by the system UDF MAOPCs, present a good basis for the formation of the objective functions and optimization of these circuits in the MATLAB software environment.

2. Parametric elements in LPTV circuits can be a source of energy, the presence of which under certain conditions can lead to a loss of the circuit stability. Therefore, the peculiarity of solving problems of the parametric circuits optimization is that, when finding the minimum, it is necessary to control their stability.

3. The Frequency Symbolic Method does not limit the number of circle parameters specified by the symbols. In addition, according to certain transfer functions, their derivatives can be formed according to the parameters of the circle, specified by symbols. Therefore, optimization functions of the MATLAB software environment of increased complexity can be chosen for optimization.

4. The LPTV circuits optimization procedure does not limit the choice of the number of varied parameters (parameters specified by symbols), as this is not limited by the Frequency Symbolic Method.

5. The objective functions $F(x_1, \dots, x_n, \omega, t)$, formed in the system UDF MAOPCs, are formed on the basis of conjugate parametric transfer functions $W(x_1, \dots, x_n, s, t)$ and are always represented by surfaces in the independent variables space, because they contain two (not one, as in the case of linear circuits with constant parameters) independent variables – complex variable s and time t .

6. As shown by computer experiments optimization functions implemented in the MATLAB software environment do not always find the optimal values of the objective function. Therefore, the resulting solutions should be checked for other start points or by other methods.

REFERENCES

- [1] Tholen, E.A. et al. Nonlinearities and parametric amplification in superconducting coplanar waveguide resonators. Appl. Phys. Lett.90, 253509(2007).
- [2] Yamamoto, T. et al. Flux-driven Josephson parametric amplifier. Appl. Phys. Lett.93, 042510 (2008).
- [3] Byeong Ho Eom, Peter K. Day, Henry G. LeDuc and Jonas Zmuidzinas. A wideband, low-noise superconducting amplifier with high dynamic range. Nature Physics, Vol.8, August 2012.
- [4] Anna Piwowar and Dariusz Grabowski, Modelling of the First-Order Time-Varying Filters with Periodically Variable Coefficients, Mathematical Problems in Engineering, vol. 2017, Article ID 9621651, 7 pages, 2017.
- [5] Byeong Ho Eom, Peter K. Day, Henry G. LeDuc and Jonas Zmuidzinas «A wideband, low-noise superconducting amplifier with high dynamic range», Nature Physics, vol.8, pp. 623-627, august 2012
- [6] Shapovalov Yu. Symbolic analysis of linear electrical circuits in the frequency domain. Fixed and variable parameters. Lviv, Lviv Polytechnic National University publication, 2014 – 324 p.
- [7] Shapovalov, Yu. Matrix Equation of L.A. Zadeh and its Application to the Analysis of the LPTV Circuits/ Shapovalov, Yu., Bachyk, D., Shapovalov, I.// Proceedings of 2018 19th International Conference Computational Problems of Electrical Engineering, CPEE 2018.
- [8] Yu. Shapovalov, B. Mandziy and D.Bachyk «Multivariate analysis and optimization of linear periodically time-variable circuits at the environment of MAOPCs», Bulletin of National Technical University of Ukraine. Series Radiotechnique. Radioapparatus building.- 2015 .-№ 60.-34-44, <http://radap.kpi.ua/radiotechnique/article/viewFile/940/988-radap.pdf>.
- [9] Yu. Shapovalov, B. Mandziy and D.Bachyk “The system functions MAOPCs for analysis and optimization of linear periodically time-variable circuits based on the frequency symbolic method”, Przegląd Elektrotechniczny, vol.91, no 7, pp. 39-42, 2015.
- [10] Holly Moore. “MATLAB for Engineers” 4th Edition, Pearson Education Limited, 2014, 672 p.
- [11] Alekseev O.V. Computer-aided design of radio electronic means: Proc. Manual for universities / Alekseev O.V., Golovko A.A., Pivovarov I. Yu. and others. Ed. O. V Alekseeva. M.: Higher. Sch., 2000. 473 p.
- [12] V.N Ilin and V.T. Frolkin, Avtomatizatsiya skhemo-tekhnicheskogo projektirovaniya. Moscow, Russia: Radio i sviaz, 1987. (Russian)
- [13] Investigation of stability reserve of linear periodically-Time-variable circuits by the frequency symbolic method/Shapovalov, Y., Mandziy, B., Bachyk, D. Proceedings - 2015 16th International Conference on Computational Problems of Electrical Engineering, CPEE 2015
- [14] Assessment of stability margin of linear parametric amplifiers by the frequency symbolic method Shapovalov, Y., Mandziy, B., Bachyk, D./Przegląd Elektrotechniczny, 2016, 92(7), pp. 108-111
- [15] https://www.mathworks.com/help/gads/patternsearch.html?s_tid=doc_ta
- [16] https://www.mathworks.com/help/optim/ug/fmincon.html?s_tid=doc_ta
- [17] https://www.mathworks.com/help/gads/noisy-objective-function.html?searchHighlight=optimization%20of%20stochastic&s_tid=srchtitle

Machine learning algorithms usage for satellites simulation and control

Yurii Bobalo
Lviv Polytechnic National University
Lviv, Ukraine
rector@lp.edu.ua

Nataliya Shakhovska
Department of Artificial Intelligence
Lviv Polytechnic National University
Lviv, Ukraine
[0000-0002-6875-8534]

Bohdan Mytnyk
Lviv Polytechnic National University
Lviv, Ukraine
bohdan.mytnyk.kn.2017@lpnu.ua

Abstract—This work provides an alternative way to control the satellite without using deterministic methods and it shows that simple algorithms show no worse results than more complex approaches in artificial intelligence (such as artificial neural networks, etc.). In this case simple algorithms are better because of their quick prediction, which is important when using these predictions on real artificial satellites. As the result of work, among the proposed simple control solutions, the random forest algorithm proved to be the best, as evidenced by accuracy metrics, as well as presented on the basis of graphs of increasing speed during the simulation

Keywords— satellite control, artificial intelligence, machine learning, PID

I. INTRODUCTION

An artificial satellite is an object placed in the orbit of the Earth or other celestial body by human effort. Sometimes called just a satellite. Satellites are divided into different types and typologies in terms of their appearance, characteristics, distance from the Earth, purpose. According to their purpose, satellites can be divided into: 1) navigation, 2) meteorological, 3) communication, 4) spy, 5) telescopes, 6) orbital stations, 7) combat satellites, etc.

Typically, the mechanical tools for the rotation of artificial satellites are wheels that rotate the satellite, using the law of momentum conservation. Also, one approach to control is nozzles that emit a directed flow of gas, thereby deploying the aircraft.

For a long time, role in the control of artificial satellites was performed by the PID (proportional-integral-derivative) algorithm [1], which is in a continuous cycle and maintains the required speed or torque. However, it was replaced by better solutions: the use of the algorithm SMC (sliding mode control), which is not in a constant cycle, but is adaptive and thus increases productivity and resistance to interference or the use of various machine learning algorithms (in particular, popular use in controllers partially or completely artificial neural networks).

The aim of the work is to develop simulation software for controlling artificial satellites of the Earth using various algorithms for their further comparison and use in the educational process.

II. RELATED WORKS

For a long time the most common approach for control systems (although it is gradually being replaced) was the PID algorithm. The purpose of this algorithm is to find such an output $U(t)$ for each input value $r(t)$ at a certain point in time, which, when used in the control system, minimizes the error value $e(t)$ between the required y and the current $y(t)$.

The algorithm works with three main components, each of which describes in its own way how the error $e(t)$ must be processed in the cycle of the algorithm:

1. The proportional component provides an initial value that will be proportional to the error value. That is why, a larger error is source for a larger output value required to correct a particular system; if the error is zero, the output is zero. The disadvantages of this component are that if the value of the coefficient is too large, the system may begin to fluctuate, and the fact that the proportional component can lead to a state of stable error.

2. Integral component serves as an auxiliary for proportional, but can also be used independently. This component helps to avoid a persistent error state by integrating the error over time.

3. Derivative component is ancillary to the PI - controller and cannot be used alone. It serves as a kind of "brake" for the controller, which responds to rapid changes in function and moves it in the opposite direction to avoid misses.

These components are reflected in the formula for finding the original $U(t)$:

$$U(t) = K_p * e(t) + K_i * \int e(t) dt + K_d * d/dt * e(t), \quad (1)$$

where K_p , K_i , K_d – the corresponding coefficients of each of the PID parts.

The error function is as follows:

$$e(t) = r(t) - y(t) \quad (2)$$

In the article [2] the problem of control of the satellite limited in communication with use of the SMC controller (Sliding Mode Controller) is considered. This controller is coordinate-independent and works only on the basis of discrete events that are embedded in the control strategy of the device (ie signals for control occur in response to certain events). The article also presents an argument against the classical PID, which is slower and inflexible to external interference, due to being in an infinite controlled cycle, rather than a reaction to individual inherent events. The result of the work was the proof that thanks to SMC the amount of communication with the aircraft can be reduced by 94.44% compared to the classic control options, which proves the quality of this method. The advantage of this work is the attention to the physical details of the simulation (taking into account errors, physical interference, etc.), in contrast to other works that also paid attention to the study of SMC.

The article [3] proposes the use of an adaptive controller based on observations to stabilize spacecraft. This approach is the ability of the controller's strategy to change from external circumstances, while remembering the latest best actions in

similar or similar situations. Further control is to combine the new strategy of the observer with the best pre-selected action. The numerical drawings and the analysis of Lyapunov stability show the reliability of the approach and resistance to interference. The advantage of the work is the large number of simulation illustrations, but the disadvantage is the lack of comparison of this control strategy with the existing accepted options, which does not allow to sufficiently analyze the improvement with the proposed method.

The article [4] considers the disadvantages of the classical approach to ensuring the stability of the FTC (finite-time controller), in particular its main disadvantages: low speed at a great distance from the equilibrium point, as well as the problem of initial input algorithm. The paper proposes to eliminate these shortcomings by using the modified Lyapunov barrier function, as well as the use of PFTC (preassigned finite-time controller) to calculate the initial input data. As a result, the authors show PFTC errors relative to FTC. Thus, the Euler angle error for the PFTC is 0.001 rad, while the FTC is 0.0015. The angular velocity error is 8×10^{-5} rad/s and 1.5×10^{-3} rad/s, respectively, which shows that this approach is more stable than the accepted options. The advantage of this work is a reasoned presentation of the problem of existing approaches, as well as proving the proposed method analytically and graphically.

Article [5], as well as Article [3], considers the use of a controller based on environmental observations, but using the OBFTTC (observer-based fault-tolerant tracking controller) method, which is a combination of FTTPC (finite-time prescribed) performance controller, which is responsible for general control, and LESO (linear extended state observer), which is responsible for state analysis and control of observations. The author argues that this approach is better than existing classical options, as well as those built on neural networks, arguing that the adaptability of the system, rather than training on a limited set of data. The result is a convergence time of 21s less than when using the classic options, which shows the advantages of the proposed controller. The advantage of the work is the comparison with the existing options for solving the problem, in particular, the justification against neural networks is interesting.

Article [6] proposes a comparison of the previously mentioned SMC with LQR (Linear Quadratic Regulator) using PSO (Particle Swarm Optimization). The work simulates the operation of both controllers in low orbit, taking into account the movement in three directions. The work shows that LQR shows worse results, because this controller could not even track the target given to it, while SMC did it in less than 30 seconds. The advantage of this work is the comparison of two different versions of controllers, which shows their relevance, feasibility and benefits, as well as a very large number of illustrations and calculations to prove and display the results.

The paper [7] considers the use of neural networks in spacecraft. This paper presents the classic controls (Guidance, Navigation and Control (GNC)), as well as their disadvantages: the high impact of errors and imperfect accuracy in the process of position adjustment. At the same time, photoactive laser sensors are mentioned as good candidates for precise control, but their main drawback - the price - is also taken into account. Therefore, the authors propose the use of neural networks in combination with accelerometers and semi-active lasers to determine the vector

of gravity and subsequent position determination, gyroscopes are discarded unnecessarily. As a result, 6 strategies for controlling aircraft using neural networks were obtained. The advantage of this work is the possibility of significant savings with the use of artificial intelligence, but the disadvantage is the lack of analysis compared to classical methods, which does not provide sufficient grounds for assessing the benefits of the method.

The publication [8] explains the application of generative models of deep learning for the recognition of anomalies in spacecraft control systems. Thus, two architectures of generative models are used using Bayesian optimization and Gaussian process to adjust hyper-parameters. Training evaluation is performed by recognizing images not shown during the training. The results show that performance depends on the operational characteristics of each of the modes used, as well as on the version of the architecture. The accuracy of the model with the first architecture is 0.996, the other - 0.984. Such a high accuracy of the proposed model is a very good result, but the paper does not indicate an alternative to similar work (for example, a comparison of energy consumption, price, speed, etc.). However, the advantage of this work is the uniqueness of the study.

In the article [9] a mathematical review of the control of spacecraft in general. The emphasis is on the possible difference between such control in our galaxy compared to distant worlds that may be discovered during the study. That is why the authors conclude that mathematical and engineering research in this area should be continuous in order to be able to ensure further control of satellites. The paper presents a controller based on the product of quaternions, Euler's angular algorithm and Kalman filtering. The advantage of this work is the proposed new method of satellite control, but the disadvantage is only its theoretical justification without simulation, this approach does not allow to assess the practicality of the controller relative to existing ones.

Article [10] considers the problem of satellite orientation during the deployment of flexible solar panels attached to the monolithic structure of the aircraft. To improve this process, the authors present a new way of satellite orientation, which is a combination of fuzzy logic techniques (where the values are not strictly 0 or 1, but are in the interval between them) with a classical PD (proportional-derivative) controller. The study shows that the classical PD-only approach takes an average of 30 seconds to deploy and orient the satellite, while a system combined with fuzzy logic takes an average of 20 seconds, proving its benefits. This work is interesting for its novelty and the presented version of the controller, special attention should be paid to simulation calculations, as well as comparing the results with the old approach.

The work [11] investigates the stabilization maneuvers of a satellite filled with liquid (fuel). To solve this problem, VSC (variable structure control) with already known adaptive control techniques is proposed. The tangential hyperbolic function is used in the algorithm for signal smoothness and resistance to interference. The stability of the system is again proved by Lyapunov analysis, but the disadvantage of this work is that it focuses only on this method, without comparison with alternative existing ones..

III. MATERIALS AND METHODS

In general, the task of rotating the satellite is to find at a certain point in time such power that when given to the engine

of the jet wheel, will cause such torque that will lead the satellite to the required speed.

Since the principle of fuzzy logic is used in this process (the value is continuous, not discrete), when using machine learning, only regression analysis algorithms are suitable.

This paper proposes the use of several regression algorithms, the task of which is, based on the difference between the current and the required speed, to provide the necessary power to gradually reduce the error between the results. The task is to reduce the training time of the model, as well as the time to obtain the result in order to apply the model in near real time

To train the models you need data showing the required power at a certain speed difference. A data set for such needs can be created using an inverse simulation, which consists of the following steps:

1. Generation of a random value of power U ;
2. Execution of the instructed simulation for a sufficiently short period of time using the constant U found during step 1;
3. Record this result in inverted form (as the power that must be applied to level the difference in speed).

After that, the models trained on this data set will be able to determine the required power, having a difference in speed, which will essentially control the simulated satellite.

To perform this task requires the use of regression analysis methods.

Regression analysis is a set of statistical methods used to estimate the relationship between a dependent variable and one or more independent variables. It can be used to analyze the strength of the relationship between variables, as well as to model the future relationship between them. Regression analysis includes variations such as linear, multilinear and nonlinear. The most common are linear and multiline models. Nonlinear regression is often used for more complex data sets in which the dependent and independent variables show a nonlinear dependence.

To learn regression models, data sets representing a set of features (or independent variables) and a corresponding value of a continuous value (dependent variable) are required. Figure 1 [12] shows an example of a data set that, depending on the year, shows the average height of snow cover (in inches).

To perform the task of predicting the power of the wheel to provide torque, such a set will be formed by means of reverse simulation. These data show the relationship between the speed differences (current and required) dw , as well as the power value u required to level this difference.

Such a data set must be created for each satellite separately, as the power to reach a certain speed will vary depending on the size of the satellite, the size of its jet wheel, as well as the maximum torque and speed of this wheel. By default, the set size is 10,000 items, but this value can be changed to suit your needs.

Year	Amount (inches)
2000	40
2001	39
2002	41
2003	29
2004	32
2005	30
2006	33
2007	15
2008	10
2009	11
2010	20
2011	24
2012	10
2013	15

Fig. 1. Initial dataset

In the process of operation, the regression algorithm for each unit of time receives the difference between the required and current speeds in rad / s, and then makes the necessary predictions for further control.

In general, the program receives the desired input speed in rad / s, which is then compared with the speed relevant in the progress of simulation.

In the simulation process, for each unit of time, the regression model predicts the required power u based on the difference between the actual and required speeds. In the future, this initial value is given to the jet engine, which forces the satellite to rotate around one of the axes.

In general, the program, based on the specified required speed, returns the following data:

1. Model metric MSE,
2. Model metric R^2 ,
3. Schedule of the simulation in each unit of time;

Among the machine learning algorithms, the following models were chosen to evaluate and compare their work on the task [13, 14]:

- decision tree regressor,
- random forest regressor,
- gradient boosting,
- linear regression.

A high-level Python programming language was chosen for the task, which is well suited for machine learning tasks for the following main reasons: good library ecosystem, low entry barrier and simplicity, flexibility, platform independence, readability, good visualization tools, community support, growing popularity. The development is performed in the PyCharm development environment, which provides a large number of convenient tools for writing code, its revisions, version control, etc.

The operation of the program requires compliance with the following minimum requirements for technical support: CPU - Intel Core i5-7xxx / Intel Core i7-7xxx, RAM - 8 GB, Storage - 4GB.

The following technical support is recommended for adequate operation of the program: CPU - Intel Core i5-9xxx / Intel Core i7-9xxx, RAM - 16 GB, Storage - 7 GB.

Training of models in the foundation of controllers takes place only after they have been selected, which avoids excessive use of resources.

Table 1 shows the hyperparameters of the models in which they are modified and applied.

TABLE 1. MODELS' HYPERPARAMETERS

No	Model	Hyperparameters
1	Gradient Boosting	learning_rate=0.1, n_estimators=100, subsample=1.0, min_samples_split=2, min_samples_leaf=1, max_depth=3
2	Decision Tree	min_samples_split=2, min_samples_leaf=1
3	Random Forest	n_estimators=100, criterion='mse', max_depth=None, min_samples_split=2, min_samples_leaf=1

After the training, the program shows the accuracy of the model using two metrics: MSE and R². Table 2 shows the results of algorithms in one of the runs of the program.

TABLE 2. MODELS' RESULTS

No	Model	MSE	R ²	Training time, s
1	Linear Regression	0.0078	0.975254	0.0004
2	Gradient Boosting	1.5229 * e-5	0.999957	0.0006
3	Decision Tree	4.4124 * e-6	0.999986	0.0004
4	Random Forest	3.2356 * e-6	0.999989	0.0005

For comparison, the learning time of a neurocontroller built on a persoptron with one hidden layer and 15 neurons in it is 17.0675 seconds, and R² is the same as for the random forest and is 0.999989.

As the result of work, among the proposed simple control solutions, the random forest algorithm proved to be the best, as evidenced by accuracy metrics, as well as presented on the basis of graphs of increasing speed during the simulation

After initializing the components, the program starts a sequential simulation using the selected controllers, as well as using the default PID controller. The use of PID is useful for comparing the deterministic approach with the artificial intelligence approach.

All algorithms have a certain jump when reaching the required speed, which is stabilized over time. A similar behavior is observed in [14], where, however, more complex neural networks are used. The advantage of the algorithms shown in the work, in comparison with neural networks, is their higher speed of prediction, which is important for use on real aircraft.

Of the algorithms developed in this paper, the fastest speed jump is localized in the random forest algorithm. Table 1 also shows that the random forest has the smallest MSE error and also shows the best R² result.

According to the obtained indicators, we can conclude that the algorithm of the random forest is best suited for this task.

CONCLUSIONS

In this paper, the possibility of controlling the Earth 's satellite based on simple machine learning algorithms was presented and implemented, which was shown with the help of a physical simulation.

All the proposed algorithms, compared to the PID algorithm, have some error when changing the speed, which is clearly seen in the graphs (the speed value is slightly higher than necessary, but over time localized), but this work is an alternative way to control the satellite without using deterministic methods. shows that simple algorithms show no worse results than more complex approaches to artificial intelligence (such as artificial neural networks, etc.).

Among the proposed simple control solutions, the random forest algorithm proved to be the best, as evidenced by accuracy metrics, as well as presented on the basis of graphs of speed increase during the simulation.

REFERENCES

- [1] "Reaction/Momentum Wheel | NASA Spinoff." <https://spinoff.nasa.gov/spinoff1997/t3.html> (accessed Apr. 21, 2021).
- [2] L. Xing, J. Zhang, C. Liu, and X. Zhang, "Fuzzy-logic-based adaptive event-triggered sliding mode control for spacecraft attitude tracking," *Aerosp. Sci. Technol.*, vol. 108, 2021, doi: 10.1016/j.ast.2020.106394.
- [3] X. Zhu, J. Chen, and Z. H. Zhu, "Adaptive learning observer for spacecraft attitude control with actuator fault," *Aerosp. Sci. Technol.*, vol. 108, 2021, doi: 10.1016/j.ast.2020.106389.
- [4] Y.-Y. Wu, Y. Zhang, and A.-G. Wu, "Preassigned finite-time attitude control for spacecraft based on time-varying barrier Lyapunov functions," *Aerosp. Sci. Technol.*, vol. 108, 2021, doi: 10.1016/j.ast.2020.106331.
- [5] X. Wu, S. Luo, C. Wei, and Y. Liao, "Observer-based fault-tolerant attitude tracking control for rigid spacecraft with actuator saturation and faults," *Acta Astronaut.*, vol. 178, pp. 824–834, 2021, doi: 10.1016/j.actaastro.2020.10.017.
- [6] M. Fakoor, S. Nikpay, and A. Kalhor, "On the ability of sliding mode and LQR controllers optimized with PSO in attitude control of a flexible 4-DOF satellite with time-varying payload," *Adv. Space Res.*, vol. 67, no. 1, pp. 334–349, 2021, doi: 10.1016/j.asr.2020.07.010.
- [7] R. de Celis, P. Solano, and L. Cadarso, "Applying neural networks in aerial vehicle guidance to simplify navigation systems," *Algorithms*, vol. 13, no. 12, 2020, doi: 10.3390/a13120333.
- [8] H. Ahn, D. Jung, and H.-L. Choi, "Deep generative models-based anomaly detection for spacecraft control systems," *Sens. Switz.*, vol. 20, no. 7, 2020, doi: 10.3390/s20071991.
- [9] S. K. Chaturvedi, S. Banerjee, S. Basu, M. Yadav, and S. Adhikary, "Mathematical review of the attitude control mechanism for a spacecraft," *INCAS Bull.*, vol. 12, no. 3, pp. 33–48, 2020, doi: 10.13111/2066-8201.2020.12.3.3.
- [10] W. Zhang, W. Zhu, S. Zhang, and X. Zhao, "Adaptive Fuzzy Control for Attitude Stabilization of Spacecraft with Deployable Composite Laminated Solar Array," *Complexity*, vol. 2020, 2020, doi: 10.1155/2020/3098684.
- [11] H. Wang, S. Lu, and X. Song, "Adaptive Neural Network Variable Structure Control for Liquid-Filled Spacecraft under Unknown Input Saturation," *Int. J. Aerosp. Eng.*, vol. 2020, 2020, doi: 10.1155/2020/6515626.
- [12] "Regression Analysis: Step by Step Articles, Videos, Simple Definitions." *Statistics How To*. <https://www.statisticshowto.com/probability-and-statistics/regression-analysis/> (accessed May 06, 2021).
- [13] F. Arzberger, "Deep Learning Attitude Control And Simulator For Satellites," p. 46.
- [14] K. Vala, "Tree-Based Methods: Regression Trees," *Medium*, Mar. 18, 2019. <https://towardsdatascience.com/tree-based-methods-regression-trees-4ee5d8db9fe9> (accessed May 07, 2021).

U-Net training models for efficient brain tumour segmentation on multi-modality CT and PET images

Estera Kot
Faculty of Electrical Engineering
Warsaw University of Technology
Warsaw, Poland
kote@ee.pw.edu.pl

Zuzanna Krawczyk
Faculty of Electrical Engineering
Warsaw University of Technology
Warsaw, Poland
zuzanna.krawczyk@ee.pw.edu.pl

Krzysztof Siwek
Faculty of Electrical Engineering
Warsaw University of Technology
Warsaw, Poland
krzysztof.siwek@pw.edu.pl

Kacper Pleska
Medicine Department
Medical University of Lodz
Lodz, Poland
kacper.pleska@stud.umed.lodz.pl

Jakub Rogalski
Faculty of Medicine
Medical University of Lodz
Lodz, Poland
jakub.rogalski1@stud.umed.lodz.pl

Piotr Czwarnowski
Nuclear Medicine Department
Medical University of Warsaw
Warsaw, Poland
pczwarnowski@wum.edu.pl

Abstract—Medicine, and particularly radiology, is an area where vision systems bring significant benefits, which results in more accurate diagnoses, predictions, and treatment plans. This paper proposes a U-Net training model and simplifies the deep learning based framework for tumour detection and semantic segmentation that shapes frames for computer-aided diagnoses (CADx) and computer-aided detection (CADE) applications. The U-Net was used to segment glioma – tumour area. A training technique is proposed and convolutional neural network models capable of being trained on a dataset of fused full-size CT and PET scans – $512 \times 512 \times 1$ – is addressed. The implemented algorithms were executed in a cloud environment, where storage was decoupled from compute (CPU and GPU). The resultant models' performance was assessed utilizing multiple metrics. Trained models fully automatically detect tumours in a given dataset. The best scored coefficient (Dice Co-Eff) for a model is 0.8750. The paper which follows is a detailed reference with training parameters for U-Net for efficient brain tumour detection on CT and PET scans where the dataset is limited — in this case, consisting of merely 20 patients.

Index Terms—U-Net, deep learning, cross-validation, brain tumours segmentation, computer vision

I. INTRODUCTION

Medicine is one of the industries and applied sciences where vision systems bring consequential benefits to end-users. The nervous system regulates the functions of the human body therefore damage in or to this area has the potential to disrupt the entire body's functioning [1]. As cancer of the nervous system is acknowledged as one of the most common types of cancers in the world, creating methods for computer-aided diagnosis (CADx) and computer-aided detection (CADE) processes are in high demand and have the potential to significantly impact both healthcare systems approaches and patient care

considerations. This paper proposes improvements in a universal deep learning based framework for brain tumours detection and semantic segmentation introduced in previous work [2]. As opposed to feeding the U-Net with cropped images $64 \times 64 \times 1$ of a given tumour, proposed training techniques including a network model capable of learning from a dataset with original sized images ($512 \times 512 \times 1$) to efficiently segment glioma are applied.

The U-Net is broadly applied for brain tumours segmentation on MRI [3], [4]. Naser et al. [5] used PET/CT for automatic segmentation of head and neck cancer based on the U-Net, but with resizing images to 144×144 pixels. Currently, there is no U-Net training on upfront fused full-sized dual modalities: CT and PET, the gap addressed within this paper.

II. PROCESSING METHODS AND EXPERIMENTS

A. Data preprocessing

Dataset consisted of 20 patients. For each, there were 148 fused CT/PET slices. Fused files are $512 \times 512 \times 1$ images, delivered and acquired by the Nuclear Medicine Department Medical University of Warsaw. The fusion was accomplished as a result of [2] using VGG19.

In order to create an environment for parallel cloud-based experiments, storage and compute were decoupled. Dataset was transferred to Azure Data Lake Storage. For the given dataset, each tumour was labeled with a polygon drawn around its shape in Azure Machine Learning Data Labeling by a subject-matter expert. Next, images labels were exported to COCO format. Following that was a script that extracted masks from polygons, as the U-Net requires a single binary mask per slice.

B. The U-Net architecture

The U-Net is a convolutional neural network created for biomedical image segmentation in the Computer Science Department at the University of Freiburg in 2015 [6]. Fig. 1 presents implemented net architecture and its main components.

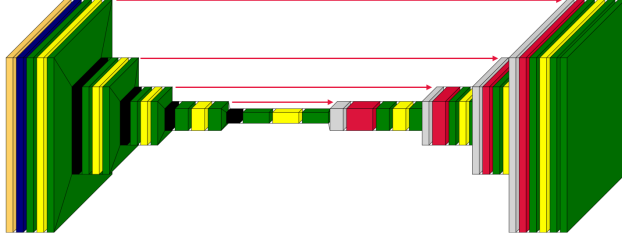


Fig. 1. Creation and implementation of U-Net architecture. Legend: starting from the left: light orange – Input Layer (instantiate a Keras tensor), navy – Lambda (applies a transformation to the input), green – Conv2D (applies 2D convolution to the input), yellow – Dropout (applies dropout to the input), black – MaxPooling2D (downsamples the input by taking the maximum value over an input window), grey – Conv2DTranspose (deconvolution), red – Concatenate (concatenates a list of inputs).

For inputs normalization purposes Lambda Layer was used. The Adam [7] optimization algorithm was used to train the algorithm with a learning rate of 0.001 and epsilon of $1e-07$. As a loss function, to compute the quantity that a model should seek to minimize during training, Binary Crossentropy was used. The model has 1 940 817 parameters. During a training, accuracy was monitored as the main metric, with an early stopping strategy applied — if in the final two epochs the accuracy does not improve – the training should be stopped to prevent overfitting. Model architecture implemented in Tensorflow2-Keras is shared [8].

C. Training on the original dataset

The training was executed with a batch size equal to 32, 50 epochs and 5-Fold cross-validation (80% training and 20% validation) with a shuffle. K-fold splits the slices in a dataset in k-groups of samples. Models evaluation was done after each fold, with the following performance metrics: selected loss function, Accuracy, Mean Squared Error (MSE), Area under the ROC Curve (ROC-AUC) and mean of Intersection over Union (IOU). Due to the ambiguous implementation of Mean IOU in Tensorflow 2.4 (that was not ignoring the background as Jaccard index defines) the Sørensen–Dice coefficient (Dice Co-Eff) was implemented and models evaluated on each slice from test dataset. For training 472 slices were used, for testing 117.

1) *Single Tumour Extracted*: The first experiment objective was to train the U-Net on the original dataset of Single Tumour Extracted. The machine used for training was - CPU - Compute optimized - 72 cores, 144 GB RAM.

Fig. 2 presents obtained visual results of the trained model run. Table I presents performance metrics.

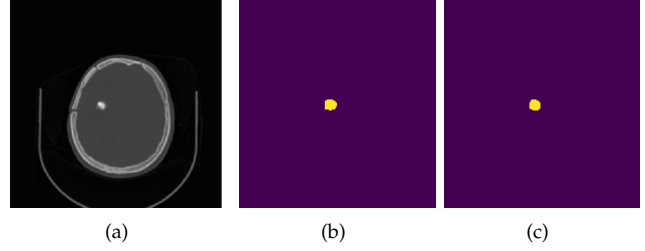


Fig. 2. (a) Fused CT/PET (b) Ground truth (c) Predicted mask

For cases where the tumour was not a solid mass, authors observed the model learned to detect correct tumour shape, however the mask used for training presents only the most giant tumour - single. Fragmented and scattered small tumours are not represented on the mask as is shown in fig. 3 which may lower the performance metrics results, causing the metrics to perform a comparison with a ground truth mask used for training.

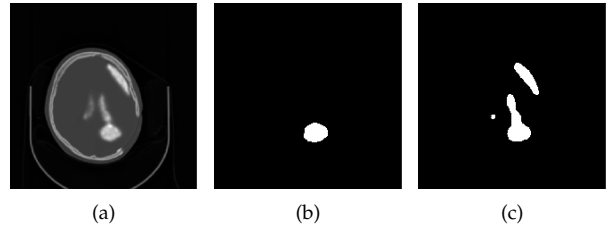


Fig. 3. (a) Fused CT/PET (b) Ground truth (c) Predicted mask

2) *Multiple Tumours Extracted*: Automated masks extraction algorithm was improved to include all marked and labelled tumours by SME, including scattered small tumours. The second experiment repeated training for the same U-Net model parameters using an updated dataset. The machine used for that experiment was CPU - Memory optimized - 20 cores, 140 GB RAM. Table I presents performance metrics.

D. Training on the augmented dataset

Augmentation is a universal method to increase a dataset size. The purpose was to initially train models without data augmentation to obtain the best possible metrics without artificially generated images.

1) *Augmentation with AugLy*: AugLy [9] is a novel open-source data augmentation library which was developed by researchers and engineers from Facebook AI Lab and newly published in mid-2021. Compared with the most commonly used Keras Image Generator, AugLy can: blur, randomly change the brightness, contrast, and saturation of an image, apply a perspective transform

so results appear similar to pictures taken from another device, saturate, and sharpen. As tumour detection is strongly based on pixel and voxel intensities, as a reflection of Hounsfield units, dataset was augmented based on transferring perspective, blurring, horizontal and vertical flipping, and rotation. The method designed for augmenting the dataset has been published and was shared [8].

The dataset was augmented twice, with different parameters. Each augmentation doubled the dataset size. As a final result dataset contains 2356 fused CT/PET and 2356 corresponding masks.

K-fold number - 5 - was kept and the training was run on 1885 pairs of images and corresponding masks were used for training with 471 for testing. Loading 2356 pairs from a decouple storage into a compute memory took 8m 58s.

2) *Single Tumour Extracted Augmented*: The third experiment objective was to train the U-Net on an augmented dataset of Single Tumour Extracted. The compute setup was transferred to a machine of 6 cores, 112 GB RAM - with a NVIDIA Tesla V100 GPU card. Due to a lack of sufficient memory, batch size was changed to 8.

3) *Multiple Tumours Extracted Augmented*: The fourth experiment objective was to train the U-Net on an augmented dataset of Multiple Tumours Extracted. The computing machine used for this experiment was the same as for the third experiment. Due to insufficient memory, the batch size was changed to 2. Fig. 4 (c) shows predicted mask for multiple tumours.

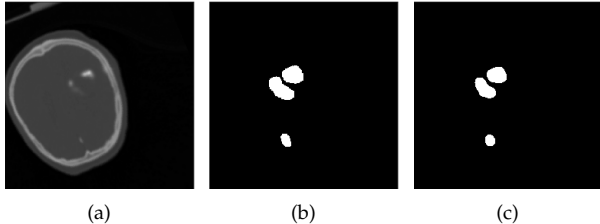


Fig. 4. (a) Fused CT/PET (b) Ground truth (c) Predicted mask for a single slice of fused CT/PET where Dice Co-Eff equals to 0.8945.

III. RESULTS AND DISCUSSION

Training for single tumour extracted and multiple tumour extracted was run on CPU machines. As the dataset contained 472 training samples, GPU was unnecessary. Comparable machines were used with one memory optimized and one compute optimized. There were few significant performance differences - for running experiments the significant differences were between CPU and GPU and capacity of the machines, not it's optimization by name. The training on the original dataset on CPU took approximately two hours. The training on the augmented dataset on CPU, without changed batch

size, took nearly 56 hours. By comparison, on GPU the average training per single fold took 00:06:50.

Tab. I shows that training with a smaller batch size generated higher accuracy and lower loss and MSE, which confirms the thesis from [10], that with a larger batch, there is a significant degradation in the quality of the model reflected as lower accuracy.

TABLE I
PERFORMANCE METRICS MEANS FOR THE U-NET. THE BEST RESULT PER METRICS IN BOLD AND BLUE.

Metrics (mean \pm std)	Experiment			
	ST ^a	ST Aug ^b	MT ^c	MT Aug ^d
Loss	0.0275 \pm 0.0127	0.0174 \pm 0.0027	0.0088 \pm 0.0008	0.0084 \pm 0.0002
Accuracy	99.53% \pm 0.03%	99.40% \pm 0.07%	99.66% \pm 0.03%	99.68% \pm 0.01%
MSE	0.0064 \pm 0.003	0.0041 \pm 0.0004	0.0025 \pm 0.0002	0.0023 \pm 0.0001
ROC-AUC	0.9921 \pm 0.0009	0.9961 \pm 0.0015	0.9928 \pm 0.0023	0.9944 \pm 0.0009
Mean IOU	49.76% \pm 0.02%	49.68% \pm 0.04%	49.48% \pm 0.02%	49.24% \pm 0.02%

a - ST - Single Tumour Extracted, b - ST Aug - Single Tumour Extracted Augmented
c - MT - Multiple Tumours Extracted, d - MT Aug - Multiple Tumour Extracted Augmented

For the augmented datasets, ROC-AUC and MSE increased, MSE and loss are lower compared to original dataset results. The differences are minuscule, especially when considering the time needed to train a model on 3x larger dataset. Fig. 5 shows the longest training required 33 epochs to be taught. For the U-Net 10 to 15 epochs may be enough to obtain an efficient algorithm.

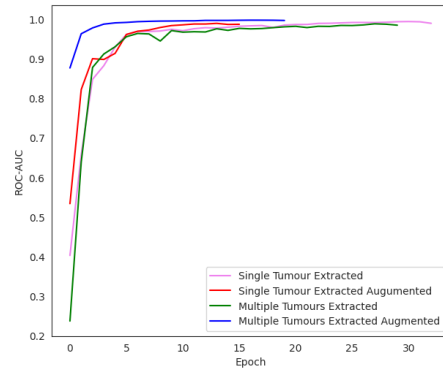


Fig. 5. Area under the ROC Curve (ROC-AUC) value per epochs for experiments.

Results were evaluated from the 5th fold models with a test dataset. The U-Net algorithms return the probability of the pixel being classified as a tumour - setting up a threshold is required. For all tests images, with nine chosen thresholds level, Dice Co-Eff was calculated. Tab. II presents results.

The higher the threshold was, the higher the maximal Dice Co-Eff were. For the final system, a higher value of mean Co-Eff is more important than high results obtained on a single slice. Augmenting the dataset significantly increased mean value of Dice Co-Eff. Consequently, for a multiple tumour extracted, both Dice Co-Eff mean and max values, for all thresholds, are significantly higher.

TABLE II
DICE CO-EFF RESULTS. PER EXPERIMENT THE HIGHEST MEAN VALUE IN BOLD AND BLUE, THE HIGHEST MAX VALUE IN BOLD AND TEAL.

Threshold	Dice Co-Eff	Experiment			
		ST ^a	ST Aug ^b	MT ^c	MT Aug ^d
0.36	max	0.9630	0.9651	0.9051	0.9706
	mean	0.6931	0.7617	0.6079	0.8750
0.38	max	0.9637	0.9600	0.9095	0.9700
	mean	0.6939	0.7620	0.6191	0.8750
0.4	max	0.9582	0.9551	0.9210	0.9696
	mean	0.6939	0.7609	0.6304	0.8746
0.41	max	0.9629	0.9545	0.9239	0.9689
	mean	0.6923	0.7609	0.6356	0.8743
0.42	max	0.9656	0.9541	0.9281	0.9691
	mean	0.6909	0.7608	0.6407	0.8740
0.43	max	0.9624	0.9537	0.9325	0.9690
	mean	0.6890	0.7603	0.6457	0.8736
0.44	max	0.9657	0.9521	0.935	0.9709
	mean	0.6857	0.7597	0.6509	0.8732
0.46	max	0.9571	0.9539	0.9395	0.9719
	mean	0.6748	0.7584	0.6605	0.8721
0.48	max	0.9388	0.9550	0.9459	0.9713
	mean	0.6507	0.7566	0.6699	0.8707

Fig. 6 shows that for the dataset augmented by a novel library – AugLy – the higher metric (Dice Co-Eff) is – overlapping between Ground Truth and Predicted Mask is higher. With augmented dataset results are better, however simultaneously, the number of false-negative cases, when the network indicated pixels as a background and by the radiologist as a tumour, is higher, and before deploying the model into an operational state, that value should be minimized.

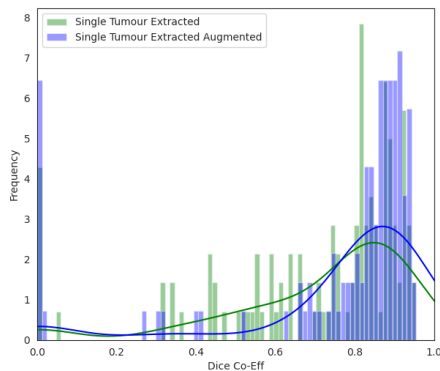


Fig. 6. Distribution of Dice Co-Eff for two experiments: Single Tumour Extracted and Single Tumour Extracted Augmented.

IV. CONCLUSIONS AND FUTURE WORK

In this paper, the methods that utilize the U-Net model for brain tumours segmentation on fused CT and PET scans is presented. The U-Net models were trained *ab initio*. The result algorithms do an automatic semantic segmentation of tumour area. Augmentation strategy was

described and shared as well with the U-Net model implementation. Visual results were included. Performance metrics confirmed efficiency of trained models. Dataset can be enriched with artificially generated images via GAN [11], considering it's potential limitation - inability to generate images with high quality. To simplify the deep learning-based framework for tumour detection and semantic segmentation, the U-Net neural network architecture could be adjusted to be feed with two inputs – separate CT and PET scans, instead of fusion that require additional preprocessing. The created U-Net model architecture can be applied for other computer vision tasks in medicine such as segmenting tumours or organs on MRI or CT, but additionally for segmenting any other object over RGB images.

ACKNOWLEDGMENT

This research is part of the “Design and development of algorithms for automatic identification, volume measurement and visualization of brain tumours and prostate cancer using deep learning methods” project and is supported by Warsaw University of Technology by the grant 504/04560/1042/43.040001 from 8 of July 2020.

REFERENCES

- [1] H. Salehiniya and K. Kalan Farmanfarma, “Brain cancer in the world: An epidemiological review,” *World Cancer Research Journal*, 03 2020.
- [2] E. Kot, Z. Krawczyk, K. Siwek, L. Królicki, and P. Czarnowski, “Deep learning-based framework for tumour detection and semantic segmentation,” *Bulletin of the Polish Academy of Sciences: Technical Sciences*, vol. 69, no. 3, p. e136750, 2021.
- [3] J. Dutta, D. Chakraborty, and D. Mondal, “Multimodal segmentation of brain tumours in volumetric mri scans of the brain using time-distributed u-net,” in *Computational Intelligence in Pattern Recognition*, A. K. Das, J. Nayak, B. Naik, S. K. Pati, and D. Pelusi, Eds. Singapore: Springer Singapore, 2020, pp. 715–725.
- [4] T. Yang and J. Song, “An automatic brain tumor image segmentation method based on the u-net,” in *2018 IEEE 4th International Conference on Computer and Communications (ICCC)*, 2018.
- [5] M. A. Naser, L. V. van Dijk, R. He, K. A. Wahid, and C. D. Fuller, “Tumor segmentation in patients with head and neck cancers using deep learning based-on multi-modality pet/ct images,” in *Head and Neck Tumor Segmentation*, V. Andrearczyk, V. Oreiller, and A. Depeursinge, Eds. Springer International Publishing, 2021.
- [6] O. Ronneberger, P. Fischer, and T. Brox, “U-net: Convolutional networks for biomedical image segmentation,” *CoRR*, vol. abs/1505.04597, 2015. [Online]. Available: <http://arxiv.org/abs/1505.04597>
- [7] D. P. Kingma and J. Ba, “Adam: A method for stochastic optimization,” *arXiv preprint arXiv:1412.6980*, 2014.
- [8] E. Kot, “Computer vision for biomedical images processing,” Aug. 2020. [Online]. Available: <https://doi.org/10.5281/zenodo.5091735>
- [9] J. Bitton and Z. Papakipos, “Augly: A data augmentations library for audio, image, text, and video.” <https://github.com/facebookresearch/AugLy>, 2021.
- [10] N. S. Keskar, D. Mudigere, J. Nocedal, M. Smelyanskiy, and P. T. P. Tang, “On large-batch training for deep learning: Generalization gap and sharp minima,” *CoRR*, vol. abs/1609.04836, 2016. [Online]. Available: <http://arxiv.org/abs/1609.04836>
- [11] C. B. et al. Liang Chen, R. Guerrero, P. Bentley, R. N. Gunn, A. Hammers, D. A. Dickie, M. del C. Valdés Hernández, J. M. Wardlaw, and D. Rueckert, “GAN augmentation: Augmenting training data using generative adversarial networks,” *CoRR*, vol. abs/1810.10863, 2018. [Online]. Available: <http://arxiv.org/abs/1810.10863>

SESSION 3 - COMPUTER MODELING

Design of bioamplifier for educational purposes

Michal Labuda, Tadeas Bednar and Marek Jarkovsky

Department of Electromagnetic and Biomedical Engineering, University of Zilina,
Zilina, Slovakia

Email: michal.labuda@feit.uniza.sk

Abstract—This paper deals with the design and construction of a single-channel bioamplifier. The theoretical part of paper describes types of biological signals and principles of their measurement. In the practical part, it is designed the single-channel bioamplifier and firmware for the device. At the end of the paper, individual measurements of various biosignals performed on the designed device are described.

Keywords—bioamplifier, ECG(Electrocardiography), EOG(Electrooculography), EMG(Electromyography)

I. INTRODUCTION

The issue of sensing biological signals is currently widespread in the field of diagnostic methods in medicine and biomedical engineering. It consists in the measurement, processing, analysis and subsequent display of sensed biological signals. The data obtained are essential in correctly determining the patient's diagnosis. In general, a signal is defined as a carrier of information. In the field of medicine and biomedicine, the signal carries information about human health. A biosignal or biological signal is any signal we can record from a living organism [1]. Bioelectrical signals are potentials that arise from the electrochemical activity of nerve, muscle and glandular cells [2].

The implemented low cost bioamplifier for sensing ECG, EOG, EMG, EEG could be used by biomedical engineering teachers and students in the teaching process in laboratory and practical exercises.

II. ELECTRICAL BIOSIGNALS

A. Electrocardiography

The basic principle of the ECG is that stimulation of a muscle alters the electrical potential of the muscle fibres. Cardiac cells, unlike other cells, have a property known as automaticity, which is the capacity to spontaneously initiate impulses. These are then transmitted from cell to cell by gap junctions that connect cardiac cells to each other [3].

The electrical impulses spread through the muscle cells because of changes in ions between intracellular and extracellular fluid. This is referred to as action potential. The primary ions involved are potassium, sodium and calcium. The action potential is the potential for action created by the balance between electrical charges (positive and negative) of ions on either side of the cell membrane [3].

However, following depolarization, the cardiac cells return to their resting charge, known as repolarization [4].

These waves of depolarization and repolarization represent an electrical current and can be detected by placing electrodes on the surface of the body. After the current has spread from the heart through the body, the changes are picked up by the ECG machine. The ECG is therefore a graphic representation of the electrical activity in the heart. The current is transmitted across the ECG machine at the selected points of contact of the electrode with the body [4].

B. Electromyography

The basic functional unit of the neuromuscular system is the motor unit. It comprises a motor neuron, including its dendrites and axon, and the muscle fibers innervated by the axon. The motor neuron is in the ventral horn of the spinal cord of brain stem where it receives sensory and descending inputs from other parts of the nervous system. The axon of each motor neuron exits the spinal cord through the ventral root, or through a cranial nerve in the brain stem, and projects in a peripheral nerve to its target muscle and the muscle fibers it innervates. Because the generation of an action potential by a motor neuron typically results in the generation of action potentials in all of the muscle fibers belonging to the motor unit, EMG recordings of muscle fiber action potentials provide information about the activation of motor neuron in the spinal cord of brain stem [5].

C. Electrooculography

Electrooculography is a technique for measuring the resting potential of the retina. The resulting signal is called the electrooculogram. An electrooculography is a device that measures the voltage between two electrodes placed on the face of a subject so it can detect eye movement. Today the use of computers is extended to every field. Many sophisticated devices like touch screen, track ball, digitizers etc. made interaction with computer ease from novice to professional. Assistive robotics can improve the quality of life for disabled people [6].

III. CONSTRUCTION OF BIOAMPLIFIER

A. Analysis of measured biological signals and measurement conditions

When designing a bioamplifier, it is necessary in the first step to analyze the biological signals to be sensed. It is important to correctly determine the frequency bands and magnitude levels of biological signals generated by the body. Each biological signal is characterized by its own specific magnitude and specific frequency band. In some cases, these bands also overlap, which must also be considered. The fundamental frequency bands and magnitude levels of the biological signals are shown in Fig 1.

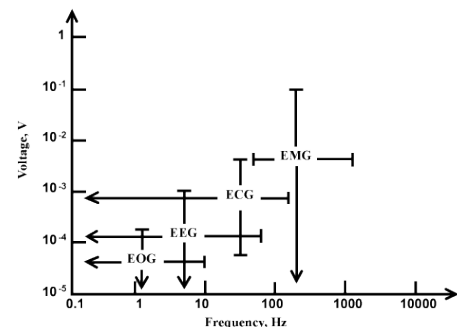


Fig. 1: Frequency bands & magnitude levels of biosignals [7]

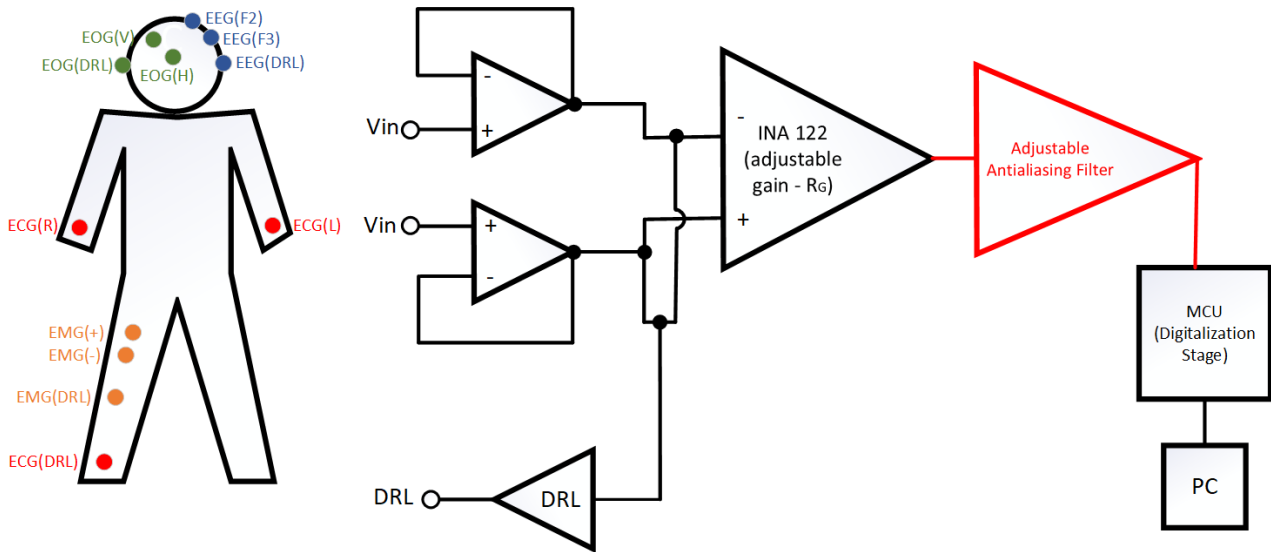


Fig. 2: Simplified schematic of bioamplifier

The second step in the design of a bioamplifier is the implementation of a system that can suppress unwanted artifacts in the measured signal and at the same time sufficiently amplify the useful part of the signal. This means that it is necessary to precisely define the frequency bands of biological signals at the hardware level using suitable filters and at the same time amplify the biological signals to the desired level, according to the magnitude of the biosignal. It is also necessary to design a circuit that can effectively suppress unwanted components of the sensed signal. Such circuits include a DRL circuit that actively suppresses compliant interference components.

When designing the circuit, we must not forget about the properties of the electrodes used, it is important to define which type of electrode is most suitable for sensing using the proposed system. Ag / AgCl electrodes are among the most used, most reliable and most cost-effective solutions.

B. Description of designed bioamplifier

The proposed bioamplifier, Fig. 2, serves as a single-lead system for measuring biological signals. When designing the system, I focused on the following biological signals and their frequency and magnitude properties: ECG, EEG, EMG, EOG. Measurement of biological signals is performed on the designed prototype using commercial Ag / AgCl electrodes. The measured signal from the electrodes passes at the input of the device through protective resistors, which protect the system from current spikes. Protective resistors are connected to the input of voltage followers, which serve as impedance separation. The signals from the voltage followers are fed to the inputs of the instrument amplifier INA122. The instrument amplifier allows adjustable gain depending on the resistance value of the resistor marked R_G . The instrument amplifier has a signal from the integrator fed to the reference input. The integrator together with the instrument amplifier serve as a high-pass filter to suppress artifacts caused by breathing. The output of the instrument amplifier is fed to an anti-aliasing filter, Fig 3.

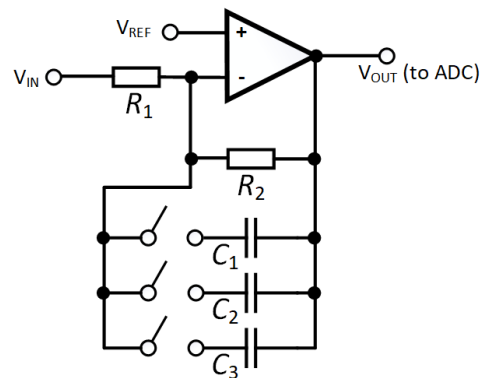


Fig. 3: Final (antialiasing & filtering) stage of bioamplifier

The filter is adjustable according to the requirements for sensing a specific biological signal. Switching between capacitors C_1 , C_2 , C_3 , it is possible to change the frequency band of the bioamplifier, TABLE I.

TABLE I. OUTPUT GAIN OF BIOAMPLIFIER

R_1 [k Ω]	R_2 [k Ω]	$C_{1,2,3}$ [nF]	f_m [Hz]	R_G [k Ω]	A_{out} [-]
10	100	33	48,23	39	101
10	100	10	158	39	101
10	100	3,3	482,3	12	217

Fig. 4 shows Amplitude-Frequency characteristics of final antialiasing & filtering stage of bioamplifier created in simulation software TinaTi (Texas Instruments). For EOG measurement there is a decrease of 3 dB at a frequency of 48 Hz. For ECG measurement there is a decrease of 3 dB at a

frequency of 158 Hz. For EMG is corner frequency of low pass filter $f_m = 482$ Hz.

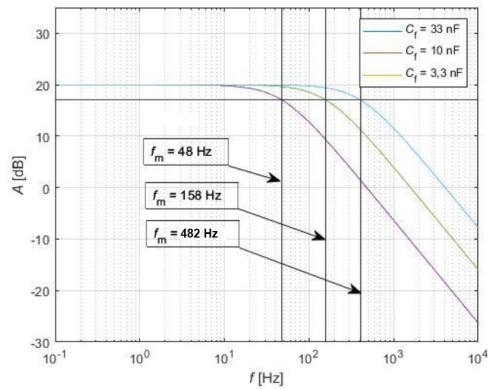


Fig. 4: Amplitude-Frequency characteristics of final stage circuit

The gain of the output stage is always the same as the value 10. The system is supplied with an asymmetrical voltage of 5V. Due to the asymmetry of the supply voltage, it is necessary to use the stroke of the measured biological signal by the DC level of the reference voltage to avoid trimming the negative parts of the sensed signal. In the case of the implemented bioamplifier, the value of the reference voltage was half the supply voltage.

An averaged signal from both inputs is also fed from the voltage followers at the input to the DRL circuit. The DRL circuit is used to suppress the positive interference component. The most significant part of the interference is network noise.

The proposed system was first tested in a non-soldering field and later the scheme was implemented in the Eagle software environment and a PCB was created. Fig. 5 shows the final version of the device. The bioamplifier is implemented as an Arduino Shield. Thus, attached to the Arduino UNO, which supplies the amplifier and performs digitization operations of the sensed biological signal and its subsequent sending to a computer. The signal is digitized using a 10-bit ADC that is part of the MCU labeled ATmega328P. The ADC reference voltage level is the same as the 5V supply voltage.

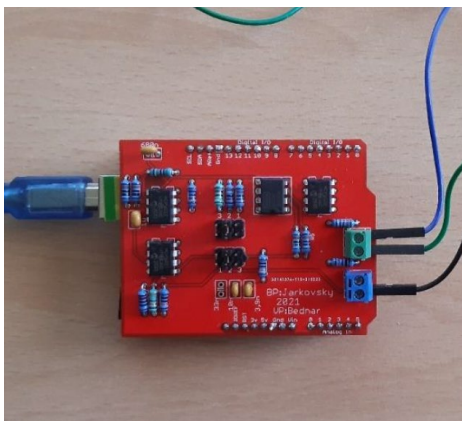


Fig. 5 Designed bioamplifier

IV. TESTING OF BIOAMPLIFIER

After the design of the bio-amplifier, it is necessary to verify whether the design principles of the bio-amplifier have

been followed. It is necessary to test whether the degree of amplification meets the requirements for a given biological signal. It is also necessary to test whether the frequency band of the given biological signal is observed, especially in the highest transmitted power.

The proposed system was tested on three biological signals. In the first test, the EOG signal was measured. The magnitude of the EOG signal ranges from 5 - 20 $\mu\text{V}/^\circ$ and the frequency band is approximately 0 - 45 Hz. The measured EOG signal using the proposed bioamplifier can be seen in Fig 6.

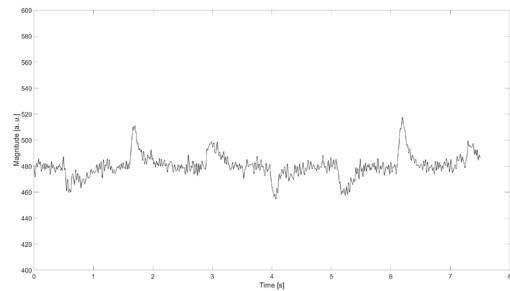


Fig. 6: Measured EOG signal

The second test was performed by measuring the EMG signal. The magnitude of the EMG signal is in the range of 10 μV - 10 mV and the frequency band is approximately 0 - 500 Hz, while the highest transmitted power of surface EMG is from 0 to 150 Hz. The measured surface EMG from the flexor carpi radialis muscle can be seen in Fig 7.

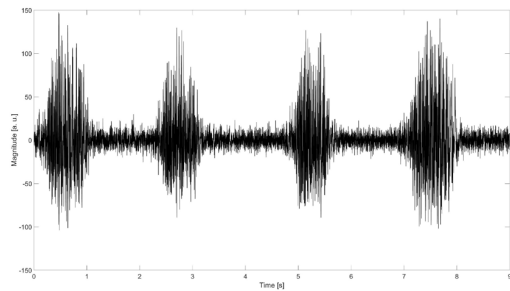


Fig. 7: Measured EOG signal

The third test was performed by measuring the ECG signal. The magnitude of the ECG signal is in the range of 0.5 - 4 mV and the frequency band with the highest transmitted power is 0.01 - 250Hz. The measured ECG (aVL) is shown in Fig 8.

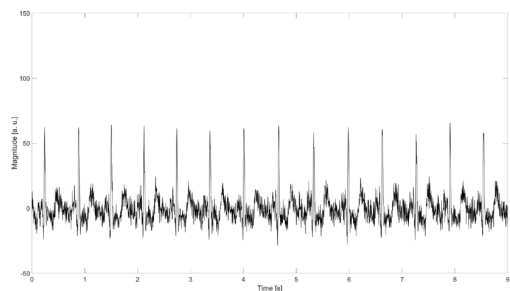


Fig. 8: Measured ECG signal

CONCLUSION

The proposed device can be used for presentation purposes for the Faculty of Electrical Engineering and Information Technology and the Department of Biomedical Engineering. The device can be used in teaching students of biomedical engineering on subjects focused on sensing biological signals and their processing or on subjects focused on the construction of medical devices. The device is a good prerequisite for a better understanding of the functioning of sensing and processing of biopotentials.

REFERENCES

- [1] J. Púčík and E. Cocherová, "ANALÝZA BIOSIGNÁLOV."
- [2] A. Čalkovská and others, "Fyziológia človeka: pre nelekárske študijné programy," *Martin: Osveta*, 2010.
- [3] J. H. Sherman, D. S. Luciano, and A. J. Vander, *Human physiology: the mechanisms of body function*. McGraw-Hill, 1985.
- [4] P. Woodrow, "An introduction to the reading of electrocardiograms," *Br. J. Nurs.*, vol. 7, no. 3, pp. 135–142, 1998.
- [5] R. Merletti and D. Farina, *Surface electromyography: physiology, engineering, and applications*. John Wiley & Sons, 2016.
- [6] U. Siddiqui and A. N. Shaikh, "An overview of 'electrooculography,'" *Int. J. Adv. Res. Comput. Commun. Eng.*, vol. 2, no. 11, pp. 4328–4330, 2013.
- [7] Y. Mahnashi and H. Alzahr, "Applying the Difference Term Approach for Low Frequency Biomedical Filter," *J. Biosens. Bioelectron.*, vol. 01, no. S11, 2012, doi: 10.4172/2155-6210.s11-004.

Numerical Integrators on Electrical Circuits' Transient Calculation

Volodymyr Moroz^{1,2}

¹⁾ Lviv Polytechnic National University,
Institute of Power Engineering and
Control Systems

Lviv, Ukraine

²⁾ Czestochowa University of Technology
Czestochowa, Poland

Volodymyr.I.Moroz@lpnu.ua

<https://orcid.org/0000-0001-7130-3525>

Anastasiia Vakarchuk

Lviv Polytechnic National University,
Institute of Power Engineering and
Control Systems

Lviv, Ukraine

anastasiia.b.vakarchuk@lpnu.ua

<https://orcid.org/0000-0002-6765-0118>

Abstract – In the research article the role of numerical methods in the calculation of transients in electrical circuits. Numerical methods are considered as digital filters that have behavioral features and have some influence. The pole/zero method is taken as a basis, which allows to obtain a graphical result and clearly demonstrates the conclusions obtained in the calculations.

Keywords – electrical circuit transient, Laplace transform, numerical integrators, pole/zero matching method.

I. INTRODUCTION

Calculations of transients in electrical circuits have come a long way: from symbolic methods using operator calculus (for example, the Heaviside method [1, 2]) and "manual" calculus using sheet of paper with manual calculation and mathematical tables up to the newest computer's methods of calculation using modern mathematical and CAD programs and appropriate computing tools [3, 4, 5]. The mathematical basis of modern modeling methods is often the use of the description of the electrical system by ordinary differential equations and their solution by numerical methods, in particular, using numerical integrators [6, 7].

At first glance, almost all the problems of using numerical methods to solve problems of technical systems' dynamics have already been solved, which is confirmed by the widespread implementation of algorithms for solving ordinary differential equations in known mathematical programs (for example, [7]). However, practitioners occasionally encounter various surprises during computer analysis of electrical (and not only electrical) systems in known mathematical applications. By the way, such problems are reported by the developers of mathematical programs (for example, [8]).

Thus, the question arises as to whether be there any other way to investigate the behavior of numerical methods that would allow us to analyze their impact on the calculation results.

II. THEORETICAL BASES

Somewhat unexpected for mathematicians, the method of analysis proposed by the developers of z-transformation in the theory of automatic control in the section on discrete systems [9]. To do this, numerical integrators are considered as digital filters and find the appropriate discrete transfer functions, for which then build frequency characteristics [9]. This method of frequency response is one of the basic in the theory of automatic control and allows you to assess the behavior of the studied automatic control system. Another method widely used in the theory of automatic control is the method of analysis of the distribution of zeros and poles of transfer functions on the complex plane, which also provides sufficient information about the behavior of the system. This article presents the results obtained by research using the method of zeros and poles of the obtained digital models based on known numerical integrators.

The method of obtaining discrete transfer functions, which, in fact, are studied, for numerical integrators is quite simple and is based on the method [4, 9, 10]. To do this, with the help of the selected numerical integrator discretize a continuous prototype and reduce it to a recurrent equation, which is then written as a discrete transfer function. An example is shown below.

Whole process to obtain the discrete transfer function for the numerical integrator and integration step size h shown by example used 3rd order implicit Adams formula [6] (also, known as Adams-Moulton formulas – denote as AM)

$$y_{i+1} = y_i + \frac{h}{12}(5x_{i+1} + 8x_i - x_{i-1})$$

based on method [9].

By the shifting theorem for z-transform [9] that affirm $y_i z = y_{i+1}$ and $y_i z^{-1} = y_{i-1}$ a discrete transfer function of this integrator has such form:

$$W_3^{AM}(z) = \frac{h}{12} \frac{(5z + 8z - z^{-1})}{z - 1} = \frac{h}{12} \frac{(5z^2 + 8z - 1)}{z^2 - z}.$$

Similarly, discrete transfer functions are found using this approach for other explicit and implicit numerical integrators of different order. For example,

- 2nd order implicit Adams integration formula (also, known as implicit trapezoid or Adams-Moulton formulas – denote as AM) has a digital transfer function

$$W_2^{AM}(z) = \frac{\frac{h}{2}(z+1)}{z-1};$$

- 4th order explicit Adams integration formula (also, known as Adams-Bashforth formula – denote as AB) has a digital transfer function

$$W_4^{AB}(z) = \frac{h}{24} \frac{(55z^3 - 59z^2 + 37z - 9)}{z^4 - z^3};$$

- 4th order implicit Adams integration formula (also, known as Adams-Moulton formula – denote as AM) has a digital transfer function

$$W_4^{AM}(z) = \frac{h}{24} \frac{(9z^3 + 19z^2 - 5z + 1)}{z^3 - z^2}.$$

These obtained discrete transfer functions of numerical integration methods are further used for research of digital models.

But let us return to continuous systems, in particular, second-order systems as simple but illustrative example. Using pole/zero matching method [4, 9-11] applied to the second order transfer function $\frac{1}{a_2s^2 + a_1s + a_0}$ (or

corresponded equivalent second-order electrical circuit; for example, it can be the RLC-circuit) we can see that this continuous system has a pair of poles: $\frac{a_1 \pm \sqrt{a_1^2 - 4a_0a_2}}{2a_2}$. There are real or complex conjugate

poles depending on coefficients' value. Thus, we note that the continuous second-order system has only two poles and they determine its appropriate behavior.

To obtain a digital model in a discrete transfer form a presentation of the structural model of such a second-order system in the observation canonical form was used [11]. The structural model of the second order system will have the presentation shown in Fig. 1. There are notations on this figure:

a_0, a_1, a_2 – polynomial coefficients of continuous second order transfer function;

$X(s)$ – input signal at Laplace domain;

$Y(s)$ – output signal at Laplace domain.

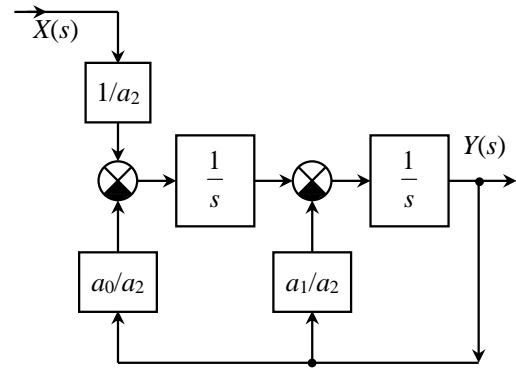


Fig. 1. Simulation diagram for second order transfer function using observer canonical form

In the next stage we replace continuous integrators (that has transfer function $1/s$) to digital transfer function of selected numerical integration method (see above). This will mean that there has been a conversion from continuous second-order transfer function to a discrete second-order transfer function using a digital integrators – there was a transition to z -domain.

Now let's check whether in the discrete model, which is described by the discrete transfer function, are there two poles left, as in the continuous prototype? To do this, we find the corresponding discrete transfer function for a second-order system with a transfer function

$$W_2(s) = \frac{1}{a_2s^2 + a_1s + a_0}$$
 using the observation canonical

form (Fig.1, [11]).

Replacing continuous integrators with the transfer function $1/s$ (see Fig. 1) by the digital integrators with discrete transfer function $W_i(z)$ and after elementary algebraic transformations we obtain:

$$W_2(z) = \frac{W_i^2(z)}{a_0W_i^2(z) + a_1W_i(z) + a_2}. \quad (1)$$

Note, that the poles of digital integrators are added to the discrete transfer function of the digital analog of the continuous system. Let's show this with a simple example using second order implicit numerical integrator with

discrete transfer function $W_2^{AM}(z) = \frac{\frac{h}{2}(z+1)}{z-1}$ (see above).

Replace $W_i(z)$ by $W_2^{AM}(z)$ in equation (1) we get discrete transfer function obtained by discretization process based on second order implicit numerical integrator:

$$W_2(z) = \frac{h^2 \cdot (z^2 + 2z + 1)}{d_2z^2 + d_1z + d_0},$$

where polynomial coefficients of discrete second order transfer function are:

$$d_0 = a_0 h^2 - 2a_1 h + 4a_2 ;$$

$$d_1 = 2a_0 h^2 - 8a_2 ;$$

$$d_2 = a_0 h^2 + 2a_1 h + 4a_2 .$$

In this situation surprise did not happen – digital system again has two discrete poles and new two discrete zeros, which, however, are not critical. Thus, we can expect minor changes in the behavior of the sampled system compared to the continuous prototype.

However, the situation becomes dramatic in occasion of high-order methods that shown in the next example – using fourth order explicit numerical integrator with discrete transfer function (see above):

$$W_4^{AB}(z) = \frac{h}{24} \frac{(55z^3 - 59z^2 + 37z - 9)}{z^4 - z^3} .$$

Replace $W_i(z)$ by $W_4^{AB}(z)$ in equation (1) we get discrete transfer function obtained by discretization process based on fourth order explicit numerical Adams integrator:

$$\frac{W_4(z)}{h^2} = \frac{81z^6 + 342z^5 + 271z^4 - 172z^3 + 63z^2 - 10z + 1}{d_6 z^6 + d_5 z^5 + d_4 z^4 + d_3 z^3 + d_2 z^2 + d_1 z + d_0} ,$$

where polynomial coefficients of discrete fourth order transfer function are:

$$d_0 = a_0 h^2 ;$$

$$d_1 = -10a_0 h^2 ;$$

$$d_2 = 63a_0 h^2 - 24a_1 h ;$$

$$d_3 = -172a_0 h^2 + 144a_1 h ;$$

$$d_4 = 271a_0 h^2 - 576a_1 h + 576a_2 ;$$

$$d_5 = 342a_0 h^2 + 240a_1 h - 1152a_2 ;$$

$$d_6 = 81a_0 h^2 + 216a_1 h + 576a_2 .$$

There are 6 independent of step size h discrete zeros and 6 discrete poles in obtained discrete transfer function. Note that the coefficients' value of the denominator's polynomial depends on the step size h , which, accordingly, causes the movement of discrete poles in the complex plane depending on the step h . And for the some step value, such poles go beyond the stability region of the discrete transfer function.

But here the most important thing – the behavior of a system with 6 zeros and 6 poles is different than the system's behavior with only two poles. Moreover, increasing the numerical integrator's order to sample the continuous system only degrades the situation due the increasing poles number.

III. EXPERIMENTAL RESULTS

Computer experiments were performed to the simple electrical circuit (it is shown in the Fig. 2 and used for investigation in paper [4] with other parameters) where

capacitor voltage $U_C(t)$ is unknown variable. Such a simple electrical circuit can be an integral part of various electrical systems. Transient process was found for voltage source E switching with zero initial. Such example is illustrative because computer calculation for this circuit can be verified by comparing with the Heaviside method (operator calculus, see [1, 2]).

Capacitor voltage $U_C(s)$ in this case using the Laplace transform in operator notation looks as:

$$U_C(s) = I(s) \cdot \frac{R_2 C_1 s}{R_2 + C_1 s} ,$$

where $I(s) = \frac{E/s}{Z(s)}$ and

$$Z(s) = R_1 + L_1 s + \frac{R_2 C_1 s}{R_2 + C_1 s} .$$

After simple algebraic conversions we have the capacitor voltage at the Laplace operator domain:

$$U_C(s) = \frac{R_2 \cdot E/s}{L_1 C_1 R_2 s^2 + (R_1 R_2 C_1 + L_1)s + R_1 + R_2} . \quad (2)$$

This equation used to obtain the time domain capacitor voltage $U_C(t)$ for verification of obtained simulation result based on the inverse Laplace transform (see [1, 2]). Again, note (pay attention to the denominator of the transfer function) that the system's behavior will be determined by a poles' pair (the part $1/s$ of the transfer function, which produce step response, is not taken into account).

The computer simulation results were compared with the symbolic solution using inverse Laplace transform obtained based on the equation (2) using symbolic computer algebra programs (such as Mathcad [12] or WolframAlpha [13] for example). MATLAB with Control Systems Toolbox [14] was used for computer simulation to confirm the assertions declarations that are put forward in the THEORETICAL BASES (part II).

Calculation results show in the Fig. 2 for the step response and poles/zeros map for the simulation step $h = 10^{-4}$ s. Note, how many zeros and poles appeared in the digital model created by fourth-order integrator instead of the two poles that continuous system has.

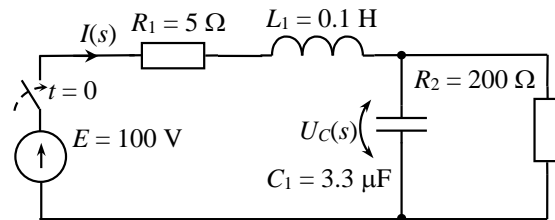


Fig. 2. Circuit under the test

V. REFERENCES

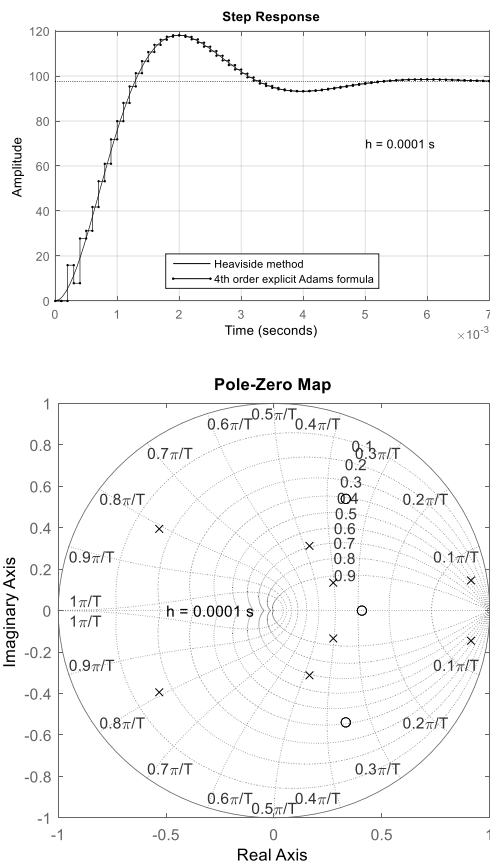


Fig. 2. Simulation results (step response and zeros/poles map) for simulation step $h = 0.0001$ s for discrete model of second order system

Due to the limited article's size, the simulation results for other step sizes and other numerical integrators are not shown. Studies have shown that increasing the numerical integrators' order adds additional zeros and poles to the discrete transfer function of the model, which certainly complicates the behavior of such a model compared to the original continuous system. In addition, with increasing numerical methods' order, the sensitivity of discrete transfer functions to the step size increases due to the wider range of zeros/poles mapping on the complex plane.

IV. CONCLUSION

Using high-order numerical integrators has some problems for transient analysis of electrical systems:

- new additional zeros and poles appeared in digital model and can dramatically change its behavior comparing to continuous prototype;
- Surprisingly, low-order numerical methods can provide higher authenticity of the studied system behavior's reproduction in a digital model.

- [1] Buschman, R. G. Integral Transformations, Operational Calculus, and Generalized Functions. – Springer, Boston, MA, 1996. – 240 p. – ISBN 978-1-4613-1283-3; <https://doi.org/10.1007/978-1-4613-1283-3>
- [2] Gustafson G. Heaviside's Method // Mathematics Department University of Utah, Salt Lake City. – [Access mode]: <http://www.math.utah.edu/~gustafso/HeavisideCoverup.pdf>
- [3] High Performance Computing in Power and Energy Systems / Siddhartha Kumar Khaitan and Anshul Gupta (Eds.) // Power Systems Series. – Springer-Verlag Berlin Heidelberg, 2013. – 384 p. [ISBN 978-3-642-32682-0].
- [4] V. Moroz, V. Konoval. High-Speed Power System Stability Analysis // Proceedings 16th International Conference on Computational Problems of Electrical Engineering (CPEE-2015). – L'viv, Ukraine. – September 2-5, 2015. – Pp. 129-131.
- [5] O. Lozynskyi, Ya. Paranchuk, V. Moroz, P. Stakhiv. Computer Model of the Electromechanical System of Moving Electrodes of an Arc Furnace with a Combined Control Law // IEEE 20th International Conference on Computational Problems of Electrical Engineering. September 15-18, 2019. L'viv, Ukraine.
- [6] E. Hairer, S. Nørsett, G. Wanner. Solving Ordinary Differential Equations I: Nonstiff Problems. Second Edition. Springer, 2008. [ISBN 978-3-540-56670-0].
- [7] Cleve Moler. Solving ODEs in MATLAB. Video and Webinar Series. © 1994-2021, The MathWorks, Inc. – [Access mode]: <https://www.mathworks.com/videos/series/solving-odes-in-matlab-117658.html>
- [8] L. Shampine, M. Reichelt. The MATLAB ODE Suite. – 1997. – [Access mode, checked 08.06.2021]: http://www.mathworks.com/access/helpdesk/help/pdf_doc/otherdocs/ode_suite.pdf.
- [9] L. Naredo et al., Z-Transform-Based Methods for Electromagnetic Transient Simulations // IEEE Transactions on Power Delivery, vol. 22, no. 3, pp. 1799-1805, July 2007, doi: 10.1109/TPWRD.2006.886793.
- [10] Smith J. M. Mathematical Modeling and Digital Simulation for Engineers and Scientists. – 2nd ed. – New York: Wiley, 1987. – 448 pp. – ISBN 0-471-08599-5.
- [11] Richard C. Dorf, Robert H. Bishop. Modern Control Systems. 12th Edition. – USA: Pearson, 2010. – [ISBN-13: 978-0136024583]. – 1104 p.
- [12] PTC Mathcad. – [Access mode] <https://www.mathcad.com/en/>
- [13] WolframAlpha. – [Access mode] <https://www.wolframalpha.com/>
- [14] Control System Toolbox: Design and analyze control systems. – [Access mode] <https://www.mathworks.com/products/control.html>

Optimization Material Characteristics for Electroheat Model Based on Calibration Material Properties

I. Petrášová¹, P. Karban¹, V. Kotlan¹, I. Doležel¹, Members, IEEE

¹University of West Bohemia, Czech Republic, {ipetraso, karban, vkotlan, idolezel}@kte.zcu.cz

Temperature-dependent material characteristics are generally burdened by many uncertainties that negatively affect the results obtained. To create the most accurate numerical model, it is necessary to determine these characteristics as accurately as possible. Data obtained from measurements during the laser welding process will be used for correct calibration.

Index Terms—optimization techniques, heat transfer, coupled problems, keyhole effect, numerical analysis

I. INTRODUCTION

One of the most important input factors influencing the accuracy of results in numerical models in technical areas is the reliability of input parameters, especially the characteristics of the material [1]. Other parameters such as the selected method, discretization, etc. can be relatively easily modified during the simulation process. In the case of uncertainties in material characteristics, it is not possible to unambiguously determine the accuracy of the resulting model, and the assumption of a correct simulation of reality and comparison with reality then makes no sense.

The article focuses on the possibilities of model calibration based on data obtained from experimental measurements. Although temperature characteristics are often known, they are only measured within a certain temperature range. For higher temperatures, the simulation already considers constant material parameters, which leads to many inaccuracies.

In the case of laser welding modeling, this is a relatively complicated issue that requires a lot of knowledge. The first problem in creating a model is the prescribed parameters of the weld, the quality of which is indicated by depth, width and microstructure. It is also necessary to determine the feed rate of the welded bodies and the power provided by the laser. Optimal setting of these quantities is a complicated inverse task. Optimization on such a complicated model would be very expensive, because it would be necessary to use a large number of variants. In the next step, it is necessary to find a sufficiently accurate simplified model (based either on the reduction of the model order or on the principle of surrogate model techniques), which will be processed several orders of magnitude faster. [2]

II. PROBLEM FORMULATION

Insufficiently accurate models can lead to mechanical defects (cracks) in welds and significantly reduce their service life [3]. The front welding model itself is very complicated because it must involve seemingly subtle but very important phenomena. The first is the keyhole effect [4], [5], which is accompanied by the flow of molten metal at the laser-irradiated site, and the second represents its partial evaporation, which

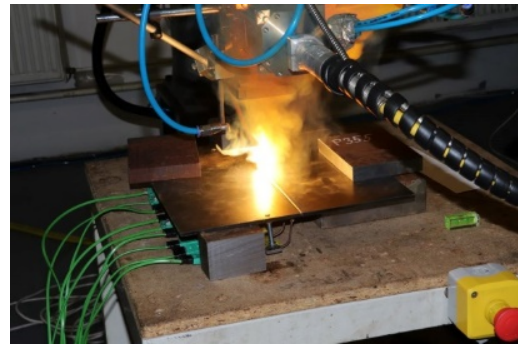


Fig. 1. Situation in transverse cut through weld

creates a plasma cloud over this site. Building these phenomena on a welding model leads to the need to calculate the flow field and significantly slow down the calculations. As for the plasma cloud, it reduces the power delivered by the laser beam to the weld and provides slower heating. Both of these effects affect the shape of the weld, especially its surface.

Consider welding of two iron plates, see in Fig. 1 and its basic arrangement is possible see in Fig. 2.

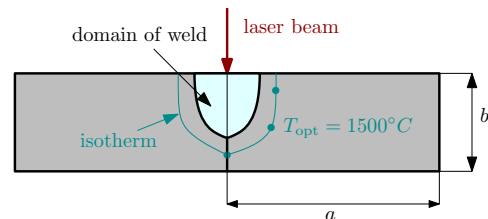


Fig. 2. Situation in transverse cut through weld

The full model of the process includes the interaction of the temperature field, field of flow, evaporation of metal and phase changes (first solid to liquid phase and then liquid to gaseous phase). But its 3D solution in the hard-coupled formulation would be extremely difficult and computationally unacceptably long. The model proposed by authors works an approximation of the physical reality that can be, however, used in industrial practice. It is verified and calibrated experimentally.

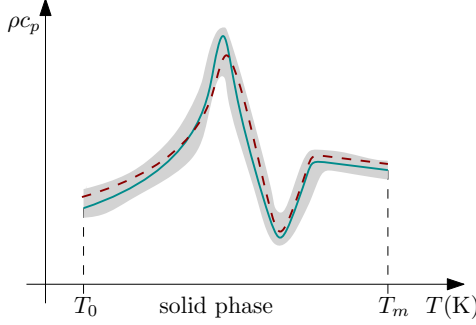


Fig. 3. Principal idea of improvement

Nevertheless, the first step to be done is to compare the thermally-affected zone of weld prepared of the real material and the same zone modeled using the same material whose characteristic ρc_p is provided by the manufacturer. The only condition is that the maximum temperatures of the measured sample and modeled case are the same.

The isotherm denoting the isotherm of melting point of the heated material) obtained using both approaches usually differ even when they should theoretically be the same. Provided that all the input data such as geometry and parameters of the laser and inductor are identical, the reason highly probably consists in the differences between the material characteristics. The principal idea follow from Fig. 3. Consider the temperature-dependent characteristic of (specific heat capacity) of a metal material. The characteristic delivered by the manufacturer is depicted by the dashed line. But when used in the model, we obtain incorrect result.

The method of solution is seemingly very easy. First, in the heat-affected zone (and even outside it) we chose n points whose temperatures are $T_{opt} = 1500^\circ C$ and T_{io} (obtained by modeling), and introduce the objective function in the form

$$OF = \sum_{i=1}^n |T_{opt} - T_{io}| \quad (1)$$

that has to be minimized.

Now, the dashed characteristic from Fig. 3 has to be optimized in order to obtain as much similar isotherms as possible. The algorithm consists of the following steps:

- 1) Selection of the tolerance band of the dotted characteristic represented by the grey zone in Fig. 2 (for example ± 8)
- 2) Replacement of the dashed characteristic by a polynomial (or rational) function with unknown coefficients.
- 3) Selection of a sufficient number of points (see Fig. 4) on the measured isotherms. Their real temperatures are and modelled temperatures after heating are .
- 4) Definition of the objective function to be minimized.
- 5) Launching of the optimization process that will find coefficients of the polynomials providing the minimum of function such that the modified characteristic lies in the selected tolerance zone.

Note that the solution is ambiguous. The shape of the optimized characteristic depends on the width of the tolerance

zone.

III. MATHEMATICAL MODEL

A. Temperature field produced by laser beam

The heat transfer equation is written in the form (no internal heat sources are present)

$$\text{div} (\lambda \text{grad } T) = \rho c_p \left(\frac{\partial T}{\partial t} + \mathbf{v} \cdot \text{grad } T \right) - w. \quad (2)$$

here, w represents the volumetric internal sources of heat in the processed material and t is time. The volumetric heat sources w are represented by the specific Joule losses w_J and specific hysteresis losses w_h . Thus,

$$w = w_J + w_h,$$

where

$$w_J = \frac{|\mathbf{J}_{ind}|^2}{2\gamma}, \quad \mathbf{J}_{ind} = \mathbf{j} \cdot \omega \gamma \mathbf{A}. \quad (3)$$

The losses w_h can often be neglected as their value is just a small fraction of the losses w_J . The boundary condition respecting both convection and radiation is expressed as

$$-\frac{\partial T}{\partial n} = -q_{in} + \alpha (T_s - T_0) + \sigma C (T_s^4 - T_r^4). \quad (4)$$

Here, T_s is the temperature of surface of the plate, α denotes the coefficient of the convective heat transfer, T_0 stands for the temperature of the surrounding medium (air), $\sigma = 5.67 \cdot 10^{-8} \text{ Wm}^{-2}\text{K}^{-4}$ is the Stefan-Boltzmann constant, C represents the emissivity of the heated part and T_r is the temperature of the surface to which heat is radiated and q_{in} corresponding to the delivered thermal flux.

B. Flow field

The field of flow is produced at the spot irradiated by the laser beam after reaching the melting temperature of the heated material. At this spot, all three phases, solid, liquid and gaseous are in a mutual interaction, which is called the keyhole effect. This phenomenon is well described in the references [6], [7] and others, but its modeling is time demanding. That is why authors offered another method for its mapping that is based on the dynamic deformation of geometry applied on the calibrated shape of the keyhole. The results do not reach the accuracy of the full model, but the computation time is by one-two orders shorter. More details can be found in [8].

IV. NUMERICAL SOLUTION

The methodology is illustrated with an example of induction-assisted laser welding of two parallel iron plates made of steel S355. Their dimensions are $b = 0.005 \text{ m}$, $l = 0.3 \text{ m}$ (l being the length) and $a = 0.15 \text{ m}$, their arrangement being shown in Fig. 2. Heating is realized by laser beam and postheating inductor. Their velocity $v = 5 \text{ mm s}^{-1}$.

The forward task providing the value of the objective function (1) is solved by the finite element method with quadratic elements. Computations are realized in COMSOL Multiphysics 5.6 supplemented by our own algorithms, using a cluster of seven high-efficient computers. Important

parameters such as stability and convergence of results were monitored; three valid digits were required for the results.

The some optimization algorithms built in COMSOL Multiphysics 5.6, particularly BOBYQA and Monte Carlo procedures, were tested.

The real characteristics of steel S355 (found in the database of materials in the corresponding module of COMSOL Multiphysics are depicted in Fig. 4.

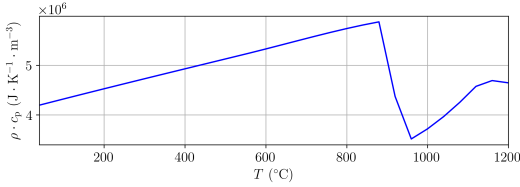


Fig. 4. Temperature dependence of specific heat capacity ρc_p of steel

Now, the model with these characteristics and without taking into account the keyhole effect provided the temperature profile of the weld. This profile naturally strongly differs from the measured profile (see Fig. 5).

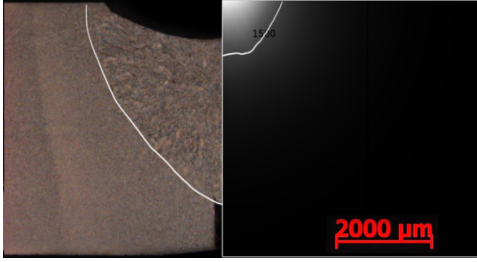


Fig. 5. Profiles of weld before optimization: left—measured, right—calculated (white line—isotherm 1500°C); left part depicts also the shape of weld surface after cooling, right part only shows temperature map of heat-affected zone after heating, the model did not take into account keyhole effect

Since the material is in the course of the welding process deformed and the material state changes, the estimation of the parameters of the material characteristics is a rather complex business as well as the creation of weld itself. In order to construct the target function as in equation (1), it is also necessary to solve the dynamic deformation of steel due to the above mentioned keyhole effect.

If the deformation of the geometry would not be taken into account, heat would propagate evenly through the material and the shape of the isotherm in the numerical model would not be able to simulate the physical reality.

During the solution heat capacity and also function that takes into account material deformation and represents the boundary condition for changing the computing network were optimized. The specific heat ρc_p was assumed as a function linear by parts according to the following Table I. Here, the symbols $x_1, x_2, x_3, y_1, y_2, y_3$ are the parameters to be optimized.

The mesh deformation function can be written in the form

$$f(x, T) = -Y \cos\left(\frac{x}{X\pi}\right)^2 \cdot F(T), \quad (5)$$

TABLE I
THE SPECIFIC HEAT CAPACITY ρc_p

$T(\text{K})$	273.15	x_1	x_2	x_3	1489
lower limit		1000	1100	1250	
upper limit		1200	1300	1450	
$\rho c_p(\text{J}/(\text{m}^3 \cdot \text{K}))$	$4.1 \cdot 10^6$	y_1	y_2	y_3	$4.1 \cdot 10^6$
lower limit			$2.5 \cdot 10^6$		
upper limit			$7.0 \cdot 10^6$		

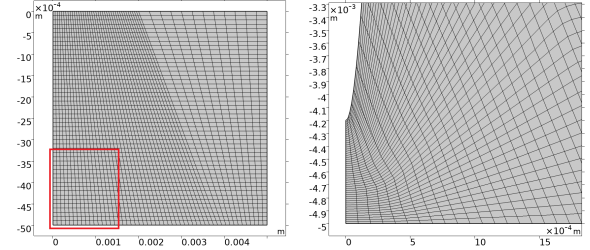


Fig. 6. The original mesh is depicted (left side) – red rectangle is area depicted in detail on right side, where final deformed mesh generated by procedure (5)

where $-Y$ and X are the parameters of the mesh deformation technique that are optimized to fit the shape of the keyhole effect and $F(T)$ is temperature dependent function respecting the phase change of the material.

The procedure based on the optimization of both parameters of the material characteristics and deformation in one step proved to be a very tough and numerically unstable business. Changing the parameters for deformation velocity of the discretization mesh and material characteristics resulted in a great instability of the model, which made it impossible to calculate it in any reasonable number of iterations.

Thus, the calculation was divided into two halves. In the first step we aimed at the material deformation. The material characteristics remained original (for steel S355) and only parameters for the material deformation function were optimized. The procedure of mesh deformation is shown in Fig. 6.

But even this calculation was unstable. It was necessary to test several variants of calculations in order to avoid numerical failures. Geometry shape optimization was performed in COMSOL using BOBYQA and Monte Carlo methods.

Only in the second step it was possible to optimize the aforementioned material characteristics. The calculation was again performed using the same algorithms.

V. RESULTS

A typical result is depicted in Fig. 7. The left subfigure shows the experimental result—cross section of the weld containing the melting point isotherm (1500°C). The right subfigure depicts the same cross section obtained by optimization of the model, where the black line shows the same isotherm. This isotherm is the main one for predicting the quality of the weld and bounds the area of solidification. Figure exhibit a good agreement. Beside the above comparison of the thermally-affected zone, also temperatures at selected points were measured for calibration of the numerical model. The optimization process (here realized using the BOBYQA algorithm) was finished after 510 steps.

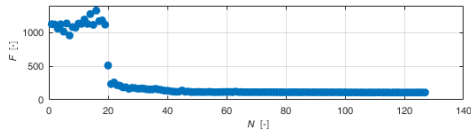


Fig. 7. Dependence of objective function on number of iterations

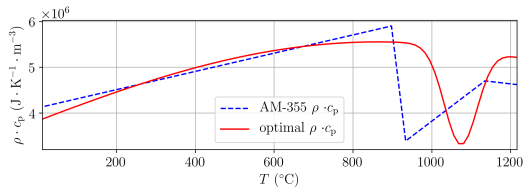


Fig. 8. Temperature dependence of specific heat capacity ρc_p of steel

Fig. 7 depicts the dependence of objective function on the number of iterations. It can be seen, that already after about 50 iterations the value of reached its minimum.

The Figure 8 contains the optimized material characteristic obtained by applying the selected algorithms. The uncertainty in knowing the exact values of the material properties is replaced by a defined uncertainty band that forms the space of the optimization parameter.

After optimization, we obtained the modelled profile as depicted in the right part of Fig. 9. Now the agreement is incomparably better.

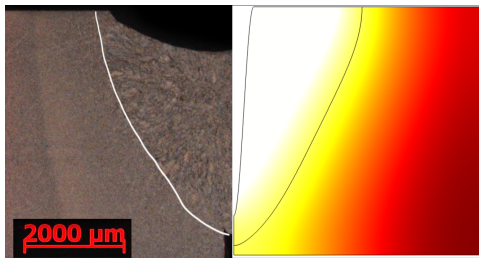


Fig. 9. Comparison of experiment and model: left part—cross section through real weld, white line showing the melting point isotherm, right part—model, black line showing the same isotherm

In the top left part of Fig. 9, a hollow is observable that is produced during the process of welding without additive material. It is a consequence of evaporation of a part of material and subsequent solidification of the molten phase. Taking into account this effect in the numerical model is extremely difficult because of mutual interaction of all three phases of metal (solid, liquid and gaseous) and field of flow in the process of evaporation characterized by stochastic aspects. The presented model tries to approach this reality on the condition of keeping the time of computations in reasonable limits, so that it could be used for on-line monitoring of the weld quality. That is why the complex process of melting and evaporation is replaced by the technique of deformation of geometry that in a similar manner as the real process makes it possible the penetration of the laser beam to the depth of material (capillarity effect). The volume between the axis and

black line in the top right part (showing the border of material at the moment of its irradiation by the laser beam) corresponds to the evaporated material and is equal to the volume of the mentioned hollow in the left part. After shifting the laser beam, the molten metal between the black and white lines would flow to this capillary. But this effect is not taken into account in the presented model.

VI. CONCLUSION

The paper presents a possibility of reconstructing the temperature-dependent material characteristics from the shape of the weld and distribution of isotherms in its cross section. The original idea was to replace the temperature-dependent characteristics by simple polynomial or rational functions, but this idea proved to be insufficient. Also other phenomena have to be taken into account, like mechanical deformation of the surface and keyhole. The optimization was, therefore, supplemented with other procedures that allow modelling deformation of the parametrized geometry and only in the second step, the material parameters are optimized. The methodology allows solving this task very efficiently (tens of seconds or minutes on a top-equipped PC).

ACKNOWLEDGMENT

This research has been supported by the internal project of UWB and University Students Project SGS-2021-011.

REFERENCES

- [1] P. Alotto, P. Molino and G. Molinari. "Optimisation of electromagnetic devices with uncertain parameters and tolerances in the design variables", *COMPEL—The International Journal for Computation and Mathematics in Electrical and Electronic Engineering*, vol. 20, no. 3, pp. 808–812, 2001.
- [2] I. Petrasova, V. Kotlan, L. Sroubova, P. Karban and I. Dolezel. "Optimization of selected electroheat models based on calibration of material properties", *IEEE Transactions on Magnetics*, vol. 56, pp. 1–4, 2019.
- [3] A. De and T. Debroy. "Reliable calculations of heat and fluid flow during conduction mode laser welding through optimization of uncertain parameters", *Supplement to the Welding Journal*, 2005.
- [4] W. Tan and Y. C. Shin. "Laser keyhole welding of stainless steel thin plate stack for applications in fuel cell manufacturing", *Science and Technology of Welding and Joining*, vol. 20, no. 4, pp. 313–318, 2015.
- [5] M. Vänskä, F. Abt, R. Weber, A. Salminen and T. Graf. "Effect of welding parameters onto keyhole geometry", *Physics Procedia*, vol. 41, pp. 199–208, 2013.
- [6] M. Courtois, M. Carin, P. le Masson, S. Gaied, and M. Balabane. "A complete model of keyhole and melt pool dynamics to analyze instabilities and collapse during laser welding", *Journal of Laser Applications*, vol. 26, no. 4, paper 042001, 2014.
- [7] A. Anca, A. Cardona, J. Risso, and V. D. Fachinotti. "Finite element modeling of welding process", *Applied Mathematical Modeling*, vol. 35, pp. 688–707, 2011.
- [8] V. Kotlan, D. Panek, R. Hamar, and I. Dolezel. "Shape optimization of deposited layer produced by combined cladding process", *IEEE Transactions on Magnetics*, vol. 54, no. 3, id. 2760906, 2018.

Face detection in a real-time videostream on Raspberry Pi

Jaroslav Podestát
Faculty of Electrical Engineering
University of West Bohemia
Pilsen, Czech Republic
podestat@fel.zcu.cz

Petr Kropík
Faculty of Electrical Engineering
University of West Bohemia
Pilsen, Czech Republic
pkropik@fel.zcu.cz

Jan Beneš
Faculty of Electrical Engineering
University of West Bohemia
Pilsen, Czech Republic
jbenes1@students.zcu.cz

Abstract—This paper is focused on the topic of the system of face detection in a real-time videostream on a low-power device. It describes the implementation and differences of two selected approaches, specifically the use of CNN or Haar classification. It explains the importance of the data preparation, especially the process of modifying the input images. Also, it deals with the problems and limitations arising mainly due to the choice of using a low-power Raspberry Pi device.

Keywords—convolutional neural network, face detection, artificial intelligence, haar features

I. INTRODUCTION

Our goal is to develop a face recognition system, so the first and important step is face detection. In addition to accurate evaluation, we decided to focus on fast detection and implementation on a low-power device. We are interested in low-power devices because they have a future, mainly due to easier installation and lower cost. However, we have to deal with hardware limitations. In recent years, new ways of detecting objects have appeared. In the area of face detection, convolutional neural network is a common solution, but there is often a need for a sufficiently powerful device. The Haar classifier method was also explored because it is not as demanding as the CNN. Careful data preparation and editing is emphasized, as this also has a significant impact, since the device then performs fewer operations during the data processing. It is good that it saves time for image detection, but it is absolutely essential for real-time video streaming. The face detection system to be covered was described in paper [1]. It is a neural network model programmed in Python and running on a Raspberry Pi 3 Model B minicomputer with a compatible camera.

II. FACE DETECTION WITH CNN

As explained in the book about Deep Learning [2], the Convolutional neural network (shortly CNN) is a type of neural network that extracts features from an image. It contains sequentially connected layers that apply modifications to the input data. Layers have parameters called weights. Finding the correct value of the weights is referred to as training. At the output, we determine whether the appropriate values were used by calculating a loss function that returns how much the prediction differs from the actual objective. This serves as feedback for us to adjust the weights, which is done by the optimizer as seen in Fig. 1. At the beginning, the weights are set to random values and after each iteration they change and the loss score is reduced. We consider the network trained when the score is sufficiently low. Among the types of optimizers, gradient descent should be mentioned. Gradient descent takes steps in the opposite direction of the gradient function. Because of that, it approaches a local minimum of the function which is equal to the minimum loss score. One of the most well-known variants of the optimizer is RMSprop which has an adaptive learning rate.

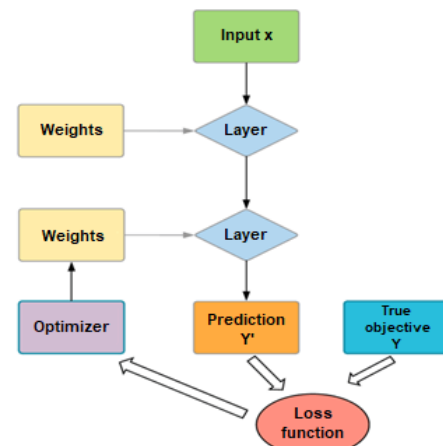


Fig. 1. Loss function as a feedback to change the weights [2]

Contour, edge extraction, sharpening and other adjustments needed for further processing are performed. This is done through the use of a kernel which can be compared to a filter. For an RGB color image, the dimensions of kernel would be 3×3 . If we convert the image to grayscale, we reduce the dimension and a kernel of 3×3 or 5×5 is sufficient. After convolution, the output matrix becomes smaller. If we want the output matrix to be the same size as the input matrix, we have to use padding. Before convolution, an appropriate number of rows and columns are added to the matrix. The convolution layer is followed by pooling, which is used to downsize the matrix, to achieve reduced computation time. Max-pooling 2×2 with step set to 2 is shown in Fig. 2. The step is set to change the position in the matrix. Max-pooling is a type of pooling that selects the maximum from the values passed through. In some cases, average-pooling is chosen instead of max-pooling. The only difference between them is that it returns the average instead of the maximum.

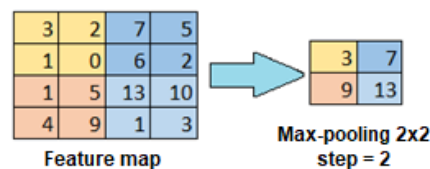


Fig. 2. Max-pooling used on a feature map

The chosen CNN model was Mask R-CNN which can be found on GitHub [3]. The website also includes list of libraries that need to be imported. Since you will be working with .xml files, you need to import the ElementTree module to read and parse these files. The numpy module is used to work with matrices. Matplotlib is the library that will be used for drawing, which will serve as a visual control. The library named mrcnn contains the Mask R-CNN functions and is

needed, for example, for loading datasets and modifying them. OpenCV (cv2) is a library for image modification.

Mask R-CNN is designed to learn to predict the BND box and mask of the intended object. The difference between the BND box and the mask is that the mask covers just the intended object, but the BND box is a rectangle that creates borders around the area containing the object. For the face dataset, annotations were created using the LabelImg program to select a region named BND box which defines the location of the face as seen in Fig. 3. It was also labelled with a label expressing what the selected object (class) is, in this case a face. It is important to note that the BND box should be as close as possible to the boundary where the object is. In our case, the masks were modified to fill the entire BND box. If we did not place the BND box at all and there were, for example, frequent images in the dataset where there is also a car, the model might start to consider it part of the class. Another option is to crop the image so that only the intended object is present. Annotation and creation of BND boxes has to be done manually so if you do not want to do it yourself you have to hire someone to do it. The dataset containing the faces was downloaded from Kaggle [4]. The dataset contains 70 thousand images of human faces of different ethnicity, gender, nationality, and age. The images have a size of 128x128 pixels.

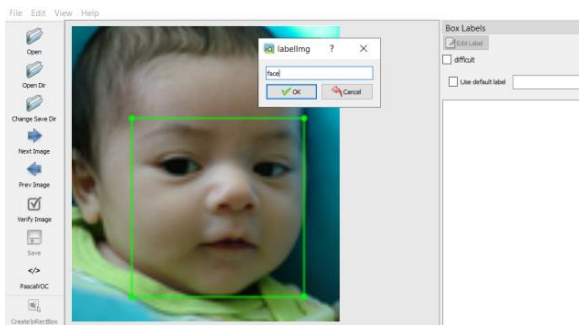


Fig. 3. Using the LabelImg program

The annotation information is stored in an .xml file for each individual image. For the purpose of determining the mAP, the dataset was split into 1600 training images and 401 test/validation images. For training, the size of the image and the coordinates of the BND box in the image needed to be stored in the worksheet. The mask is a matrix of zeros and ones. So, a matrix full of zeros was created from which the zeros in the BND box area were replaced by ones. Then the prepared data could be loaded and training could begin.

In addition to the prepared files, the number of epochs is set before training begins. The number of epochs corresponds to how many times the model passes through all of the images. Training was set to 50 epochs and after each epoch the model was saved as a .h5 file. Epoch 29 was chosen here because of a sufficiently low loss score of 0.1. The later epochs were not chosen because of overfitting, where the model would only recognize the training data well but the test data poorly.

When we train the model, we get numerical information about how accurate the detection is. This helps us to adjust the network parameters and learn if overfitting has occurred. Overfitting is often caused by a lack of samples in the dataset which can be solved by taking additional photographs. Another solution is augmentation, which is the modification

of existing photos, where one of the modifications like rotation, stretching or more such changes are applied. Simply obtaining a dataset is therefore usually not enough and it is necessary to use augmentation.

For augmentation, the selected modifications must make sense. It makes sense to use rotation or stretching of the image because when detecting, the person does not have to stand still, at a specific distance, directly in front of the camera. Zooming, shifting or rotating the image may be applicable in this case. However, a rotation of about 180 degrees is inappropriate, since we do not assume that the person would be upside down in front of the camera. It is advisable to check the output images after transformation to ensure that there are no faces in a form that the camera would not realistically detect.

The quality of model recognition is evaluated by mean average precision, shortly mAP. For this, we need to evaluate the intersection over union, shortly called IoU. IoU equals to how much of the same covered area is shared by the predicted and real BND boxes. If the predicted one was in exactly the same position as the real one, the IoU would be equal to 1. For us, IoU greater than 0.5 was considered as positive. Next, the average precision (AP) of all images, i.e., the percentage of positive IoUs, was calculated. From the AP, the mean average mAP was calculated. The training mAP was 0.998 which is 99.8 % and the test mAP was 0.953 which is 95.3 %. This means that the detection should be reliable.

The results could also be verified visually by first showing the actual real face region in one image and then marking the predicted region in another image. The visual check was actually useful because, thanks to this, a mistake was found in the creation of the BND boxes. More specifically, the mistake was that the BND boxes were created too large and contained the entire head. Detection worked fine, but it detected a whole head instead of just face, so it had to be fixed. In addition to reducing the selected area from head to just face, we reduce the amount of possible problems in recognition, so we do not have to deal with possible issues like different hairstyles or hats.

The OpenCV library was used to obtain real-time detected images from the camera video stream. It was set that it could read images from the stream at 2 FPS. While loops were used to store the camera image into a variable so the image size could be adjusted to speed up the computation. The final detection including the border at the detection location can be seen in Fig. 4. The figure still shows the model where the head was originally detected instead of the face.

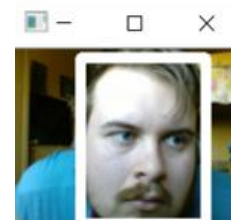


Fig. 4. CNN head detection in a real-time video stream

III. FACE DETECTION WITH HAAR CLASSIFIER

The Haar classifier is an OpenCV algorithm, and you are likely to notice some similarities with CNN in its approach. For CNN it was necessary to have only one dataset, but two different datasets are needed in this case. The positive dataset

must contain the intended object and the negative dataset can contain anything but the object. Another difference is that it works with the kernel equivalent that works with manually set features. The input image is sequentially scanned by a filter of specific size which checks if the image contains the searched features or not. In the case of a human face, some of these are the eyes, nose or mouth. It is important to convert the image to grayscale so every pixel has intensity between white and black, in numerical representation it is between 0 and 1. The difference between the ideal feature and the detected real feature can be seen in Fig. 5.

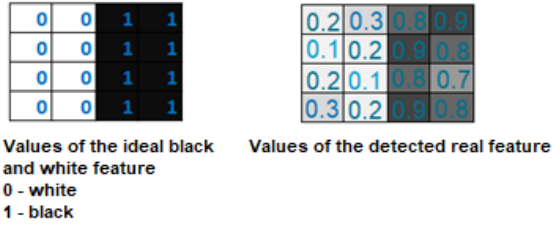


Fig. 5. The difference between the ideal feature and the real feature

As described here [6], the chance of detecting a Haar feature (Δ) can be described as (1). In an ideal case it would equal to 1 (2). In a real case the result should be close to 1 (3). The closer it is, the higher is the chance to detect the feature.

$$\Delta = \text{dark} - \text{white} = \frac{1}{n} \sum_{\text{dark}} I(x) - \frac{1}{n} \sum_{\text{white}} I(x) \quad (1)$$

$$\Delta = \text{dark} - \text{white} = 1 - 0 = 1 \quad (2)$$

$$\Delta = \frac{4 \cdot 0.8 + 3 \cdot 0.9 + 0.7}{8} - \frac{4 \cdot 0.2 + 2 \cdot 0.3 + 2 \cdot 0.1}{8} = 0.83 - 0.2 = 0.63 \quad (3)$$

However, too many calculations are needed this way because multiple different features are used for the same regions and it would take too much time for larger images. The solution is to convert the original image to an integral image so less calculations are needed. At first, there were approximately 180,000 haar features, but this large amount was undesirable. Some of these features may recognize characteristics that have little or no relevance to the intended object. Through the AdaBoost algorithm, those that were evaluated to be irrelevant were eliminated. Chosen simple needed features are labeled as weak learners and from them desirable strong learners are created. In the end, this leaves only 6000 most important features in the output. To further speed up the detection, the Attentional Cascade approach was used. In this approach, the simpler features are searched for in the given regions first. If they do not exist, then it moves on to the next region. If they are found, the region continues the process with more complex features.

For the purpose of implementation on the Raspberry Pi 3 Model B [7] with the Raspbian OS, Python was chosen as the programming language. The official Raspberry Pi Camera Module v2 [8] was chosen because it is capable of real-time recording and it is compatible with Raspberry Pi. As the positive dataset, the same dataset as for CNN was used [4] and the negative dataset was downloaded from the Kaggle website [5]. Next, it is converted to grayscale and afterwards it has to

be annotated and cropped. The cropping was done with the help of the CNN model which was created earlier. After the model detected the face in the picture we could overwrite the original image with the image which included only the cropped face. So, if you already have a working and reliable model, you can automatically crop the dataset images so you do not have to do it manually.

For the training the Haar classifier needs a text file with a .txt extension containing the BND box coordinates in the positive face dataset. Since the images have different sizes, they were scaled to the same size of 80x85 pixels so that the same coordinates could be used for all images. This file is then converted to a vector file with a .vec extension. A separate text file was also required for the negative dataset, but here we did not need to annotate or crop the dataset, so we just saved the file names in there. Also, it should be mentioned that this file is not converted into a .vec file.

Each epoch took approximately 10 minutes. As a result in the output it returns an .xml file containing the relevant features. With this file we can finally set up a video capturing and test the face detection in a real-time video stream. The Raspberry Pi could run a video stream at only 8 FPS which was insufficient. To fix this problem, a function was created to shrink the image by 25 % before detection and then enlarge it back with the detected face area, before sending it to the output. The image resizing is set to 25 % because this is an aspect ratio where the image compression is not yet irreversible. This process results in an increase to 30 FPS.

In Fig. 6, we can see the Haar classifier face detection which also correctly predicts only the face and not the whole head. To be clear, this correct face detection is due to proper annotation and BND boxes setting so it can also be achieved with CNN.

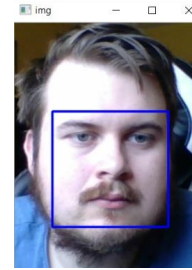


Fig. 6. Haar classifier face detection in a real-time videostream

IV. FUTURE DEVELOPMENT

When detection was successfully completed, development and future expansions were then researched. One of them is censoring and another is face recognition. The simple application of censoring was functional in the case of human faces. It is set to automatically trigger censoring when any face is detected. It is set to randomly swap the position of nearby pixels and the level of censoring can be changed with settings. Figure 7 shows 3 different settings for this censoring.



Fig. 7. Censoring the detected face with three different settings

If we consider other options, we do not necessarily have to stick with face detection, but we can detect different things instead. However, it heavily depends on whether a large enough dataset for the object can be collected. We are not planning anything specific in this area yet, but we do not rule out future use. Currently, we find face recognition to be more useful. An idea for the AI face recognition based on school attendance system was inspired by the problems encountered in the current pandemic conditions. The checking which people should be allowed to enter the school building has become important especially now because of the ongoing pandemic. Teachers and students are allowed to visit school only if they agreed to specific terms. At the entrance, the doorkeeper lets in only people who show a filled form with affidavit. In this form visitors have to state that it has been at least 22 days since they have been vaccinated or that they were reliably tested by an authorized person and the result of the test was negative. However, the doorkeeper can never be sure that the filled statement is actually true. Also, it is impossible for him to thoroughly check each visitor's statement especially when a lot of students arrive at the same moment.

An option could be to register incoming people with camera and use a face recognition to check data stored in school database to see if they have a permission to enter the building. There are cameras installed in the building, but the doorkeeper can see only what happens in real-time. Theoretically, the camera footage could be saved with a permission from the visitors. We should also assume that a host not affiliated with school could come. Let's define how system should behave after face recognition in different scenarios:

- The visitor exists in the school database and gave a permission so the system will record the visitor's presence.
- The visitor exists in the school database but did not give a permission so the system will not record the visitor's presence.
- The visitor does not exist in the school database and did not give a permission so the system will not record the visitor's presence.

It might be too ambitious to immediately start with a development and installation of this solution. It is safer to begin with a simpler system on a smaller scale so it will be easier to run tests and try to solve potential problems.

The current proposition is that it will be situated at the entry to the Department of Electrical and Computational Engineering. In total, there are 36 people who work there and even if we consider that some of them would not want to participate or would not be present there should still be a sufficient number of people. It would not use the mentioned forms needed to enter the school but only the rules defined above. This would result in an attendance system for checking the arrival and departure of employees.

V. CONCLUSION

The implementation of face detection on Raspberry Pi 3 Model B was accomplished. This was achieved in the case of both Haar classifier and CNN. The problem of unintentionally incorrectly set BND boxes in the program Labelling had to be fixed. Although the faster detection on a low-power device has been achieved by the Haar classifier, solutions with CNNs will continue to be tested. In particular, what is possible to achieve in the case of CNN implementation on devices specifically compatible with CNN will be explored. The implemented CNN model was not considered suitable for real-time video stream detection. It was able to be used as an image cropping tool, which can make dataset preparation easier.

So far, detection is successful with satisfactory results and the next step is to look for how to extend this under these conditions to face recognition. There were two ways to continue with the development and these were censoring and face recognition. Simple censorship experiments have been tested, but no further developments are planned yet. Development will continue in the area of face recognition because there are opportunities for useful application. The desired goal is to have a face recognition based attendance system on a small low-power platform. The detection is successful with satisfactory results and the next step is to extend the detection with mentioned requirements to face recognition.

ACKNOWLEDGMENT

This work has been supported from the grant project of the University of West Bohemia SGS-2021-011.

REFERENCES

- [1] J. Beneš, Real-time automatic video modification system based on AI, Pilsen: University of West Bohemia, 2021.
- [2] F. Chollet, Deep Learning with Python, Praha: Grada Publishing, 2019.
- [3] W. Abdulla, "Mask R-CNN for Object Detection and Segmentation," GitHub, 2017. [Online]. Available: https://github.com/matterport/Mask_RCNN. [Accessed 4 July 2021].
- [4] GreatGameDota, "Flicker-Faces-HQ High Quality Human Faces Data Set," GitHub, 2019. [Online]. Available: <https://www.kaggle.com/greatgamedota/ffhq-face-data-set>. [Accessed 5 July 2021].
- [5] M. Khalid, "Negative Images for Haar Cascade," GitHub, 2020. [Online]. Available: <https://www.kaggle.com/muhammadkhalid/negative-images>. [Accessed 4 July 2021].
- [6] D. Adakane, "What are Haar Features used in Face Detection?," Analytics Vidhya, 2019. [Online]. Available: <https://medium.com/analytics-vidhya/what-is-haar-features-used-in-face-detection-a7e531c8332b>. [Accessed 8 July 2021].
- [7] "Raspberry Pi 3 Model B," Raspberry Pi Foundation, 2016. [Online]. Available: <https://www.raspberrypi.org/products/raspberry-pi-3-model-b/>. [Accessed 8 July 2021].
- [8] "Camera Module V2," Raspberry Pi Foundation, 2016. [Online]. Available: <https://www.raspberrypi.org/products/camera-module-v2/>. [Accessed 8 July 2021].

Sweep frequency eddy current testing: numerical simulation of various probe types

Filip Vaverka
Department of Electromagnetic
and Biomedical Engineering
University of Zilina, Faculty of
Electrical Engineering and
Information Technology
Zilina, Slovak Republic
filip.vaverka@feit.uniza.sk

Milan Smetana
Department of Electromagnetic
and Biomedical Engineering
University of Zilina, Faculty of
Electrical Engineering and
Information Technology
Zilina, Slovak Republic
milan.smetana@feit.uniza.sk

Daniela Gombarska
Department of Electromagnetic
and Biomedical Engineering
University of Zilina, Faculty of
Electrical Engineering and
Information Technology
Zilina, Slovak Republic
daniela.gombarska@feit.uniza.sk

Ladislav Janousek
Department of Electromagnetic
and Biomedical Engineering
University of Zilina, Faculty of
Electrical Engineering and
Information Technology
Zilina, Slovak Republic
ladislav.janousek@feit.uniza.sk

Abstract— The article deals with electromagnetic nondestructive evaluation of conductive materials. The sweep-frequency eddy current method is used for this purpose. Numerical simulation based on FEM method, of three different types of probes and their ability to detect of defined inhomogeneities, is the main aim of this work.

Keywords—sweep frequency eddy current testing, material inhomogeneities, eddy-current probes, harmonic excitation

I. INTRODUCTION

The demand for perfect material is important in a variety of industries, whether in terms of safety, reliability, or, most notably, finance. For these reasons, it is necessary to test the material throughout the manufacturing process. The material is generally damaged and unusable during the inspection. The advantage of non-destructive testing is that the material can be utilized again after inspection. Therefore, non-destructive testing has gained popularity in recent years.

The focus of this research is on non-destructive examination techniques of conductive materials. Electromagnetic (EM) approaches are one of the methods used to explore such materials. The eddy current testing (ECT) method is one of the most widely used non-destructive electromagnetic methods.

II. EDDY CURRENT TESTING METHOD

A. The basics of the method

In eddy current testing, the flow and distribution of eddy currents in a material are used to acquire information about the tested material. Eddy currents are caused by the EM induction phenomenon. Induced eddy currents occur when a time-varying EM field is close to an electrically conductive material. According to Faraday's Law, these currents are created. The source of this time-varying EM field is a coil. The material's eddy currents generate their own secondary EM field, which, according to Lenz's law opposes the primary EM field. The primary field is disrupted, and this change is reflected in the coil's impedance and induced voltage. The presence of a flaw in the material disrupts the flow of eddy currents in the material, resulting in a change in the secondary EM field, which can be detected by changing the coil's impedance. The flow and distribution of eddy currents are disrupted when the material is inhomogeneous. The secondary field and coil impedance both change as a result of this disruption. The presence of a defect is demonstrated by the difference in impedances or measured voltages. [1],[2],[3],[7], [8].

To model the ECT, a quasi-stationary EM field approach can be used when the time variations in the EMF are relatively

slow, this technique often produces accurate results, allowing the displacement current to be ignored ($\mathbf{J} \gg \frac{\partial \mathbf{D}}{\partial t}$). Because the conductive current is substantially higher than the displacement current in conductive materials, this EMF situation holds even at higher frequencies. These four Maxwell equations can be used to describe the quasi-stationary EM field:

$$\text{curl } \mathbf{E} = -\frac{\partial \mathbf{B}}{\partial t} \quad (1)$$

$$\text{curl } \mathbf{H} = \mathbf{J} \quad (2)$$

$$\text{div } \mathbf{D} = \rho_0 \quad (3)$$

$$\text{div } \mathbf{B} = 0 \quad (4)$$

where \mathbf{H} [A.m⁻¹] is the magnetic intensity vector, \mathbf{E} [V.m⁻¹] is the electric intensity vector, \mathbf{B} [T] is the magnetic flux density vector, \mathbf{D} [A.s.m⁻²] is the electric displacement vector, \mathbf{J} [A.m⁻²] is the conducting current density vector and ρ_0 [C.m⁻³] is the volume density of a free charge.

B. Sweep frequency eddy current testing

Because the induced currents in the conductive material are close in a loop, they are called eddy currents. They are perpendicular to the magnetic flux that causes them; therefore, they usually flow parallel to the coil winding and parallel to the material's surface. The eddy currents attenuate as the depth increases, and the detecting capability reduces. Therefore, the depth of penetration is an important factor in the investigation. Excitation frequency, electrical conductivity, and magnetic permeability are all elements to consider. Changing the excitation frequency is the main way to increase the depth of penetration. In traditional ECT, a single frequency is used, and the probe investigates the entire material. For better detection of not only surface and subsurface inhomogeneities, but also deeper inhomogeneities, a modification of the conventional method was developed. It's known as sweep frequency eddy current testing (SFECT). It is a method in which a static probe examines a specific area in which inhomogeneity is predicted. The method is based on signal excitation over a large frequency range. Data is obtained in this form from various frequencies and, as a result, from various depths of material. Higher frequencies have a lower penetration depth but a higher sensitivity, while lower frequencies have a higher penetration depth but a lower detection sensitivity. Their combination achieves the required detection rate. [1],[2],[3]

III. PERFORMED SIMULATIONS

The most appropriate design of probe is required to evaluate the use of sweep frequency eddy current testing. The behavior of three different types of probes is simulated before the measurement. Numerical simulations are performed using the CST Studio Suite application. CST Studio Suite is a problem-solving software for electromagnetic fields. For calculation and analysis, the program uses the finite integration method (FIT). Instead of the differential form previously mentioned, FIT discretizes the following integral version of Maxwell's equations:

$$\oint_l \mathbf{E} \cdot d\mathbf{l} = - \int_s \frac{\partial \mathbf{B}}{\partial t} \cdot d\mathbf{S} \quad (1)$$

$$\oint_l \mathbf{H} \cdot d\mathbf{l} = \int_s \left(\frac{\partial \mathbf{D}}{\partial t} + \mathbf{J} \right) \cdot d\mathbf{S} \quad (2)$$

$$\oint_s \mathbf{D} \cdot d\mathbf{S} = \int_v \rho_0 \cdot dV \quad (3)$$

$$\oint_s \mathbf{B} \cdot d\mathbf{S} = 0 \quad (4)$$

The low-frequency domain solver is chosen as the solver. This solver is based on Maxwell's Grid Equations in the time-harmonic case. The Magnetoquasistatic (MQS) equation type is selected from this solver. The MQS equation is solved using a vector potential formulation:

$$\mathbf{B} = \text{curl } \mathbf{A}, \quad (5)$$

where \mathbf{A} [T.m] is the magnetic vector potential. The displacement currents in Ampere's law are not used in the MQS equation type. This approximation is ideal for applications where the magnetic field is the most important factor.

A. Tested probes

Three different types of probes were simulated, as previously stated. Coreless probe, probe with ferrite core, and probe with ferrite core and aluminum shield were simulated. Probes consist of two coils. The first coil is the transmitting coil (Tx), which is excited by an exciting signal, and the second coil is the receiving coil (Rx), which is used to acquire the response signal. The coils have the same composition and dimensions as the real coils used in [6]. The coils were then modeled in CST based on the composition and dimensions of this article.

B. Inspected specimen

Following that, a material specimen was modeled. A specimen was a block with a square base and an edge length of $l = 100$ mm and a height of $h = 10$ mm (Fig. 1). The electromagnetic and mechanical properties of this material are identical to those of austenitic steel AISI 316L. In the middle, axially symmetrically to the specimen, is inhomogeneity. For each simulation, the dimensions of inhomogeneities are changed to obtain the signal's response to each dimension change. The depth of inhomogeneity changes first, then the length of inhomogeneity, and finally both parameters change at the same time. As a reference value, a simulation of defect-free material is made. All dimensions of inhomogeneities are summarized in Table. 1.

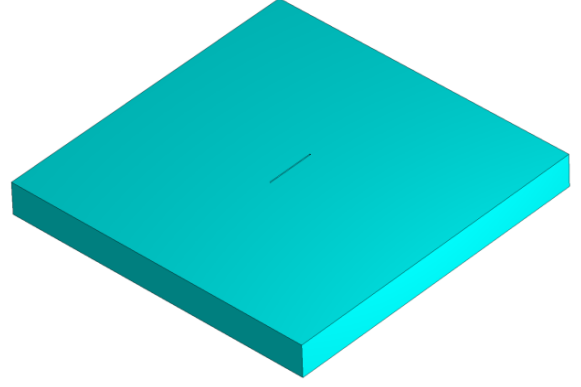


Fig. 1. Simulated model of the specimen using CST Studio Suite

C. Excitation signal

The sweep frequency ECT method requires discretely sweeping the excitation signal through a wide band of frequencies. The excitation coil (Tx) is driven by a harmonic signal in these simulations. The signal's frequency is chosen from a range of $f = <1 \text{ kHz}; 1.5 \text{ MHz}>$. The frequency is changing linearly, with a step size of $f_s = 10 \text{ kHz}$. The signal has a magnitude of $V_{pp} = 100 \text{ mV}$.

IV. RESULTS

A. Mathematical operations

The coils' parameters (voltage, impedance, and current) are obtained from the simulation. Induced voltage of the Rx coil is practically the most important. The simulation's values for this parameter are then mathematically adjusted. The induced voltage of the Rx coil simulated with the probe in the air is subtracted from the results. This removes the induced voltage from the Tx coil, leaving only the material's response. Subsequently, are results normalized to the absolute value of the Rx coil's voltage in the air:

TABLE I. SIMULATED INHOMOGENEITIES AND THEIR GEOMETRY

Simulation No.	Simulation name	Inhomogeneity dimension		
		Depth [mm]	Length [mm]	Width [mm]
1.	Depth 1	1	10	0.25
2.	Depth 3	3	10	0.25
3.	Depth 5	5	10	0.25
4.	Depth 7	7	10	0.25
5.	Depth 9	9	10	0.25
6.	Length 10	5	10	0.25
7.	Length 15	5	15	0.25
8.	Length 20	5	20	0.25
9.	Length 25	5	25	0.25
10.	Length 30	5	30	0.25
11.	Defect 1	1	3	0.20
12.	Defect 2	3	5	0.20
13.	Defect 3	5	15	0.25
14.	Defect 4	7	21	0.25
15.	Defect 5	9	27	0.25

$$\dot{V}_{R_{xnormalized}} = \frac{\dot{V}_{R_{xmaterial}} - \dot{V}_{R_{xair}}}{|\dot{V}_{R_{xair}}|} \quad (5)$$

where $V_{R_{xmaterial}}$ [V] is the voltage induced on Rx coil from simulation with material (with and without defect), $V_{R_{xair}}$ [V] is the voltage induced on Rx coil from simulation of the probe

in the air, and $V_{R_{xnormalized}}$ [-] is the normalized value of voltage. Equations (6) and (7) are used to calculate magnitude V and phase ϕ [rad] from normalized values:

$$|\dot{V}_{R_{xnormalized}}| = \sqrt{\text{Re}\{\dot{V}_{R_{xnormalized}}\}^2 + \text{Im}\{\dot{V}_{R_{xnormalized}}\}^2} \quad (6)$$

$$\phi = \tan^{-1} \frac{\text{Im}\{\dot{V}_{R_{xnormalized}}\}}{\text{Re}\{\dot{V}_{R_{xnormalized}}\}} \quad (7)$$

Calculated values are plotted in the individual graphs.

B. Graphs

The processed results of the simulations are shown in the following graphs.

The graph in Fig. 2 shows the results of the coreless probe for simulations No. 11 to No. 15. In these simulations, all dimensions of inhomogeneity are changing. It can be seen from the graph, that in the interval of lower frequencies, curves of larger defects are well separated. The dimensions of the defect in simulation No.11 (Defect 1, red curve) are too small to distinguish it from defect-free (Defect free, dark blue curve) material in the low-frequency region. However, the difference in values between 100 kHz and 1.5 MHz is just about 1%. This indicates that the SFECT method is suited for non-destructive testing and that data from a wide range of frequencies is important.

Fig. 3 shows a graph of the same number simulations, but of the probe with ferrite core. In the low-frequency band, a probe with a ferrite core also shows well-separated curves of large defects. In contrast to the coreless probe, the values increased rather than decreased in the higher frequency region. The advantage of the second coil, on the other hand, was the difference in values in the higher frequency range, which reached approximately 2%.

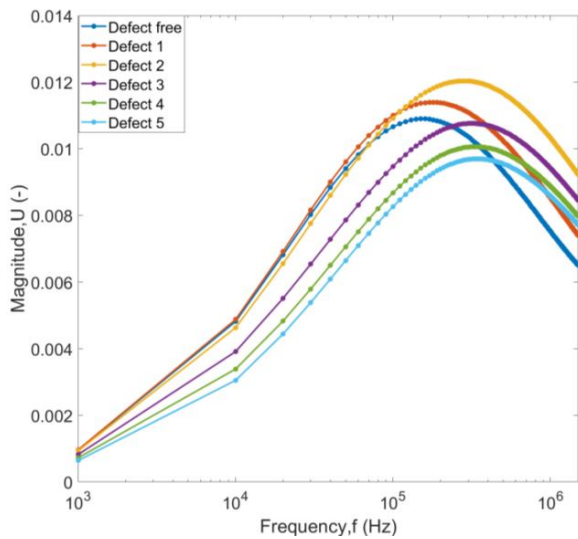


Fig. 3. Numerical simulation results: magnitudes of coreless probe, simulations No. 11 to 15

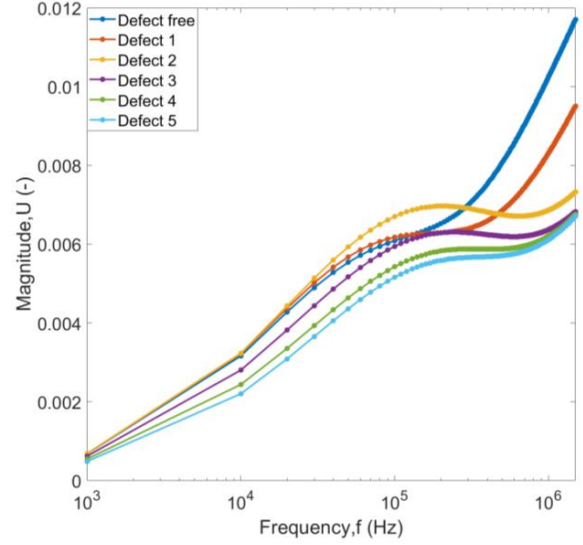


Fig. 2. Numerical simulation results: magnitudes of probe with ferrite core, simulations No. 11 to 15

Fig. 4 shows the results of adding a metal cover to the ferrite core probe. The probe with ferrite core and the aluminum cover showed very well separated curves, as did prior results. It may even be stated that it outperformed the prior two probes in terms of outcomes. Individual defects can be identified at a frequency of 10kHz, as can be shown in the graph. The benefit of using an aluminum cover is that the frequency of the region of interest is shifted lower.

The simulation results for the change in depth and the change in defect length for the probe without core and the probe with core and cover indicated similar conclusions as defect change. Only the ferrite core coil results were difficult to differentiate.

The calculations of the phase shift of the induced voltage also offered interesting results. A phase shift of 2π rad occurred in each simulation. The resonant frequency might be to cause of that phenomenon. However, it's important to note that the phase shift appeared at various frequencies for

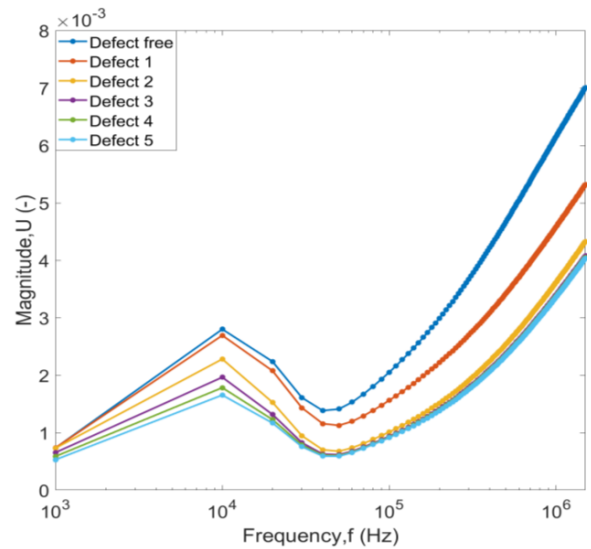


Fig. 4. Numerical simulation results: magnitudes of probe with ferrite core and aluminum shield, simulations No. 11 to 15

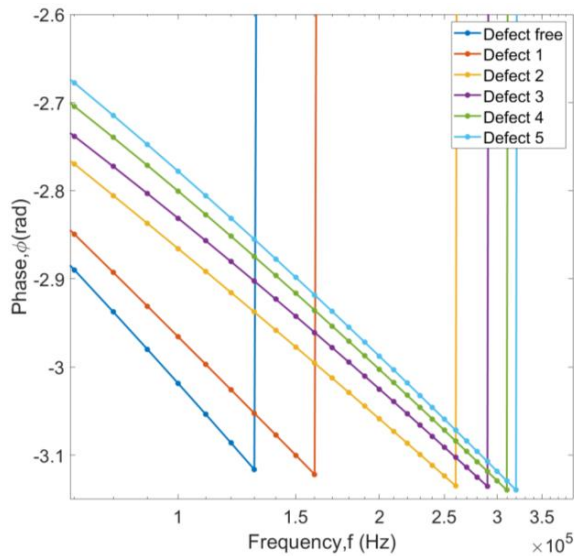


Fig. 6. Numerical simulation results: cut out of graph, coreless probe, simulations No. 11 to 15, phase shift

different dimensions of the defect. Fig. 5 depicts an example of a phase shift. This is a part of the phase shift graph of a probe without a core for simulations No. 11 to 15. The phase shift appeared at the same frequency in some graphs (see Fig.6). At a frequency of 300 kHz, a phase shift occurred at a defect length of 20 mm and a defect length of 25 mm, as shown in the graph. This can be caused by a large step of changing the excitation frequency.

CONCLUSION

In this article, the SFECT method was discussed as a method of non-destructive testing of conductive materials. Three different types of the SFECT probes were simulated.

The results show that all three types of probes are appropriate for use with the SFECT method. The coreless probe, on the other hand, produces the best findings in both magnitude versus frequency and phase shift plots. The probe with ferrite core and aluminum shield head the advantage of shifting the region of interest to a lower frequency range. This means that the excitation frequency does not need to be dispersed widely, which reduces testing time.

Another finding was that by using the SFECT method, a phase shift can be used to detect the defect. The specifications of the defect can also be determined based on the frequency with which the shift occurs.

The outcomes of simulations will be compared to the data from [6] in future research to see if they reflect the simulation results.

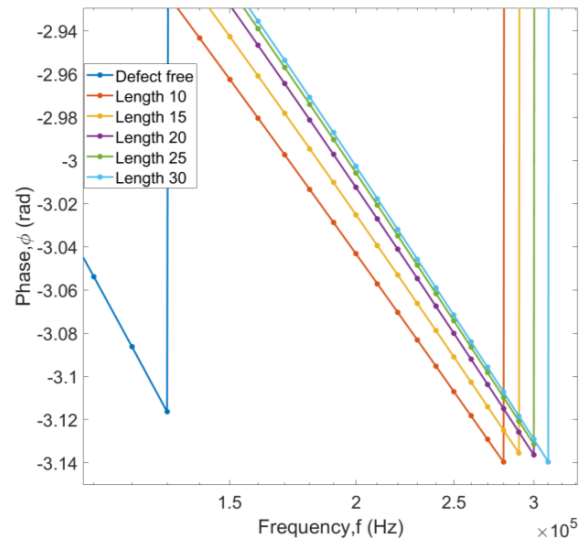


Fig. 5. Numerical simulation results: cut out of graph, coreless probe, simulations No. 6 to 10, phase shift

ACKNOWLEDGMENT

This work was supported by the project APVV-19-0214 of Slovak Research and Development Agency, with acronym "LIFE".

REFERENCES

- [1] B.P.C. Rao, Practical Eddy Current Testing. Alpha industries International Ltd.J.2007.
- [2] J. García-Martín, J. Gómez-Gil, and E. Vázquez-Sánchez, "Non-destructive techniques based on eddy current testing," in *Sensors*, vol.11, 2011, pp. 2525-2565.
- [3] N. Bowler, Eddy-Current Nondestructive Evaluation. Springer, 2017.
- [4] R. Konar, M. Mician, M. Smetana, and V. Chudacik, "Real biomaterial evaluation by eddy current and ultrasonic inspection", 2016 *ELEKTRO*, 2016, pp. 578-582.
- [5] L. Janousek, A. Stubendekova, and M. Smetana."Novel insight into swept frequency eddy-current non-destructive evaluation of material defects", in *Measurement*, vol. 116, 2017, pp. 246-250.
- [6] F.Vaverka, M.Smetana, D. Gombarska and L. Janousek, "Nondestructive Evaluation of Conductive Biomaterials Using SFECT Method" 2021 13th *International Conference on Measurement*, 2021, pp. 27-30.
- [7] Karban, P., Panek, D., Kropik, P. Utilization of algebraic multigrid for solving electromagnetic field by HP-FEM. In: *ELEKTRO 2016: proceedings*. [S.l.]: IEEE, 2016. ISBN 978-146738698-2, s. 527-532.
- [8] Mach, F. Reduction of optimization problem by combination of optimization algorithm and sensitivity analysis. In: *IEEE Transactions of Magnetics*. ISSN 0018-9464, 2016, art. no. 7003104.

Cell-centered, geometric multigrid field solver for Particle-in-Cell simulations

Bartosz Chaber

Warsaw University of Technology

Warsaw, Poland

bartosz.chaber@ee.pw.edu.pl

Abstract—A geometric multigrid solver is tested as a field solver for Particle-in-Cell simulations. The convergence of the multigrid solver for different boundary conditions is verified. The iterative solver reuses the solution from the last timestep in order to decrease the number of iterations. An electron avalanche in argon gas is a test example for the method to check the performance in a self-consistent field simulation. Performance of multigrid method was compared with LU decomposition which seems to be a viable alternative even for moderate-sized problems.

Index Terms—multigrid method, finite volume method, Particle-in-Cell, iterative solvers, LU decomposition.

I. INTRODUCTION

Many interesting plasma phenomena can be simulated using a Particle-in-Cell (PIC) [3], [13]. One of them is the formation of electron avalanche in the presence of a strong electric field. A free electron might appear in otherwise non-ionized gas due to cosmic radiation that happen to hit a neutral gas atom and create an ion-electron pair in the ionization event. If the electric field is low enough, then after some time such a pair will recombine with either the gas particles or with some solid material. However, when such an ionization event happen in the presence of a strong electric field, an electron might acquire a significant kinetic energy. We mainly consider only the electrons movement as they are more than three orders of magnitude lighter, therefore accelerate much faster. When such a fast moving electron hits a neutral gas atom it can ionize it creating additional electron (and also an ion). When the loss of electrons due to surface recombination is lower than their generation, we can observe a series of ionization events that result in an exponential increase in the total number of electrons. At one point, the space charge density from the charged particles might affect the background electric field distribution and it can lead to a development of a streamer [4].

Due to the timescale of such a process, many timesteps have to be taken to analyze it, as the time discretization is related to the other parameters of the model: its spatial dimensions, electric field values, etc. In electrostatic PIC, at each timestep, one has to solve the Poisson equation to find the electric potential distribution due to the boundary conditions and the spatial charge distribution. Often, the time spent by the field solver is a significant part of the computations performed at each timestep. Therefore, efficient field solvers have attracted much attention, especially for large problems [10], [11]. This

work explores such an efficient field solver using a geometric multigrid method.

II. EFFICIENT POISSON EQUATION SOLVER

Many codes using Particle-in-Cell discretize the Poisson equation on a uniform, structured grid using Finite Difference Method. Such an approach is easy to implement and yields a sparse system of linear equations. The system of linear equations can be solved using different methods, either direct or iterative. Gaussian elimination and LU decomposition are two examples of direct methods [9]. Iterative solvers, like Gauss-Seidel, successive over-relaxations (SOR) or generalized minimal residual method (GMRES) are popular, iterative methods used for solving the Poisson equation [6].

Direct solvers need a fixed number of computational steps to calculate the final solution. LU decomposition methods splits the process of finding the solution into two stages: decomposition stage and solution of two triangular systems of linear equations. A significant advantage of LU decomposition is that the result of the first stage might be reused for solving the same equation for different source term.

Problems involving a detailed field distributions require a fine computational grid (an increase in number of particles following from the improvement of grid resolution is not considered in this paper). Different solvers for the Poisson equation scale differently relative to the number of total grid nodes. High memory requirements or long computational time might render some of them unusable for a sufficiently fine grids. In general, the iterative methods seem to be more memory efficient than direct methods. They also need an initial guess, so they allow starting from an approximate solution. However, they might exhibit a poor convergence rate for large systems of linear equations. This is exactly the case for Gauss-Seidel or Jacobi method, where the methods need many iterations to converge to the exact solution due to their local stencil [12].

An interesting approach that gained a lot of attention in computational electromagnetics is the geometrical multigrid method. It uses an iterative solver on a series of grids with a varying spatial resolution. As the Gauss-Seidel or Jacobi stencils span effectively wider on a coarser grid, the convergence is improved.

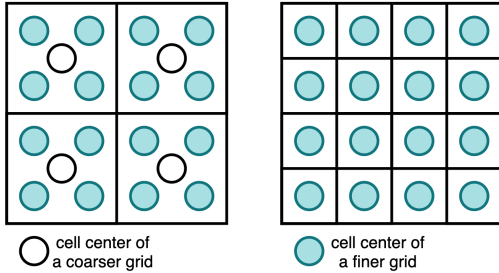


Fig. 1. Two Finite Volume Method grids with different levels of discretization. The finer grid (4×4 cells, shown on the right) is not embedded in the coarser grid (with 2×2 cells, show on the left).

III. CELL-CENTERED GEOMETRIC MULTIGRID METHOD

We have implemented a plasma simulation code using Particle-in-Cell method and an electric field solver on uniform, structured grids. It has to be noted, that the discretization of the Poisson equation is done using Finite Volume Method rather than Finite Difference Method. The two methods yield rather similar systems of linear equations, however they rely on different problem formulation. In Finite Difference Method, we assume that we only seek the unknown field values at the nodes of our computational grid. The nodes at the boundary are treated in a special way by applying appropriate boundary conditions. On the other hand, Finite Volume Method operates on an *averaged* values of the unknown quantity in each grid *cell*. Boundary conditions are defined at faces of the boundary cells. The fact that the unknowns are located at cell centers rather than at the grid nodes is important also for the implementation of the multigrid solver.

In order to boost convergence, a hierarchy of computational grids of decreasing resolution is generated. In our implementation, each 2D grid has half of the number of cells in each spatial dimension. This means that the finest grid has to be composed of 2^k cells in each direction (with total of 2^{2k} cells in the whole grid). This allows a generation of k computational grid, where the coarsest grid has 2×2 cells. As mentioned earlier, coarser grids are not embedded in finer grids (their cell centers don't overlap). An example of such two grids is presented in Fig. 1.

A detailed description of a cell-centered multigrid methods is described in [5]. In our implementation, the multigrid method uses bilinear interpolation to map quantities between the grids in the hierarchy. The prolongation (mapping from a coarser to a finer grid) and restriction (mapping from a finer grid to a coarser one) operators are pre-computed as sparse matrices. The operators use kernels that take into account different types of the boundary conditions on the boundaries of the square domain. For now only the basic V-cycle scheme has been implemented, where at the coarsest grid level, we use a direct solver, while for the finer levels a few iterations of Gauss-Seidel method are being applied. In the following experiments we assume performing $\nu_1 = 2$ iterations of Gauss-Seidel *before* going to the coarser grid, and $\nu_2 = 1$ iteration

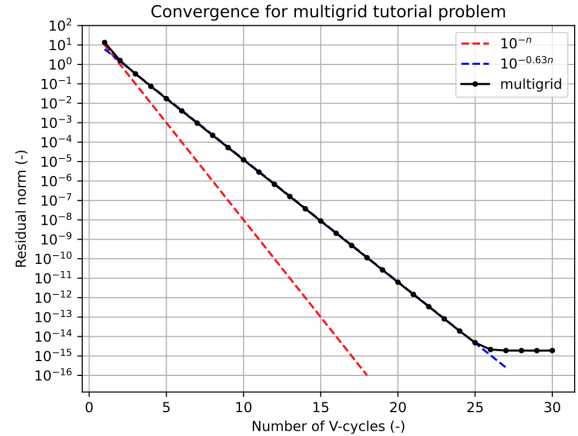


Fig. 2. Convergence plots for the multigrid tutorial problem, solved on $k = 8$ grid levels on a unit square domain with homogeneous Dirichlet boundary conditions; $\nu_1 = 2$, $\nu_2 = 1$.

of Gauss-Seidel computed *after* correcting the solution on the finest grid from the coarser grid.

IV. CONVERGENCE AND PERFORMANCE ASSESSMENT

The following series of experiments aims at assessing the properties of the implemented multigrid solver. Much effort has been put in efficient implementation of each of the methods in the comparison. Our multigrid solver has been implemented in Julia programming language that allows finer control on the resulting low-level code than Python or MATLAB. The number of dynamic memory allocation has been limited and the use of vectorized operations has improved overall performance. The only suboptimal choice is leaving three allocations for intermediate matrices per each V-cycle. They could be eliminated but that would require explicitly passing additional pre-allocated buffers.

The cell-centered multigrid solver has been compared with UMFPACK's LU procedure in two different settings. In the first, the result of LU decomposition has been used for computing the solution and the decomposition has been discarded to be repeated in the next timestep. The reason was to make it behave more like Gaussian Elimination. The other setting has been reusing decomposition results and was only solving the two triangular systems of equations each timestep. It has to be noted, that LU procedure from UMFPACK tries to preserve sparsity of the matrices L and U [8].

For checking the convergence properties of multigrid method, two examples have been considered:

- a test problem with homogeneous Dirichlet boundary conditions from [2],
- a parallel plate capacitor problem with electric potential on the top and bottom boundaries (Dirichlet boundary condition) and with zero normal electric field on the left and right boundaries (Neumann boundary condition).

The convergence plots of residual norms after each V-cycle has been presented in Fig. 2 and Fig. 3. (starting from

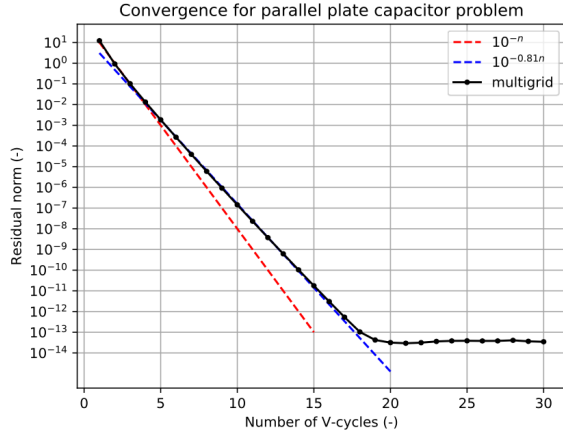


Fig. 3. Convergence plot for a parallel plate capacitor problem, solved on $k = 8$ grid levels on a unit square domain with Dirichlet boundaries and Neumann boundaries; $\nu_1 = 2$, $\nu_2 = 1$.

a random initial guess). Both cases were solved on eight grid levels, where the final solution were obtained for the finest grid with 256×256 cells.

A better convergence can be observed for the parallel plate capacitor problem, where about 5 V-cycles are needed to decrease the error by four orders of magnitude.

The parallel plate capacitor problem will be solved to measure the mean time of the solution procedure for the three mentioned cases: direct method (LU without reusing decomposition results), LU solution time of two triangular systems of equations and solution time of one V-cycle ($\nu_1 = 2$, $\nu_2 = 1$). For each $k = 4, 5, \dots, 8, 9$, the V-cycle has been operating on all k grids. The mean time has been calculated based on at least 10 repetitions to omit the influence of Julia's just-in-time compiler. The performance comparison of solution time related to the number of degrees of freedom (number of cells in the computational grid 2^{2k}) can be seen in Fig. 4. It can be seen that for large problems (more than 5 000 cells) one V-cycle is faster than LU solution procedure. Of course, during the time, the direct solver obtains the final solution, while after one V-cycle the residual of the solution decreases more or less one order of magnitude. The one-time cost of pre-computing necessary operators (i.e. assembling of the sparse system of linear equations or computing the decomposition of the matrix \mathbf{A}) hasn't been compared as it is assumed that it is negligible for long-running simulations.

V. MULTIGRID SOLVER IN PARTICLE-IN-CELL

A great advantage of using an iterative method is an ability of reusing the last solution as an initial guess to boost the convergence [1]. It is the most beneficial in the case of slow changes of the field distribution as time progresses. To verify the usefulness of the concept two additional problem have been analyzed.

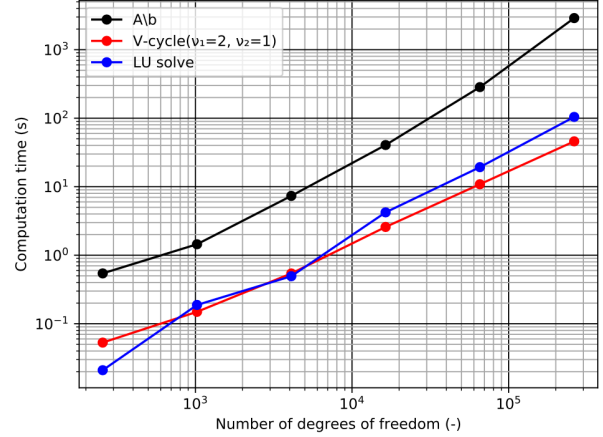


Fig. 4. Performance comparison of three solvers for the Poisson equation for different numbers of degrees of freedom.

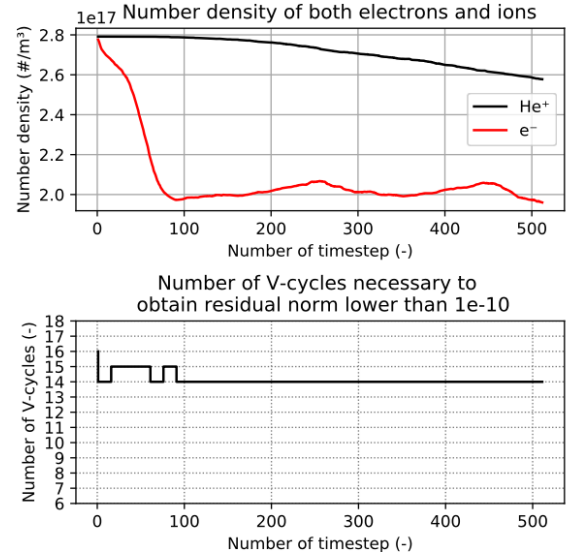


Fig. 5. Top: change of number densities of electrons and helium ions in the RF discharge simulation, bottom: number of V-cycles in each timestep of the simulation

A. Radiofrequency capacitive discharge

The problem described in [7] as a 1D benchmark problem for testing a collisional plasma will be here extended to a 2D case, with decreased number of timesteps and lower number of particles per computational cell. The computational grid will be uniform and square. The simulation starts with an initial distribution of electrons and helium ions. They start to oscillate driven by a voltage sine wave applied to the top and bottom electrodes.

Particles that hit the electrodes are discarded (they are absorbed), while the particles leaving open boundaries are reintroduced in the computational domain from the other side (they are wrapped). To make the computations faster, the computational domain uses 32×32 cells, and only the first

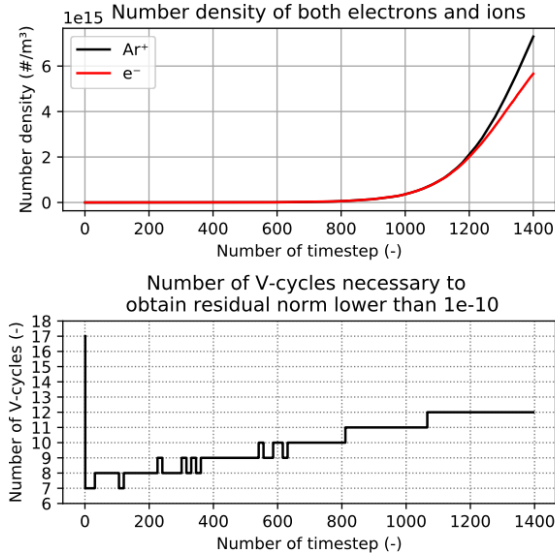


Fig. 6. Top: change of number densities of electrons and argon ions in the electron avalanche simulation, bottom: number of V-cycles in each timestep of the simulation

512 timesteps are computed. The multigrid solver has been reconfigured so that it performs at most 20 cycles, but finishes earlier when the residual norm is lower than 10^{-10} . The result from the last timestep is used as the initial guess in the next timestep. The plot of the variation in number densities of the electrons and ions is presented at the top of Fig. 5. The bottom plot in Fig. 5 shows the number of iterations to obtain the given maximal residual norm. No significant change in the number of V-cycles is visible during the simulation. In this case, the field does change from timestep to time step, given the external oscillating excitation.

B. A formation of an avalanche in argon gas

In the following problem a constant, relatively high voltage $U = 400$ V is applied between two planar electrodes at the top and bottom of a small chamber (with width and height equal to 8 cm) filled with neutral argon gas at pressure 41.4 Pa. In this setting, a single electron is put in the middle of the computational domain. It is then accelerated by the uniform electric field and starts a series of ionization events. As can be seen in the upper plot in Fig. 6, after about 800 timesteps the number of electrons and ions start to increase exponentially. That means that the generation rate of electrons overcomes the loss of electrons and an electron avalanche has started.

Our multigrid solver uses the solution from the last timestep as the initial guess for the next one. As depicted in the lower plot of Fig. 6, except the first timestep (where the initial guess is a random solution), the first 800 timesteps need at most 10 V-cycles to obtain a solution with residual norm lower than 10^{-10} . After that, the space charge is significant enough to influence the external electric field and more V-cycles have to be performed to reach the desired residual norm.

VI. CONCLUSIONS

A single V-cycle of our multigrid solver starts to be more time efficient than LU solver for about 5 000 degrees of freedom, however they are not directly comparable in terms of solution accuracy. The convergence analysis shows that about 15-25 V-cycles are needed to decrease residual norm to the value of 10^{-14} . Reusing a solution from the last timestep is of little use in the case of changing boundary conditions as presented in the results of RF discharge simulation. On the other hand, it was able to decrease the number of V-cycles needed for in the case of electron avalanche in argon. Lower number of V-cycles was necessary when the electric potential was unaffected by the space charge density of the generated electrons and ions. Decreasing the timestep would limit the number of required iterations even further.

In the case of 2D simulations for moderate-sized problems (with number of cells lower than 512×512) LU solvers seems a viable alternative to multigrid solver in terms of computation time and memory consumption.

However, the multigrid solver offers a greater flexibility of controlling the quality of the solution. In this paper only one set of parameters (ν_1 , ν_2 and number of grid levels k), although a detailed study regarding optimizing their values might be useful.

REFERENCES

- [1] Z. Pekárek, M. Lahuta, and R. Hrach, "Improving performance of multi-dimensional Particle-In-Cell codes for modelling of medium pressure plasma," J. Phys.: Conf. Ser., vol. 63, p. 012009, Apr. 2007, doi: 10.1088/1742-6596/63/1/012009.
- [2] W. Briggs, V. Henson, and S. McCormick, "Implementation" in "A multigrid tutorial," SIAM, 2000, ch. 4, pp. 64-68.
- [3] C. Li, U. Ebert, and W. J. M. Brok, "Avalanche-to-Streamer Transition in Particle Simulations," IEEE Trans. Plasma Sci., vol. 36, no. 4, pp. 910-911, Aug. 2008, doi: 10.1109/tps.2008.922487.
- [4] E. Bazelyan, Yu. Raizer, "Avalanche and streamer mechanisms of gas breakdown" in "Spark Discharge," CRC Press, 1998, ch. 1.3, pp. 10-12.
- [5] J. Molenaar, "A simple cell-centered multigrid method for 3D interface problems," Computers Mathematics with Applications, vol. 31, no. 9, pp. 25-33, May 1996, doi: 10.1016/0898-1221(96)00039-9.
- [6] M. Becker, "Development of a parallel multigrid field solver for large-scale particle-in-cell applications," Ph.D dissertation, Justus-Liebig-Universität Gießen, Gießen, 2018.
- [7] M. M. Turner et al., "Simulation benchmarks for low-pressure plasmas: Capacitive discharges," Physics of Plasmas, vol. 20, no. 1, p. 013507, Jan. 2013, doi: 10.1063/1.4775084.
- [8] T. A. Davis, "Algorithm 832," ACM Trans. Math. Softw., vol. 30, no. 2, pp. 196-199, Jun. 2004, doi: 10.1145/992200.992206.
- [9] Kahfeld, D., Schneider, R., Matyash, K., Lüskow, K., Bandelow, G., Kalentev, O., Duras, J., Kemnitz, S. "Solution of Poisson's equation in electrostatic Particle-In-Cell simulations," APS Division of Plasma Physics Meeting Abstracts, APS Division of Plasma Physics Meeting Abstracts, 2016, TO7.002.
- [10] Lewandowski, J.L.V. "Multigrid particle-in-cell simulations of plasma microturbulence," Physics of Plasmas, 10(8), 3204-3211, 2003.
- [11] T. Wang, V. Khudik, G. Shvets "WAND-PIC: A three-dimensional quasi-static particle-in-cell code with parallel multigrid solver and without predictor-corrector," arXiv:2012.00881 (physics), 2021.
- [12] Press, W. H., Flannery, B. P., Teukolsky, S. A., Vetterling, W. T., "Multigrid Methods for Boundary Value Problems" in "Numerical Recipes in C: The Art of Scientific Computing," Cambridge University Press, 1992, ch. 19, sec. 6, pp. 874-875.
- [13] V. Vahedi, M. A. Lieberman, M. V. Alves, J. P. Verboncoeur, and C. K. Birdsall, "A one-dimensional collisional model for plasma-immersion ion implantation," Journal of Applied Physics, vol. 69, no. 4, pp. 2008-2014, Feb. 1991, doi: 10.1063/1.348774.

Parallel implementation of a Particle-in-Cell code in Julia programming language

Wiktor Łodyga
 Warsaw University of Technology
 Warsaw, Poland
 wiktlor.lodyga@ee.pw.edu.pl

Bartosz Chaber
 Warsaw University of Technology
 Warsaw, Poland
 bartosz.chaber@ee.pw.edu.pl

Abstract—An original GPU implementation of a Particle-in-Cell code has been presented. Performance has been measured for a simple 1D problem of two collisionless, counter-propagating streams of charged particles. The aim of this paper is to assess the scalability of two codes: one computing solely on a CPU and a multithreaded code running the most computation-intensive tasks on a GPU. Both codes are implemented in the same programming language (Julia) solving the two-language problem.

Index Terms—CUDA, parallel computing, Particle-in-Cell

I. INTRODUCTION

Particle-in-Cell (PIC) algorithm is a versatile method for simulating charged particles. By itself, it does not consider collisions between particles other than their interaction via Coulomb forces. One of the biggest strengths of the method is its versatility, as it needs relatively few assumptions. It has to be contrasted with alternative methods for simulations of interactions of charged particles using fluid dynamics, as they require assumptions of the velocity distribution function and mobility coefficients for each fluid species.

In PIC methods, both position and velocity of particles have to be tracked, and equations of motions have to be integrated using a high-order ODE solver. One of the obvious disadvantage of PIC is its computational complexity. As a stochastic method, more statistically significant results can be obtained using more particles. However, often the large number of particles that have to be tracked in a simulation may easily lead to a slow time-stepping as each particle is handled sequentially. Using multiple CPU threads does not help much, as the number of particles is much larger than the number of cores available in most CPUs. Situation is different with GPU, as such a device contains thousands of processing cores.

II. PARTICLE-IN-CELL ALGORITHM AND IT'S POTENTIAL FOR PARALLELIZATION

Particle-in-Cell algorithm overcomes the $\mathcal{O}(N^2)$ complexity of a naïve, direct simulation of pair-wise interaction between N particles by using a separate, computational grid which defines a *field* which represents the aggregated contribution from each individual particle. As such, we can distinguish between *kinetic* variables describing particles and *field* quantities that are defined on the grid. In it's basic form, the control flow in PIC algorithm is presented in Fig. 1. After an initial

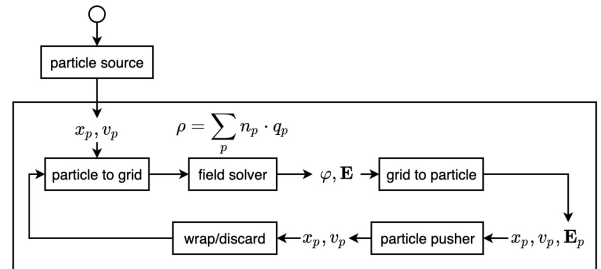


Fig. 1. Control flow in the Particle-in-Cell algorithm. The circle is the start node of the algorithm, where arrows show the direction of the data passing in the algorithm. Data names are the following: x_p, v_p – are lists of positions and velocities of particles of species p , ρ – spatial charge distribution calculated using number density n_p of each species p and charge of their particles q_p . \mathbf{E} is the electric field calculated using the gradient of the electric potential field φ . \mathbf{E}_p is the electric field evaluated at the coordinates of each particle in the system.

loading of the computational domain by a particle source, the main loop of Particle-in-Cell starts. The loop begins with the charge associated with the particles being deposited onto the grid nodes as a field ρ . After the (so called) scatter phase, the charge interpolated to the grid nodes might be used as the source term in the Poisson equation that will be solved to obtain the electric potential field φ due to boundary conditions and space charge distribution. On the basis of φ , the electric field \mathbf{E} is calculated as $\mathbf{E} = -\nabla\varphi$ which is still defined on the computational grid. In order to advance the particles' positions, the electric field has to be interpolated (gathered) to the positions of the individual particles \mathbf{E}_p . Only after that the particle pusher calculates the effect of the field on the new particle positions and velocities. The last stage of the algorithm's loop is handling particles that might fall outside the computational domain. Often they will be reintroduced in the domain or removed. After that, the time is advanced by the timestep and the new number density and charge distribution are interpolated on the computational grid. The loop continues to run until the final time has been reached.

In a two-dimensional grid, each cell has four nodes. The particles seldom store the index of the cell they belong to as it is expected to change often and it would be cumbersome to keep track of. Instead, the cell's index can be calculated for

each particle. It is trivial in the case of uniform, structured grids where the size of grid cells is constant Δh .

III. LITERATURE OVERVIEW

Parallel implementations of collisionless PIC algorithm became the object of interest in the late 80's [5], [6] and since then continuously gained attention alongside the development and dissemination of computers. The parallelization scenario has been changing through the years from cluster-oriented computing in the early studies to the utilization of general purpose graphical processing units (GPGPU) nowadays. Beside the performance improvement resulting from the advancement in technology, the main difference compared to the older solutions is the number of computing cores which can be utilized. Early implementations on clusters were using even as little as 32 processors [5] and modern supercomputers employing multiple GPUs per node are achieving millions of GPU cores (even over 140 million in Summit supercomputer). The possibility of using many cores resulted in developing massively parallel 2D and 3D accelerators which were able to obtain speedup values over $50\times$ [7]. An efficient implementation of Particle-in-Cell with Monte Carlo Collisions is described in [1].

Although the parallel implementations of collisionless PIC seem to be well explored, most of the best performing applications require writing highly specialized GPU kernels in C++ or FORTRAN which still are attractive among scientific community for computationally-intensive problems. Both C/C++ and FORTRAN are nowadays considered low-level programming languages (at least compared to languages like Python or MATLAB). They offer the meticulous control on the code's performance at the expense of being less expressive and dynamic. On the other hand, Julia [10] is a language that aims at allowing a lot of dynamism and easy extendibility of the codebase, while still generating a high performance code.

Julia is a high-level, dynamic language for technical computing, designed for performance. It has been created as a next step, surpassing two-tiered architectures which were based on a combination of high-level logic expressed in dynamic language and compute-intensive code, which still had to be written in C/C++ or FORTRAN. Several benchmarks showed that Julia is at least comparable with these two and even seems to perform better in few cases [10], [11].

Over past few years work has been carried out to provide a efficient Julia compiler that emits code to be run on a GPU. As for now, the most complete and mature package seems to be CUDA.jl, developed with NVIDIA GPUs in mind. Unlike many CUDA API wrappers (e.g. PyCUDA) which require writing actual kernels in CUDA C, the kernels in CUDA.jl are written in pure Julia. Beside the non-negligible fact that performance of CUDA.jl compiled kernels can outperform CUDA C [9], in many cases the codebase developed for the CPU can be re-used with CUDA.jl only by changing the array type [12]. In our paper we take advantage of this features, and present possible approaches and achieved results of pure Julia implementation of parallel, collisionless PIC algorithm.

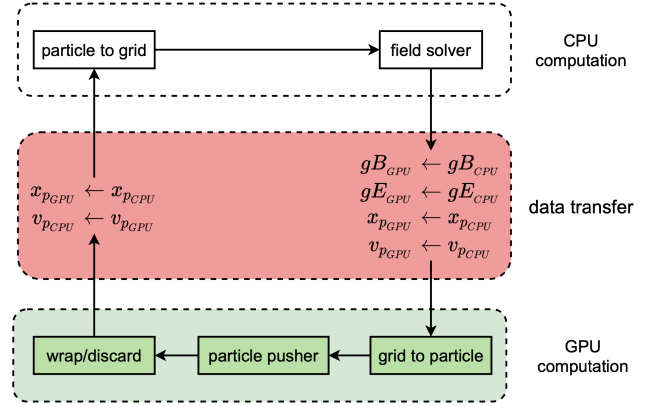


Fig. 2. Diagram showing distribution of computation between CPU and GPU of different parts of PIC algorithm. **Legend:** $x_{pCPU}, x_{pGPU}, v_{pCPU}, v_{pGPU}$ – arrays containing particle positions and velocities on CPU and GPU respectively, $gE_{CPU}, gE_{GPU}, gB_{CPU}, gB_{GPU}$ – arrays holding E and B fields distribution on grid.

IV. GPU IMPLEMENTATION

This section describes different part of our simulation code. It highlights effect of running some of the tasks on GPU.

A. Gather – interpolation from grid to particles

Particle-in-Cell operates on two types of data: kinetic data describing charged particles and field data located on parts of computational grid. Interpolation schemes (e.g. cloud-in-cell – which is a bilinear interpolation [8]) allow mapping quantities between kinetic description (fields are evaluated at particles' positions) and fields located on a grid (at grid nodes, centers of grid cells, etc.) and other way around. Interpolation from grid onto particles' positions operates on the field values located at grid nodes. Then for each particle we find their corresponding grid cell and a weighted contribution from the grid cell's nodes is *gathered* and evaluated at the particle's coordinates. As it can be seen, this part of PIC algorithm is straight-forward for parallelization, as the main loop is over each particle.

B. Boris pusher

A module responsible for integrating equations of motions of charged particles moving in the presence of electromagnetic field is called in PIC nomenclature a *pusher*. In order to be able to track particles' trajectories over long timescales, symplectic pushers are preferred over non-symplectic ones (like the 4th order Runge-Kutta integrator). Symplectic pushers conserve energy over time. Boris pusher is a well tested and widely used method for advancing particles' positions and velocities [4].

It is a well-contained module, that expects the current positions and velocities of each particle, interpolated values of the electric (and magnetic) field evaluated at the position of each particle. The advancing of each particle requires repeating the same calculation for every particle, which might be well over one billion. Multithreaded computations on CPU are not a viable solution as each thread still has to operate on thousands of particles.

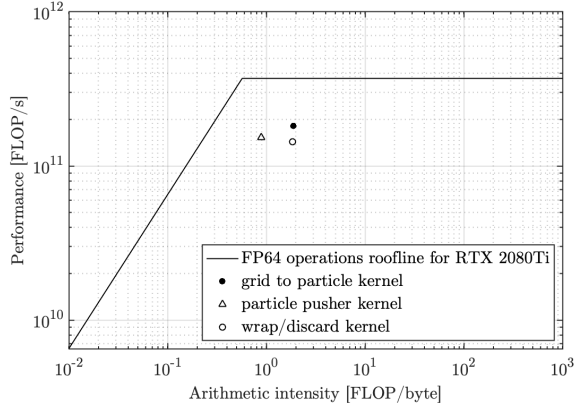


Fig. 3. Roofline chart for RTX 2080 Ti double precision operations together with performance of the implemented kernels.

C. Handling of particles outside of the domain

After each timestep, the pusher might push a particle outside of the computational domain. A massively parallel handling of such outsiders is rather easy in the case of rectangular domains. Most often, such a particle might be either wrapped (reintroduced in on the other side of the domain) or discarded. Removal of the particles is a nontrivial operation which might not be optimal in the case of CUDA kernel implementation, as it requires shuffling the list of particles.

D. Scatter – interpolation from particles to grid

After advancing all of the particles, space charge distribution changes. On the basis of the new particle’s positions, their charge should be scattered onto the nodes of a grid cell holding each of the particles. In contrast to gather operation, now many particles might contribute to the grid nodes, and the deposited/scattered charge has to be synchronized between different threads.

E. Performance analysis of kernels implementation

As a consequence, three CUDA kernels had been implemented for `grid to particle`, `particle pusher` and `wrap/discard`. The final distribution of computational tasks along with the necessary data transfers is presented in Fig. 2. It has to be noted that in the current implementation, the interpolation from particles to grid is performed on CPU. This part of the algorithm requires an additional memory synchronization as different threads will contribute to the same nodes of the computational grid.

In order to assure reasonable GPU utilization, a kernel profiling has been performed in NVIDIA Nsight Compute tool. The performance of the implemented kernels in terms of utilization of GPU can be seen in Fig.3.

As visible, the kernels are performing calculations in double precision, which is undoubtedly sub-optimal as RTX 2080Ti GPU performance in 64-bit floating point operations is $32\times$ worse than 32-bit. However, this decision has been made in

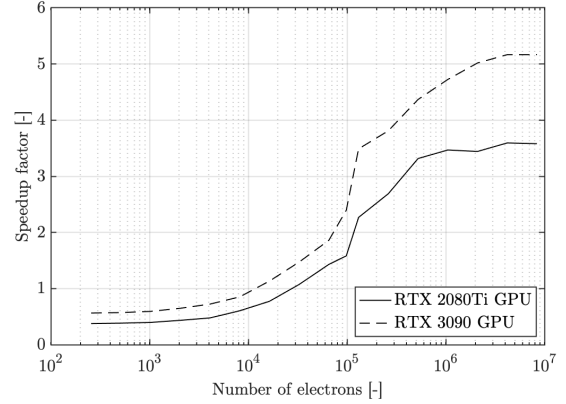


Fig. 4. Speedup factor over Intel i7-9800X CPU in function of electron count.

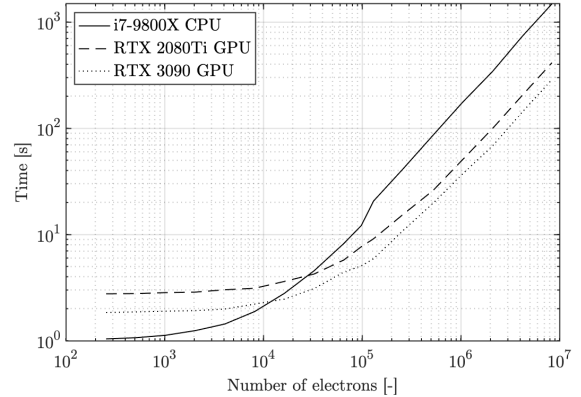


Fig. 5. Execution time of 100 iteration two-streams benchmark simulation in function of electron count.

order to ensure seamless CPU to GPU transition as well as a fair comparison of benchmarks.

Because of the fact that for most of the analyzed cases the number of particles exceeds the number of cores on GPUs, the particles had to be distributed between threads in batches. The distribution had been done by assigning particles to threads one after another until all the particles are assigned. For smaller simulation sizes, with number of particles lower than number of GPU cores, number of threads in blocks had been adjusted in order to utilize all of GPU Streaming Multiprocessors.

A series of simulations have been performed with the increasing number of particles in the system. The resulting speedups over Intel i7-9800X CPU are presented in Fig. 4. For simulation of $8 \cdot 10^6$ particles the acceleration can achieve values of $3.42\times$ and $5.15\times$ for RTX 2080Ti and RTX 3090 respectively. Experiments show that for more than 10^7 particles no further speedup occurs. It should be noted that for smaller problems (below 10^4 particles) the CPU outperforms both GPUs, probably because of communication overhead and poor GPU utilization (see Fig. 5).

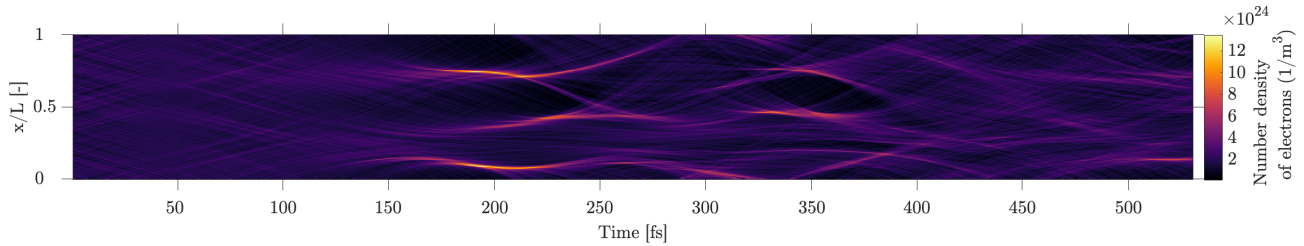


Fig. 6. Evolution of electron number density computed on i7-9800X CPU for $N_e = 2\,560$ electrons.

V. TWO-STREAM INSTABILITY

In this paper we solve a test problem of an instability of two, counter-propagating streams of electrons. It is one of the simplest (but nontrivial) tests of a code for collisionless plasma simulations. This test was chosen as it exercises all the necessary parts of PIC code, namely: particle pusher, electric field solver and interpolation between particles and the computational grid. The setup of the problem is similar to [3].

In this problem, electron particles (with charge $-q_e$) are split into two equal groups (N particles each) that have an initial drift velocities $\pm v_{drift}$ and a small, random velocity due to their non-zero temperature $v_{thermal}$. At the beginning of the simulation the total of $2N$ particles are placed randomly in the computational domain. To neutralize the electric field from such a space charge density, $2N$ positively charged particles $q_i = +q_e$ are initialized exactly in the same positions as the initial electron's distribution. However, as the ions are much heavier than electrons, they remain immovable during the rest of the simulation.

For a certain range of velocities, the collective effect of the particles starts creating vortices in the electron's phase space and bunching can be observed (the lighter color in Fig. 6 represents higher density of electrons). When the velocity is low enough, no significant interaction between the streams is observed. Because we use 64-bit floating point numbers on both CPU and GPU, the results should match as the particles are randomly loaded only before the first timestep and it is done on CPU. We use the same seed for the pseudo-random number generator in each run.

VI. CONCLUSIONS

The application of the two-streams benchmark problem as our test problem allowed us to easily verify the correctness of our implementations. Thanks to retaining the double precision of calculations the results from GPUs were exactly the same as CPU. Nevertheless it is one of the first changes to be made in order to improve the GPUs performance.

Using Julia programming language we were able to solve the two-language problem. Our study showed that it is perfectly possible to implement performant CUDA kernels using pure Julia approach. With the help of the convenient tools as NVIDIA Nsight Compute we were able to analyze the

performance of our kernels and provide necessary improvements. Achieved values are reasonably satisfactory, although further optimization can be done and should improve the performance even more. The CUDA.jl package incorporate the vast majority of functionality compared to more mature CUDA compilers, so it still leaves some room for further, advanced optimizations.

REFERENCES

- [1] Z. Juhasz, J. Ďurian, A. Derzsi, Š. Matejčík, Z. Donkó, and P. Hartmann, "Efficient GPU implementation of the Particle-in-Cell/Monte-Carlo collisions method for 1D simulation of low-pressure capacitively coupled plasmas," *Computer Physics Communications*, vol. 263, p. 107913, Jun. 2021, doi: 10.1016/j.cpc.2021.107913.
- [2] T. Besard, C. Foket and B. De Sutter, "Effective Extensible Programming: Unleashing Julia on GPUs," in *IEEE Transactions on Parallel and Distributed Systems*, vol. 30, no. 4, pp. 827-841, 1 April 2019, doi: 10.1109/TPDS.2018.2872064.
- [3] B. Chaber, "Particle-in-Cell code for gas discharge simulations," presented at the 2020 IEEE 21st International Conference on Computational Problems of Electrical Engineering (CPEE), Sep. 2020. doi: 10.1109/cpee50798.2020.9238682
- [4] H. Qin, S. Zhang, J. Xiao, J. Liu, Y. Sun, and W. M. Tang, "Why is Boris algorithm so good?," *Physics of Plasmas*, vol. 20, no. 8, p. 084503, Aug. 2013, doi: 10.1063/1.4818428.
- [5] P. C. Liewer, V. K. Decyk, "A general concurrent algorithm for plasma particle-in-cell simulation codes," *Journal of Computational Physics*, vol. 85, no. 2, 1989, pp. 302-322, doi: 10.1016/0021-9991(89)90153-8.
- [6] V. K. Decyk, "Skeleton PIC codes for parallel computers," *Computer Physics Communications*, vol. 87, no. 1-2, 1995, pp. 87-94, doi: 10.1016/0010-4655(94)00169-3.
- [7] V. K. Decyk and T. V. Singh, "Particle-in-Cell algorithms for emerging computer architectures," *Comput. Phys. Commun.*, vol. 185, no. 3, pp. 708-719, 2014.
- [8] C. K. Birdsall and A. Bruce Langdon, *Plasma physics via computer simulation*. New York: Taylor & Francis, 2005.
- [9] T. Besard, "Abstractions for programming graphics processors in high-level programming languages," *Universiteit Gent. Faculteit Ingenieurswetenschappen en Architectuur*, 2019.
- [10] J. Bezanson, S. Karpinski, V. B. Shah, and A. Edelman, "Julia: A Fast Dynamic Language for Technical Computing," *ArXiv*, abs/1209.5145, 2012.
- [11] J. Bezanson, S. Karpinski, V. Shah, and A. Edelman, "Julia Micro-Benchmarks," *Julialang.org*. [Online]. Available: <https://julialang.org/benchmarks/>. [Accessed: 03-Jul-2021].
- [12] T. Besard, V. Churavy, A. Edelman, and B. D. Sutter, "Rapid software prototyping for heterogeneous and distributed platforms," *Adv. Eng. Softw.*, vol. 132, pp. 29-46, 2019.

SESSION 4 - HIGH FREQUENCY APPLICATIONS

Real-time Mobile-Based Platform for Determining Level and Location of Radiation Background

Roman Diachok
Specialized Computer Systems Dpt.
Lviv Polytechnic National University
Lviv, Ukraine
rodyachok@gmail.com

Halyna Klym
Specialized Computer Systems Dpt.
Lviv Polytechnic National University
Lviv, Ukraine
klymha@yahoo.com,
halyna.i.klym@lpnu.ua

Ivanna Vasylychshyn
Theoretical and General Electrical
Engineering Dpt.,
Lviv Polytechnic National University,
Lviv, Ukraine
ivanna.i.vasylychshyn@lpnu.ua

Abstract — Mobile-moving platform for determining the level and location of the radiation background with simultaneous control of temperature and atmospheric pressure of potentially dangerous areas in real time has been designed, implemented and investigated. The system is able to processing data, form a researched route and send information to a remote repository for further processing. The structural scheme of the system is proposed, which contains two subsystems with the necessary connection of all necessary components. The system could be controlled via a radio channel and the Internet. System has the ability to form a researched route on a remote cloud service, which allow to view the accumulated data for the entire period of the system and to make an overall assessment of the pollution of a particular area. The operation of the system in real conditions is investigated. It is shown that the prospected system works correctly, the assembled data transmitted to remote depository on cloudy service. All system's tasks pass real-time with the use of relational database. Also, there is a possibility of local monitoring of the system.

Keywords — mobile-moving platform, radiation background, cloud service, monitoring.

I. INTRODUCTION

Today the task of determining the state of environmental pollution is very important, because with the development of science and technology in free use and access are more and more devices that can be used as in useful so in harmful purposes. The greatest danger is the elevated radiation background [1], because radiation is difficult to measure without the use of special measuring instruments. In the military sphere, where is a high probability that the enemy has used nuclear weapons, the problem of determining the harmfulness of the environment is even more relevant. In order to avoid harmful influence on human health, it is necessary to conduct to conduct a reconnaissance operation. To perform such an important and extremely dangerous task autonomous mobile-moving system must be used. Such systems can independently get all necessary data from the environment and it will avoid human casualties [2].

In addition to it, such systems can be used in agriculture, food industry to assess exposure in general, determine the distribution of probabilities of location and intensity of the radiation source [3], etc. Considerable attention of researchers is focused on the development various of mobile-moving systems, as ground so air, to determine the radiation dose, the accumulation of information for a certain period, as well as supply of alarms when the equivalent dose rate exceeds the norm [4]. Most of them are focused on monitoring the radiation background.

The main purpose of this work was to design a system for determining the level and location of radiation with

simultaneous control of microclimatic parameters and deploy the system on a mobile-moving platform. The system will carry out measurements of a radiation background on a given area, process the data, form the investigated route and send data to a remote repository for the further processing. The main digital part of the system will be responsible for reading the ionizing radiation level from the dosimeter installed on the autonomous platform, temperature sensors, atmospheric pressure, also tracking the coordinates of the current location using a GPS module, collect the data and transmit data via GSM wireless channel. The system will be control will be carried out by two ways: direct control using an application on a smartphone or pre-setting the route which must be explored.

II. DESIGN OF THE SYSTEM

The block diagram of the system shown in Fig. 1. It contains the main functional parts (element, device, functional group, functional unit) the relationship between components and components purpose. The programmable microcontroller is the basis of a mobile-moving platform for determining the level and location of the radiation background. The designed system will consist of two independent subsystems. The first independent subsystem is responsible for collecting, processing and transmitting accumulated data to the cloud service, and the second independent subsystem is responsible for managing the movement of the mobile-moving agent in a set area and will implement a system of direct management.

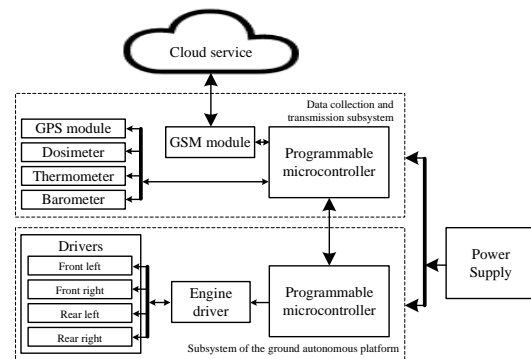


Fig. 1. Block diagram of the designed system.

Unicameral microcomputer Raspberry Pi 3B was used to build the system for collecting, processing and transmitting the accumulated data. The determination of the radiation background level was based on the Geiger counter. This data will be measured and transmitted to the microcontroller and processed according to a certain algorithm. In order to increase the accuracy of the indicators, the average value for

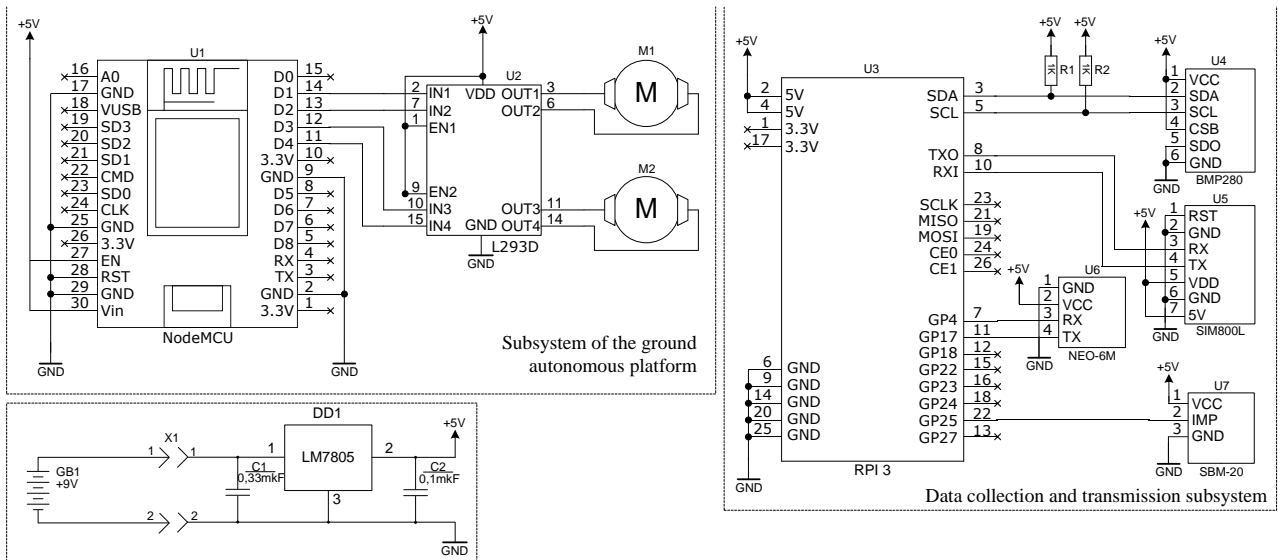


Fig. 2. Electrical schematic diagram of the designed system for determining the level and location of the radiation background

a given time interval will be determined. After processing and accumulating this data, the firmware packs it together with the indicators of other sensors and the coordinates of the current location obtained from the GPS module. The next step is to send the data to the cloud service using the Internet and GSM GPRS module.

Hardware platform was used to build a data movement management system. The control will be carried out either directly by uses of a radio remote control, which can be a normal smartphone, or the platform will be controlled by a pre-programmed algorithm, moving along set route of the study. The developed system consists of the following components: Raspberry Pi unicameral microcomputer, GSM module, GPS module, Geiger counter, temperature and atmospheric pressure sensor, programmable ESP8266 microcontroller - four DC motors, motor drivers.

The data acquisition and transmission subsystem contain all the necessary sensors: thermometer, barometer, GPS module for determining the exact coordinates of the location of the platform and a dosimeter to determine the level of radiation background. The motion control subsystem consists of a set of motors, a power plant required to control the motors (motor drivers) and a microcontroller that will be responsible for moving the platform in space. A separate block is the cloud service, which will provide a user-friendly interface for viewing the accumulated data on the map in the form of labels on a given route.

The electrical schematic diagram of the designed specialized mobile-moving system for determining the level and the location of the radiation background, required for the design of the printed circuit board of the device, is shown in Fig. 2.

To designed the subsystem of the terrestrial autonomous platform Lolin NodeMCU V3 was used, which generates control signals and the power-plant of direct control of engines. Subsystem based on the L293D motor driver chip and two DC motors (Fig. 2). The U2 L293D motor driver has four control pins what are connected to the digital pins D1-D4 with PWM support for the U1 NodeMCU microcontroller. Two pins are responsible for the direction of rotation of each individual engine, and the other two for the frequency of

rotation. The rotational frequency regulated by the level of applied voltage to the control pins by means of PWM.

Two power supply wires were used to connect each of the M1 and M2 DC motors. By changing the polarity of the power supply, the direction of rotation of the motors will be changed, that allowed the platform to move as forward so backward. To control rotation frequency of the motors, it is necessary to reduce or increase the level of voltage applied.

The U3 Raspberry Pi 3B microcomputer was used to build the system for collecting, processing and transmitting the accumulated data to cloud service.

The Internet connection was made by using the GSM module U5 SIM800L, which using GPRS network technology. This module was connected to the microcomputer via the UART interface to the corresponding RXI and TXO ports, ports 8 and 10, respectively. The U6 NEO-6M GPS module connected to the digital pins of the microcomputer via the UART interface was used to determine the current coordinates of the system location.

The U4 and U5 modules are Bosch BMP280 temperature and atmospheric pressure sensors, and the U7 is a cylindrical Geiger meter based on the SBM-20. The BMP280 sensor is connected to the microcomputer via the I2C interface to the corresponding pins 3 and 5, SDA and SCL, respectively. The Geiger counter is connected to the pin 22, which received pulses for counting. The power supply of the designed specialized mobile-moving system for determining the level and location of the radiation background consists of a "crown" battery at 9 V and a voltage regulator LM7805 with capacitors at the input and output.

The PCB was designed in the Sprint-Layout 6.0 software package. The designed and etched printed circuit board with drilled holes and electrical tracks is shown in Fig. 3.

Taking into account the designed mobile-moving system for determining the level and location of the radiation background consists of two functionally complete subsystems, the approach to the implementation of the program code of each of the subsystems will be different.

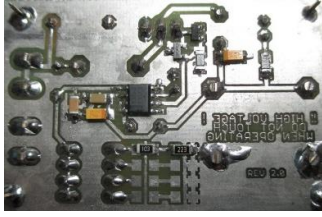


Fig. 3. Designed printed circuit board.

For the development of software, a subsystem control module that is responsible for collecting, processing and gearing accumulated data to a cloud service, a high-level Python programming language with an extremely large open source libraries has been used. This programming language is clear and easy to understand, which allow to quickly master the basic features and learn to reuse ready-made solutions. For the convenience of writing code, we used the PyCharm Community Edition development environment, which is free to download from the official website.

To develop a software for managing a subsystem control of a terrestrial autonomous platform that is responsible for controlling the movement of a mobile-moving agent according to a given area and implements a direct control system, a specialized development environment for the Arduino IDE software for the ARDUINO software-hardware platforms. The algorithm of the mobile-moving system is presented in Fig. 4.

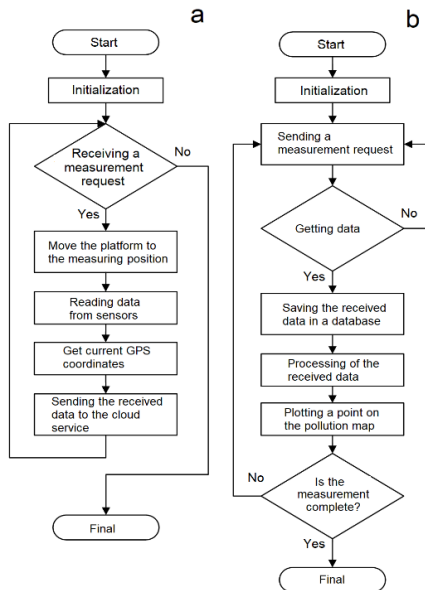


Fig. 4. Graph diagram of the algorithm of mobile measuring platform (a) and cloud service (b).

The principle of operation for a mobile-moving measuring platform. After initialization, the mobile-moving agent enters the state of waiting for the measurement request. Next, when a measurement request is received, together with the coordinates of the desired point, the mobile-moving platform moves in the direction of the desired measurement point, navigating using the built-in GPS module. When the platform has completed its movement, the process of collecting data from all sensors, measuring the radiation background with a built-in dosimeter and obtaining accurate GPS coordinates of the current location begins. The next step is to send the collected data to the cloud service via the Internet using a GSM module that supports GPRS wireless technology. Then

the system goes back to the standby mode of the new measurement requests, reduced energy consumption to a minimum. The system enters standby mode, with a set delay time, and power saving. This process will be cyclic in the presence of supply voltage.

The principle of operation for cloud service. After starting the application on the remote cloud service, the initialization took place. The next step is a request for measurements, which may include GPS coordinates of the desired point, where want to measure the temperature, atmospheric pressure and radiation level. The generated message-request is sent via the Internet to an autonomous mobile-moving platform for data processing. Next, the cloud service goes into standby mode to receive the data from the mobile-moving agent. In case of such data has not been received within the specified time interval, a second request is will be sent. When the data has been received, the received information is unpacked and saved the data to the database. The next step is to process the data with special algorithms for filtering false data in order to reduce the statistical error by filtering the information for the presence of noise. The point on the map of pollution is formed, which shows the measured and processed information about the measured ambient temperature, atmospheric pressure and the level of the radiation background. If the operator decides to complete the measurement, the system switches to energy saving mode. Otherwise, the process is repeated cyclically, until it is possible to generate a request for measurement, and electricity will be supplied.

Coordinates of the current location of the designed mobile-moving platform, the Pynmea2 library has been loaded and installed, which allows to decipher NMEA 0183 protocol - Special protocol of geopositioned data layout. For connected GSM module and accessing the Internet using GPRS Python Library SIM800Modem library was used. Connecting temperature sensors and atmospheric pressure was carried out using Python BMP280 libraries, which provides a user-friendly interface for receiving. To determine the level of radiation background, it is necessary to calculate the number of pulses for a certain period of time. Therefore, the Geiger counter was connected to one of the GPIO ports.

The remoteXY open source library, which was added to the program code of the NodeMCU Lolin module and the cross-platform RemoteXY application installed on the smartphone, is used to control the movement of the platform.

III. IMPLEMENTATION AND STUDY OF THE PLATFORM

In general, the integrated system consists of a movable mechanical platform, which will be moved by four DC motors placed on it by a Geiger counter, GPS and GSM modules, as well as temperature and atmospheric pressure sensors. The appearance of the mobile-moving platform is shown in Fig. 5.



Fig. 5. Assembled mobile platform.

To check the operability of the designed device, it is enough to submit a power supply and the system immediately, after loading and initialization, the specialized system goes into a state of waiting for a request for measurement. Next, when a measurement request is received, the mobile-moving platform begins movement in the direction of the required measurement point, navigated by the built-in GPS module. When the platform is moved, the process of collecting data from all sensors, measuring the radiation background with a built-in dosimeter, and obtaining accurate GPS coordinates of the current location begins.

To control an autonomous platform can be used remote control - a smartphone, using the service RemoteXY. This service allows quickly create a mobile application that can connect directly to the platform via a wireless Wi-Fi network interface or via the Internet. In Fig. 6. shows the required minimum of objects for managing a stand-alone platform.



Fig. 6. Direct control panel.

To test the work of a mobile-moving platform, the necessary mobile application was created, that was connected to the mobile platform via a wireless Wi-Fi network interface. The autonomous platform was controlled using a joystick or G-sensor built into the smartphone. During the test of mobile-moving platform, the correctness of the platform's reaction to the control commands was checked.

The research of the developed platform for assessing the level and location of the radiation background was conducted in a certain area. In general, twelve measurements were made. Each measurement was performed during 30 seconds, which reduced the error level to a minimum. After completing a series of measurements, the system formed a table of collected data in a relational database (Table 1). The results of the study show in Fig. 7.

TABLE I. DATABASE OF MEASURED INDICATORS

No	GPS coordinates	Radiation level, $\mu\text{Sv/h}$	Temperature, $^{\circ}\text{C}$	Atm. pressure, mmHg
1	49.818090. 24.012752	12	6.2	760
2	49.818254. 24.012956	11	6.1	762
3	49.818509. 24.013300	12	6.2	762
4	49.818398. 24.013463	12	6.2	758
5	49.818242. 24.013450	11	6.3	761
6	49.818048. 24.013434	11	6.2	763
7	49.817888. 24.013420	11	6.1	757
8	49.817715. 24.013410	11	6.0	760
9	49.817527. 24.013399	12	6.0	761
10	49.817531. 24.013058	11	5.9	759
11	49.817543. 24.012715	11	6.0	764
12	49.817819. 24.012731	12	5.9	761

The obtained dependences show that the level of radiation background around the studied object is in the range of 11-12

$\mu\text{Sv/h}$, which is a natural radiation background. No radioactive contamination of the territory was detected.

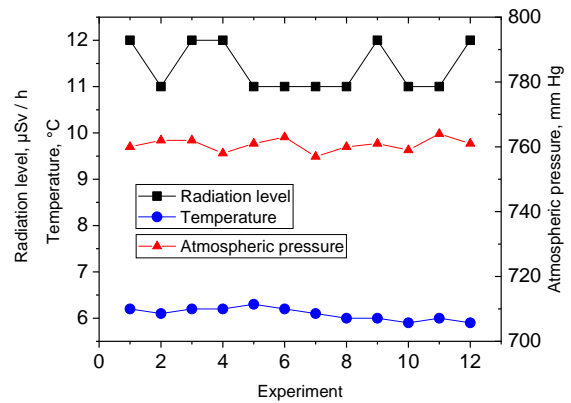


Fig. 7. Graph of dependence of measured indicators.

IV. CONCLUSION

In this work a specialized mobile-moving system for determining the level and location of the radiation background were developed. The efficiency of the system was tested on the model of a research mobile agent based on a wheeled platform. Measuring devices were manufactured using dosimeter based on a microcontroller and a gas discharge tube (Geiger counter), thermometer and barometer. A GPS module was used to determine the exact geological coordinates of the site. The GSM GPRS wireless network technology module was used to build a wireless control system for the autonomous system and transfer the collected data to the cloud service. The simplicity of the components used ensures reliability, ease of implementation and use. An algorithm for the operation of the system and the control program has been developed. Methods of measuring the background radiation in the open were analyzed. The results of this work can be used to design specialized systems of various applications and capacities, replacing only the set of measuring devices installed on the platform. In addition, proposed approaches will be used to design mobile platforms with nanostructured sensors and nanocomposites as protective coatings [5].

ACKNOWLEDGMENT

H. Klym thanks to the Ministry of Education and Science of Ukraine for support (project No. 0119U100435).

REFERENCES

- [1] V.A. Kulikova, V.V. Yakovlev, A.Y. Tumanov, V.A. Tumanov, and A.V. Kulinkovich, "Remote radiation monitoring device," Journal of Physics: Conference Series, vol. 1614, No. 1, pp. 012108, 2020.
- [2] A.H. Zakaria, Y.M. Mustafah, J. Abdullah, N. Khair, and T. Abdullah, "Development of autonomous radiation mapping robot," Procedia Computer Science, vol. 105, pp. 81-86, 2007.
- [3] R.B. Andersonl, M. Pryor, and S. Laondsberger, "Mobile robotic radiation surveying using recursive bayesian estimation," 15th International Conference on Automation Science and Engineering (CASE), pp. 1187-1192, 2019.
- [4] A. Holovatyy, V. Teslyuk, N. Kryvinska, and A. Kazarian, "Development of microcontroller-based system for background radiation monitoring," Sensors, vol. 20(24), pp. 7322, 2020.
- [5] I. Karbovnyk, I. Olenych, O. Aksimentyeva, H. Klym, O. Dzendzelyuk, Y.Olenych, O. Hrushetska. "Effect of radiation on the electrical properties of PEDOT-based nanocomposites." Nanoscale Reseach Letters, vol. 11, pp. 84, 2016.

Prediction of GNSS Horizontal Navigation System Error (HNSE) using Artificial Neural Networks

1st Krzysztof Paczuski

Faculty of Electronics and Information Technology
Warsaw University of Technology
Warsaw, Poland
01124575@pw.edu.pl

2nd Mikołaj Kowalczewski

Faculty of Electronics and Information Technology
Warsaw University of Technology
Warsaw, Poland
01121768@pw.edu.pl

3rd Karolina Krzykowska-Piotrowska

Faculty of Transport
Warsaw University of Technology
Warsaw, Poland
ORCID: 0000-0002-1253-3125

Abstract—Artificial neural networks are a huge achievement in the field of computer science. Thanks to them, it is possible to solve simple problems, as well as those in which finding a complete mathematical model is difficult or impossible. They can find dependencies between data and, as a result, predict one data from others with a certain accuracy. In addition, the huge availability of various powerful libraries responsible for creating and testing neural networks allows you to use their benefits in many problems.

Index Terms—prediction, HNSE, GNSS, ANN

I. INTRODUCTION

The aim of the project is to develop an effective way to navigate for a companion robot - an autonomous machine that helps people in their daily activities. Considering the situation when such a robot will have to move around an area unknown to it, satellite navigation seems to be the best solution.

The commercially available GNSS navigation is one of the basic tools for determining the position, but its accuracy is not perfect. Many factors, such as solar activity, humidity, temperature or pressure may disturb the signal sent from the navigation satellites, which will result in the calculation of a slightly different location than it actually is. In some areas, such as sea navigation, aviation sector, geodesy and many others, too large errors are unacceptable, so special systems are used to correct them. An example would be the EGNOS service. EGNOS uses GNSS measurements taken by accurately located reference stations deployed across Europe. Measured GNSS errors are transferred to a central computing centre, where differential corrections and integrity messages are calculated and then they are broadcast over the covered area using geostationary satellites that serve as an augmentation, or overlay, to the original GNSS message. Thanks to the amendment, these devices will know how to scale the received signal to make the calculated location more accurate.

EGNOS is a very convenient solution, but what if these satellites are not available? You cannot risk an autonomous robot miscalculating its location suddenly step onto a road.

For this purpose, an additional method for determining GNSS signal correction should be developed. Knowing what publicly available parameters have a significant impact on the accuracy of satellite navigation, an artificial neural network can be taught to predict errors from these parameters.

This is what the following article is devoted to - development of a neural network that allows for the best possible prediction of errors in satellite navigation signals based on publicly available parameters such as: cloudiness, humidity, precipitation, average temperature, pressure, number of sun-pods and number of visible satellites.

II. SATELLITE SYSTEMS

The operational limitation of satellite systems usage can be caused by various errors that are inherent in the operation of these systems. In general, errors in satellite systems can be divided into four groups: signal propagation errors (ionospheric errors, tropospheric errors, multipath errors); relativistic errors; system operation errors (satellite ephemeris errors, satellite clock errors); receiver errors, including DOP (Dilution of Precision) [1].

GNSS augmentation systems are susceptible to the influence of different errors. Changes in the ionosphere or troposphere can cause local or regional delays that cannot be corrected in real time. Such cases are rare and the likelihood of their occurrence varies by region, but cannot be excluded. As a result, errors which arise may distort information and should be taken into account at the system design stage. Determining the requirements for the parameters of the satellite signal and the implementation of augmentation systems are the key processes for introducing satellite navigation. In Europe, the turning point in this activity was launch of the SBAS - EGNOS (Satellite Based Augmentation System - European Geostationary Navigation Overlay Service) system. It was also time of reaching a milestone in Poland in implementing procedures based on GNSS navigation [3], [6].

The EGNOS system is an European GPS and GLONASS augmentation system in field of air, maritime and road transport. It was designed by the ETG (European Tripartite Group) group, which includes: the European Space Agency ESA, the European Commission EC and the European Organization for the Safety of Air Navigation EUROCONTROL. The aim of EGNOS is to monitor the integrity of GPS and GLONASS and to increase their accuracy by introducing data corrections [5]. The principle of operation is based on the reception of GNSS signals by ground reference stations. The EGNOS terrestrial segment includes, among others, RIMS (Ranging and Integrity Monitoring Stations) stations. RIMS can be analyzed in terms of the channels constituting them (A, B, and C). Data from channel A is used to calculate data needed for EGNOS messages. Data from the B channel is used to verify the message calculated from the A channel. Data from the C channel is to detect errors in the signal provided by the GNSS satellites. The task of RIMS is to collect data from GNSS satellites and verify them. By dividing RIMS stations into three channels, the EGNOS data waveform is presented in two separate but related cycles, which according to the minimum fault warning requirements should take a total duration of no more than 6 seconds. The first cycle is the processing cycle. It uses only channel A. The course of this cycle consists of measuring the pseudorange to the satellites through the antennas and receivers of the A channel of the RIMS station, then transmission of the received data to the MCC (Mission Control Center) cell: CPF (Central Processing Unit), then generating corrections, integrity information and the entire navigation message that is sent by the NLES (Navigation Land Earth Stations) stations to the EGNOS geostationary satellites. The second cycle is the checking one. The B and C channels are used in here. Data collected by RIMS antennas and receivers from EGNOS satellites and other navigation satellite systems are sent to the MCC-CPF cell. In the CPF, these data are checked and verified for accuracy, correctness, truthfulness and integrity of information. In case of detection of an error in emitted information, the so-called alarm flag informing system recipients of an error or failure is sent [2].

Accuracy for EGNOS is that is, the error of the determined position; in GNSS it is the difference between the designated and actual position; for the designated position, the probability should be at least 95% - then the measurement error is within the established accuracy. The requirements for accuracy show that for a large set of independent samples, at least 95% of them should meet certain requirements (given in meters for each type of satellite system). Such accuracy must be met with respect to the worst geometry of the satellite constellation for which the system is to be available. Note that position errors, for example in the case of GPS, consist of satellite clock errors and ephemeris errors. They do not include ionospheric or tropospheric delays, multipath errors, or receiver own noise. The latter are always included in receiver standards [4].

Owing to the measurements of the EGNOS satellite system signal carried out by, among others, the Polish Air Navigation Services Agency, it is possible to analyze this signal

on the basis of its parameters every day. The agency uses a specialized receiver (Septentrio PolaRx3) and appropriate software (PEGASUS 4.7.5.) that can decode the EGNOS data. PEGASUS, developed for research purposes, determines the difference between position identified by the EGNOS system and known position of the EGNOS receiver. It is then possible to obtain a positioning error and a number of other important quantities. This software was developed to test performance of SBAS and GBAS (Ground Based Augmentation System) systems in the first place. For each of the geostationary satellites, PEGASUS automatically generates a report once a day.

The analysis and interpretation of PEGASUS reports is particularly important for the purposes of this article. In the conducted researches the data from 2014 for the EGNOS PRN120 and PRN126 satellites operating in this period were used.

III. ARTIFICIAL NEURAL NETWORKS

Artificial Neural Networks are mathematical models that imitate neural networks in human brain to solve, e.g., complex, nonlinear problems [7]. The human brain has billions of interconnected neurons [8]. Each neuron consists of cell body, dendrites, axon and synapses. Neurons pass signal to other neurons after being activated by chemical processes. The chemical signal is passed through the axon which is ended with multiple synapses. Axon synapses are connected to other neuron dendrites which can viewed as an inputs to the neuron. If the input stimulus is strong enough, an action potential appears and a neuron sends information down an axon away. Changes in cell polarization result in the signal being propagated down the length of the axon.

The action potential is always a full response. There is no intermediate action potential. Instead, it is an all-or-nothing process. This minimizes the possibility that information will be lost along the way. The pulse is transmitted by changing the electric potential between the inside of the cell and its surroundings, which is maintained by the active transport of calcium and potassium ions. As a result, the nerve cell has a limited activation period. In result in some types of neurons, the entire up-and-down cycle takes place in a few thousands of a second. [7], [8].

ANN's can solve problems to which they have been built after a training process. During training, weights for connections between nodes are constantly updated to better match the requested output for given input to the network.

Artificial Neural Networks are widely used for problems such as classification, pattern recognition, prediction [9].

A. Classification

Classification problem is defined as a problem of finding for unknown object a class to which this data object belong. Typically, the process of classification is to match unknown entity against features of known classes [10], e.g., determine whether input image displays a dog or a cat.

TABLE I
TABLE OF PARAMETERS

Parameter	Value
Number of inputs	7
Number of outputs	1
Number of hidden layers	5
Activation function	ReLU for hidden layers Linear for output
Neurons in each layer	128
Training algorithm	Adam
Size of Training set	1042
Size of Testing set	1042
Number of epochs	700

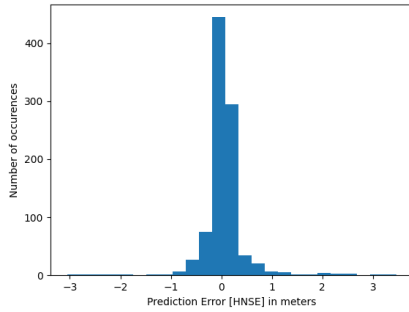


Fig. 1. Histogram of position error (HNSE) Best model

B. Pattern recognition

Pattern Recognition is a field of science to correctly describe and classify object to correspond classes by automatic discovery of regularities in data [11]–[13].

C. Use in this article

We have used ANN as they allow to predict HNSE values based on multiple input values such as meteorological conditions in real-time without the need to calculate mathematical complex formulas. Therefore, trained model can be implemented in all type of devices which lack of computational power and need to reduce GNSS error to correctly calculate position, e.g., autonomous robots.

IV. NEURAL NETWORK MODEL

In this paper a Deep Neural Network that consist of five fully connected hidden layers have been proposed. Each of the hidden layer has 128 neurons and ReLU as an activation function. The input to the network consist of seven neurons, namely cloudiness, humidity, precipitation, average temperature, pressure, number of sunpods and number of visible satellites. Neural Network has only one output neuron which is the predicted HNSE value. For this neuron we used linear function as an activation function. For the optimizer and loss function Adam has been chosen with learning rate of 0.001 and Mean Absolute Error.

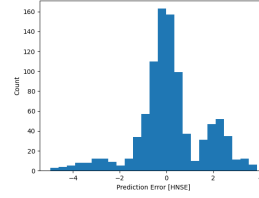


Fig. 2. Histogram of position error (HNSE) Model 1

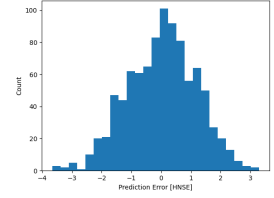


Fig. 3. Histogram of position error (HNSE) Model 2

A. Data

Data-set used for training contained 1042 records of measurements. Measurements took place in four polish cities: Warsaw, Cracow, Poznan and Rzeszow and were held for nearly a whole year. For each day for every city one record has been saved. For some cities, measurements have not been recorded for every month.

Each record contains multiple measurements. Measured values are: cloudiness, humidity, precipitation, average temperature, minimum and maximum temperature, pressure, number of sunpods, number of visible satellites, HNSE and satellite's availability for APVI PRN120 and APVI PRN126 satellites.

B. Data preparation

Before feeding Neural Network with data all records that might have negative impact on the training process and in summary on the trained model have been removed. Therefore, all records for which satellites availability was lower that 0.99 have been removed. Due to lack of information when during the day the measurements were held daily minimum and maximum temperatures had to be removed and it has been decided to kept only daily average temperatures. After removing unnecessary records input values have been normalized to values within [0,1] range. To accomplish this min-max transformation was used as a scale function. The transformation is given by following equation:

$$X_{transformed} = (X - X_{min}) / (X_{max} - X_{min}) \quad (1)$$

where $X_{transformed}$ is a input vector of values to normalize, X_{min} and X_{max} are the minimum and maximum of values.

Equation (1) has been applied to all values taken as an input values to the Neural Network.

C. Training and Validation sets

Resulting data-set after reduction and normalization contains 939 records. Training Neural Networks requires to have test data-set to check whether results are acceptable and also a validation set. Due to the fact that resulting data-set had small number of records and each record consisted of measured HNSE values for two different satellites first satellite's calculated HNSE value has been used as a training set and the other satellite's HNSE as a validation and test sets. This enabled using whole data-set for training. The training

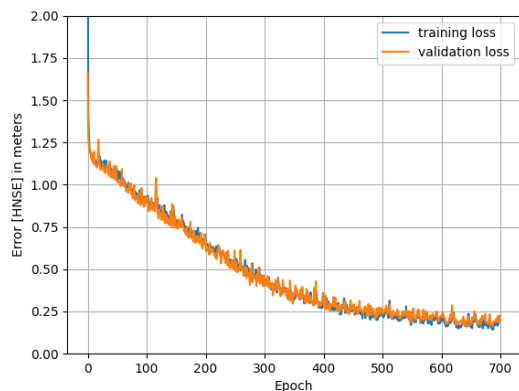


Fig. 4. Loss value during training for both validation and train sets

was split into 700 epochs and the training set was shuffled before training.

D. Results

Deep Neural Network model proposed in section IV has been chosen in trials. Three different training algorithms have been tested namely Stochastic gradient descent (SDG), Levenberg–Marquardt (LM), RMSprop and Adam. To differentiate and calculate performance between algorithms Mean absolute error metric has been used. LM algorithm that was valued as best performing algorithm in literature [14]. In this case it was found out that this method under-performed compared to the other algorithms that have been tested. Additionally, to the training algorithm, multiple network structures and activation functions namely ReLU and Sigmoid have been tested. The optimal structure was found to be five hidden layers with 128 neurons for each hidden layer and ReLU as an activation function. Fig. 1 represents error between predicted HNSE value on test data and actual HNSE value measured for satellite APVI PRN126. This shows that for more than half of the records in test set, HNSE value have been predicted with error between $[-0.5, 0.5]$ meters. Fig. 4 shows how loss function was changing during training for training and validation sets. Blue curve represents change in loss value for training set and orange curve for validation set. Flattening of both curves starts near 600 epoch which means that the training is not progressing since that epoch. Loss value stops near 0.25 meter for both validation and training sets which is calculated as a mean absolute error between predicted value and measured value and is a satisfactory result.

Fig. 2 and fig. 3 show histogram for HNSE prediction error for test data for other test models. Fig. 2 shows a model with similar structure as the best model, however, ReLU activation function for hidden layers was exchanged with Sigmoid activation function. Model for fig. 3 LM algorithm was used for training. Remaining parameters for this model remained the same. Those histograms shows that for those trained models error for most of records is between $[-2, 2]$

meters. In can be concluded that those results are inferior to results retrieved for model proposed at the beginning of this section.

V. SUMMARY

Multiple algorithms and different Artificial Neural Networks structures have been tested to accurately predict HNSE value. Results showed that for seven input values namely cloudiness, humidity, precipitation, average temperature, pressure, number of sunpods and number of visible satellites, network with five hidden layers composed of 128 neurons each with Adam optimizer gives the most promising results. The aim of this study was to show that is it possible to accurately predict HNSE value using meteorological conditions with help of ANN. Furthermore, this showed that is it possible to achieve satisfactory results using relatively small training set which consisted of nearly thousand of records.

ACKNOWLEDGMENT

Research was funded by the Centre for Priority Research Area Artificial Intelligence and Robotics of Warsaw University of Technology within the Excellence Initiative: Research University (IDUB) programme (Contract No. 1820/29/Z01/POB2/2021).

REFERENCES

- [1] Siergiejczyk, M.; Krzykowska, K.; Rosiński, A. "Evaluation of the influence of atmospheric conditions on the quality of satellite signal. Marine Navigation and Safety of Sea Transportation" 2017, Eds: Adam Weintrit, CRC Press Taylor&Francis Group. <https://doi.org/10.1201/9781315099132>
- [2] European Space Agency. (2021). EGNOS Fact Sheet. Available: march 2021. www.egnos-pro.esa.int
- [3] Tossaint, M.; Samson, J.; Toran, F.; Ventura-Traveset, J.; Hernandez-Pajares, M.; Juan, J.M.; Sanz, J.; Ramos-Bosch P. "The Stanford – ESA Integrity Diagram: A New Tool for The User Domain SBAS Integrity Assessment." Navigation-Journal of The Institute of Navigation 2014, 54(2). <https://doi.org/10.1002/j.2161-4296.2007.tb00401.x>
- [4] Krzykowska, K.; Krzykowski, M. "Forecasting Parameters of Satellite Navigation Signal through Artificial Neural Networks for the Purpose of Civil Aviation." International Journal of Aerospace Engineering 2019. <https://doi.org/10.1155/2019/7632958>
- [5] Aguilera, C.; Lorenzo, J. M. "EGNOS in aviation: strategy and implementation status." EGNOS Service Provision Workshop; 2017; Athens.
- [6] Bijjahalli, S.; Ramasamy, S.; Sabatini, R. "A GNSS Integrity Augmentation System for Ground Vehicle Operations." Energy Procedia 2017, 110, pp. 149-155. <https://doi.org/10.1016/j.egypro.2017.03.120>
- [7] Graupe, D.; "Principles of artificial neural networks". World Scientific, vol. 7, pp. 1–8, 2013.
- [8] Abraham, A.; "Artificial neural networks. Handbook of measuring system design.", 2005.
- [9] Abiodun, OI; Jantan, A.; Omolara, AE; Dada, KV; Mohamed, NA; Arshad H.; "State-of-the-art in artificial neural network applications: A survey". Heliyon. 2018 Nov 1;4(11):e00938.
- [10] Clancey, WJ.; "Classification problem solving. Stanford, CA: Stanford University"; 1984 Aug 6.
- [11] De Sa, JP Marques. "Pattern recognition: concepts, methods and applications". Springer Science & Business Media, 2012.
- [12] Liu, J.; Sun, J.; Wang, S.; "Pattern recognition: An overview." IJCSNS International Journal of Computer Science and Network Security, 6(6), 2006, pp. 57–61.
- [13] Bishop, Christopher M.; "Pattern recognition and machine learning". springer, 2006, pp. 1–5
- [14] Mohammednour, A. B.; Özdemir, A. T.; "GNSS positioning accuracy improvement based on surface meteorological parameters using artificial neural networks" Int J Commun Syst. 2020; e43731

Impact of thermal shielding on heating efficiency of SiC in single mode microwave resonant cavity

Stanislav Cichon
Institute of Physics
Czech Academy of Sciences
Prague, Czech Republic
cichon@fzu.cz

Jan Machac
Faculty of Electrical Engineering
Czech Technical University in Prague
Prague, Czech Republic
machac@fel.cvut.cz

Abstract—Microwave heating of a susceptor in the form of SiC disc was simulated in a single mode resonant cavity. The microwave applicator consisted of a waveguide of rectangular cross section WR340 excited by dominant TE₁₀ mode at the industrial frequency 2.45 GHz. Heating efficiency was investigated in two principal configurations represented by 1) an exposed susceptor and 2) a susceptor surrounded with thermal shielding in the form of three coaxial tubes of microwave transparent ceramics. It was found that a relatively high value of the real part of dielectric permittivity of the insulation ceramics leads to a non-negligible modification of the field pattern inside the cavity. This could significantly improve heating efficiency. Consequently, for the design of an efficient microwave applicator, actual sample as well as insulation geometry and dielectric properties should be highly regarded. The analysis has been supported by experiment.

Keywords—microwave heating, single mode resonator, heating efficiency, silicon carbide

I. INTRODUCTION

Microwave energy is used in increasingly more and more areas of technology for its outstanding performance and efficiency [1-5]. With regard to heating applications, it is volumetric, targeted and fast. High temperature microwave applicators, which are employed for instance for ceramics and metal sintering, solid state syntheses or glassmaking, often comprise heat shielding for the sake of efficiency and temperature homogeneity. The heat insulation mostly takes form of assemblies of refractory bricks, wool and other vessels with very low dielectric loss surrounding the sample. Often compounds of Al₂O₃ and or SiO₂ are used as heat insulation materials [1,5]. They fulfill the following conditions with respect to application for microwaves: low thermal conductivity, high melting point, very low loss and chemical durability.

SiC is an extremely common microwave susceptor [1, 3, 5]. It is used in “low” temperature technology in the form of a reaction vessel in organic syntheses. On the other hand, ceramics sintering is an example of its high temperature application.

This study models and analyses behavior and effect of heat insulation during high temperature processing of SiC inside a single mode cavity. In fact, computational treatment of high temperature microwave processing usually puts main focus to the sample while sample support and heat insulation elements are simplified. It is shown that more precise definition of the insulation should provide more realistic results.

II. MICROWAVE APPLICATOR

The applicator for microwave heating is in the form of a single mode resonator. The system is fed through the waveguide of rectangular cross section with metallic walls

WR340 by dominant TE₁₀ mode at the industrial frequency 2.45 GHz. The resonator sketch is shown in Fig. 1. The waveguide is terminated by a sliding short used to match the structure to get maximum power lost in the heated disc. The applicator consists of a quartz glass tube inserted into a vertical waveguide of circular cross section. The tube separates the sensitive parts of the microwave system from the working volume. The vertical waveguide is at 2.45 GHz under cut-off as the cut-off frequency for its diameter equal to 50 mm is 3.5 GHz assuming waveguide filled by air.

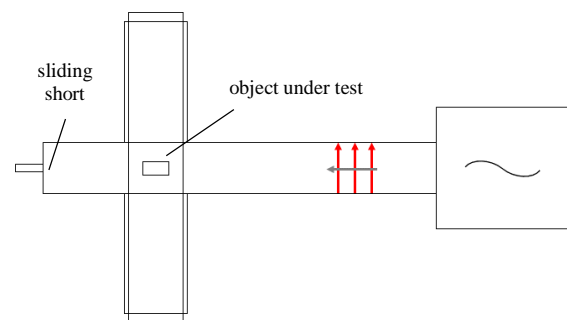


Fig. 1 Sketch of single mode resonator. Details of the sample position are presented in Fig. 2.

Dimensions of the heat insulation were selected such that the entire diameter of the vertical waveguide is utilized. Hence, it was possible to apply three concentric tubes in total making a very potent heat insulation hindering heat loss by radiation and convective transport. In result, the insulation assembly could accommodate a sample with 15 mm diameter.

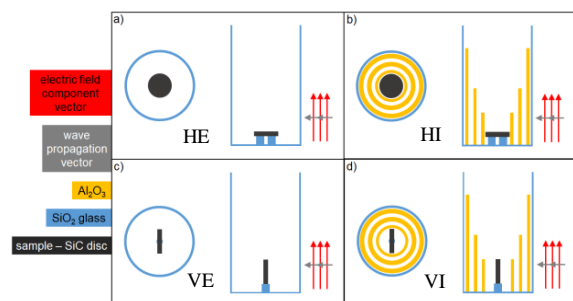


Fig. 2 Scheme of two experimental configurations and two sample orientations in single mode resonator; (a) horizontal placement in exposed configuration, further abbreviated as HE, (b) horizontal placement with thermal insulation – HI, (c) vertical placement in exposed configuration – VE, (d) vertical placement with thermal insulation – VI. Red arrows show the electric field intensity orientation originating from the TE₁₀ mode feeding the structure through the waveguide of rectangular cross section. Images lie in x-z plane.

Discs composed of hexagonal SiC are used as samples to be heated. Dielectric properties of SiC were taken from [6]. Real part of relative permittivity is equal to 9.66, loss tangent is equal to 0.1. These values correspond to a lower temperature regime of operation. Temperature dependence is not considered. The SiC disc is inserted into the cavity in two principal positions: horizontal position and vertical position, see Fig. 2.

III. ANALYSIS

Analysis of the single mode resonator shown in Fig. 1 was performed by the Computer Simulation Technology Microwave Studio (CST MwS) [7]. The feeding port is the waveguide port at the waveguide of the rectangular cross section. The ends of the vertical waveguide of circular cross section are in the model again terminated by waveguide ports. The analysis is performed without taking into account accompanied thermal effects. The performed analysis gives as result the value of power lost due to thermal losses in the SiC disc. This power represents only a normalized value corresponding to the normalized amplitude of feeding TE₁₀ mode in the waveguide port. The power is calculated as

$$P = \frac{1}{2} \iiint \omega \epsilon_r'' \epsilon_0 |E|^2 dV, \quad (1)$$

where ω is angular frequency, $\epsilon_r'' \epsilon_0$ is product of imaginary part of relative permittivity and permittivity of vacuum, E is electric field intensity, integration is performed over the SiC disc volume. The integral in (1) is calculated by the CST MwS. The imaginary part of relative permittivity is defined by the loss factor $\tan \delta_e$ or by material conductivity σ

$$\epsilon_r'' = \epsilon_r \tan \delta_e = \frac{\sigma}{\omega \epsilon_0}. \quad (2)$$

Load matching optimization, in the form of adjusting waveguide length (sliding short) and sample position in the vertical sense, have been performed in several iterations such that maximal losses in the sample have been found.

Fig. 3 shows the calculated distribution of electric field vector across the structure with the horizontal position of SiC disc, see Fig. 2a,b. In HE arrangement, Fig. 3a, the simulation shows that the electric field vector is oriented vertically. Due to boundary condition, the electric field inside the disc is perpendicular to the disc base and is ϵ_r times lower than outside, where ϵ_r is SiC permittivity (9.66). Here, the power loss in the SiC disc is equal to 0.000898 W. However, in HI arrangement, Fig. 3b, it is obvious that the original vertical orientation of the electric field becomes altered. Within the sample and its vicinity, the field becomes oriented horizontally. This leads to a large proportion of the sample surface aligned with the electric field. In this case the boundary condition dictates a high intensity of the field (equal to the field out of disc) and thus high power absorption. The power loss is equal to 0.001660 W.

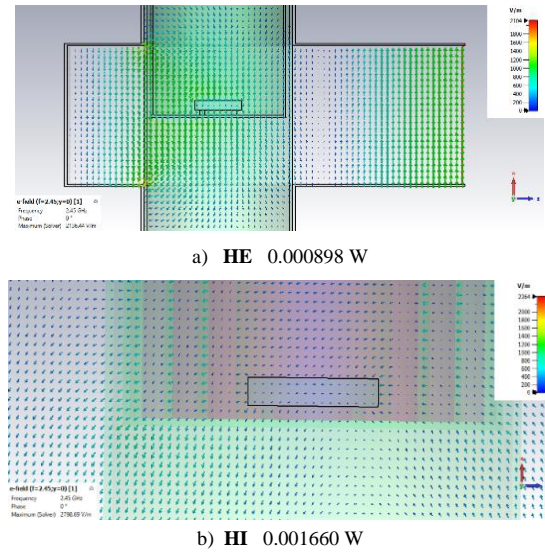


Fig. 3 Distribution of the electric field intensity in the volume of the resonator in the x-z plane; (a) HE, (b) HI.

For the vertical disc position, VE, VI, see Fig. 2c,d, the resulting situation is different, see Fig. 4. In VE arrangement, the electric field vector is parallel to the disc bases, therefore its maximum is inside the SiC material. The power loss for this arrangement is equal to 0.006580 W. In VI arrangement, the field distribution is nearly the same as for the VE arrangement in terms of the field pattern in the sample and the sample vicinity. However, it must be pointed out that load matching and high resonance state in VI arrangement are not achieved until an optimal sample vertical position is found. This particular position is more upwards in comparison with other arrangements. The power loss is equal to 0.002610 W.

There is obvious another effect of the insulation. In the horizontal sample placement (HI), presence of the insulation leads to rotation of the electric field vector in the sample vicinity by $\sim 90^\circ$. On the other hand, when the sample is oriented vertically (VI), there is no such a rotation.

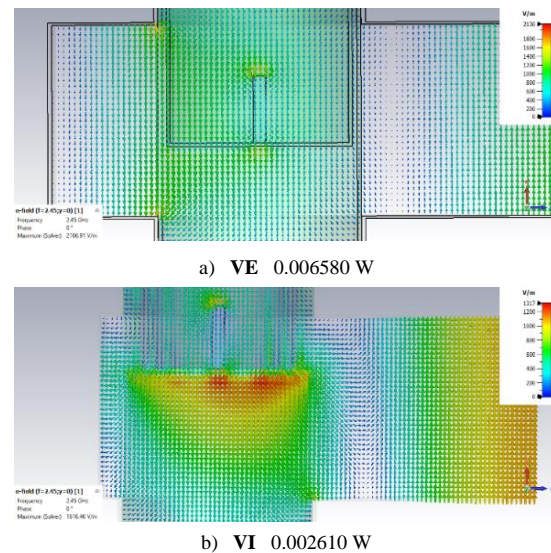


Fig. 4 Distribution of the electric field intensity in the volume of the resonator in the x-z plane; (a) VE, (b) VI.

The key cause of the above presented results lies in the relatively high permittivity of Al_2O_3 , $\epsilon_r \sim 10$ [5]. A microwave field passing through a mass of Al_2O_3 becomes deflected. The heat insulation consists of three layers of Al_2O_3 vessels separated by air gaps and so the degree of the deflection becomes significant. The reason for this is the behavior of electric field on the surface of a high permittivity dielectric material that to some extent copies the surface of a well conducting material where the electric field vector is perpendicular to this surface.

Comparison of power losses shows that the highest heat generation is realized at the sample vertical exposed arrangement (VE) while the horizontal exposed arrangement (HE) results in roughly 7 times smaller loss. This has been found to be caused by a strong geometrical dependence in the interaction of the sample and the field. Power losses in arrangements comprising heat insulation are roughly in the middle of the above two. The heat insulation improves the heat distribution in the sample and minimizes thermal losses. The influence of the thermal insulation significantly improves the homogeneity of the electric field intensity distribution in the studied structure HI and therefore the homogeneity of the resulting temperature distribution. Fig. 5 presents the field distribution displayed in x-y plane for the case of sample in HI arrangement.

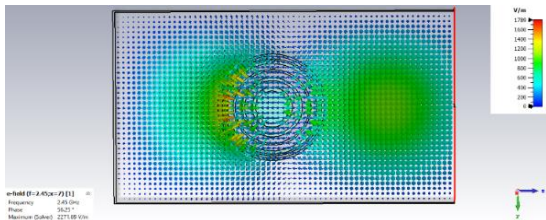


Fig. 5 Distribution of the electric field intensity in the volume of the resonator in the x-y plane; HI arrangement. The plot shows the homogeneous field distribution.

IV. EXPERIMENTAL RESULTS

Experiments were performed with feeding power load up to 800 W. Sample surface temperature was measured with a MICRO-EPSILON ratio pyrometer operating in the temperature range $650^\circ\text{C} - 1800^\circ\text{C}$ at the wavelength of $1 \mu\text{m}$. Optimal load matching for the lowest reflected power was attained by adjustment of the position of the sliding short, sample vertical position and triple stub tuner connected between the microwave generator and the resonator (not shown in Fig. 1).

Experiments were pursued in the HE and HI arrangements. A sufficient temperature increase of the sample, i.e. over 650°C , being the low temperature limit of the pyrometer, was attained from 200 up to 300 W of feeding power. Actually, below feeding power equal to 200 W, most of the power was reflected from the resonator. Results are summarized as a plot in Fig. 6.

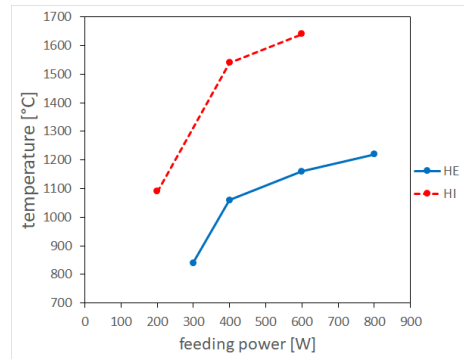


Fig. 6 Plots of temperature – power curves for heating experiments.

Experimental results show that the sample with heat insulation indeed reached significantly higher temperatures in comparison with the exposed sample. This justifies results of performed analysis shown in Fig. 3.

The expression (black body radiation)

$$P = e\sigma_{\text{SB}}A(T_{\text{sample}}^4 - T_{\text{surroundings}}^4) \quad (3)$$

was employed for assessments of heat loss by radiation where P stands for total radiated power, e for sample emissivity taken to be equal to 1, σ_{SB} represents Stefan-Boltzmann constant ($5.670374419 \times 10^{-8} \text{ W m}^{-2} \text{ K}^{-4}$), A is sample surface (disk of diameter equal to 15 mm, and 1.5 mm in height) and T is temperature in Kelvin [8]. For input power equal to 600 W (3) gives $T_{\text{HE}} = 1160^\circ\text{C}$, $T_{\text{HI}} = 1640^\circ\text{C}$, and the corresponding radiated powers are $P_{\text{HE}} = 118 \text{ W}$ and $P_{\text{HI}} = 375 \text{ W}$. These powers represent the thermal radiation from SiC disk, and they should be in the equilibrium state equal to the powers lost in the SiC disk (1). Their ratio is 3.18 that does not correspond to the ratio of the powers calculated by the CST MwS, see Fig. 3. Numerical analysis described in the previous paragraph resulted in powers determined by (1) equal to 0.000898 W for HE, and 0.001660 W for HI. The ratio of these values is 1.85 that is lower than the ratio of powers P_{HE} and P_{HI} . Formula (3) takes into account only radiation of thermal energy, not energy guided, and other effects as the influence of thermal shielding. Therefore it is not simple to compare values P_{HE} and P_{HI} with the powers calculated in the previous paragraph by (1) where only normalized amplitudes of exciting dominant TE_{10} mode have been used. The dependence if SiC permittivity on temperature is not taken into account.

V. CONCLUSIONS

The paper theoretically investigates behavior of thermal shielding in a single mode resonant cavity for microwave heating experiments. The shielding comprises three coaxial Al_2O_3 tubes representing typical microwave transparent refractory ceramics employed as heat insulation of a SiC sample. Presence of the thermal shielding results in an alteration of the field distribution due to a relatively high value of ϵ_r of Al_2O_3 . This has consequences for power losses in the sample. The highest heat generation can be achieved without thermal shielding but sample geometry plays an important role. With the shielding present, heat generation decreases but is still favorable and the effect of sample geometry is less important. However, it is understood that the total heating efficiency is superior with heat insulation as it inherently slows down heat flow out of the sample.

It is evident that a practical realization of an efficient microwave heating system should regard actual sample as well as insulation geometry and dielectric properties.

For better agreement of results, some calibration of the performed experiment and of the numerical analysis must be used. The application of the black body radiation is not straightforward.

REFERENCES

- [1] H. J. Kitchen, S. R. Wallace, J. L. Kennedy, N. Tapia-Ruiz, L. Carassiti, A. Harrison, A. G. Whittaker, T. D. Drysdale, S. W. Kingman, D. H. Gregory, "Modern Microwave Methods in Solid-State Inorganic Materials Chemistry: From Fundamentals to Manufacturing," *Chemical Reviews*, 114, pp 1170-1206, 2014.
- [2] J. Haala, W. Wiesbeck, "Modeling Microwave and Hybrid Heating Processes Including Heat Radiation Effects," *IEEE Transactions on Microwave Theory and Techniques*, vol 50, No. 5, pp. 1346-1354, May 2002.
- [3] S. Tamang, S. Aravindan, "3D Numerical Modelling of Microwave Heating of SiC Susceptor," *Applied Thermal Engineering*, 162, 114250, 2019.
- [4] J. Sun, W. Wang, Q. Yue, "Review on Microwave-Matter Interaction Fundamentals and Efficient Microwave-Associated Heating Strategies, *Materials*," 9, 231, 2016, doi:10.3390/ma9040231
- [5] M. Bhattacharya, T. Basak, "A review on the susceptor assisted microwave processing of materials", *Energy*, 97, pp 306-338, 2016.
- [6] T. A. Baeraky, "Microwave Measurements of the Dielectric Properties of Silicon Carbide at High Temperature," *Egypt. J. Sol.*, Vol. 25, pp. 263-273, 2002.
- [7] CST Microwave Studio, <https://www.3ds.com/products-services/simulia/products/cst-studio-suite>, <https://www.3ds.com>
- [8] R. D'Ambrosio, A. Cintio, A. Lazzeri, G. Annino, "Design of an overmoded resonant cavity-based reactor for ceramic matrix composites production", *Chemical Engineering Journal*, Vol. 405, 126609, 2021.

Human exposure to mobile phone EMF inside shielded space

1st Mariana Benova
*Department of Electromagnetics and
Biomedical Engineering
FEEIT, University of Zilina
Zilina, Slovak Republic
mariana.benova@feit.uniza.sk*

2nd Milan Smetana
*Department of Electromagnetics and
Biomedical Engineering
FEEIT, University of Zilina
Zilina, Slovak Republic
milan.smetana@feit.uniza.sk*

3rd Andrea Cikaiova
*Hospital of Zilina
Zilina, Slovak Republic
acikra@centrum.sk*

Abstract— The measurements of human exposure to electromagnetic (EM) field by mobile phone inside different shielded spaces is presented and discussed in this paper. The obtained values of electric field strength and power density of EM radiation were compared to the limits for human safety general purposes and regulations. The measurements were performed in those cases where people were exposed to long-term EM field generated by the cell phones during ongoing phone call via Safe and Sound Pro II professional EMF measuring device.

Keywords — *electromagnetic field, railway, cell phone, modelling and simulation of electromagnetic field, measurements*

I. INTRODUCTION

Mobile phones are a common part of a person's daily life and we are often unaware of their use, so their connection with human health is also an important global issue due to EM radiation. The International Commission on Nonionizing Radiation Protection (ICNIRP) sets a limit of exposure for human safety purposes of EM fields [1]. Those limits for devices of wireless communication have been determined based on the wireless device purpose and universally with an open space considering, e.g., an office environment or a home. However, in more compound surroundings, such as automobile applications [2]; [3] or a railway vehicle [4] is the situation more difficulted for use of any wireless devices. Their frames have the metallic blocks of cubical frame form with irregular boundaries. Generally, the EM field reflection and scattering effect close to metallic walls have been identified which could modify the values of EMF characteristics significantly [4] - [7]. The values obtained by researchers have shown that the EM field strength inside the enclosed space is more intense by reason of the resonance effect, scattering and reflections of EM fields from the walls with the increasing these values by comparing with the free space [7]. The sensitivity of usage models is significant.

The aim of this study is to measure and analyze values of electric field strength E [V/m] and power density of EM radiation PD [W/m²] relatively close to the human body due to active mobile phone within different shielded and unshielded environment. In the first case, a human body is under exposure of the cell phone with ongoing phone call, and it is located inside the shielded space, (the cellar), in the car, in the railway and in the elevator, respectively. The device that is used for the measurements is Safe and Sound Pro II measuring instrument. We have also realized the measurements of those EM field values that were presented in the open area, for comparison of the obtained results for

both different conditions of boundaries, and finally, to compare these results with the official limits for the human body safety purposes.

II. MEASURING DEVICE AND SOURCE OF EMF

The Safe and Sound Pro II measuring device 9ci SaS Pro II RV: 02/2020 [8] is a sensitive metering device, which can measure potentially harmful RF or microwave radiation from any continuous or pulsed digital sources. To help identify these various sources, the Safe and Sound Pro II includes a built-in speaker with adjustable volume levels. It has a true ± 6 dB response from 400 MHz - 7.2 GHz and a full frequency response from 200 MHz - 8 GHz •ability to detect very short pulses ($< 5 \mu\text{s}$) including 5G, high sensitivity and resolution at low levels, long battery life: > 15 hours with speaker on, a clear display with PEAK, MAX & AVG readings and measures up to 2.5 mW/m².

We used the Xiaomi Mi A3 cell phone as a source of electromagnetic radiation at given frequency.

III. MEASUREMENTS PERFORMED WITHIN DEFINED ENVIRONMENTS

All the measurements were performed in different environments. It was also important to choose the distance between the measurement device and the EMF source. There were chosen three distance levels, which could not be kept in some cases due to the geometry of the given space. In concrete, these are distances of 0.3 m, 1 m and 3 m from the EMF source. As a shielded space was chosen a cellar, an elevator, a car, and a railway wagon in static position. In addition, the measurements were also performed in a home environment to compare the results - the living room and the garden court.

However, it is very important to record the activity of the transmitting device. The generated EMF values change depending on the actual regime. We have chosen activities as: voice telephoning, voiceless telephoning, Bluetooth pairing, data transfer at full-speed upload, data on and watching video via internet, Wi-Fi on full-speed upload and watching videos via internet. These activities mean set up to different carrier frequency, based on definition of the mobile networks, as follows: 2G = 900 MHz, 3G = 2100 MHz, 4G = 2600 MHz, local Wi-Fi = 2400 MHz.

The measurement started by storing the source in a certain place at defined position. We placed the switched-off phone 0.8 m above the ground, either on a wooden chair or by holding it in the hand. At the beginning of the measurement, we measured the background noise-level without the source.

The background level is of non-zero level, because in common surroundings, interfering sources are located almost everywhere and there is always some interfering device around us. Firstly, we performed the measurements at 0.3 m distance from the source at the same height as the source was placed. Subsequently, after measuring and recording the results, which of 10 seconds, we moved the measuring device to 1 m and recorded the measured results for 10 seconds in the table. The last distance, if possible, was 3 m, where we also recorded the results in the table after measuring for 10 seconds. At each of these steps, we set the phone's activities on the EMF source and acquire the values in the appropriate line, where we repeated the measurement itself in each situation twice and wrote the higher measured values, even if they did not differ significantly. For a better idea of the situation, each measurement is drawn in the picture, where Z represents the source - the phone, black dots represent the measuring device. Our goal was to measure and analyze values of electric field strength E [V/m] and power density of EM radiation PD [W/m²] and compare those values for different shielded/unshielded space. The measured data were compared with the limit values of the Decree No. 534/2007 of the Slovak Republic.

A. Measurements in the cellar

The situation of performed measurements in the cellar is shown in the Fig.1, where Z represents our source of the electromagnetic field, the black dots represent the three measuring places used for our measurement.

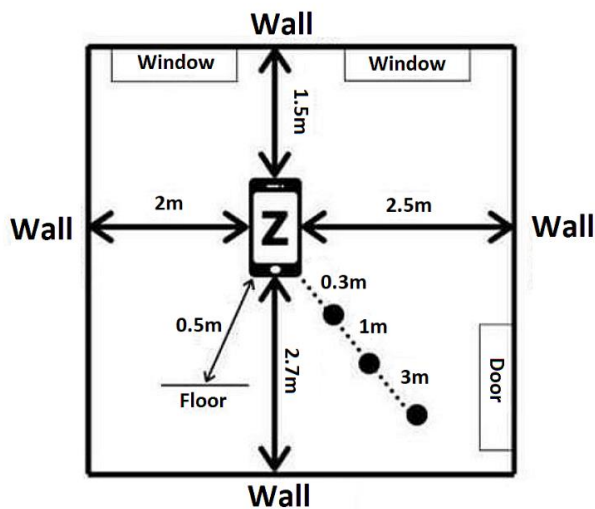


Fig. 1. Experimental set-up: situation during the measurement in the cellar

The highest measured value in this scenario is for calling in a 2G network with a voice at 0.3 m distance, which represents power density of EM radiation $PD = 520$ mW/m² which response value of electric field strength $E = 14$ V/m. On the contrary, the smallest value was recorded in the Bluetooth pairing mode at 3 m distance, namely $PD = 7.24$ μ W/m² and $E = 0.05$ V/m.

B. Measurements in the car

The car is one of the best shaded areas for a given measurement. In the car, people usually make phone calls, or use data or Wi-Fi to watch videos or other things on long journeys. We performed this measurement in a car, which was situated in the garden close to rush street.

We placed the phone on the back-right seat at the height of a person's head of 0.8 m. The situation of performed measurements in the car is shown in the Fig.2 with the similar conditions as previous scenario, where Z represents our source of the EMF and the black dots represent the measuring places used for our measurement.

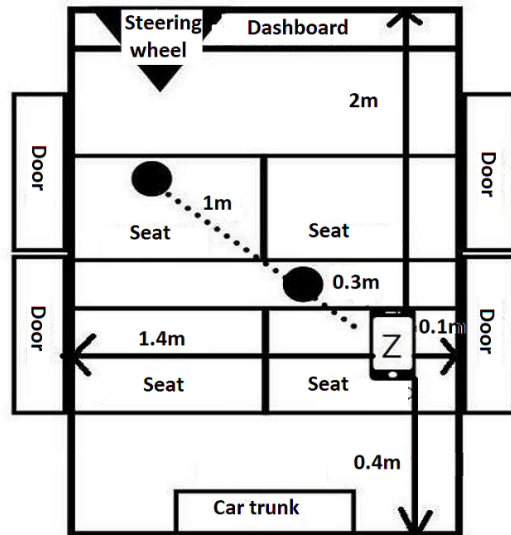


Fig. 2. Experimental set-up: situation during the measurement in the car

The highest measured value in this scenario is for calling within the 3G network with a voice at 0.3 m distance, which represents power density of EM radiation $PD = 44$ mW/m² which response value of electric field strength $E = 4.07$ V/m. On the contrary, the smallest value was recorded in the Bluetooth pairing mode at 1 m distance, namely $PD = 356$ μ W/m² and $E = 0.37$ V/m.

C. Measurements performed in the railway wagon

The railway wagon is one of the most perfectly shielded space, it's a quasi-Faraday's cage. The passengers inside the railway are surrounded by a lot of metal-sheet blocks, also the more modern the railway system, the more perfect the cage. The obstacle is also formed by windows, which are mostly tinted with metal plating to prevent the passage of intense UV radiation from the Sun. Thus, the railway reflects thermal radiation, solar radiation, but also electromagnetic waves, including the RF signal.

During the measurements, we proceeded the situation as follows: the cellphone as a source, was placed at the height of the passenger's head, at 0.8 m distance above the ground of the wagon. A sketch of the situation is drawn in the Fig.3.

The highest measured value in this scenario is for calling within in the 3G network with a voice at 0.3 m distance, which represents power density of EM radiation $PD = 935$ mW/m² which response value of electric field strength $E = 18.77$ V/m. On the contrary, the smallest value was recorded for the watching the video via Wi-Fi at 2.6 m distance, namely $PD = 426$ μ W/m² and $E = 0.4$ V/m.

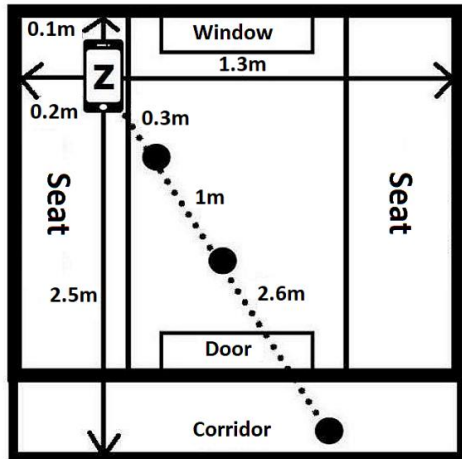


Fig. 3. Experimental set-up: situation during the measurement in the wagon

D. Measurements in the cabine of an elevator

The measurement of this scenario was performed on the top floor of a residential building (4 floors). A sketch of the situation is drawn in the figure Fig.4, where Z represents our source of the electromagnetic field, which was located at the height of the human head, 1.5 m from the ground of the elevator.

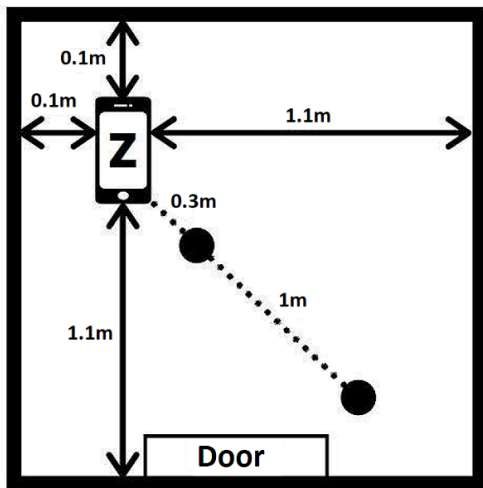


Fig. 4. Experimental set-up: situation during the measurement in the elevator

The highest measured value in this scenario is for calling in a 3G network with LTE mode for using data transfer at 0.3 m distance, which represents power density of EM radiation $PD = 182 \text{ mW/m}^2$ which response value of electric field strength $E = 8.82 \text{ V/m}$. On the contrary, the smallest value was recorded for the voice call in 3G at 1 m distance, namely $PD = 457 \text{ } \mu\text{W/m}^2$ and $E = 0.42 \text{ V/m}$.

E. Measurements in the unshielded space

The measurement of this scenario was performed on the garden-court, close to building in the city center. A sketch of the situation is drawn in the figure Fig.5. The source, which is shown in the sketch of the situation under the letter Z, was placed on a wooden table at a height of 0.5 m from the ground.

The highest measured value in this scenario is for calling in a 3G network with the voice call in 2G at 0.3 m distance,

which represents power density of EM radiation $PD = 32.6 \text{ mW/m}^2$ which response value of electric field strength $E = 3.51 \text{ V/m}$.

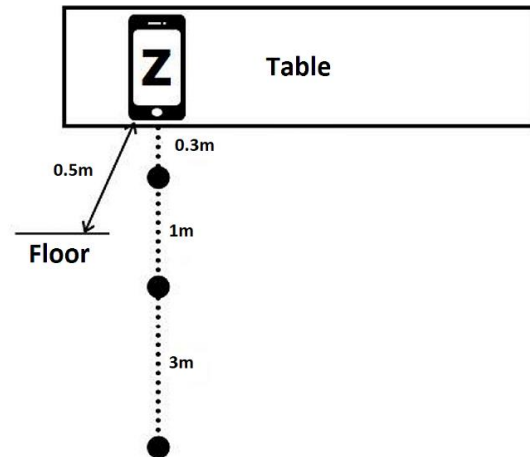


Fig. 5. Experimental set-up: situation during the measurement in the garden-court

On the contrary, the smallest value was recorded for the watching to the video via data transfer in 4G at 3 m distance, namely $PD = 81.4 \text{ } \mu\text{W/m}^2$ and $E = 0.18 \text{ V/m}$.

IV. RESULTS AND DISCUSSION

Our goal was to measure and analyze values of electric field strength E [V/m] and power density of EM radiation PD [W/m²] relatively close to the human body due to active mobile phone within different shielded and unshielded environment. We realize a set of measurements with different conditions of mobile phone use. The summarized results of highest EMF values in each case of environment are shown in Table 1.

TABLE I. SUMMARIZED RESULTS OF HIGHEST MEASURED VALUES OF EMF FOR VARIOUS ENVIRONMENTS

Type of environment	distance from EMF source [m]	E [V/m]	PD [$\mu\text{W/m}^2$]	Type of mobile network
cellar	0.3	14	520	2G
car	0.3	4.07	44	3G
railway wagon	0.3	18.77	935	3G
cabine of elevator	0.3	8.82	182	data
unshielded space	0.3	3.51	32.6	2G

As we can see the highest values of electric field strength were obtained in railway wagon what should be connected with a lot of metallic constructions parts of this enclosed space, e.g., the EM field strength inside the enclosed space with metallic parts is more intense by reason of the resonance effect, scattering and reflections of EM fields from the walls.

On the other hand, we can state, that values obtained by simulations or measurements are significantly lower than global limit value for EM field emissions from mobile devices for human safety purposes according ICNIRP, such is 41.25 V/m for 2G (900MHz frequency of EM field source), and 58.34 V/m for 3G (1800MHz) [1]. However, it is worth noting that those limits were set only on the known thermal effects.

V. CONCLUSION

The issue of investigating of electromagnetic fields is currently very topical. The reason is the sharp increase in devices that use mainly wireless communication for their operation. The areas of interest of scientific teams are currently mainly microwave EM fields, which are generated by mobile communication devices.

In the presented article we dealt with measuring of the EM fields of specific microwave sources in specific areas. These were mainly those spaces that have the adjective shielded spaces. The choice of these specific areas was chosen because the standard setting EM field limits considers the exposure of fields and humans only in unshielded areas. In addition, it is realistic to assume that the limit values may be exceeded in certain areas in the circumstances. From the achieved measurement results in the case of short-term exposures to such EM fields, their effect is probably negligible. However, the question is what effects on biological structures can be expected in the case of long-term effects. It is necessary to emphasize that in everyday life we are exposed to EM fields in such spaces, both at work and at home. Measured and calculated quantities characterizing EM waves are proof that it makes sense to deal with the issue. In addition, the results need to be confronted with the general professional public, especially from the medical environment, to determine the possible effects (both positive and negative) on the human body.

ACKNOWLEDGMENT

This work was supported by the project APVV-19-0214 of Slovak Research and Development Agency, with acronym "LIFE".

REFERENCES

- [1] EN 62209-1:2006. "Human exposure to radio frequency fields from hand-held and body-mounted wireless communication devices – Human models, instrumentation, and procedures – Part 1: Procedure to determine the SAR for hand-held devices used in close proximity of the ear (frequency range of 300 MHz to 3GHz)", 2006.
- [2] Chan, K.H., Leung, S.W., Siu, Y.M., 2010. "Specific Absorption Rate Evaluation for People using Wireless Communication Device in Vehicle". 2010 *IEEE International Symposium on Electromagnetic Compatibility*, Fort Lauderdale, Florida, USA, 5711364
- [3] Salah, I.Y., Yazen, A.Khalil. "High Resolution Numerical Modelling of In-Vehicle Mobile Cars". *International Journal of Electromagnetics and Applications* 2015, 5(1):66-72
- [4] Mydlova, J., Benova, M., Stefancova, V., Pitlova, E. "Assessment of SAR in human body model with the cochlear implant inside a railway vehicle." Proc. of the 13th Int. Scientific Conference on Sustainable, Modern and Safe Transport, Transportation Research Procedia
- [5] Atanasov, N. T., Atanasova, G. L. "An investigation impact of user's positions in closed space over SAR in the head induced from mobile phone". *Environmentalist* 31: 181-186, Springer Science-Business Media, LLC 2011.
- [6] Dominguez, H., Raizer, A. and Carpes, W.P., Jr. "Electromagnetic fields radiated by a cellular phone in close proximity to metallic walls", *IEEE Trans Magn* 38 (2002), 793-796
- [7] Tang, C. K., Chan, K. H., Fung, L. C. and Leung S. W. "Effect on radio frequency human exposure of mobile phone inside an enclosed metallic elevator", *MICROWAVE AND OPTICAL TECHNOLOGY LETTERS* / Vol. 50, No. 8, August 2008
- [8] User Manual for the Safe Living Technologies Safe and Sound Pro II RF Meter, [online] [2021-06-15] available at: <https://safelivingtechnologies.com/content/Products/RFMeterSafeAndSoundProIIUserManual.pdf>

Simulations of electromagnetic exposure system for irradiation of biological cultures: comparison of CST Studio Suite and COMSOL Multiphysics

Zuzana Judáková, Ladislav Janoušek, Lucia Čarnecká, Dominika Oreničová
Department of Electromagnetic and Biomedical Engineering
Faculty of Electrical Engineering and Information Technology, University of Žilina
Žilina, Slovak Republic
zuzana.judakova@feit.uniza.sk

Abstract— The proposed paper deals with the comparison of simulation results of an exposure system intended for irradiating biological cells performed using two commercially available simulation software – CST Studio Suite and COMSOL Multiphysics. The purpose is to compare the results of numerical simulations of the identical model with respect to the magnetic flux density distribution and its homogeneity in a defined area of interest. The results clearly show that the rms values of the magnetic flux density obtained from both simulation programs differed at most at the level of 101 μT , which represents a difference of 4.17% of the target value $B = 2.4 \text{ mT}$.

Keywords — *finite element method, finite integration technique, low frequency, exposure system, coil, incubator, biological cells.*

I. INTRODUCTION

There are still more questions than answers about the influence of the external artificial electromagnetic field on living organisms. To predict the harmful effects of electromagnetic field (EMF) on living organisms, it is important to know information about the applied electromagnetic field - magnetic flux density magnitude and homogeneity. Modern simulation software permit to calculate level of applied EMF by direct numerical methods. The results of numerical simulations are a useful tool in the transition from the theoretical to the experimental level of the study of the biological action of EMF.

The simulations presented in this paper form the basis for performing experiments based on the Lednev's ion parametric resonance (IPR) theory. The experiment lies in applying magnetic field (MF) generated by a parallel combination of static and time-varying MF. The theory of IPR considers the nonthermal effect of MF on ions in living cells such that a protein-bound ion of mass m and charge q can be considered as a harmonic oscillator [1]. The correct application of the theory presupposes the application of time-varying MF with a frequency corresponding to the cyclotron frequency of the target bound ion, calculated according to the formula:

$$f = \frac{1}{n} \frac{1}{2\pi} \frac{q}{m} B_{\text{DC}} \quad (1)$$

where q is the electric charge of target ion, m is the molecular mass of the target ion and B_{DC} is the value of static magnetic flux density - Earth's magnetic field. The goal of our interest is calcium ions $^{40}\text{Ca}^{2+}$ with the cyclotron frequency of 29.89 Hz. It is therefore an application of low frequency EMF. There is several software on the market suitable for this type of simulation, e.g., Ansys Maxwell, Abaqus, Opera, FEMM, COMSOL Multiphysics (CM), CST Studio Suite.

To obtain credible results it is useful to use different simulation tools. The aim of the work is to compare the results of numerical simulations of the exposure system performed in CST Studio Suite (use the Finite Integration Technique – FIT in frequency domain solver) and COMSOL Multiphysics (use the Finite Element Method - FEM in frequency domain solver).

The object of interest of simulations is an exposure system intended for irradiating biological cells with a low-frequency electromagnetic field to study the impact of the electromagnetic field on the cells. Beer yeast *Saccharomyces cerevisiae* are used as a model organism [2] [3] [4] [5]. The use of beer yeast is justified for the following reasons:

- it is a single-celled eukaryote, has 16 pairs of chromosomes and shares about 1/3 of its genes with humans,
- molecular, cellular, and biochemical similarities with more complex eukaryotic organisms, including humans,
- rapid reproduction,
- cultivation in acidic conditions with a high sugar content - these conditions prevent the multiplication of bacteria, thus preventing contamination,
- low cultivation and storage costs. [6]

In the research of the impact of electromagnetic field on cells it is important to secure as homogeneous magnetic flux density field (B-field) as technically possible in the volume of irradiated samples. The target inhomogeneity set in this paper based on previous simulation results and technical possibilities is at the level of 2%.

The setup of experiments comprises performing parallel experiments, assuring identical ambient experimental conditions of both biological samples, i.e., the exposed ones and the control sample. Cell proliferation is compared between samples exposed to MF and control samples representing a state without intervention. The source of electromagnetic field is represented by a cylindrical coil.

II. MATERIALS AND METHODS

The aim of the work is to compare the results of numerical simulations of the exposure system performed in CST Studio and COMSOL. The basic configuration of the exposure system consisting of two cylindrical coils is presented in [7]. In the next step two other components have been added - an incubator and a shielding for the control coil. The complete exposure system is composed of the exposure coil, control coil, metallic incubator, metallic shielding, and 10 samples symmetrically distributed with respect to the center of the coil, Fig. 1. The samples are placed in the cavity of the coil, and they are representing Erlenmeyer flask with culture

medium. Both coils are 1000 mm long, have 2000 turns, and they have an inner diameter of 135 mm. The exposure coil is supplied with a current 0.7 A to achieve a magnetic flux density of 2.4 mT at a frequency of 29.89 Hz. The walls of the incubator are made from a metal sheet with a thickness of 2 mm, the shielding is made from a metal sheet with a thickness of 3 mm. The electromagnetic parameters of the metal sheet are the ones from the simulation software library:

- $\epsilon_r = 1$
- $\mu_r = 1000$
- $\sigma = 1.04 \cdot 10^7 \text{ S.m}^{-1}$.

The shielding with dimensions 1000x160 mm² (height x width) is placed exactly in the middle between the coils. The distance between the edges of coils is 174 mm. The modeled incubator represents an incubator Q-Cell 240 with dimensions 1315x504x320 mm³ (height x width x depth).

This complete exposure system is numerically modeled in both simulation software – CST Studio and COMSOL. The inhomogeneity of B-field in each sample is investigated. The samples are in simulation marked as an area of interest (AOI). The AOI comprise 10 cylinders marked with the letters A to E in the exposure coil and the control coil, Fig. 1, each with dimensions width: 68 mm, height: 40 mm and a volume of 145 cm³ and is filled with the distilled water. The end samples are located 100 mm from the respective edges of the coil. For calculating inhomogeneity there is created 90 evaluating points, 9 in each AOI, Fig. 2 The B-field as root mean square value (rms) is calculated at these evaluating points. From these values of the B-field at evaluating points the maximum B_{max} and the minimum B_{min} values are determined to calculate inhomogeneity of the B-field (IFL):

$$IFL = \frac{(B_{max} - B_{min}) \times 100}{B_{max}} [\%] \quad (2)$$

The target inhomogeneity is determined for the exposure coil. For the control coil it is important to keep the magnitude of the B-field lower than half of the Earth's magnetic field value 39 μT measured at the location of the realization of the experiments.

The whole numerical space is discretized by using a tetrahedral mesh in the CST Studio and the low-frequency domain solver employing magnetoquasistatic equation is applied. Any symmetry cannot be applied to the model because of the presence of the two coils, the shielding, and the incubator. Built-in function *Symmetry Planes* cannot be applied as in previous simulations [7], the boundary condition in XY, YZ and YX planes were set to open. For this reason and due to available computing capacity, the simulations are performed with the accuracy of 10^{-3} .

In COMSOL, the model is created in 3D spatial layout discretized by using an automatic generated tetrahedral fine mesh. The multiphysical interface *Electromagnetic Heating*, and the *Frequency-Transient* study is applied. The comparison of B-field layout in both employed software is presented in the Figure 3.

To estimate the inhomogeneity in each AOI, the magnetic flux density values are evaluated at 9 evaluating points as defined before. The rms values of B-field for the exposure

coil and for the control coil are stored in a table and the IFL is calculated for each AOI separately. The value marked as Ref. [%] in Table 1 and Table 2 is the IFL calculated from the reference value at point p4 in the sample C considered as B_{max} in formula (2). The point p4 of the sample C is placed in the geometrical middle of the coil. The differences in μT between the values obtained from the simulation in CST and the ones from COMSOL are presented in the Figure 4.

In Table 1 they are listed the IFL and Ref. values for the exposure coil. The IFL values are quite similar except sample E, where the value of inhomogeneity calculated in CST is 0.57% and in COMSOL 3.85%. The Ref. values of inhomogeneity are significantly different in samples A and E.

The IFL and Ref values for the control coil are given in Table 2. The IFL values are similar in samples B, C, and D. The difference is almost double in the sample A. In the Ref. values of inhomogeneity there is a significant difference only in sample C.

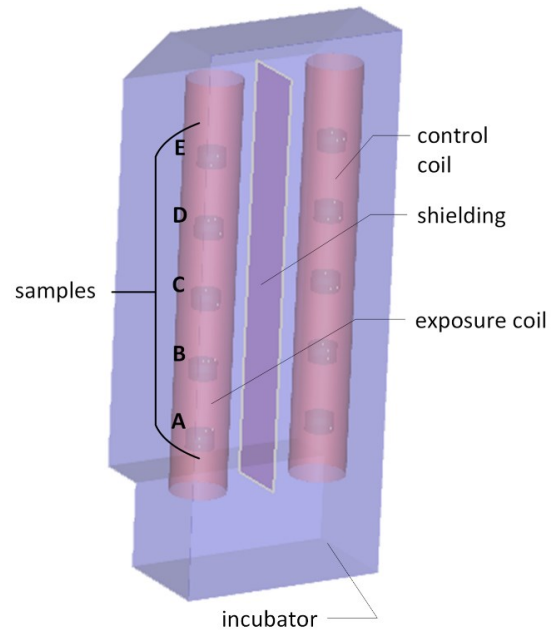


Figure 1 The geometrical layout of components in simulation

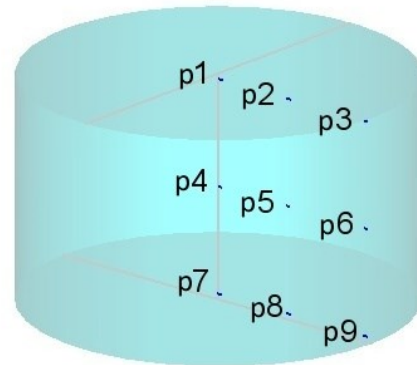


Figure 2 Evaluating points layout in the sample

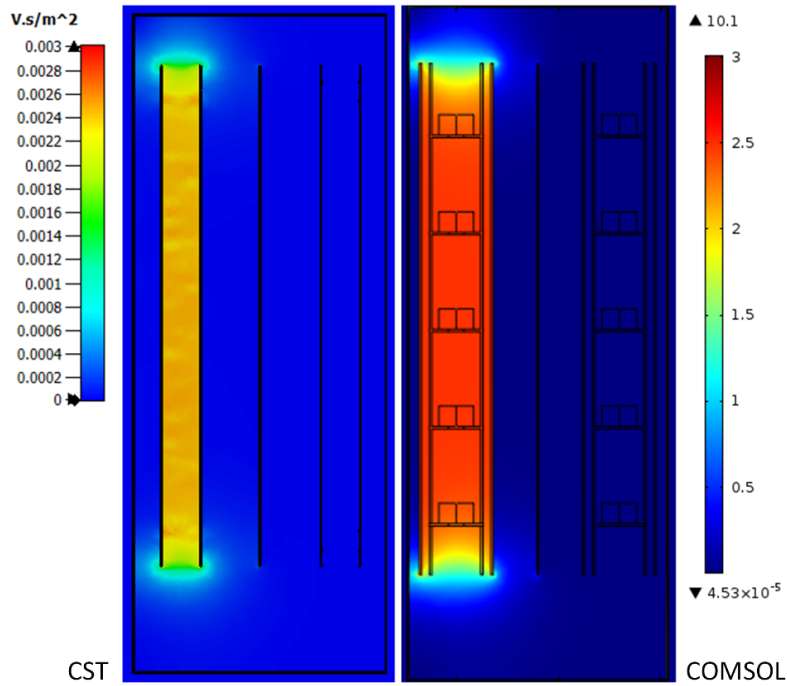


Figure 3 Comparison of B-fielded layout in CST Studio and COMSOL

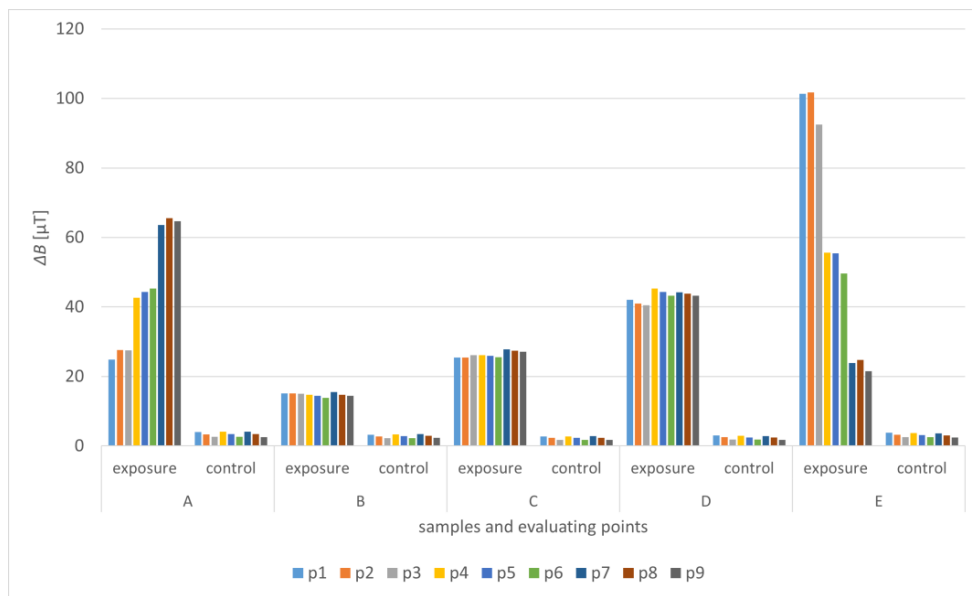


Figure 4 The difference between rms values of B-field obtained by simulation in CST Studio and COMSOL

Table 1 The inhomogeneity of B-field at evaluating points in CST Studio and COMSOL in exposure coil

sample/ software	A		B		C		D		E	
	CST	CM	CST	CM	CST	CM	CST	CM	CST	CM
IFL [%]	2.40	3.98	0.15	0.15	0.10	0.02	0.13	0.14	0.57	3.85
Ref. [%]	3.83	7.45	0.15	0.29	0.07	0	0.97	0.28	2.13	7.25

Table 2 The inhomogeneity of B-field at evaluating points in CST Studio and COMSOL in control coil

sample/ software	A		B		C		D		E	
	CST	CM	CST	CM	CST	CM	CST	CM	CST	CM
IFL [%]	9.91	18.75	10	9.84	8.75	5.46	9.64	8.62	9.18	14.71
Ref. [%]	26.58	25	2.53	5.77	7.59	0	5.06	1.92	12.66	11.54
max B [μT]	11.1	8.0	9.0	6.1	8.0	5.5	8.3	5.8	8.78	6.8

The target inhomogeneity 2% is reached in all samples of the exposure coil except samples A, where the IFL is 2.40/3.98 (CST/COMSOL) and except sample E only for COMSOL result, where the IFL is 3.85. The IFL calculated from the reference value at point p4 in the sample C considered as B_{\max} in formula (2) and in results marked as Ref. [%] meets the condition 2% inhomogeneity in three medium samples B, C, D. In edge samples A and E is the Ref. value 3.83/7.45 and 2.13/7.25 (CST/COMSOL).

In the control coil is the target maximal value of B-field reached in all samples.

III. CONCLUSION

This article was focused on the comparison of simulation results of an exposure system intended for irradiating biological cells performed using two commercially available simulation software – CST Studio Suite and COMSOL Multiphysics. The complete exposure system is composed of the exposure coil, control coil, metallic incubator, metallic shielding, and 10 samples symmetrically distributed with respect to the center of the coil. Within the simulation results, the inhomogeneity and magnitude of the magnetic flux density field is compared.

The inhomogeneity calculated from both simulation programs is comparable in the center of exposure coil and control coil. The homogeneity values from the upper edge of the exposure coil differ significantly.

The rms values of the magnetic flux density (B) obtained from both simulation programs differed at most at the level of 101 μT , which represents a difference of 4.17% of the target value $B = 2.4 \text{ mT}$. Significant differences are especially in area close to the exposure coil upper edge.

The difference in the obtained values is acceptable and is caused by a different calculation method of the investigated software programs, Finite Integration Technique vs. Finite Element Method.

Further work will focus on the construction of the simulated exposure system, on performing measurements of magnetic flux density field with a suitable instrument and on comparison of measured data with values obtained by presented simulations.

ACKNOWLEDGMENT

This work was supported by the Slovak Research and Development Agency under the Contract no. APVV-19-0214, and by Grant System of University of Zilina No. 1/2020.

REFERENCES

- [1] N. A. Belova and V. A. Panchelyuga, "Lednev's model: Theory and experiment," *Biophysics (Oxf)*, vol. 55, no. 4, pp. 661–674, 2010, doi: 10.1134/S0006350910040263.
- [2] M. Choe, W. Choe, S. Cha, and I. Lee, "Changes of cationic transport in AtCAX5 transformant yeast by electromagnetic field environments," *J. Biol. Phys.*, vol. 44, no. 3, pp. 433–448, 2018, doi: 10.1007/s10867-018-9500-0.
- [3] M. Iwasaka, M. Ikehata, J. Miyakoshi, and S. Ueno, "Strong static magnetic field effects on yeast proliferation and distribution," *Bioelectrochemistry*, vol. 65, no. 1, pp. 59–68, 2004, doi: 10.1016/j.bioelechem.2004.04.002.
- [4] H. Y. Lian, K. W. Lin, C. Yang, and P. Cai, "Generation and propagation of yeast prion [URE3] are elevated under electromagnetic field," *Cell Stress Chaperones*, vol. 23, no. 4, pp. 581–594, 2018, doi: 10.1007/s12192-017-0867-9.
- [5] R. Pereira, "The use of calcium blockers to study biochemical behaviour of *Saccharomyces cerevisiae* cells," *Mol. Cell. Biochem.*, 2001, doi: 10.1023/A:10133279.
- [6] F. Foury, "Human genetic diseases: A cross-talk between man and yeast," *Gene*, vol. 195, no. 1, pp. 1–10, 1997, doi: 10.1016/S0378-1119(97)00140-6.
- [7] Z. Judakova and L. Janousek, "Design of electromagnetic exposition system for irradiation of biological cultures," *Proc. 2020 IEEE 21st Int. Conf. Comput. Probl. Electr. Eng. CPEE 2020*, pp. 8–11, 2020, doi: 10.1109/CPEE50798.2020.9238697.

Modeling and simulation of biological structures exposition to 5G network

Zuzana Psenakova, Daniela Gombarska, Milan Smetana, Miroslav Janovicik

*Department of Electromagnetics and Biomedical Engineering, Faculty of Electrical Engineering and Information Technology
University of Zilina*

Zilina, Slovakia

<https://orcid.org/0000-0001-8898-5438>

Abstract— Compared to its predecessor, the 4G network, the 5G mobile network offers an increase in speeds and a significant reduction in response time. It is a standard that will help both in industry and professional usage. It will also affect the use of the smartphone of the average user. However, the introduction of 5G networks means a prospective jump in the number of transmitters. High transmission speeds only work over a very short distance and spread poorly in buildings. For this reason, the debate on health hazards is still open. In this article, we deal with the creation of a simple model and simulations of the electromagnetic field around a 5G mobile phone and its penetration into nearby tissue. The resulting values for the two modeled frequencies in the upper range of 5G frequencies 28GHz and 39GHz are presented in the text.

Keywords— 5G, model, electromagnetic field, exposure, living tissue.

I. INTRODUCTION

The continually growing number of devices connected to the network, whether they are smartphones, smart homes, or the rapidly evolving "Internet of Things" (IoT), is putting the challenge for engineers to develop technologies capable to provide network services. The current state requires the transmission of more and more data with higher data rates, which should be provided by fifth-generation or 5G mobile communication. Discussions about the 5G mobile network began in 2012 when the term 5G was used to refer to a specific new wireless access technology. These days the 5G term is often used to indicate the wide range of technologies and services available in 5G mobile communication. Due to 5G demands significant innovations are needed to accommodate increased requirements. To meet these requirements, new technologies are developed. The 5G system uses various new technologies to meet its requirements, such as throughput (speed) 1 – 20 Gbit/s, latency (delay) - maximum 1 ms, massive connection with super high speed, 1000 connected devices, and 1000x higher bandwidth per unit area (capacity), 100% coverage with 99% availability, high energy efficiency, -90% reduction in power consumption and 10-year battery life for massive machine-type communication or mMTC. [1] [2]

A. Exposure to electromagnetic radiation

Electromagnetic radiation is omnipresent in our living environment. Although undetectable by human senses, in some cases it may affect wellness. During the 20th century, the exposure of the environment as well as humans to electromagnetic radiation has increased significantly and is still growing. The continuous increase is caused by the rising demand for electricity and constantly evolving technologies, which require the constant creation of new artificial sources of electromagnetic radiation. While natural sources, for example, the Sun radiation, the Earth's magnetic field, or storms, are present in the environment during the whole known existence

of mankind, artificial sources of radiation, created by man, are present only a fraction of the time. Artificial sources are all sources of radiation in the spectrum from microwaves to long waves. For example, every single socket may be included among low-frequency sources, high-frequency electromagnetic radiation, in turn, is used to transmit information, such as television antennas, radio or aerial antennas, or mobile phone base stations, X-rays might be emitted due to medical diagnostic methods. During life, everyone is exposed to weak, mixed electromagnetic radiation, whether at home or work. People are irradiated by electromagnetic fields generated by many sources from electricity lines, through commonly used appliances to mobile devices and telecommunications. The major goal is to create a healthy and safe living as well as a working environment.

As a part of normal bodily functions occur small electric currents in the human body that arise because of chemical reactions. It occurs even without the influence of external electromagnetic fields. As an example, could be mentioned the transmission of the action potential through nerves. Most biochemical reactions, whether digestion or brain activity, is related to the passage of charged particles. Likewise, the heart is electrically active. [8]

Low-frequency fields may not only affect charged particle materials but also the human body as they induce currents in the human body, where the strength of the current depends on the intensity of the external magnetic field. With a certain size of the magnetic field, they can stimulate nerves and muscles or affect other biological processes. Although electric and magnetic fields can induce currents in the body, even under high voltage lines, the fields are not large enough to affect biological processes. Raising the temperature is the main biological effect of radiofrequency fields. This phenomenon is commonly used, for example in microwave ovens and food heating. However, humans are not normally exposed to such strong fields that significant heating of biological tissue occurs. The thermal effects of electromagnetic radiation form the basis for determining exposure limit values. Significant thermal effects occur only at high electric field strength in the high-frequency band. The average person does not have the opportunity to encounter such an electric field. The thermal effects therefore mainly concern workers who operate transmitters or base stations and are in the vicinity of these devices for a long time. If the intensity of EMP exceeds a level at which thermoregulation of the body fails to dissipate heat, body temperature rises, and organ damage or death can occur. The human body cools down through the skin, so the internal organs are more at risk. Nevertheless, the external or superficial parts of the human body are most heated. At very high frequencies, there is much less penetration of fields into the body, which means that at 5G frequencies, especially those parts that are on the surface can be affected. The eyes do not

have sufficiently fast thermoregulation and are probably the most temperature-susceptible organ. Workers operating high-frequency transmitters are at increased risk of developing cataracts. Brain tissue is also very prone to rise temperatures on its surface. The surface of the head can warm up slightly even during a long conversation via cell phone when the phone is close to the ear. This phenomenon is not dangerous in terms of short-term exposure. With greater heating of the brain tissue, disorders of the neural connections can occur, and thus, for example, the mental state of a person can be negatively affected. With the increased body temperature, the body's ability to thermoregulate must increase. That leads to increased blood flow in the blood vessels and places a greater demand on the cardiovascular system. Also, reproductive organs are very sensitive to temperature changes due to EMP, and sensitive reproductive tissue can be damaged. There may also be damage to the foetus in the womb of pregnant women. [8] [9] [10] [12]

The non-thermal effects of EMF are effects that cannot be clearly attributed to direct heating of the tissue due to radiation. Non-thermal effects are manifestations that arise from long-term human exposure to low-intensity EMF. As an example, it may occur for everyday users of mobile phones, or computers, and other various electrical devices that emit EMP. Investigating the non-thermal effects of EMF on humans is very difficult because it works with very long-time intervals (including the entire life span of a person). It is also a problem to distinguish which phenomenon is due to the long-term effects of EMP and which may be due to other causing circumstances.

One of the long-discussed issues is the impact of EMP as a carcinogen. In 2010, the World Health Organization published the results of extensive research, which pointed to the possibility that long-term frequent use of a mobile phone may increase the likelihood of developing a nervous system tumour (most commonly in the brain) by up to 40%. The research involved people who used a mobile phone for about 1640 hours for 10 years, about half an hour a day. This study also adds that due to the inaccuracy of the length of time a mobile phone is used by individual users, this data is not demonstrable. We can conclude that cancers due to EMP are not confirmed or refuted. Based on this research, VF EMP was classified as a potentially possible carcinogen.

Furthermore, there exist hypersensitive people who, after exposure to EMP, with values that do not exceed hygienic limits, can observe symptoms such as fatigue, headache, and the like. There are also many other cases in which it is not possible to clearly determine the link between EMP and specific manifestations, such as the effect on the nervous system. [8] [10]

1) 5G limits

Some scientific studies question current limit values and suggest conflicts of interest. 5G is being introduced without a detailed examination of the risks to health and the environment, which has sparked debate among individuals in many countries. Many scientists and doctors have appealed to the European Union and called for a moratorium on the introduction of 5G until the possible negative consequences have been scientifically evaluated. The EU did not confirm this request.

International limits on human exposure to EMFs, such as those recommended by the International Commission on Non-

Ionizing Radiation (ICNIRP), or limits set by the US Federal Communications Commission (FCC), have been established with safety margins to protect against excessive tissue heating due to energy absorption. ICNIRP issued new guidelines for radio frequency radiation on March 11-th 2020 for frequencies 100kHz - 300GHz, which includes 5G. Experimental studies include several non-thermal effects, but these guidelines are not fully covered in these studies. [5] [14]

To protect humans from the adverse effects of the electromagnetic field, limit values for exposure to the electromagnetic field are set as a function of frequency and the following quantities shall be used:

- exposure limit values for current density J [A/cm²] - protection of the cardiovascular and central nervous system,
- exposure limit values for SAR [W/kg] - protection against overheating of biological tissues,
- exposure limit values for power flux density (W/m²) - protection against overheating of biological tissues. [14]

TABLE I. BASIC STANDARDS FOR EXPOSURE TO ELECTROMAGNETIC FIELDS. (14) (15)

Type of exposition	Frequency range	Average SAR - whole body (W/kg)	Electric field strength (V/m)	Local SAR - head / torso (W/kg)	Local SAR - limb (W/kg)	Power flux density (W/m ²)
Working	100 kHz – 6 GHz	0,4	-	10	20	-
	>6 GHz – 300GHz	0.4	-	-	-	100
General public	100 kHz – 6 GHz	0.08	-	2	4	-
	>6 GHz – 300GHz	0.08	1.4*10 ²	-	-	20

2) Specific absorption rate

A specific rate of absorption – SAR, expresses the amount of power from electromagnetic radiation absorbed by the body or head. ICNIRP, as well as other organizations, set safety limit values for this quantity. If the SAR values are exceeded, there is an increased risk of an adverse effect of the electromagnetic field. The value of SAR [W/kg] depends on the magnitude of the electric field strength and other tissue properties

$$SAR = \frac{\sigma |E|^2}{\rho}$$

where σ expresses the electrical conductivity of the tissue [S/m], ρ is the bulk density of the biological tissue [kg/m³] and E is the vector of the electrical intensity of the field [V/m] at a certain point in the tissue. The SAR value is calculated using the whole body, limb, or small tissue sample (1g or 10g). If the exposure time of the high-frequency electromagnetic field is short, heating occurs mainly on the surface of the body. With prolonged exposure, the internal organs also begin to overheat, which can damage them. At the same time, the blood temperature rises. [15]

3) Electromagnetic fields above 6 GHz

With the introduction of 5G mobile communications and the use of higher frequency bands (above 6 GHz), existing regulations on human exposure to electromagnetic radiation

may limit the maximum output power of user equipment to levels much lower than those allowed for lower frequencies.

Since the correlation between SAR and rising temperature at frequencies above 6 GHz is not as strong as at lower frequencies and the depth of EMP penetration into biological tissue decreases with increasing frequency, SAR is not used to assess EMP field exposure at frequencies above 6 GHz. The FCC, ICNIRP, and IEEE have determined that instead of measuring a SAR focused on a small volume of tissue sample, power density is taken as the measure. [16]

The incident power density is defined as the modulus of the complex Poynting vector

$$S_{inc} = |\mathbf{E} \times \mathbf{H}^*|$$

where S_{inc} is the power density, \mathbf{E} is the electric field intensity vector and \mathbf{H} is the magnetic field intensity vector. * indicates a complex associated number. The power density must be averaged over 4 cm² of irradiated area if we want to compare it with the limit values. [13]

II. MODEL OF DEVICE AND THE BIOLOGICAL TISSUE

For the 5G model purpose, we design an antenna that can operate in the high-frequency band, specifically above 24 GHz. The requirements for such an antenna are low weight, compact dimensions, low production costs, easy installation, the ability to adapt to different surfaces, mechanical resistance, etc. In this work, a microstrip "patch" antenna is proposed, which should be a suitable candidate to meet the requirements.

Since 5G mobile communication uses the MIMO system, or beamforming, a patch antenna with one element is not suitable for use in this area. Therefore, it is necessary to create an array of antennas for the model. The created arrays of antennas are then imported to the mobile phone model. The mobile phone model is downloaded from the CST Studio Suite library. The work does not address the effect of the location of antennas in the mobile device, the fields are simply inserted on the back of the mobile phone, Fig. 1 a.

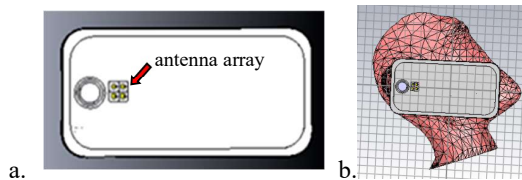


Fig. 1. a. Antenna array located on the back of the mobile phone, b. Model for simulations containing part of the SAM Phantom model and a mobile phone with an array of antennas

We use the homogeneous SAM Phantom model for 5G frequencies simulation. During the simulation, the CST Studio Suite program divides the given model into individual cells, the dimensions of which are given based on the wavelength. Since we work in the high-frequency band, in larger and more complex models, the number of cells will be extremely high, which makes it impossible to simulate using a "transient solver", or the computation time will be too long. Simplified model SAM is used for simulations at frequencies 28 GHz and 39 GHz. The combined model containing the slice of SAM and the mobile phone is shown in Fig. 1 b..

During the simulations, quantities such as electric and magnetic field strength are monitored, as well as a "power

flow monitor". The power flow monitor expresses the Poynting vector of the electromagnetic field. It corresponds to the real component of the Poynting vector, evaluated at a specific frequency. Subsequently, the Poynting vector must be averaged over the area required by the ICNIRP standards, namely 4 cm². In this way, we obtain the magnitude of the incident power averaged over a given area.

Fig. 2 shows the resulting values for the individual distances as well as the limit values for the two chosen frequencies.

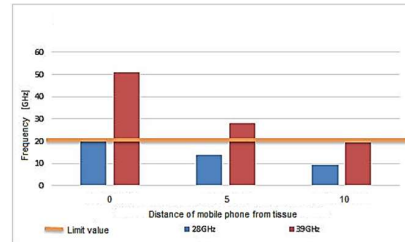


Fig. 2. Values of locally absorbed power, for individual antenna distances and frequencies

It can be seen that for an antenna with a frequency of 28 GHz, the values of the incident power were below the limit values at each distance, but the antenna with a frequency of 39 GHz meets the limit values only at 10 mm.

The H-field monitor displays the intensity of the magnetic field, which is highest at the feed pins of individual antennas, with a value of up to 208 A/m for the frequency of 39 GHz and 135 A/m for the frequency of 28 GHz. The maximum calculated value of the magnetic field strength in the head models is 0.8437 A/m for the frequency of 39 GHz and 0.616 A/m for the frequency of 28 GHz. The highest maximum values are detected at the lowest distance between the tissue and phone.

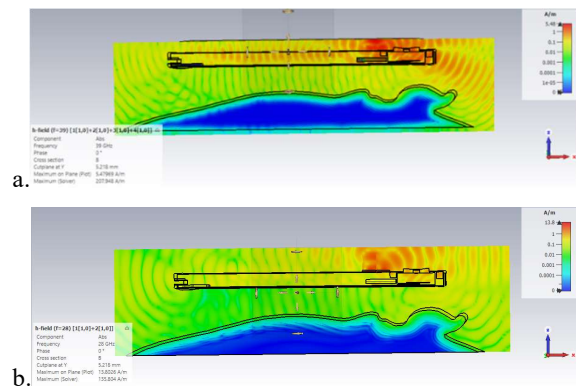


Fig. 3. Distribution of the magnetic field near the head for a. 39 GHz, b. 28 GHz source

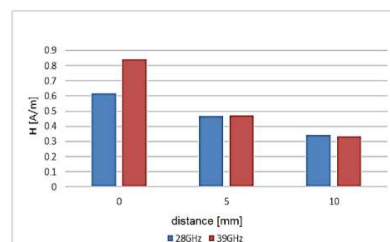


Fig. 4. Magnetic field strength values for different frequencies and distances of the radiation source from the biological model

Fig. 5 shows the maximum values of the magnetic field intensity H in biological tissue models for different distances of this model from the radiation source.

The E-field monitor displays the values of the electric field intensity, where at the frequency of 39 GHz the maximum value is 51.641 V/m and for the frequency of 28 GHz the maximum value of the electric field intensity is 31.144 V/m. The maximum values of the electric field intensity in the biological tissue models were recorded at the lowest distance of the radiation source from the biological tissue model, namely 126.41 V/m for the frequency of 39 GHz and 74.72 V/m for the frequency of 28 GHz.

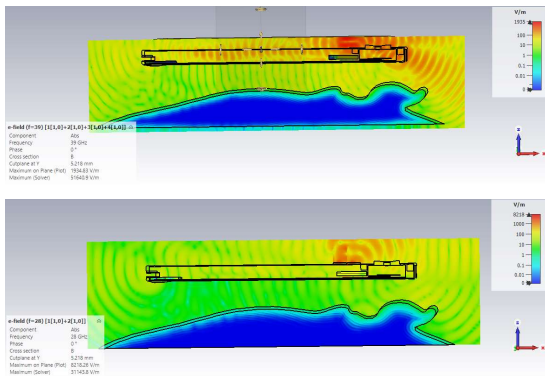


Fig. 5. Distribution of the electric field near the head for a. a 39 GHz, b. 28 GHz source

Fig. 6 shows the maximum values of the electric field intensity E in biological tissue models for different distances of this model from the radiation source.

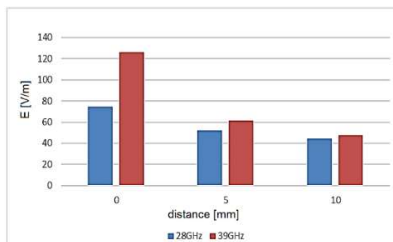


Fig. 6. Electric field strength values for different frequencies and distances of the radiation source from the biological model

III. CONCLUSION

We created model in CST Studio Suite program containing the mobile phone with patch antenna array optimised for 28GHz and 39GHz and a slice of the SAM model for modelling the human tissue. In individual simulations, it was found that the model of the source of electromagnetic radiation, located on the back of the mobile phone, met the limit values for the frequency of 28 GHz for all distances of the device from the head. For frequencies of 39 GHz, it met the limit values only at a distance of the device 10 mm from the head, from which we can conclude that at shorter distances and the use of a given source of electromagnetic radiation, adverse effects of electromagnetic field could occur, specifically overheating of tissue. However, the data obtained may also be affected by the orientation of the antenna. If the antenna is rotated in another direction, the individual values may differ significantly. Alternatively, it would be necessary to shield the radiation from the antenna

with different materials, which may be the subject of further investigation.

ACKNOWLEDGMENT

This work was supported by the Slovak Research and Development Agency under the Contract no. APVV-19-0214.

REFERENCES

- [1] Dahlman, Erik. 5G NR: The Next Generation Wireless Access Technology. s.l. : Elsevier, 2018. 978-0-12-814323-0.
 - [2] Hui, Hongxun, Ding, Yi a kol. "5G network-based Internet of Things for demand response in smart grid: A survey on application potential." [Online]
 - [3] Jian Pang, Yun Wang a kol. "A 28-GHz CMOS Phased-Array Transceiver Based on LO Phase-Shifting Architecture With Gain Invariant Phase Tuning for 5G New Radio", [Online]
 - [4] Bhardwaj, Anshu. "5G for Military Communications". [Online] Procedia Computer Science, Volume 171, 2020, Pages 2665-2674
 - [5] E. Dahlman, S. Parkvall, J. Skold, "5G NR: The Next Generation Wireless Access Technology, 1st Edition". Elsevier, 2018. 978-0-12-814323-0.
 - [6] Hui, Hongxun, Ding, Yi a kol. Ideas. 5G network-based Internet of Things for demand response in smart grid: A survey on application potential. [Online] [Date: February 14., 2021.]
 - [7] ElectronicsNotes. 5G NR New Radio - 5G NR or 5G New Radio is the new radio air interface being developed for 5G mobile communications. [Online] [Date: January, 14.,2021.]
 - [8] World Health Organization. Radiation: Electromagnetic fields. [Online] 4. 8. 2016. [Date: 1. 12. 2020.] <https://www.who.int/news-room/q-a-detail/radiation-electromagnetic-fields>.
 - [9] Marshall, Trevor G. a Heil, Trudy J. Rumann. NCBI. Electromog and autoimmune disease. [Online] 13. 7. 2016. [Dátum: 11. 2. 2021.] Electromog and autoimmune disease. Marshall, Trevor G. a Heil, Trudy J. Rumann. s.l. : online, 2016. PMC5406447..
 - [10] Roman Radil, Jan Barabas, Ladislav Janousek, Martin Bereta: „Frequency dependent alterations of *S. Cerevisiae* proliferation due to LF EMF exposure" [electronic] In: Advances in Electrical and Electronic Engineering [print, electronic]. - ISSN 1336-1376. - Year. 18, No. 2 (2020), s. 99-106
 - [11] C. Johnson, A. Guy. ScemanticScholar. Nonionizing electromagnetic wave effects in biological materials and systems. [Online] 1972. [Dátum: 15. 1. 2021.] <https://www.semanticscholar.org/paper/Nonionizing-electromagnetic-wave-effects-in-and-Johnson-Guy/4be923cca3d3eddb8cb85e7621975f16611fa3d7>.
 - [12] Lennart Hardell, Michael Carlberg. PMC. Health risks from radiofrequency radiation, including 5G, should be assessed by experts with no conflicts of interest. [Online] 15. 7. 2020. [Date: February, 15., 2021.] <https://www.ncbi.nlm.nih.gov/pmc/articles/PMC7405337/>. 1792-1082.
 - [13] Nariadenie vlády. o minimálnych zdravotných a bezpečnostných požiadavkách na ochranu zamestnancov. s.l. : Slovenská republika, 2016. 209/2016.
 - [14] ICNIRP. RF EMF GUIDELINES 2020. [Online] 3. 2020. [Dátum: 1. 12. 2020.] <https://www.icnirp.org/en/activities/news/news-article/rf-guidelines-2020-published.html>.
 - [15] Gustafsson, Mats. RF EMF Exposure Compliance of mmWave Array Antennas for 5G User Equipment Application. Stockholm : Department of Electromagnetic Engineering, School of Electrical Engineering, 2017. s. 18.
 - [16] CST. CST - Computer simulation technology. [Online] 11. 3. 2019. [Dátum: 24. 3. 2021.] <https://www.cst.com/products/csts2>.
 - [17] Magus, Antenna. Information Browser.
 - [18] Rütshlin, Marc. The Simulia Blog. 5G Antenna Design for Mobile Phones. [Online] 19. 3. 2020. [Dátum: 15. 1. 2021.] <https://blogs.3ds.com/simulia/5g-antenna-design-mobile-phones/>.
 - [19] Darboe, Omar, Konditi, Dominic Bernard Onyango a Manene, Franklin. A 28 GHz Rectangular Microstrip Patch Antenna for 5G Applications. s.l. : International Research Publication House, 2019. 0974-3154.
- CST. CST - Computer simulation technology. [Online] [Date: April, 17., 2021.] <https://www.cst.com/products/antennamagus>.

Modeling and simulation of high frequency electromagnetic field influence to tumor tissue

Zuzana Psenakova, Daniela Gombarska, Zuzana Judakova, Lucia Carnecka, Frederika Bacova
Department of Electromagnetics and Biomedical Engineering, Faculty of Electrical Engineering and Information Technology
University of Zilina
Zilina, Slovakia
<https://orcid.org/0000-0001-8898-5438>

Abstract— Modeling and simulation of the high-frequency electromagnetic field (EMF) influence tumor tissue is the main topic of this paper. It investigates the distribution of specific absorption rate (SAR) in a heterogeneous woman's breast model. We apply the frequency of EMF, commonly used in hyperthermia. The location of the tumor in the breast is changed for seven different positions to radiating antennas. The results were compared and evaluated. The lowest maximum SAR value in the tumor tissue was in case the tumor model was tilted by 10 mm to the side of the radiation axis of the antenna.

Keywords—modeling, simulation, electromagnetic field (EMF), tumor tissue, high frequency

I. INTRODUCTION

The effect of a high-frequency (HF) electromagnetic field (EMF) is mostly associated with thermal effects. The thermal effect is well reproducible with an almost linear course of the effect, depending on the amount of absorbed energy. In addition to thermal effects, EMF also has non-thermal effects. The results of studies examining non-thermal effects are often contradictory. It should be noted that the biological effects of the HF and low-frequency (LF) EMF overlap, and it is not possible to separate them. Each organism is unique in its biological response. Thus, specific exposure conditions may elicit a biological response in one but not in others. Therefore, it is important to select an adequate test group, organism, or cell.

Some effects of HF EMF have not been confirmed but are supposed, such as: the ability to induce changes in central nervous system nerve cells, including neuronal cell apoptosis, changes in the function of neural myelin sheaths and ion channels, induce malignant / non-malignant tumors, activate autophagic processes, adverse effects on the male and female reproductive organs and the potential to induce leukemia in children. Other effects have been confirmed by statistically significant results from various studies: neurological cognitive disorders such as headaches, tremors, dizziness, memory loss, loss of concentration, changes in EEG, sleep disorders and an increased incidence of schwannomas. [1] [2]

In 2011, the International Agency for Research on Cancer (IARC) reviewed the published literature and categorized radio-frequency electromagnetic field as a “possible” (Group 2B) human carcinogen.

The most frequently exposed tissue of the human body to high-frequency EMF is the brain due to widespread globally using of mobile phone, which is generally held to the ear. In 2001, the first indications of an elevated risk of brain tumors linked to the usage of cell phones were reported. [3] The impact of mobile phones on the development of malignant and

benign brain tumors was proven in the following years and it was found that most of RF energy, 97–99%, is absorbed in the brain hemisphere on the side where the phone is used. [4]

Effect of EMF field on cancer cells is different and depends on e.g., time of exposure, used frequency or cell type. The exposure of prostate cancer cell by 2.4 GHz EMF was examined here [5]. The effect of the field caused significant decrease in viability after 24 hours of incubation and a significant increase in viability after 48 and 72 hours, compared to the control samples. Significant increase of viability of another cancer cells, the human promyelocytic leukemia HL-60 cells, continuously exposed to 900 MHz RF-EMF for 1h per day for 3 consecutive days was reported. [6] Vice versa better survival rate of T lymphoblastoid leukemia cells exposed to 900 MHz have reported here. [7]

Some non-thermal bioeffects and adverse health effects are demonstrated at levels significantly below existing exposure standards given by ICNIRP/WHO and IEEE/FCC. To protect public health around the world, new biologically based exposure regulations for public are urgently needed. Rather than waiting for confirmation of danger, EMF exposure should be minimized now. [9][12]

Hyperthermia is a method of anticancer treatment that is relatively well known. However, only in the last 15 years has it become more widely known to the professional public. There were several reasons, such as unknown mechanisms of the effects of hyperthermia at the cellular and subcellular level, improving the technical equipment for performing hyperthermia, and publishing randomized studies evaluating the effect of adding hyperthermia to other modalities of anticancer therapy.

Hyperthermia utilizes the exposure of body tissue to high temperatures, which may reach up to about 40-50 °C. Several studies have shown high temperatures damage or destroy cancer cells, with less damage to normal healthy tissues. The tumour cells have worse blood flow, resulting in more sensitivity to temperature changes. Hyperthermia can be used to shrink tumours by destroying cancer cells and damaging proteins in their cell structures.

II. MODEL DESCRIPTION

Microstrip patch antennas are known for their performance, various types of designs, light construction, or lightweight. The use of these types of antennas has expanded in commercial areas due to low material and manufacturing costs in general. However, they are mainly known for their wide variety of uses. The range is wide including e.g. medical applications, satellites, and also in military systems. From medical applications, it is telemedicine, where are used in emergency and intensive care, in the care of chronic patients or it can be used in the treatment of malignant tumours. The

most commonly used antennas are those with an operating frequency of 2.45 GHz. This antenna is wearable and suitable for WBAN (Wireless Body Area Network). Compared to other types of antennas, microstrip patch antennas achieve a higher gain and radiation ratio from front to back and half-directional radiation, which prevents unwanted exposure of the patient. Here, microwave energy is considered to be the most effective way to induce hyperthermia. The design of the radiator used for this purpose should be easy to handle, durable, and light. These requirements are met in particular by microstrip patch antennas. The antenna is composed of a circular microstrip disk in the L-band, the device also contains two connected microstrip lines, which are separated by a flexible separation used to measure the temperature of the human body. [10]

For the antenna design, we set the minimum and maximum frequency so that the required value of 2.45 GHz is in the middle of the frequency band. We simulated the model for a frequency of 2.45 GHz.

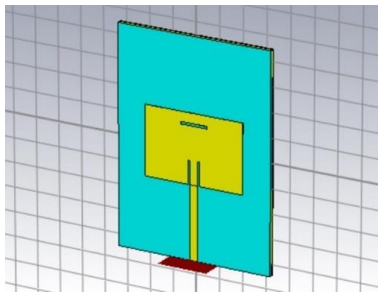


Fig. 1. Designed patch antenna

For the realization of the breast model and the realization of the simulation, we used the "CST Voxel Family" designed especially for the CST Studio Suite program. For the model, we chose the "EMMA" model, where we selected only the part containing the tissue structures of the breast, Fig.2.

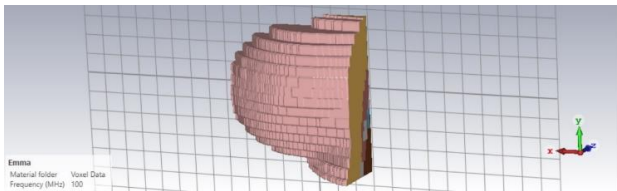


Fig. 2. Breast model – part of the EMMA heterogeneous woman model

For the tumour tissue, we used a simple spherical model with a diameter of 10 mm, the representation of which is in Fig. 3. For the creation, we use material properties that correspond to the parameters used in the expert article [11], Table 1.

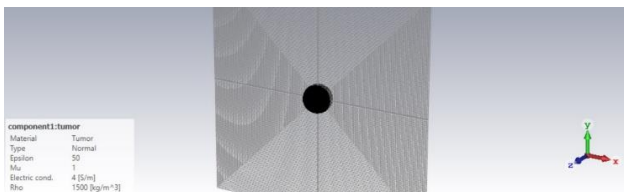


Fig. 3. Tumour tissue

Subsequently, we connected all the parts into one piece. The resulting model is shown in Fig. 4. We used two antennas to create the transmitter.

TABLE I. MATERIAL PROPERTIES OF TUMOR

Material	tumor
Type	normal
ε	50
μ	1
ρ	1500 kg.m ⁻³
σ	4 S.m ⁻¹

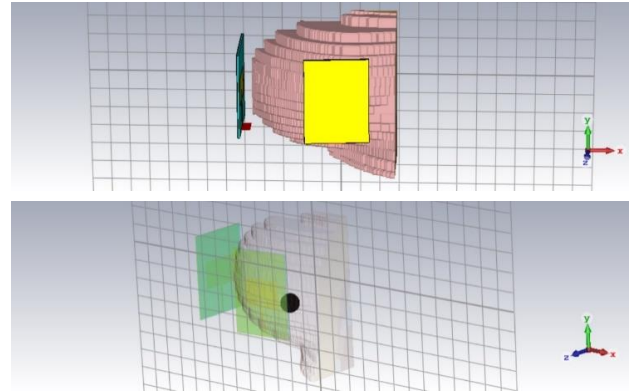


Fig. 4. Final model of transmitter and breast with tumour tissue

III. NUMERICAL MODELING

This work is based on electromagnetic fields modelling using the Finite Integration Technique (FIT) implemented within CST Microwave Studio. The FIT-based time-domain solver was applied on hexahedral mesh. The spatial-averaged SAR [W.kg⁻¹] in 10 g of tissue was calculated utilizing the algorithm described in the IEEE C95.3-2002

$$SAR(\mathbf{r}) = \frac{1}{V} \int_{element} \frac{\gamma(\mathbf{r})|\mathbf{E}(\mathbf{r})|^2}{\rho_m(\mathbf{r})} d\mathbf{r}^3 \quad (1)$$

Specifically, the values of SAR depend on γ – electrical conductivity [S/m], $|\mathbf{E}|$ – maximal value of intensity of the electric field [V/m], ρ_m – mass density [kg/m³] and \mathbf{r} – position [m], all of them in the tissue, using equation (1). [12], [13]

The exposure limits for EM fields have been established by International institution ICNIRP. [13] The recommended safety values are shown in the Table I.

TABLE II. THE SAR BASIC RESTRICTIONS FOR RANGE OF FREQUENCY BETWEEN 10MHZ AND 10 GHZ [13]

Exposure characteristics	Whole-body average SAR [W/kg]	Localized SAR (head and trunk) [W/kg]	Localized SAR (limbs) [W/kg]
Occupational exposure	0,4	10	20
General public exposure	0,08	2	4

We realize simulations for seven different cases by changing the position of the tumour tissue to monitor the effect of the optimal position on the transmitter.

To simulate the first case, we place the tumour tissue within the breast as close as possible to antenna number 1. The specific absorption rate, SAR has the highest value for this model 6.135 W.kg^{-1} , while its value in the middle of the tumour tissue is 3.637 W.kg^{-1}

In case 2 the tumour tissue model is displaced in the z-axis direction 10 mm deeper into the breast than in the previous model. The highest total SAR value for this simulation is 4.380 W.kg^{-1} , whereas in the tumour tissue is 2.732 W.kg^{-1} .

The following simulation case 3 has a model of tumour tissue compared to the simulation of model no. 1 shifted along the x-axis by 10 mm to the left. By calculating the SAR, we can notice that its maximum power for this model is 4.191 W.kg^{-1} and for tumour tissue is 1.928 W.kg^{-1} . Such a low SAR value in tumour tissue may also be due to a deviation of the tumour tissue model from the direct radiation direction of the nearest antenna.

In the case 4 simulation, we move the tumour tissue model in the direction of the y-axis by 20 mm higher compared to model no. 1. In the simulation we obtain a total SAR value of 4.578 W.kg^{-1} and the value in the middle of the tumor tissue from the simulation is 2.961 W.kg^{-1} .

In the simulation of case 5, we move the tumor tissue model in the direction of radiation of the second antenna, which is rotated by 90° . In contrast to the simulation of model no. 1, we displace the tumor tissue in the z-axis by 35 mm and in the x-axis by 70 mm. The resulting total SAR value for both antennas is 4.992 W.kg^{-1} and the highest value for tumor tissue is 3.690 W.kg^{-1} .

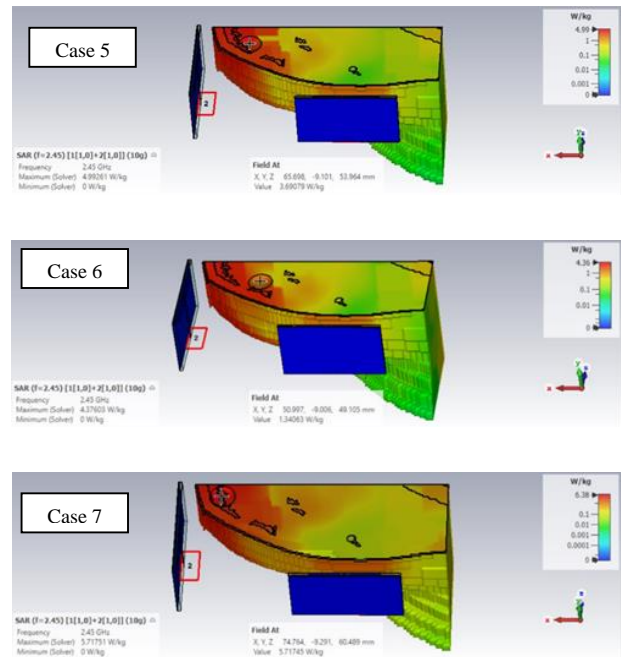


Fig. 5. The resulting SAR value in breast and tumor tissue for all cases.

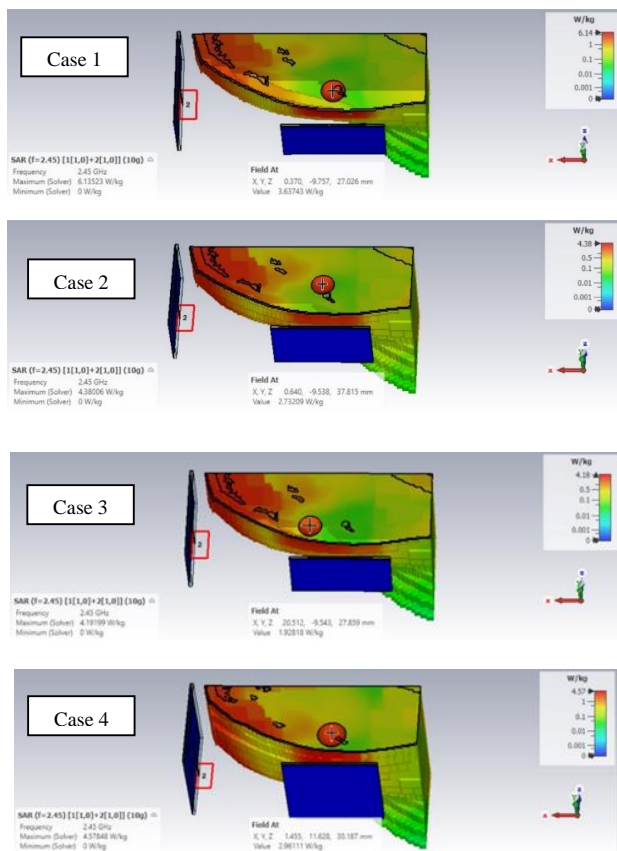
In case 6, we displace the tumor tissue from model no. 1 by 30 mm in the z-axis and by 50 mm on the x-axis. We obtain a SAR value of 4.376 W.kg^{-1} , while in the middle of the tumour tissue we measured a value of only 1.340 W.kg^{-1} , which could be caused by a greater distance from the primary irradiation antenna.

In the last simulation, we insert the tumor tissue close to the edge of the breast tissue, exactly 5 mm from the edge. The maximum SAR value and the SAR value in the middle of the tumor tissue are the same 5.717 W.kg^{-1} .

IV. CONCLUSION

We performed a total of 7 simulations in the CST Studio Suite environment. We observed a change in the value of the SAR, with a change in the distance of the tumor tissue from the antennas, as well as the effect of both antennas on the tumor tissue.

From the results shown in the paper, we can evaluate that the position of the tumor tissue had a huge effect on the electromagnetic field emitted by the antennas. The highest maximum value of the SAR was in the case of simulation of model no. 1, where it reached the value of 6.135 W.kg^{-1} . As for the maximum value in the middle of the tumor tissue, it was recorded in case 7 (antenna number 2) and its value was 6.388 W.kg^{-1} . From the results of case 1 and case 7, we can see how antennas interact with each other. Both tumor models had the same distance from the antennas and also from the edge of the breast tissue, but the tumor tissue was placed once near antenna number 1 and then in case 7 at antenna number 2. In case 1, the maximum SAR value in the middle of the tumor was 3.637 W.kg^{-1} , this tumor is lying in both radiation axes of the antennas. Compared to simulation case 7, the SAR value was almost half as high as 6.388 W.kg^{-1} , but the tumor tissue model was located outside the radiation axis of antenna number 1. This may be caused by the antenna coupling phenomenon.



The lowest maximum SAR value in the tumor tissue was in case 3 when the tumor model was tilted by 10 mm to the left of the radiation axis of antenna number 1. The SAR value was 1.928W.kg-1, which could be caused mainly by the fact that the tumor tissue was not located in either center of the radiation axis of any antenna.

In case 4, when the tumor tissue was shifted 20 mm higher than in the simulation of model no. 1, the SAR values in the middle of the tumor tissue did not differ much. Thanks to this case, we can conclude that the movement of the tumor tissue higher within the center of the radiation axis of the antenna does not have such an effect on the values of the specific rate of absorption - SAR.

Finally, we can assess that the SAR values were highest in cases where the tumor tissue was as close as possible to the antennas, and with increasing distance or lateral movement, the values in the middle of the tumor tissue decreased. We can also conclude from the results that both antennas influenced the SAR value of tumor tissue models, although it was influenced more by the antenna to which the tumor tissue was placed within its radiation axis.

ACKNOWLEDGMENT

This work was supported by the Slovak Research and Development Agency under the Contract no. APVV-19-0214.

REFERENCES

- [1] Falcioni, L., L. Bua, E. Tibaldi, M. Lauriola, L. De Angelis, F. Gnudi, D. Mandrioli, M. Manservigi, F. Manservigi, I. Manzoli, I. Menghetti, R. Montella, S. Panzacchi, D. Sgargi, V. Strollo, A. Vornoli A F. Belpoggi. Report of final results regarding brain and heart tumors in Sprague-Dawley rats exposed from prenatal life until natural death to mobile phone radiofrequency field representative of a 1.8 GHz GSM base station environmental emission. *Environmental Research* [online]. 2018, 165(December 2017), 496–503. ISSN 10960953. doi:10.1016/j.envres.2018.01.037
- [2] KIM, Ju Hwan, Jin Koo LEE, Hyung Gun KIM, Kyu Bong KIM a Hak Rim KIM. Possible effects of radiofrequency electromagnetic field exposure on central nerve system. *Biomolecules and Therapeutics* [online]. 2019, 27(3), 265–275. ISSN 20054483. Dostupné z: doi:10.4062/biomolther.2018.152
- [3] HARDELL, L., K. H. MILD, A. PÅHLSON a A. HALLQUIST. Ionizing radiation, cellular telephones and the risk for brain tumours. *European journal of cancer prevention* [online]. 2001, 10(6), 523–529. Dostupné z: https://journals.lww.com/eurjcancerprev/Abstract/2001/12000/Ionizing_radiation,_cellular_telephones_and_the.7.aspx
- [4] Cardis, E., I. Deltour, S. Mann, M. Moissonnier, M. Taki, N. Varsier, K. Wake A J. Wiart. Distribution of RF energy emitted by mobile phones in anatomical structures of the brain. *Physics in Medicine and Biology* [online]. 2008, 53(11), 2771–2783. ISSN 00319155. Dostupné z: doi:10.1088/0031-9155/53/11/001
- [5] Górski, Romuald, Agnieszka Nowak-Terpiłowska, Paweł Śledziński, Mikołaj Baranowski A Stanisław Wosiński. Morphological and cytophysiological changes in selected lines of normal and cancer human cells under the influence of a radio-frequency electromagnetic field. *Ann Agric Environ Med* [online]. 2021, 28(1), 163–171 [vid. 2021-07-02]. Dostupné z: doi:10.26444/aaem/118260
- [6] Jin, Zongda, Chunyan Zong, Bingcheng Jiang, Zhen Zhou, Jian Tong A Yi Cao. The Effect of Combined Exposure of 900 MHz Radiofrequency Fields and Doxorubicin in HL-60 Cells. *PLoS ONE* [online]. 2012, 7(9), 3–7. ISSN 19326203. Dostupné z: doi:10.1371/journal.pone.0046102
- [7] Marinelli, F., D. La Sala, G. Ciccioiti, L. Cattini, C. Trimarchi, S. Putti, A. Zamparelli, L. Giuliani, G. Tomassetti a Caterina CINTI. Exposure to 900 MHz Electromagnetic Field Induces an Unbalance between Pro-Apoptotic and Pro-Survival Signals in T-Lymphoblastoid Leukemia CCRF-CEM Cells. *Journal of Cellular Physiology* [online]. 2004, 198(2), 324–332. ISSN 00219541. Dostupné z: doi:10.1002/jcp.10425
- [8] Radil R.; Barabas, J.; Janousek, L., Bereta, M.: Frequency dependent alterations of *S. Cerevisiae* proliferation due to LF EMF exposure ; *Advances in Electrical and Electronic Engineering* [print, electronic]. - ISSN 1336-1376. - Roč. 18, č. 2 (2020), s. 99-106. SCOPUS; Web of Science Core Collection
- [9] MISEK, J.; VETERNIK, M.; TONHAJZEROVA, I.; JAKUSOVA, V.; JANOUSEK, L.; JAKUS, J.: Radiofrequency Electromagnetic Field Affects Heart Rate Variability in Rabbits, *PHYSIOLOGICAL RESEARCH*, ISSN 1802-9973 (online), 2020 Institute of Physiology of the Czech Academy of Sciences, Prague
- [10] Singh, Indrasen a Tripathi, V.S. . Micro strip Patch Antenna and its Applications. [Online] Október 2011. [Dátum: 28. Február 2021.] <https://citeseerx.ist.psu.edu/viewdoc/download?doi=10.1.1.208.7887&rep=rep1&type=pdf>.
- [11] Ouerghi, K., a ini. arxiv.org. [Online] 2017. [Dátum: 5. November 2020.] <https://arxiv.org/ftp/arxiv/papers/1801/1801.05068.pdf>.
- [12] Mydlova, J.; Benova, M.; Pitlova, E.: Assessment of SAR in human body model with the cochlear implant inside a railway vehicle; January 2019; *Transportation Research Procedia* 40:1489-1496; DOI: 10.1016/j.trpro.2019.07.206
- [13] Psenakova, Z. ; Benova, M.; Laukova, T.: Investigation of Specific Absorption Rate (SAR) near Model of Fetus in Uterus, 2020 ELEKTRO conference, DOI: 0.1109/ELEKTRO49696.2020.9130308

Amplitude synthesis of linear antenna array by Taguchi method

Deubauh Cedrick Dassrah GNAWA, Pavel Karban* *University of West Bohemia, Univerzitni 26, 306 14 Pilsen, Czech Republic, gnawa{karban}@fel.zcu.cz

Abstract—In this paper, Taguchi method, which is a relatively novel optimization technique, is employed. Based on the concept of the orthogonal array, Taguchi method effectively reduces the number of tests required in an optimization process. This method has been successfully applied in many fields such as chemical engineering, mechanical engineering, IC manufacturing, power electronics, etc. In this work, the Taguchi method is applied to optimize linear array antennas for sidelobe level reduction. The optimization process is carried out by controlling the array parameter specifically the element excitations amplitude. The numerical results optimized by Taguchi's method are compared by uniform amplitude linear antenna array.

Index Terms—Radiation Pattern, Amplitude, Array Factor, Linear Antenna Array, Synthesis Method, Taguchi's Method

I. INTRODUCTION

Optimizations of linear antenna arrays have received great attention in the electromagnetics community for many civilian and military applications. In fact, the synthesis of antenna arrays plays a very important role in communication systems. one of the problems related to linear array design is the quantization of the amplitudes. The traditional technique of amplitude synthesis is analytical methods such as Fourier, Chebyshev, Binomial, Blackman, Hamming, Gaussian, Kaiser-Bessel, etc. [1].

Recently, another global optimization technique such as Taguchi's method [2], has been introduced to the electromagnetic and antennas communities[3], [4], [5], [6], [7]. It was successfully used to optimize linear antenna arrays, ultra-wideband antenna, planar microwave filter design, and coplanar waveguide (CPW) slot antenna. In this paper it's used to regulate amplitude parameter to achieve minimum side lobe level .This paper is organized as follows. Taguchi's method and The formulation of the array factor for linear are briefly described in Section II. The numerical results are given in Section 3. Finally, section 4 makes conclusions.

II. MATERIALS AND METHODS

Taguchi's optimization method will be briefly described here. Using the concept of the orthogonal array (OA), Taguchi method effectively reduces the number of tests required in an optimization process. For more details, the interested reader may consult [3], [4], [5], [6], [7]. The steps taken in Taguchi's optimization can be illustrated in Fig.(1)) [3]

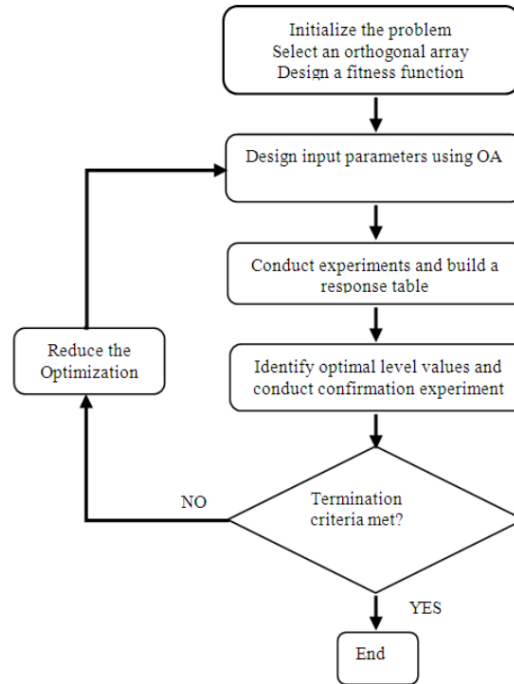


Fig. 1. Flow chart of Taguchi Method

A. Taguchi's Optimization Method

• Initializing the Problem

The optimization procedure begins with the problem initialization, which includes the selection of a proper OA [8], and an appropriate design of the fitness function. The selection of an OA depends on the number of input parameters of the optimization problem, and the number of levels of each parameter. Usually three levels are necessary for each input parameter to describe the non linear effect. The fitness function is devised according to the optimization goal. In an evaluation algorithm, usually either the maximum or minimum fitness is to be achieved [3]

• Designing Input Parameters Using an OA

In this step, the input parameters are selected to guide the experiments (i.e., the evaluation of the fitness function) For an orthogonal array with $s = 3$, the value of the level 2 for each parameter is chosen at the center of the optimization range corresponding to that parameter. Then, the values of the other levels(1 and 3) are respectively evaluated by subtracting and

adding a specific "level difference" (LD) to the value of level 2. The equation which determines the level difference in the first iteration is taken as [3].

$$LD_1 = \frac{(max - min)}{s + 1} \quad (1)$$

where "max" and "min" are the upper and lower bounds of the optimization range respectively. in our case min=0.1 and max=1

• Conducting Experiments

After converting the OA entries to proper input values, the fitness function for each experiment can be calculated analytically or through numerical simulations. The fitness value is used to calculate the corresponding S/N ratio (η) in Taguchi's method[1] through the following formular:

$$\eta = -20 \log (Fitness) \quad (dB) \quad (2)$$

After conducting all the experiments and finding the fitness values and the corresponding S/N ratio, a response table is built by averaging the S/N for each parameter n and level m using[3].

$$\bar{\eta}(m, n) = \frac{1}{N} \sum_{i, OA(i,n)=m} \eta_i \quad (3)$$

• Identifying Optimal Level Values and Conducting Confirmation Experiment

When the response table is established, the optimal level for each parameter can be identified by finding the largest S/N ratio in the corresponding column of the response table. Next, a confirmation experiment is done by using the combination of the optimal level values, ($a_n|_i^{opt}$) determined in the response table. The fitness value obtained from the optimal combination is regarded as the fitness value of the current iteration [3].

• Reducing the Optimization Range

If the termination criteria are not satisfied, the optimal level for the current iteration will be the center of the next iteration.

$$a_n|_{i+1}^2 = a_n|_i^{opt} \quad (4)$$

Also, the optimization range for the next iteration is minimized by multiplying the current level difference by the reducing rate (rr) eq.(5). rr can be set between 0.5 and 0.9 according to the problem[3]. So for $(i + 1)^{th}$ iteration

$$LD_{i+1} = RR(i) \times LD_1 = rr^i \times LD_1 \quad (5)$$

Where $RR(i) = rr^i$ is called the reduced function [3]-

• Checking the termination criteria

Each time the number of iteration increases, the level difference of each element decreases. So the level values are near to each other and the fitness value of next iteration is close to the fitness value of the current iteration. The next equation

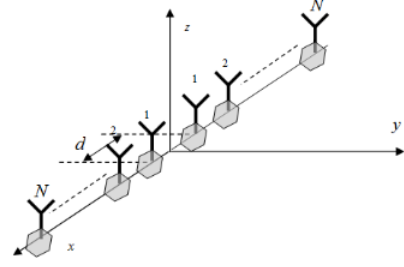


Fig. 2. Geometry of 2N-element symmetric linear antenna

can be used as a termination criteria for the optimization procedure.

$$\frac{LD_{i+1}}{LD_1} \leq \text{converged value} \quad (6)$$

Usually, the converged value can be set between 0.001 to 0.01 depending on the problem. If the the design targets are achieved or eq.6 is satisfied, the optimization process will finish. Finally, the above steps are repeated until a specific number of iteration is reached.

B. Design of a Linear Antenna Array

In this section Taguchi's is used to synthesis of linear antenna array to minimize the maximum side lobe level(SLL) by controlling only amplitude of each antenna. In fig ?? the geometry of the antenna is presented.

Which has N equally spaced elements along the axis x. The element spacing is half-wavelength and the excitations of array elements are symmetric with respect to the axis z.

For a 2N elements symmetrical array shown in Figure 2 , the array factor (AF) can be written as:

$$AF(\theta) = \sum_{n=1}^{2N} I_n e^{j[kx_n \cos(\theta) + \varphi_n]} \quad (7)$$

Where k is the wave number, and I_n , x_n , φ_n are respectively, the excitation amplitude , phase, and location of elements [9]

Equation 7 can be simplified to equation 8 if we assumed that the 2N isotropic radiators are placed symmetrically along the x-axis.

$$AF(\theta) = 2 \sum_{n=1}^N I_n \cos [kx_n \cos(\theta) + \varphi_n] \quad (8)$$

From equations8, we can conclude that three parameters are controlling the AF: the amplitudes, the phases, and the positions of the elements. In this study, only the amplitudes are considered, so the phase shift weights(zero degree) and the positions element((half-wave length) are constant. the array factor can be written in the below equation9 and 10:

$$AF(\theta) = 2 \sum_{n=1}^N I_n \cos [(n - 0.5)\pi \cos (\theta)] \quad (9)$$

And in its normalized form:

$$AF(\theta) = \frac{1}{N} \sum_{n=1}^N I_n \cos [(n - 0.5)\pi \cos (\theta)] \quad (10)$$

This equation represents a mathematical description of the antenna radiation pattern and can be used by optimization algorithms. The Taguchi algorithm is able to search for optimal amplitudes weights using a fitness function based on this array factor.

III. NUMERICAL RESULTS

The following examples were used to demonstrate the performance of the Taguchi algorithm. We will regulate the amplitude parameter to reduce the side lobe (SSL). To resolve the problem the excitation magnitude of the 2N- elements will be optimized in the range [0.1, 1], 10 elements, 16 elements, and 24 elements linear antenna (LA) will be examples of the optimization using Taguchi's method.

The following fitness function can be used in the optimization.

$$fitness = \min(\max(20 \log(|AF(\theta)|)) \quad (11)$$

Subject to $\theta = [0, 76]$ and $[104, 180]$

Using equation 11 and applying Taguchi's optimization method on 10 elements LA, the obtained radiation pattern is shown in Figure 3. The results were as follows:

[1. 0.90180965 0.72774012 0.51533462
0.41584578]

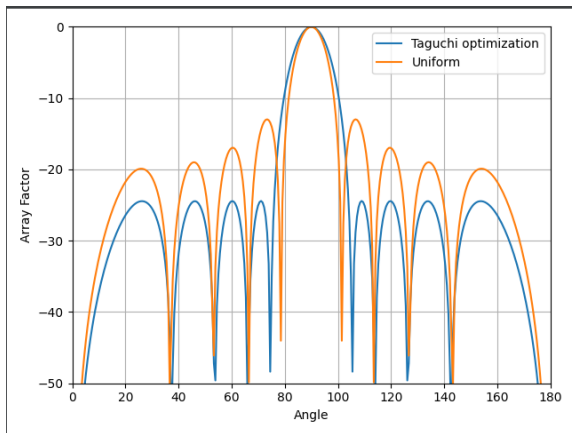


Fig. 3. pattern of 10 elements array optimized with Taguchi with respect to amplitudes, compared with conventional array.

The goal of the optimization is obtained after 70 iterations. Figure 4 shows the convergence of the fitness function versus the iteration number. Figure 3 shows the radiation pattern in the azimuth plane compared with uniform array.

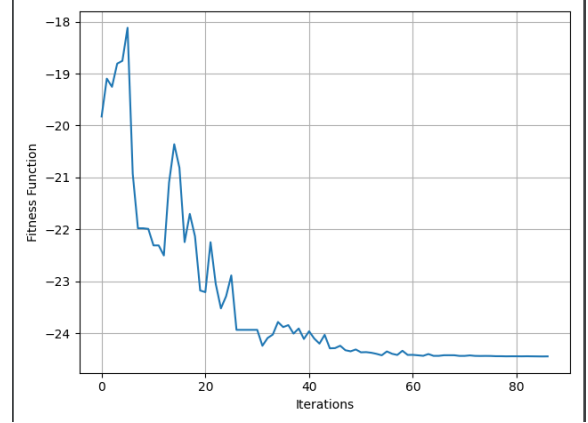


Fig. 4. curve of the fitness value of the 10-elements LA.

The maximum obtained SLL is -24.4467 dB, while the maximum SLL of the uniform one is -12.9651 dB. The obtained SLL is less than the uniform one of about 11.4816 dB.

In this example, Taguchi's optimization method will be applied on 16 elements LA. the radiation pattern is shown in Figure 5, and the results are as follows: The optimum values of the amplitudes are [1. 0.95217331 0.86399057 0.74308687 0.60203718 0.45697653 0.31829103 0.29046641]

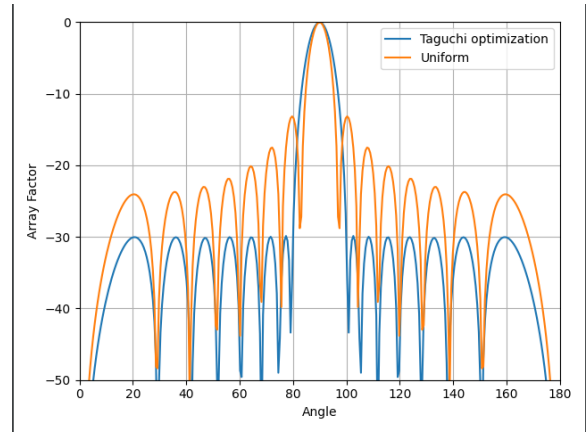


Fig. 5. pattern of 16 elements array optimized with Taguchi with respect to amplitudes, compared with conventional array.

The max SLL for the uniform array is -13.1480, while the max SLL for the optimized array is -30.0192 dB.

The goal of the optimization can be obtained after 70 iterations. Figure 6 shows the convergence of the fitness function versus the iteration number. Figure 5 shows the radiation pattern in the azimuth plane compared with uniform array. The maximum obtained SLL is -30.0192 dB, while the maximum SLL of the uniform one is -13.1480 dB. The obtained SLL is less than the uniform one of about 16.8712 dB.

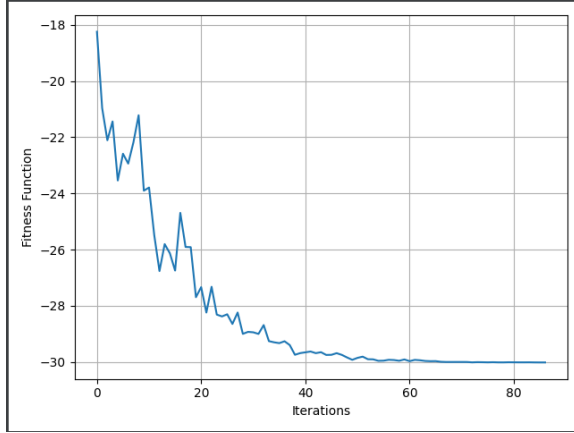


Fig. 6. curve of the fitness value of the 16-elements LA.

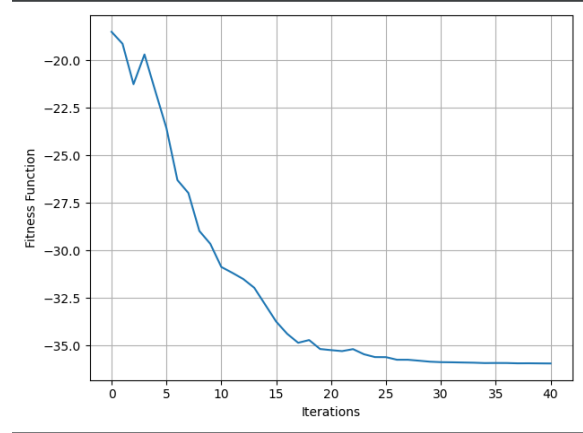


Fig. 8. curve of the fitness value of the 24-elements LA.

The radiation pattern of an optimized 24 elements LA is shown in Figure 7. The optimum values of the amplitudes are:

[1. 0.99349205 0.9516717 0.86907703 0.76493135
0.66250827 0.56634471 0.46401296 0.36497682
0.27034795 0.16613199 0.17135853]

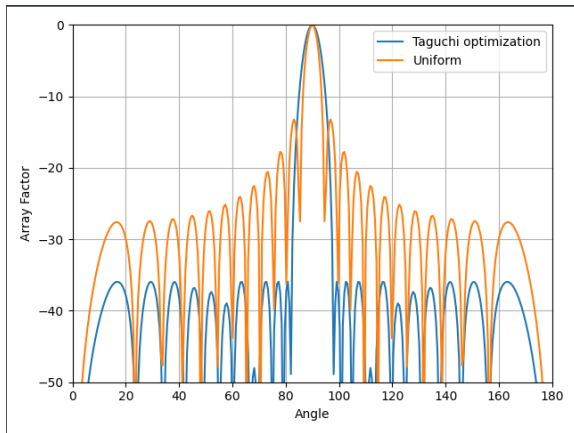


Fig. 7. pattern of 24 elements array optimized with Taguchi with respect to amplitudes, compared with conventional array.

The goal of the optimization can be obtained after 40 iterations. Figure 8 shows the convergence of the fitness function versus the iteration number. Figure 7 shows the radiation pattern in the azimuth plane compared with uniform array. The maximum obtained SLL is -35.9489 dB, while the maximum SLL of the uniform one is -13.9545 dB. The obtained SLL is less than the uniform one of about 21.9944 dB.

IV. CONCLUSION

In this paper, a global optimization technique based on Taguchi's method is used in the synthesis of linear antenna array. Optimized results show that the suppression of array factor side lobe, are successfully obtained. The results prove that Taguchi's method is a good candidate for optimizing various electromagnetic applications.

ACKNOWLEDGMENT

This work was supported by grant of the Czech Science Foundation (GACR), project No. 20-02046S and by an internal project SGS-2021-011.

REFERENCES

- [1] T. Vu, "Simultaneous nulling in sum and difference patterns by amplitude control," *IEEE Transactions on Antennas and Propagation*, vol. 34, pp. 214–218, Feb. 1986. Conference Name: IEEE Transactions on Antennas and Propagation.
- [2] "Taguchi's Quality Engineering Handbook | Wiley."
- [3] W.-C. Weng, F. Yang, and A. Elsherbeni, "Electromagnetics and Antenna Optimization Using Taguchi's Method," *Synthesis Lectures on Computational Electromagnetics*, vol. 2, pp. 1–94, Jan. 2007. Publisher: Morgan & Claypool Publishers.
- [4] A. El-Hajj, K. Kabalan, and M. Al-Husseini, "Antenna array design using spreadsheets," *IEEE Transactions on Education*, vol. 46, pp. 319–324, Aug. 2003. Conference Name: IEEE Transactions on Education.
- [5] A. Safaai-Jazi, "A new formulation for the design of Chebyshev arrays," *IEEE Transactions on Antennas and Propagation*, vol. 42, pp. 439–443, Mar. 1994. Conference Name: IEEE Transactions on Antennas and Propagation.
- [6] W.-C. Weng, F. Yang, and A. Z. Elsherbeni, "Linear Antenna Array Synthesis Using Taguchi's Method: A Novel Optimization Technique in Electromagnetics," *IEEE Transactions on Antennas and Propagation*, vol. 55, pp. 723–730, Mar. 2007. Conference Name: IEEE Transactions on Antennas and Propagation.
- [7] W.-C. Weng and C. T. M. Choi, "Optimal Design of CPW Slot Antennas Using Taguchi's Method," *IEEE Transactions on Magnetics*, vol. 45, pp. 1542–1545, Mar. 2009. Conference Name: IEEE Transactions on Magnetics.
- [8] "Orthogonal Arrays."
- [9] "Antenna Theory: Analysis and Design, 4th Edition | Wiley."

SESSION 5 - ELECTROMECHANICAL SYSTEMS

Kinematics of the movement of the pilot of a paraglider simulator

P. Stašek¹, P. Karban¹, Members, IEEE

¹University of West Bohemia, Czech Republic, {stasekp, karban}@fel.zcu.cz

This paper deals with kinematics and the design and implementation of the paraglider simulator drives. Part of this article contains the necessary calculations, that are important for the mechanical design and manufacture of drives. There are given reasons which led to using 3D printing. The project aims to present the design of drives control, which includes the solution to the kinematics problem of the simulator. Finally, the equations determining the length of ropes for a given point of the seat in space are shown.

Index Terms—Paragliding simulator, paragliding, 3D printing, design of actuator, linear actuator, drum winch, cable-driven parallel robot, forward kinematics, inverse kinematics

I. INTRODUCTION

Paraglider is a lightweight, free-flying, foot-launched glider aircraft with no rigid primary structure. The pilot sits in a harness suspended below a fabric wing. Wing shape is maintained by the suspension lines, the pressure of air entering vents in the front of the wing, and the aerodynamic forces of the air flowing over the outside.

The simulator aims to simulate flying in a paraglider as reliably as possible and thus train pilots in various situations that may occur while flying. This can be realized by means of coordinated movements of the seat with the support of virtual reality.

II. PROBLEM FORMULATION

The paraglider simulator was designed using 5 drives. One provides movement in the vertical direction and 4 then movement in the vertical direction, tilting and pivoting in the axis. Their layout is shown in Figure 7 and was determined based on several control calculations. The vertical seating of the individual side drives can be changed (more details in [1]).

The harness is attached to the structure behind the free ends, which in real flight are tied to the ropes that connect them to the canopy. The lower part of the seat is attached to the side drives and serves to deflect it during the simulation.

The other two drives are used to simulate the control of the glider's control ropes, which deform the trailing edge of the canopy. However, these drives do not serve to move the harness directly and will not be considered in the following text.

The simulator uses an application developed within the project solution written in the Unity3D environment to visualize the glider's flight in space. The pilot can choose between displaying on a monitor or using 3D glasses and virtual reality. VR significantly increases the experience of flying a paraglider. In the virtual environment, several important places are currently prepared for flying on PG, such as Javorový vrch or Raná in the Czech Republic, and other places in the world are being prepared. The simulations are based on the physical principles of the glider's flight in free space and will suitably influence the pilot's position in the simulator's working window thanks to the drives. Paraglider flight can

be described with sufficient approximation with the help of Newtonian physics [3], [4].

The simulator will be used to acquaint pilots with new terrains, search for the optimal route for landing in various conditions and training of standard and non-standard flight conditions. It is mainly a direct flight, finding the minimum and maximum speed of the glider, turn, asymmetric folding and frontstall in turbulent conditions. This will allow beginners and advanced pilots to safely practice the conditions that can occur during a real flight.

III. MATHEMATICAL MODEL

The mathematical model of the kinematics of the harness movement in the simulator can be derived from the following ratios. Figure 1 is basic for further calculations. It serves to imagine the basic state in the horizontal plane, when the dimensions of the seat are neglected and it is replaced by the point S , which is randomly placed in space.

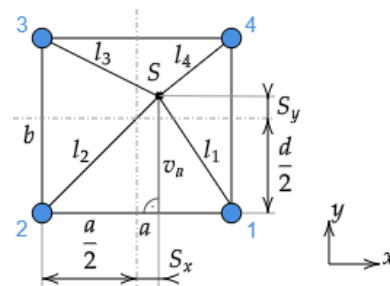


Fig. 1. Randomly selected position in the horizontal plane

If the coordinates of the point S and the distance between the drives a and b are given, it is possible to calculate the lengths of the ropes using right triangles. Because the drives on the simulator are placed at the corners of the structure with a slight offset to the center of the walls of the block structure, the distances between the drives form a rectangle with sides of a and b . The lengths of the individual can then be expressed as

$$l_1^2 = \left(\frac{a}{2} - S_x\right)^2 + \left(\frac{b}{2} + S_y\right)^2,$$

$$l_2^2 = \left(\frac{a}{2} + S_x\right)^2 + \left(\frac{b}{2} + S_y\right)^2,$$

$$l_3^2 = \left(\frac{a}{2} + S_x\right)^2 + \left(\frac{b}{2} - S_y\right)^2,$$

$$l_4^2 = \left(\frac{a}{2} - S_x\right)^2 + \left(\frac{b}{2} - S_y\right)^2.$$

Now the construction will be a bit complicated by introducing the spacing of the harness mountings again in the shape of a rectangle of dimensions e and f and including the crossing of ropes, thanks to which the harness can be rotated by an angle μ .

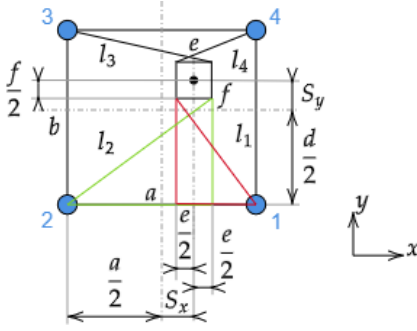


Fig. 2. Selected position including the crossing of the rope attachment

The configuration is shown in the following Fig. 2 and expressions similar to the previous solution are given below

$$l_{1,h}^2 = \left(\frac{a}{2} + \frac{e}{2} - S_x\right)^2 + \left(\frac{b}{2} - \frac{f}{2} + S_y\right)^2,$$

$$l_{2,h}^2 = \left(\frac{a}{2} + \frac{e}{2} + S_x\right)^2 + \left(\frac{b}{2} - \frac{f}{2} + S_y\right)^2,$$

$$l_{3,h}^2 = \left(\frac{a}{2} + \frac{e}{2} + S_x\right)^2 + \left(\frac{b}{2} - \frac{f}{2} - S_y\right)^2,$$

$$l_{4,h}^2 = \left(\frac{a}{2} + \frac{e}{2} - S_x\right)^2 + \left(\frac{b}{2} - \frac{f}{2} - S_y\right)^2.$$

Now comes the last step in solving the length of the ropes from the perspective of the xy -plane - including the rotation of the angle μ . Along with the rotation, the coordinates of the harness mounts also change and these must be derived. The handles are again arranged in the shape of a rectangle with sides e and f , for calculations it is necessary to determine half the length of the diagonal of the rectangle according to the following relationship

$$k = \sqrt{\left(\frac{e}{2}\right)^2 + \left(\frac{f}{2}\right)^2}. \quad (1)$$

As shown in the Fig. 3, all four lengths of the side drive ropes can now be determined from the perspective of the xy -plane. The terms of $\frac{e}{2}$ and $\frac{f}{2}$ are replaced by new terms

$$k_{\delta_s}^+ = k \cdot \sin\left(\frac{\delta}{2} + \mu\right), \quad k_{\delta_s}^- = k \cdot \sin\left(\frac{\delta}{2} - \mu\right),$$

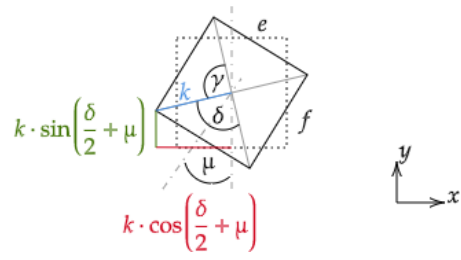


Fig. 3. Rotation of ropes in the plane

$$k_{\delta_c}^+ = k \cdot \cos\left(\frac{\delta}{2} + \mu\right), \quad k_{\delta_c}^- = k \cdot \cos\left(\frac{\delta}{2} - \mu\right).$$

The result is the following relationships

$$l_{1,r} = \sqrt{\left(\frac{a}{2} + k_{\delta_s}^- - S_x\right)^2 + \left(\frac{b}{2} - k_{\delta_c}^- + S_y\right)^2}$$

$$l_{2,r} = \sqrt{\left(\frac{a}{2} + k_{\delta_s}^+ + S_x\right)^2 + \left(\frac{b}{2} - k_{\delta_c}^+ + S_y\right)^2}$$

$$l_{3,r} = \sqrt{\left(\frac{a}{2} + k_{\delta_s}^- + S_x\right)^2 + \left(\frac{b}{2} - k_{\delta_c}^- - S_y\right)^2}$$

$$l_{4,r} = \sqrt{\left(\frac{a}{2} + k_{\delta_s}^+ - S_x\right)^2 + \left(\frac{b}{2} - k_{\delta_c}^+ - S_y\right)^2}$$

These relations completely express the length of the ropes of individual drives from the point of view of the xy -plane, but in reality they are inclined in the y -axis due to the different height of the drives compared to the rope seat. It is therefore necessary to include this inclination in the calculations and thus calculate the actual lengths of ropes $l_{n,C}$. The idea leading to the calculation of these lengths is shown in the Fig. 4. It

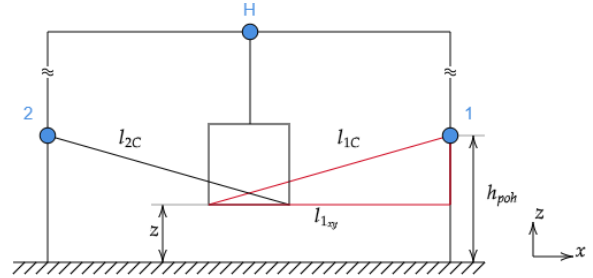


Fig. 4. Inclusion of the inclination of the ropes in the y -axis

follows from this sketch that the actual length of the rope is calculated as a hypotenuse of the red marked triangle, the first slope of which is the length $l_{n,xy}$ calculated in the previous relations and the second slope is the height of the drive location h_p reduced by the specified seat coordinate z . According to the following relationship

$$l_{n,t} = \sqrt{l_{n,xy}^2 + (h_p - z)^2}.$$

it is already possible to determine the final form of the relations for calculating the length of the ropes, which, however, take into account the rigid construction of the seat in the form

$$l_{1,t} = \sqrt{\left(\frac{a}{2} + k_{\delta_s}^- - S_x\right)^2 + \left(\frac{b}{2} - k_{\delta_c}^- + S_y\right)^2 + (h_p - z)^2},$$

$$l_{2,t} = \sqrt{\left(\frac{a}{2} + k_{\delta_s}^+ + S_x\right)^2 + \left(\frac{b}{2} - k_{\delta_c}^+ + S_y\right)^2 + (h_p - z)^2},$$

$$l_{3,t} = \sqrt{\left(\frac{a}{2} + k_{\delta_s}^- + S_x\right)^2 + \left(\frac{b}{2} - k_{\delta_c}^- - S_y\right)^2 + (h_p - z)^2},$$

$$l_{4,t} = \sqrt{\left(\frac{a}{2} + k_{\delta_s}^+ - S_x\right)^2 + \left(\frac{b}{2} - k_{\delta_c}^+ - S_y\right)^2 + (h_p - z)^2}.$$

The correctness of the derived relations was verified by simple simulations in the GeoGebra [5] application and they correspond to the real simulator with sufficient accuracy.

IV. EXPERIMENTAL VERIFICATION

Experimental verification of derived equations is currently being tested on a prototype simulator. The construction was constructed from universal aluminum profiles and thanks to them it is easy and disassembled and adjustable. The software part is developed in the Unity3D environment and is run on a computer with a powerful graphics card. Communication between the servomotor driver and the computer is ensured by means of several Arduino [2], on which our own state machine is developed.

The vertical drive (see Fig. 5) is dimensioned for a nominal load of a pilot weighing 100 kg. For the drive of this axis, a linear type of drive with a ball screw was chosen, the great advantage of which is minimal friction losses, high accuracy and, with suitable lubrication, also a long service life. The drive unit of the drive is a Kinco SMH110D-0157-30ABK-4HKC brake servomotor with a nominal power of 1.6 kW, a torque of 5 Nm at a maximum speed of 3000 RPM and a nominal current of 6 A. A maximum speed of 0.8 m/s can be determined from the drive and ball screw parameters. Such speed is sufficient for the simulator.

The main supporting element of the drive consists of an aluminum milled plate, on which two bearing housings of a ball screw and two rails of a precise linear ball guide are mounted. The movable part of the drive is then formed by a milled sliding cube, on which two carriages of a linear guide and a flange nut of a ball screw are fixed. Furthermore, the sliding cube contains two suspension eyes, one for the seat rope and the other oppositely oriented for the steel rope carrying the counterweight. The servomotor is attached to the structure by a third milled aluminum part. The mechanical connection of the servomotor and the ball screw is formed by a flexible coupling that absorbs shocks acting on the motor shaft (see Fig. 6). An important element of the construction are also 3 inductive sensors, monitoring the starting and end positions.

The side drives are dimensioned for a force of 490 N due to the maximum expected deflection (30 degrees) of the pilot

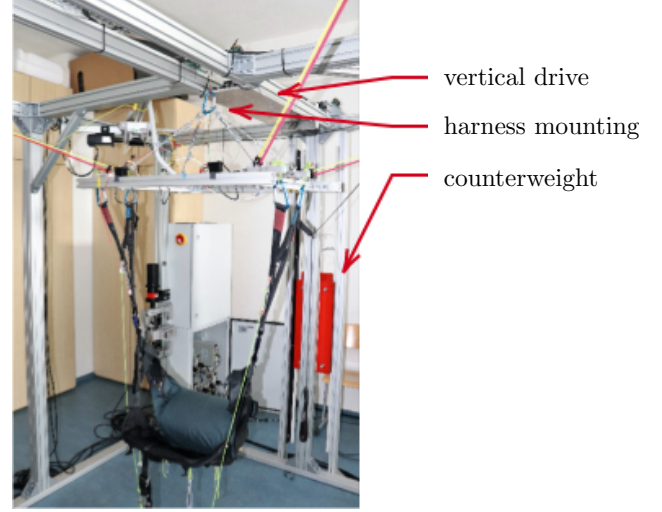


Fig. 5. Vertical drive of the paraglider simulator

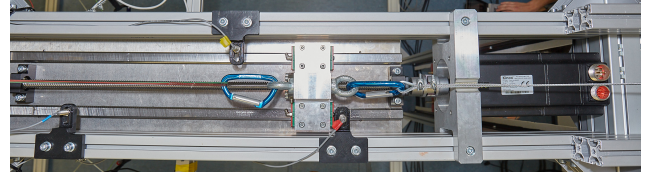


Fig. 6. Detail of vertical drive of the paraglider simulator

in harness. Unlike the z -axis drive, the side drives not only require faster movement with less load, but also move with a rope length of approximately 1.5 m. Linear feed is no longer very suitable for such an application and would also be much more spacious, so a drive in the form of a winding drum was chosen. In order to make better use of the power of the servomotor, it is necessary to use a gearbox, with a suitable flange that matches the used Kinco SMH80S-0100-30AXK-3LKX servomotor with a nominal power of 1.0 kW, a torque of 3.2 Nm at a maximum speed of 3000 RPM and a nominal current of 6.3 A (see Fig. 7).

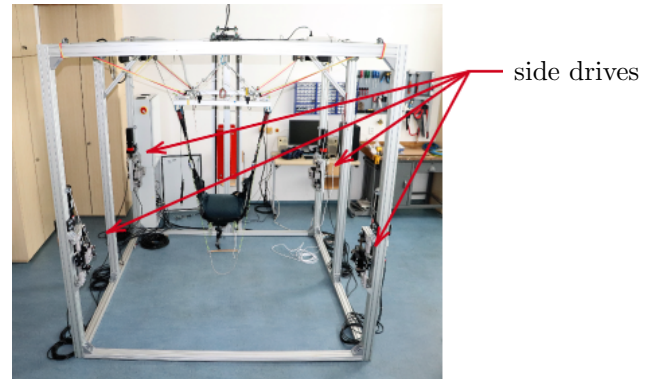


Fig. 7. Side drives of the paraglider simulator

In the case of the winding drum, there is a risk that the wound cable will tangle during rapid unwinding, so the drive

has been provided with a guide device which allows the rope to be placed in an orderly manner on the winding drum.

Much lower safety requirements are placed on the side drives than on the top drive. In the extreme case - failure of multiple drives, the user sitting in the seat will automatically return to an equilibrium position with a low probability of injury. For this reason, the costly production of a large number of parts on a CNC milling machine was abandoned, instead the FFF/FDM 3D printing technology applied to as many parts as possible was chosen. This method of production allows considerable flexibility in the design and assembly of drives. The disadvantage of elements created by 3D printing is their worse mechanical properties compared to plastic parts, which are created, for example, by means of injection molding machines, but for the needs of the simulator the strength of the parts is sufficient.

The material, which has the most suitable parameters for the production of many stressed drivers parts is PETG. It has good mechanical properties and is printed well. Good material for the cases of rollers in the guide device is FLEX material, which is softer than PETG and this causes better grip of the rope. Before printing, it is important to configure the part in the slicer correctly. It is necessary to monitor the direction of the load and the lowest possible material consumption. After the end of the project, serial production can take place, so the parts must be printed in the shortest possible time. In the current version, it took approximately 400 hours to print the parts for the four side drives.

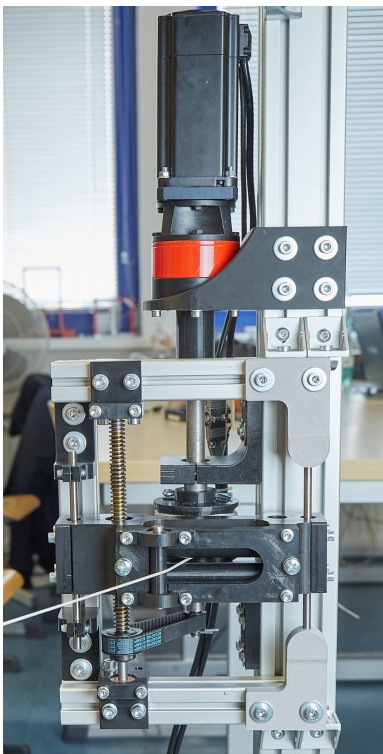


Fig. 8. Detail of side drive of the paraglider simulator

V. COMPARISON WITH REAL FLIGHT

The tilting movement of the seat in the vertical direction will be confronted with the feelings of real flight on a paraglider. At present, flight data such as position, speed and acceleration are collected at every moment of the flight on real flight terrains (Doubrava in the Pilsen Region). This data will be used together with the data from the simulation in Unity3D to evoke the most reliable feeling from the flight. The derived kinematic model will be used to adjust the position and rotation of the harness using servomotors.

VI. CONCLUSION

A kinematic model of harness movement with a pilot in a paraglider simulator was presented. The movement is realized using the technology of rope robots and its purpose is to induce a feeling of real flight. The hardware part is supplemented by software with virtual reality using glasses.

Further research will be directed to mapping other flight terrains and setting both parts of the simulator according to real situations that occur during the flight (use of rising thermal hot air [6], XC flights, landing on accuracy) or non-standard situations to which the pilot must respond adequately quickly. The simulator significantly changes the way new pilots train in training centers and increases the safety and readiness of pilots. The research is supported by the Light Aircraft Association of the Czech Republic (LAA).

ACKNOWLEDGMENT

This research has been supported by the project of the Technology Agency of the Czech Republic with number FW01010257: Paragliding Flight Simulator and internal project of UWB and University Students Project SGS-2021-011.

REFERENCES

- [1] Stašek, P.: Design of Main Drives of Paraglider Simulator (written in Czech), bachelor thesis, UWB in Pilsen, 2021.
- [2] Sivera, R.: Advanced Control of Servomotors for Paraglider Simulator (written in Czech), bachelor thesis, UWB in Pilsen, 2021.
- [3] Müller, Marcel, Abid Ali, and Alfred Tareilus. "Modelling and simulation of a paraglider flight." In Proceedings of The 9th EUROSIM Congress on Modelling and Simulation, EUROSIM 2016, The 57th SIMS Conference on Simulation and Modelling SIMS 2016, no. 142, pp. 327-333. Linköping University Electronic Press, 2018.
- [4] Falquier, R.: "Longitudinal Flight Mechanics of Paraglider Systems," Dissertation, Department of Aerospace Engineering, Stockholm, Sweden, 2019
- [5] Hohenwarter, M. : GeoGebra: Ein Softwaresystem für dynamische Geometrie und Algebra der Ebene (in German), Paris Lodron University, Salzburg, Austria, 2002.
- [6] Tallman, Jake, David Yu, and Maria Pantoja. "Thermal Detection for Free Flight." Journal of Physics: Conference Series. Vol. 1828. No. 1. IOP Publishing, 2021.

Deep CNN ensemble for recognition of face images

Robert Szmurlo

Faculty of Electrical Engineering,
Warsaw University of Technology,
Warsaw, Poland
robert.szmurlo@pw.edu.pl

Stanislaw Osowski

Faculty of Electrical Engineering, Warsaw University of
Technology, and Electronic Faculty, Military University of
Technology, Warsaw, Poland
stanislaw.osowski@ee.pw.edu.pl

Abstract — The paper considers the problem of recognition of face images using an ensemble of deep CNN networks. The solution combines different feature selection methods and three types of classifiers: support vector machine, a random forest of decision trees, and softmax built into the CNN classifier. Deep learning fulfills an important role in the developed system. The numerical descriptors created in the last locally connected convolutional layer of CNN flattened to the form of a vector, are subject to four different selection mechanisms. Their results are delivered to the three classifiers which are the members of the ensemble. The developed system was tested on the problem of face recognition. The dataset was composed of 68 classes of greyscale images. The results of experiments have shown significant improvement of class recognition resulted from the application of the ensemble.

Keywords— CNN, ensemble of classifiers, face recognition, feature selection, deep networks.

I. INTRODUCTION

Automated facial recognition plays nowadays very important role in many branches of our everyday life [1,2]. Many companies and other institutions use the face as a form of biometric authentication of a person (Face ID). International airports use facial recognition as a part of an inspection program that compares a traveler's face to their photo stored on the passport. The Police apply facial recognition technology during public events to identify wanted and suspicious individuals. Therefore, face recognition, although being on the well-developed stage is still of high interest from a research point of view.

Many different methods have been used in the past for solving this problem [1,2]. Few important problems have to be solved to develop a well-performing face recognition system. The first is the extraction of the numerical descriptors of an image, which properly characterize the face. The extraction of descriptions is usually followed by the selection of the limited number of the most important descriptors forming the so-called diagnostic features delivered to the final classification stage of the system. This final step of classification decides the efficiency of the developed system.

The solutions to the problem proposed in the past include linear principal component analysis (PCA) and its different modifications applied either directly or indirectly in the definition of diagnostic features [1,2]. The best results of recognition have been obtained at the application of neural classifiers (multilayer perceptron, support vector machine, etc.) or a random forest of decision trees.

Nowadays the best results of image recognition are obtained using deep networks, such as autoencoder,

convolutional neural networks, etc. [3,4,5]. The most important advantage of deep approaches is a combination of two basic steps (generation of numerical descriptors and classification rule) in one common architecture [3]. Thanks to this the process is simplified since the most difficult stage of image processing is done automatically by the system. Moreover, the internally developed numerical descriptors of the image are well correlated with the recognized classes, and thanks to this the great improvement of class recognition accuracy is possible.

In a typical approach to image recognition, the numerical descriptors are taken from flattened last locally connected layer. They are delivered to the softmax classifier as the diagnostic features applying the dropout ratio as the regularization.

In this paper, we investigate different strategies. The numerical descriptors are subject to a special selection procedure, applying different feature selection methods. Since each method operates on a different mechanism of selection the chosen features form different sets. Each set may present the input signals to the classifier. Applying few classifiers and associating them with each set of selected diagnostic features creates many results of classification (ensemble of results). Integrating them by majority voting into one final verdict of the whole ensemble can increase the accuracy of the system in a significant way.

In our solution, we have applied transfer learning based on ALEXNET architecture of CNN. The numerical descriptors are taken from fc6 layer of the network of the size 4096. They undergo the selection using five selection procedures: stepwise fit, nearest neighbor analysis, relief, chi2 test, and minimum redundancy maximum relevance methods [6,7,8,9]. Two, carefully selected classifiers have been applied in forming the ensemble. One is the support vector machine and the second the random forest of decision trees [10,11]. Associating them with 5 selection procedures and supplementing with a softmax classifier built into ALEXNET results in creating 11 classifying members of the ensemble. Moreover, the classification task may be repeated many times for randomly split training and testing data and generate the results, which are integrated into the final verdict of an ensemble. The decision of the ensemble is taken by majority voting.

Different arrangements of classification units have been created and tested. One is the composition of only one type of classifier (softmax, SVM, or random forest), each combined with the specific set of diagnostic features. The second represents the combination of many types of classifiers in the

ensemble. The results of such combinations will be compared, and the best choice used in final experiments.

The efficiency of the proposed solution will be investigated on the problem of recognition of face images representing different people. The database used in numerical experiments is composed of 68 classes. The results will be presented for individual classifiers, the mean of their actions, and the results integrated into an ensemble. They confirm the significant improvement of class recognition resulted from the application of the ensemble.

II. ARCHITECTURE OF THE CLASSIFICATION SYSTEM

A. Convolution Neural Network

The convolutional neural network used in the system is built on ALEXNET architecture [4,9]. It contains 5 locally connected convolutional layers and three fully connected layers (the input layer representing 4096 numerical descriptors used as the input signals to softmax classifier, hidden layer of K ReLU neurons, and an output layer of M neurons representing the recognized classes. In our solution, this classical network will represent one member of the ensemble.

B. Other members of ensemble

The other members of the ensemble will be created from two different classification units: the support vector machine (SVM) of Gaussian kernel [10] and random forest (RF) of decision trees [11]. Both classifiers will be fed with the specially selected numerical descriptors coming from fc6 layer of the CNN.

The support vector machine belongs now to the most efficient classifiers of a very special learning algorithm, in which a hyperplane in a high-dimensional space is constructed in such a way, that the nearest training data of different classes are separated by the widest margin of separation. Nonlinear mapping of the set of original points \mathbf{x} into the hyperplane using a kernel function $K(\mathbf{x}, \mathbf{x}_i)$ allows much more complex discrimination between the data of two opposite classes. Thanks to this, the SVM classifiers perform very well (good generalization ability) in difficult high-dimensional classification problems.

The Breiman random forest represents an ensemble of decision trees, that operates by constructing many decision trees at training time and outputting the class pointed by their majority [11]. The very good generalization ability of the classifier is obtained by applying randomness in selecting the learning data, as well as using the limited set of randomly selected features chosen in each node of the trees.

C. Feature selection procedures

The important role in the presented solution performs the feature selection methods. They operate on the set of 4096 numerical descriptors generated in fc6 layer of the CNN. The key point in this phase is to provide an independent operation of selection techniques. This is achieved here by choosing the methods, which rely their operation on different mechanisms of feature importance assessment. Five methods are applied in this work: stepwise fit, nearest neighbor analysis (NCA), relief, chi2 test, and minimum redundancy and maximum relevance criteria [6,7,8,9].

D. Ensemble of classifiers

The ensemble of the classifiers is composed of many members working in majority voting mode. To provide proper operation of ensemble its members should be of comparable accuracy and act independently which was obtained in the following ways.

- Different mechanisms of classification. It was obtained by applying different classifier types: SVM of Gaussian kernel, RF, and softmax.
- Different sets of input signals to the classifiers, selected from the 4096 numerical descriptors by applying various selection procedures.
- Different contents of the learning data, by selecting randomly the learning and validation subsets from the available data set.
- Application of different parameter values in the applied classifiers, for example, a different number of hidden units, varied dropout ratio in the final softmax classifier, or a different number of trees in the forest.
- In the case of softmax, the structure of a fully connected network was varying, by applying different number K of hidden neurons in fc7 layer (population of neurons changing from 300 to 1500), as well as using different dropout ratio (from 0.3 to 0.6).

Moreover, the ensemble system will be subjected to n independent runs. Thus, the maximum size of the results subjected to ensemble integration may achieve the value of $11n$. The condition of independent operation of all ensemble members between the runs has been achieved in various ways and their results analyzed and compared.

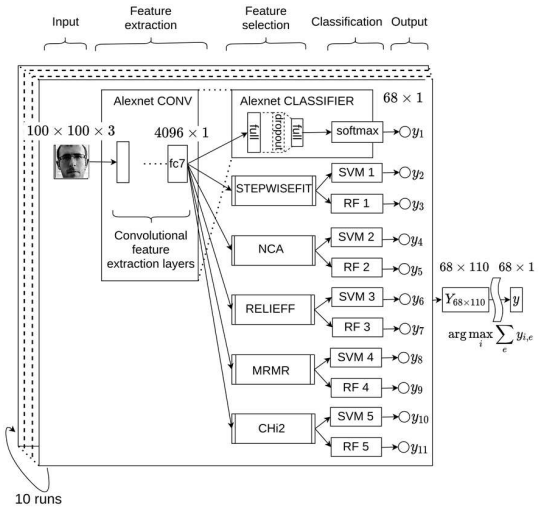


Fig. 1 The general CNN-based ensemble structure used in experiments.

Since all systems have applied randomness in all phases of their learning operation (random choice of learning and validation data, random initialization of internal parameters, randomness included in some selection procedures), we have multiplied the ensemble size by repeating the learning and testing processes n times.

Fig. 1 presents the most general structure of the proposed ensemble classification system created by the CNN-

based ensemble structure. The pre-trained ALEXNET delivers the set of 4096 numerical descriptors of the data. They are subject to 10 selection procedures delivering a smaller number of features. These features represent the input signals to SVM and RF. The 11th classifier was built directly in the CNN structure and used the softmax principle in classification combined with the dropout technique in feature selection.

Based on this general structure the different ensemble combinations can be extracted and analyzed. This architecture is used in $n=10$ different runs of analysis. Their results are integrated into the final verdict of the system.

III. DATABASE USED IN EXPERIMENTS

The developed classification system was tested using the database containing the faces of 68 people, which are treated as 68 classes. Each class was composed of 20 photographs of the same person made in different poses at varying lighting conditions. The size of the original images in all cases was the same and equal 100×100 .



Fig. 2 The examples of face images representing 3 classes of data. The photographs are taken in different scales and positions.

Fig. 2 presents some chosen set of original images taking part in experiments. The same people are photographed in different poses and at varying illumination. Some images show the face with glasses and some without glasses. The faces are shown in different scales, representing either full-face or only a limited part of it. The significant differences among the representatives of the same family of persons are visible.

IV. RESULTS OF NUMERICAL EXPERIMENTS

A. Organization of experiments

The results of numerical experiments will be presented for the presented above database. Experiments aim to check how the inclusion of a different number of independently working classifiers arranged in the form of an ensemble affects the quality of results. This quality will be assessed based on the accuracy in recognizing the particular class. The results of different arrangements of an ensemble will be compared to the individual results of its members.

The database was split into teaching parts (70% of randomly selected samples representing all classes) and the remaining 30% of the data representing the testing part (common to all classifiers in the ensemble). The learning part was once again randomly split into learning (80%) and validation part (20%). The cross-entropy formulation of the cost function was applied. The SGDM (stochastic gradient descent with momentum) learning algorithm with an initial learning rate of $1.3e-4$ was selected in teaching. The mini-batch size was equal to 10 and the number of epochs limited to only 20. The typical validation accuracy at the application of the softmax learning algorithm achieved on the validation set a value around 98%.

The signals from fc6 layer representing 4096 numerical descriptors of the images are the basis for further processing. These signals will be subjected to many different operations in the classification stage of the algorithm. The results will be presented for different arrangements of the ensemble.

B. Statistical results

The first investigated structure applied only a softmax classifier and integrated the results of 10 runs of experiments. The independence of the results of each run has been provided by different random selection of learning and validation data, various dropout ratios in softmax learning, and different number K of hidden units (random choice around mean of 700).

Table I depicts the results related to an ensemble composed of only softmax classifiers. The ensemble contains n members. They are related to the accuracy corresponding to different statistics: accuracy of the ensemble (ACC_{en}), mean of accuracy in individual results (ACC_{mean}), a median of individual results (ACC_{med}), maximum (ACC_{max}), and standard deviation of individual results (std).

TABLE I. The statistical results in 68 class recognition problem at the application of ensemble applying softmax classifiers only

n	ACC_{en}	ACC_{mean}	ACC_{med}	ACC_{max}	std
5	96.3%	90.7%	90.9%	93.4%	1.84%
10	97.3%	91.4%	92.0%	92.9%	2.53%
55	97.8%	91.3%	91.9%	96.1%	2.39%

The accuracy of the ensemble is much higher than the average of non-integrated individual members and this difference is very high (97.8% of ensemble versus 91.3% of the mean). The interesting point is the increase of accuracy over the best individual member (97.8% of ensemble versus 96.1% of the best individual result). The results suggest, that the additional

calculational effort required to increase the accuracy by 0.5% when the number of ensemble members changed from 10 to 55 is not reasonable. Thus, the total number of all ensemble members equal to 10 for the tested dataset is assumed as optimal.

The next experiments have been directed to apply different classifiers in ensemble. Two solutions have been tried: the SVM and random forest of decision trees. To achieve good generalization ability, we must limit the number of their input signals. This was done by applying different feature selection methods. Application of various mechanisms of feature assessment should result in different contents of the feature set, which is desirable for providing the independence of operation of the ensemble members.

The following selection procedures have been applied: stepwise fit, NCN, relief, MRMR, and chi2 [6,7,8,9]. They were combined either with SVM or treebagger in an ensemble. The number of selected features was limited to 2000 supporting the highest rank descriptors. The next experiments were performed using only one type of classifier (SVM or RF). The results of the application of an individual classifier associated with five preselected feature sets at 10 runs of experiments are given in Table II.

TABLE II. The statistical results in 68 class recognition problem at the application of ensemble composed of either SVM or random forest classifiers

Classifier	ACC _{en}	ACC _{mean}	ACC _{med}	ACC _{max}	std
SVM	96.3%	90.9%	90.9%	94.4%	1.6%
Random forest	83.3%	76.3%	76.1%	80.6%	2.6%

The results have shown the advantage of SVM over the random forest. However, both are inferior to the classical softmax classifier (accuracy of 96.3% of SVM compared to 97.3% of Softmax). The next experiments aimed to increase the number of units in an ensemble by combining different types of classifiers. The statistical results of such experiments are presented in Table III.

TABLE III. The statistical results in 68 class recognition problem at the application of ensemble combined from different types of classifiers: softmax, SVM and random forest at 10 runs of experiments

Classifier	ACC _{en}	ACC _{mean}	ACC _{med}	ACC _{max}	std
Softmax+SVM	96.4%	91.3%	91.4%	94.8%	1.5%
Softmax+random forest	87.3%	81.0%	79.3%	95.1%	5.6%
Softmax+SVM+random forest	92.4%	84.0%	87.9%	93.6%	7.5%
SVM+random forest	93.9%	85.0%	85.4%	94.6%	6.9%

The numerical results presented in the tables show the advantage of the relatively simple softmax classification

principle over very good classical classifiers (SVM and RF). The least efficient in all cases is the random forest. Including RF into the ensemble deteriorates the final verdict. It confirms the general opinion, that ensemble should be combined from the classifiers of similar accuracy. In our opinion, the main reason for the worse performance of classical classifiers is the very small population of the learning data. The high number of descriptors generated by CNN results in a complex structure of the classical classifiers and the need for a large population of learning samples. The classical softmax is better suited in such a mode of operation.

V. CONCLUSIONS

The paper has presented the application of the ensemble approach for improving face recognition accuracy. The results obtained by the ensemble integrated with majority voting outperformed the best outcomes of single ensemble members. The tests have shown the best results of ensemble based on the application of softmax classifiers.

The results have confirmed the advantage of the application of an ensemble composed of many classifiers, integrating their results into one final verdict by majority voting. In each case, the ensemble results have dominated over the results of individual units (over their mean and even the best individual result).

VI. REFERENCES

- [1] C.C. Loy, X. Liu, T.K. Kim, et al. "Editorial: Special issue on deep learning for face analysis", *Int. J. Computer Vision*, 127, 533–536 (2019). <https://doi.org/10.1007/s11263-019-01179-z>
- [2] M. Wang and W. Deng, "Deep face recognition: a survey", *Neurocomputing*, 429, 215-244 (2021), DOI: 10.1016/j.neucom.2020.10.081A.
- [3] I. Goodfellow, Y. Bengio and A. Courville, *Deep learning*, MIT Press, 2016.
- [4] Krizhevsky, I. Sutskever, G.E. Hinton, "ImageNet classification with deep convolutional neural networks" *Communications of the ACM*, 60(6) 84–90 (2014).
- [5] K. Siwek, S. Osowski, Deep neural networks and classical approach to face recognition – comparative analysis, *Przegląd Elektrotechniczny*, 94(4), 1-4 (2018).
- [6] R. Robnik-Sikonja and I. Kononenko, "Theoretical and empirical analysis of Relief and RRelief". *Machine Learning*, 53, 23–69 (2003).
- [7] W. Yang, K. Wang, and W. Zuo., "Neighborhood component feature selection for high-dimensional data", *Journal of Computers*, 7, 161-168 (2012).
- [8] Peng, H.C., Long, F., and Ding, C., "Feature selection based on mutual information: criteria of max-dependency, max-relevance, and min-redundancy", *IEEE Transactions on Pattern Analysis and Machine Intelligence*, 27(8) 1226–1238 (2005).
- [9] *Matlab user manual*, MathWorks, Natick, USA, 2021a.
- [10] B. Schölkopf and A. Smola, *Learning with kernels*, Cambridge, MIT Press, MA, 2002.
- [11] L. Breiman, "Random forests", *Machine Learning*, 45(11), 5–32 (2001).

Definition System of Human Body Position in Virtual Reality

Roman Diachok
Specialized Computer Systems Dpt.
Lviv Polytechnic National University
Lviv, Ukraine
rodyachok@gmail.com

Halyna Klym
Specialized Computer Systems Dpt.
Lviv Polytechnic National University
Lviv, Ukraine
klymha@yahoo.com,
halyna.i.klym@lpnu.ua

Ivanna Vasylychshyn
Theoretical and General Electrical
Engineering Dpt.,
Lviv Polytechnic National University,
Lviv, Ukraine
ivanna.i.vasylychshyn@lpnu.ua

Ivan Karbovnyk
Electronics and Computer
Technologies Dpt.,
Ivan Franko National University of
Lviv,
Lviv, Ukraine
ivan_karbovnyck@yahoo.com

Abstract—System for determining the position of the human body in the virtual world has been designed, implemented and researched. The system consists of two independent subsystems: subsystem for collecting, processing and transmitting data on the position of the human body and subsystem for visualizing collected data to the virtual world. In general, the system measures the position of the human body, processes the data, generates the set of commands for the virtual world and sends these commands to the virtual reality helmet for processing. Schemes of the system and algorithm of system's functioning are offered. The system using quaternions and Euler angles was investigated. Also was shown that the system works more efficiently when using quaternions.

Keywords—microprocessor system, quaternions, subsystems, positioning, virtual reality.

I. INTRODUCTION

This template, modified in MS Word 2007 and saved as a "Word 97-2003 Document" for the PC, provides authors with most of the formatting specifications needed for preparing electronic versions of their papers. All standard paper components have been specified for three reasons: (1) ease of use when formatting individual papers, (2) automatic compliance to electronic requirements that facilitate the concurrent or later production of electronic products, and (3) conformity of style throughout a conference proceedings. Margins, column widths, line spacing, and type styles are built-in; examples of the type styles are provided throughout this document and are identified in italic type, within parentheses, following the example. Some components, such as multi-levelled equations, graphics, and tables are not prescribed, although the various table text styles are provided. The formatter will need to create these components, incorporating the applicable criteria that follow.

Currently, the conditions and way of life reflect the news of the characteristics of the information society. Young people are considered as a "main consumers" of innovative services, feel the need for improvements very acutely and that is why more and more demands are made on the content, level and quality of the interactive process. Therefore, virtual technology will help to individualize user-centric programs, increases the level of interaction between computer systems and people [5-7].

Most research works are focuses on creating cyber-physical systems for virtual reality [8,9] with a large number of sensors for training [10], designing robotic mechanisms [11], hand simulators [12], for medical applications [13], in machine learning [14,15], etc. However, the most common of these developments have proven themselves when interacting with virtual computer systems.

In view of all the above, in this work was proposed to design and study a wireless system to determine the position of the human body in virtual reality. That is, it is necessary to design a system that will take measurements of the body position in the real world, process these data and project into the virtual world.

II. DESIGN OF THE SYSTEM

The block diagram of the designed system for determining the position of the human body in the virtual world is shown in Fig. 1. System will consist of two independent subsystems: the first subsystem - is responsible for the collection, processing and transmission data about the position of the human body, and the second subsystem - for the visualization of processed data to the virtual world.

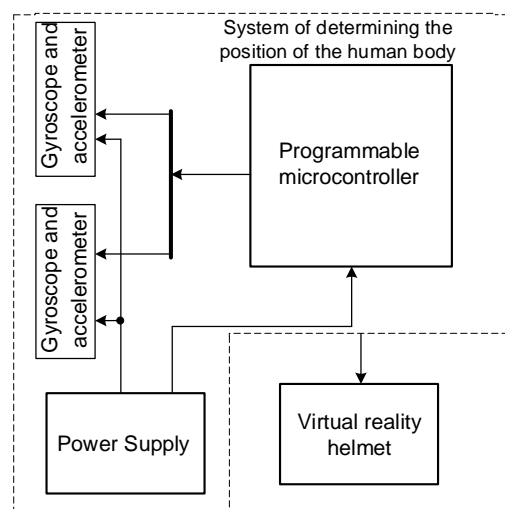


Fig. 1. Block diagram of the designed system for determining the position of the human body in the virtual world.

The ESP8266 microcontroller was used to build a system for collecting, processing and transmission the accumulated data. Determining the position of human body parts will be based on the on the indicators of gyroscope and accelerometer readings on the GY-521 module. The data will be measured and transferred to the microcontroller and processed according to a certain algorithm. In order to increase the accuracy of the indicators, a simple filtering by the Kalman method will be performed. After the date would be processed and accumulated, the firmware packs this data. The next step, is sending packed data to a virtual reality helmet using Wi-Fi technology.

The subsystem that is responsible for displaying the received data to the virtual world is controlled by its own CPU, and also must have a graphical processor and a wireless connection module. The data acquisition and transmission subsystem have all the necessary sensors: accelerometers and gyroscopes. A separate block is a virtual reality helmet, which will provide the ability to visualize user movements to view them in the virtual world.

The electrical schematic diagram of the designed specialized system is shown in Fig. 2. During current research work, was used the software and hardware platform Wemos D1 mini, which generates control signals of the GY-521 modules and is responsible for collecting, processing and transmitting information.

The main board of the microcontroller connects to the GY-521 modules via the I2C interface and acts as a master device. At a certain interval, the microcontroller interrogates the modules and forms a data packet based on them, which will be transmitted to the virtual reality field. The GY-521 modules themselves measure readings continuously and process them using DMP (Digital Motion Processor).

To connect each of the modules also necessary to output power in the range from +3V to +5V. Since the power supply module has a constant voltage of +5V, the board with the microcontroller and modules would be powered from +5V, and their GND outputs will be combined. These elements have demonstrated high performance and noise immunity in a digital noise environment, because each component has a filter from high-frequency obstacles.

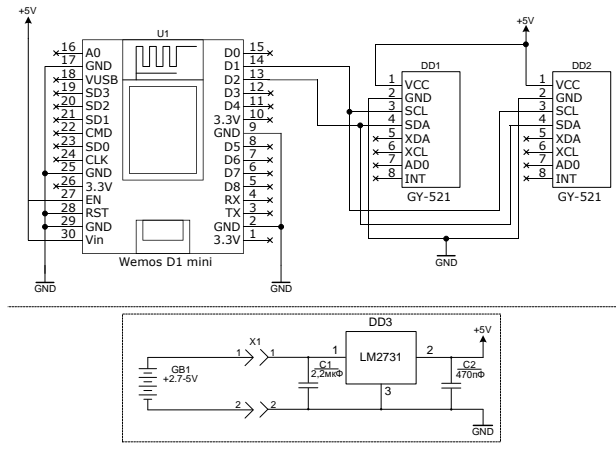


Fig. 2. Electrical schematic diagram of the designed system.

For the correct operation of the designed specialized system for determining the position of the human body in the virtual world, it is also necessary to develop software that will

be responsible for the perception and processing of information, as well as the transmission and visualization of data.

Taking into account that the designed system consists of two functionally complete subsystems, the approach to the implementation of the program code of each of the subsystems will be different.

For the development of software subsystems determining the position of body parts, a specialized development environment for the development of ARDUINO IDE software for the ARDUINO software-hardware platforms has been used.

For the development of software, the data visualization subsystems are used by a special development environment of 3D unity3d applications. This environment will allow you to move human movements in the real world in a virtual way to replace the limbs to the corresponding 3D models. It also allows you to interact with virtual objects and move to the virtual world.

The algorithm of the designed system is shown in Fig. 3.

According to the given block diagram of the iteration of the algorithm after initialization, the system begins to read data from the accelerometers and gyroscopes of the modules for determining the position of the human body. Then the data packages are formed, and would be transmitted to the helmet. That process would be done in several stages, first of all the data filtered in accordance with previous data. To did this was used a primitive implementation of the Kalman filter and functions that limited the range. Filtered data placed in a certain order, which allowed to quickly operate on the side of the receiver. Next step is to transmit the data packages to the virtual reality helmet via a wireless interface. Each packet is assigned an identifier to arrange to the correct order. The task of the program, which runs on a virtual reality helmet, is to received data packages, where each of the indicators will be assigned to the corresponding virtual models. The angle of rotation of each axis of the module, which was fixed to the real parts of the human body, would be assigned to a virtual model analogous to the body part of people in the virtual world. Then the program on the helmet of virtual reality visualizes the position of the human body in the virtual world.

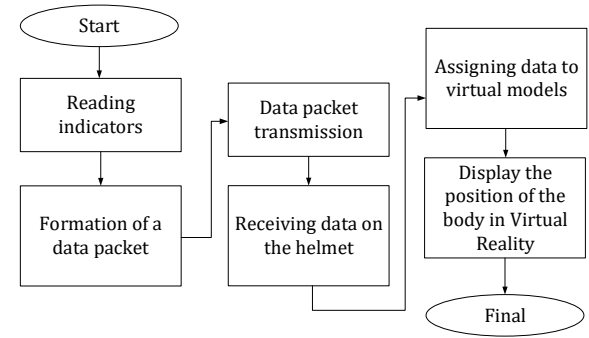


Fig. 3. Graph diagram of one iteration of the algorithm to determine the position of the human body.

In order to easily and simply connect the positioning module GY-521, and receiving the angles of rotation and acceleration values of the place where it is located, the MPU6050DMP library was additionally downloaded and installed. Library allows to read directly the values of the module's memory registers and work with a digital motion

processor (DMP). This approach allowed to continuously measure the performance of the module and obtained the latest data on request.

For the possibility of transferring data via the built-in Wi-Fi microcontroller board and access to the Internet, the ESP8266 library was used, which allowed easily and quickly create an Internet connection, sent and received bytes of information, which is exactly what is needed in the designed specialized system to determine position of the human body in the virtual world.

It has been established that the developed algorithm occupies only 19% of free space in the non-volatile memory of the microcontroller and 20% of the RAM. This means that the selected hardware and software platform Wemos D1 mini fully satisfied the required amount of resources required to perform the control algorithm of a specialized system to determine the position of the human body in the virtual world.

As mentioned above, Unity3D environment is used to visualize the position of the human body. For correct work, a new scene has been created and an object has been added to it, which would be responsible for receiving and transmitting data with the positioning system of human body parts. The result of these actions is shown in Fig. 4.

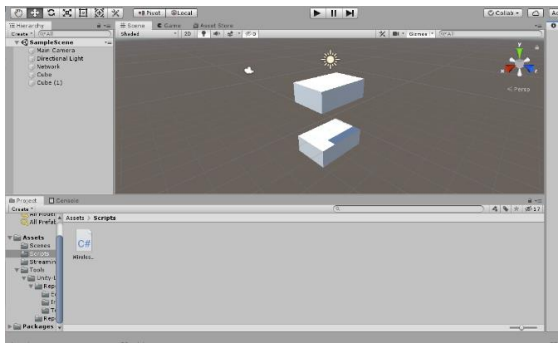


Fig. 4. Added items in the Unity3D editor

Then was created a new .cs extension file and described the behavior for receiving and transmitting data. Since the transfer took place via Wi-Fi, it would be convenient to use sockets and client-server architecture.

In general, a holistic developed system consists of a virtual reality helmet and a system for determining the position of the human body (see Fig. 5).



Fig. 5. View of the designed system for determining the position of the human body in the virtual world.

There may be several such subsystems. Because all communication is via a wireless connection, no additional contacts are required. Regular controllers must also be used for the helmet to work properly. Power is connected directly to the positioning module via standard connectors. The power supply of the virtual reality helmet is built-in.

To test the system, just apply power and run the application on a virtual reality helmet. After that, the system will immediately begin to transmit the position of the part of the body to which it is attached. In the configurator, you can change the part of the body you want to track and put on a positioning system if needed. To check the correctness of the system, several tests were performed with different parts of the body to check the behavior of the system when changing the location of the positioning modules.

III. RESEARCH OF THE POSITIONING AND TESTING MODULE OF THE SYSTEM

The positioning module is one of the key elements of a specialized system for determining the position of the human body in the virtual world. As before, system consists of two GY-521 modules and a microcontroller. For system's correct operation, this module must be properly placed the human body. The basic idea is that any human limb can be divided into vectors and determine their rotations relative to each other. Thus, the final position could be got from the latest vector relative to the human body. The system of positioning modules could be placed on other parts of the human body. To do this, should be change the configuration in the application of visual display of data on the helmet of virtual reality.

Quaternions or Euler's angles could be used to read and transmit data from positioning modules [16,17]. There is a theory that the use of quaternions is more accurate, but requires more computational resources [18]. This could be explained by the fact that the quaternion is a set of four parameters that determine the vector and the angle of rotation around this vector, and Euler's angles is a set of only three parameters that determine the rotation vector. In quaternions, the parameters of a unit vector are multiplied by the sine of half the angle of rotation. The fourth component is the cosine of half the angle of rotation. In Euler angles, the parameters of the unit vector are the angles of rotation around the axes.

The use of Euler's angles has a significant disadvantage - the assembly of frames. Rotation lock (frame assembly) is a term that refers to the field of gyroscopes and inertial navigation. For a free gyroscope in a biaxial suspension, the term describes an event that may occur when the inner frame of the gyroscope rotates 90 degrees relative to the outer frame, and the kinetic moment vector will be directed along the axis of the outer frame. In this position, the gyroscope will lose its main property - to maintain the direction in the inertial space, which is given by the vector of kinetic moment. The accuracy of the system using quaternions and Euler angles is shown in Fig. 6.

As could be seen from the above dependences, the use of quaternions is more acceptable, because when using Euler's angles, the accuracy of the system suffers at critical points, when the axes of the gyroscope are close to the effect of folding the frame. The use of quaternions completely eliminates this effect and in practice there is no rapid unplanned change in the angles of rotation of the virtual part of the human body.

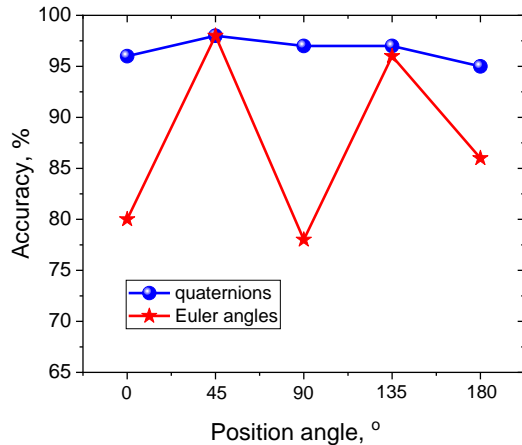


Fig. 6. System accuracy using quaternions and Euler angles.

Regarding to the analysis of the speed of quaternions and Euler's angles, no difference was found. This is due to the very small amount of time per iteration of the algorithm (approximately 0.1 ms). It is not possible to add the time of several iterations because the time to visualize the work is much longer (approximately 10 ms), which will lead to the accumulation of a large error. Therefore, the processing time of quaternions or Euler's angles in the total processing time of data from positioning modules can be neglected, which makes the use of quaternions more acceptable.

The placement of the system on the hand was used to check the system. In conclusion, the video sequence varied depending on the position of the human body. When using quaternions, dead zones were not found. When using Euler's angles, there were situations with the so-called hinged lock, which affected the perception of virtual reality. That is, the use of quaternions is more promising in the broad masses.

During the test of movement of parts of human bodies, the correctness of the reaction of the visual part to the control commands was also checked.

IV. CONCLUSION

System for determining the position of the human body in the virtual world has been designed. System consists of two independent subsystems: the collection, processing and transmission of data on the position of the human body and data visualization in the virtual world. The first subsystem is based on the ESP8266 microcontroller. Determining the position of human body parts is based on the indicators of the gyroscope and accelerometer located on the module GY-521. A system for determining the position of the human body, which could be used with third-party virtual reality helmets, was assembled and tested. Studies of the system have also shown that it will work more efficiently when using quaternions as opposed to Euler's angles.

The advantage of the system, in addition to ease of use, is the fact that the data in the system can be updated at a frequency of about 200 Hz, what is more than enough for comfortable use. All collected data on the position of the body is almost instantly transmitted to the helmet of virtual reality and visualized there. During testing, the specialized system worked correctly and successfully performed its functions.

ACKNOWLEDGMENT

H. Klym thanks to the Ministry of Education and Science of Ukraine for support (project No. 0119U100435).

REFERENCES

- [1] D. Mavrikios, V. Karabatsou, D. Fragos, and G. Chryssolouris, "A prototype virtual reality-based demonstrator for immersive and interactive simulation of welding processes," *International Journal of Computer Integrated Manufacturing*, vol. 19(03), pp. 294-300, 2006.
- [2] M.J. Kim, C.K. Lee, and T. Jung, "Exploring consumer behavior in virtual reality tourism using an extended stimulus-organism-response model," *Journal of Travel Research*, vol. 59(1), pp. 69-89, 2020.
- [3] C. Ferguson, E.L. van den Broek, and H. van Oostendorp, "On the role of interaction mode and story structure in virtual reality serious games," *Computers & Education*, vol. 143, pp. 103671, 2020.
- [4] V. Hohmann, R. Paluch, M. Krueger, M. Meis, and G. Grimm, "The Virtual Reality Lab: Realization and application of virtual sound environments," *Ear and Hearing*, vol. 41(Suppl 1), pp. 31S, 2020.
- [5] D. Flynn, P. Van Schaik, T. Blackman, C. Fencott, B. Hobbs, and C. Calderon, "Developing a virtual reality-based methodology for people with dementia: a feasibility study," *CyberPsychology & Behavior*, vol. 6(6), pp. 591-611, 2003.
- [6] L.I. Yang, J. Huang, T.I.A.N. Feng, W.A.N.G. Hong-An, and D.A.I. Guo-Zhong, "Gesture interaction in virtual reality," *Virtual Reality & Intelligent Hardware*, vol. 1(1), pp. 84-112, 2019.
- [7] Y. Zhao, E. Cutrell, C. Holz, M.R. Morris, E. Ofek, and A.D. Wilson, "SeeingVR: A set of tools to make virtual reality more accessible to people with low vision," *Proceedings of the 2019 CHI Conference on Human Factors in Computing Systems*, pp. 1-14, 2019.
- [8] F. Hu, Q. Hao, Q. Sun, X. Cao, R. Ma, T. Zhang, ... and J. Lu, "Cyberphysical system with virtual reality for intelligent motion recognition and training," *IEEE Transactions on Systems, Man, and Cybernetics: Systems*, vol. 47(2), pp. 347-363, 2016.
- [9] T.I. Erdei, Z. Molnár, N.C. Obinna, and G. Husi, "Cyber physical systems in mechatronic research centre," *MATEC Web of Conferences*, vol. 126, pp. 01006, 2017.
- [10] H. Yamada, N. Tao, and Z. DingXuan, Z. "Construction tele-robot system with virtual reality," *IEEE conference on robotics, automation and mechatronics*, pp. 36-40, 2008.
- [11] Y. Park, I. Jo, J. Lee, and J. Bae, "A dual-cable hand exoskeleton system for virtual reality," *Mechatronics*, vol. 49, pp. 177-186, 2018.
- [12] M.S. Cameirão, S.B. i Badia, L. Zimmerli, E.D. Oller, and P.F. Verschure, "The rehabilitation gaming system: a virtual reality based system for the evaluation and rehabilitation of motor deficits," *Virtual Rehabilitation*, pp. 29-33, 2007.
- [13] D. Gachet Páez, F. Aparicio, M. De Buenaga, and V. Padrón, "Personalized health care system with virtual reality rehabilitation and appropriate information for seniors," *Sensors*, vol. 12(5), pp. 5502-5516, 2012.
- [14] C. Buche, C. Bossard, R. Querrec, and P. Chevallier, "PEGASE: A generic and adaptable intelligent system for virtual reality learning environments," *International Journal of Virtual Reality*, vol. 9(2), pp. 73-85, 2010.
- [15] J. Radianti, T.A. Majchrzak, J. Fromm, and I. Wohlgenannt, "A systematic review of immersive virtual reality applications for higher education: Design elements, lessons learned, and research agenda," *Computers & Education*, vol. 147, pp. 103778, 2020.
- [16] J. Diebel, "Representing attitude: Euler angles, unit quaternions, and rotation vectors," *Matrix*, vol. 58(15-16), pp. 1-35, 2006.
- [17] M.K. Ozgoren, "Comparative study of attitude control methods based on Euler angles, quaternions, angle-axis pairs and orientation matrices," *Transactions of the Institute of Measurement and Control*, vol. 41(5), pp. 1189-1206, 2019.
- [18] A. Janota, V. Šimák, D. Nemeč, and J. Hrbček, "Improving the precision and speed of Euler angles computation from low-cost rotation sensor data," *Sensors*, vol. 15(3), pp. 7016-7039, 2015.

CNN-based character recognition for a contextless text input system in immersive VR

Szymon Kuś
Faculty of Electrical Engineering
Warsaw University of Technology
Warsaw, Poland
szymon.kus2.stud@pw.edu.pl

Robert Szmurło, PhD.
Faculty of Electrical Engineering
Warsaw University of Technology
Warsaw, Poland
robert.szmurlo@pw.edu.pl

Abstract— The paper investigates the applicability of deep neural networks and transfer learning procedure to developing a handwriting recognition system for typing contextless content in a Virtual Reality system. Inputting special characters in such systems is still a nontrivial task, even nowadays. Most algorithms for editing text focus on contextual text recognition from speech or gestures. Unfortunately, these approaches fail for text containing not only letters additionally in the context of words, phrases, and trivial punctuation characters. In the paper, the authors explore the possibility of typing more advanced structures, which for example, can be observed in source code editing. The aim of the paper is to verify if modern machine learning algorithms can facilitate text typing in a context-free environment. The authors have chosen a transfer learning procedure utilizing already trained convolutional layers from ALEXNET [1], followed by deep network classification layers. The methods and procedures implemented for the Virtual Reality system used to acquire data necessary to train the recognition model are also presented.

Keywords—CNN, deep network, Virtual Reality, character recognition

I. INTRODUCTION

Text input in immersive virtual reality (VR) systems presents obstacles typically not present in other real-world situations. Currently, the most common solution for creating immersive VR makes use of a head-mounted display (HMD) which obscures the wearer's vision instead of supplying them with a view of a virtual world. The HMD tracks its movement to respond to the wearer's move of his head which plays the key role in immersion.

Early HMDs supported 3 degrees of freedom (3DoF), i.e.: yaw, pitch, and roll. The primary limitation of such a system is lack of response to translational movement, contributing significantly to VR sickness [2]. Whilst in this case the text input is not too much of a problem (a physical keyboard in front of the user works in most situations), it is not the case in 6DoF systems, which track the user's 3D position and respond to it. Thus, the user can move around freely within the confines of a room and would be inconvenienced to move to a specific part of the room every time it is necessary to type.

The rising popularity of commercial virtual reality has led to 6DoF becoming the industry standard. Most commercial solutions are made with gaming in mind, although other potential uses are also marketed. Apart from an HMD, they typically include two motion controllers allowing the user to control the virtual world with his hands. Throughout this paper, such 6DoF virtual reality systems, including an HMD and two handheld controllers, will be referred to as simply "VR". Examples of such systems are SteamVR and Oculus environments, which are currently the most popular on the market.

The presented paper investigates the applicability and accuracy of deep neural networks with a transfer learning approach to character recognition for contextless content. The classification system responsible for character recognition is fed with data acquired from real VR user sessions with custom software developed by the authors. The collected contours of controller motion are subjected to Bezier curve interpolation and later, bitmap rasterization. The rasterized characters representing the user movement are passed to convolutional layers of the ALEXNET network. The pretrained weights by original authors of the network architecture were used here[1]. Then the results are passed on to the classification layers composed of two fully connected layers (ReLU), one dropout layer for improving generalization properties of the network and finally a softmax classifier. [11]

The paper aims to confirm the applicability of this approach to contextless text input application. The main novelty of the paper is trying to construct a system for contextless content containing special characters like tabs, spaces, parenthesis, etc.

II. REVIEW OF EXISTING TECHNIQUES

Text input methods were investigated for a long time, and a lot of methods and solutions have been proposed. Apart from the hardware solutions using typical and custom keyboards there exist several other techniques. Most focus has been given on techniques that can be utilized in a natural language context. In this paper we focus on a contextless system, capable of recognizing individual characters. Such a system can prove to be useful in a programming setting, for instance, or in inputting a password.

A. VR text input techniques overview

The current standard for VR text input is a virtual floating keyboard operated using ray casting from motion controllers. The average typing speeds achieved this way are significantly smaller than on a typical physical keyboard. It is currently the main method for text input in SteamVR as well as Oculus environments.

A variation of such ray casting inspired by the popular Swype keyboard has been proposed [3], although the study has not yielded satisfactory results. The method would rely on continuous motion along keyboard keys rather than discrete key presses.

Another proposed alteration of the ray casting method has involved implementing additional buttons on the controller under the user's fingers. The main idea behind the system was to reduce the necessary precision in selecting buttons on the virtual keyboard. Instead, portions of the keyboard were selected with the ray casting and individual keys on the portion were selected by button presses. The system did not

prove to be more efficient than ray casting in terms of typing speed [4].

A similar approach has been presented by Boletsis and Kongsvik [5] in an implementation of a drum-like VR keyboard. The interface utilized the 3D nature of the virtual environment and the controllers. The keyboard responded to collision with the models of the controllers providing visual feedback of keys being depressed. The solution achieved better or comparable performance than other interfaces in terms of typing speed. The error rate was moderately high in comparison. The results appear comparable overall to the ray casting method.

Controller-less interfaces have also been proposed. In the absence of motion-tracked controllers the HMD tracking itself can be utilized. The user can, for example, point with his gaze at a key on a virtual keyboard for an extended time to input a character. An auxiliary button could also be used. Such gaze- or head-based text input techniques have been studied by Chun Yu et al. [6].

Much more efficient methods can be achieved with numerical input, utilizing numerical keypads, gamepads, or special sensory gloves [7].

Stationary input techniques dominate in terms of typing speed. Not only interfaces with physical input keyboards have been investigated, but also touch virtual interfaces, utilizing finger tracking methods, such as that which can be found at [8]. Those interfaces can often achieve better results than the ray casting method.

A more comprehensive and in-depth review of existing text input techniques in virtual reality can be found at [9].

III. HARDWARE AND SOFTWARE

The prototype dedicated to collecting data necessary to train the classification system was created using Unreal Engine 4.25. It was implemented on a VR-capable PC running Windows 10 in a typical, medium-sized room setting. All the calculations were done locally on the computer.

A. The apparatus

The Valve Index VR system was used. It consists of three crucial parts: The HMD, the controllers, and two base stations. The base stations are necessary for precision 3D tracking, taking on the role of passive infrared light-emitting “lighthouses”. The tracking itself is done by the HMD presented in Fig. 1. The information is sent to the PC through a wired connection.



Fig. 1. The HMD

Even though the system provides two controllers (see Fig.2.), in the prototype only the right one was used. The controller contains two buttons, trigger, touchpad, and joystick. In the prototype the trigger and the buttons were made use of.



Fig. 2. The VR controller

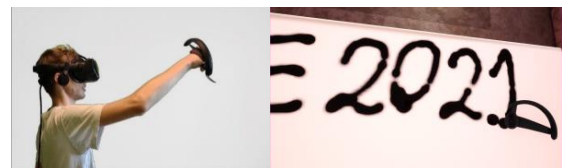


Fig. 3. The VR system in use

B. The software

The Unreal Engine prototype of the system mixed the use of Unreal-specific blueprint visual language [10] and C++. The 3D environment and data acquisition logic were contained in this module. In Fig. 3. an example of a real user session typing CPEE 2021 text can be seen. The core character recognition and neural network logic were implemented separately in Python, with the help of Tensorflow and Keras libraries.

IV. SOLUTION ARCHITECTURE

The prototype was composed of two independent modules: the 3D environment for data collection and the data analysis module coded in Python. In the final solution, we would expect to integrate the data analysis module with the system for the recognition to happen in real time. In this section, we propose a concept for the final architecture of the system.

Ideally, the Python prediction software would be located on a remote server. The server could store collected data and periodically re-train itself for improved recognition.

The 3D environment uses a simple “spray paint” analogy. The user points with a virtual laser on the board and pulls the VR controller trigger to draw. We deemed a “marker on a whiteboard” analogy cumbersome because of the lack of pushback feedback in a VR environment. We used one controller button for confirming every character after it is written and another for discarding it. Ideally, the software could recognize individual characters by itself, which would improve writing speed. The discarding button could prove to be useful as a simple backspace. The remaining buttons (e.g., on the other controller) could be used to quickly input common characters, such as space or newline.

The text display could be substituted for any kind of text input field in a VR app. In this case the whiteboard would act as an overlay over another environment, similar to how current virtual keyboards function.

The characters are collected in the form of a list of strokes, each of which is a list of points collected once every frame. The strokes are then subject to piecewise Bézier interpolation. We use a simple Gaussian brush to draw along every Bézier curve path of an initially empty 28 pixels by 28 pixels bitmap. The resulting bitmap is passed into the predictor. The stages of the data transformation is presented in Fig. 4.

Character A	Character A	Character #

Fig. 4. The examples of characters: registered points, Bezier interpolation and final bitmaps used for the training model.

After conversion to bitmap format the following steps are taken by the Alexnet prediction sub-module:

- scale images to Alexnet resolution,
- Alexnet convolutional layers,
- classification layers.

The returned predicted class is ideally the character written by the user.

V. THE DATASET

The data collected consisted of 115 classes in total. The classes are best broken into the following subsets (the ranges are inclusive):

- classes 0-9: numbers 0-9
- classes 10-35: uppercase Latin alphabet letters A-Z.
- classes 36-44: uppercase Polish alphabet-specific letters: $\text{Å, Ć, Ę, Ł, Ń, Ó, Ś, Ź, Ż}$.
- classes 45-70: lowercase Latin alphabet letters a-z.
- classes 71-79: lowercase Polish alphabet-specific letters: $\text{ą, ć, ę, ł, ń, ó, ś, ź, ż}$.
- classes 80-111: printable ASCII special characters not listed above, in order of their ASCII code.
- classes 112-114: whitespace characters, i.e., space, tab, newline.

It is necessary to mention that the collected “0” (zero) characters were crossed through to differentiate from the capital letter “O”. “Pipe” characters (|) were written as broken bars, like so: “|”. Moreover, for whitespace characters appropriate pictograms were used, i.e., “ $_$ ” for space, “ \rightarrow ” for tab and “ \leftarrow ” for newline.

The total collected contours count was 2539, which amounted to an average number of 22 representants per class. Due to the random nature of data collection, there was a variation in sizes of individual classes. No class had less than 13 representants.

All the collected contours were converted into 28 pixels by 28 pixels bitmap format with the algorithm utilizing Bézier interpolation.

In Fig. 5 we explore the images and preview a few of them.

A	Å (A with ogonek)	#

Fig. 5. The examples of characters collected during VR session representing 3 classes of data – three characters: A, Å and #.

There is a visible variance in the shape of the characters in the examples in Fig. 5. All the collected contours were drawn by a single person, however. As such, the specifics of their handwriting might have played a role in the obtained results. The results may vary from person to person.

The data collection was randomized during the sessions, i.e., individual characters randomly selected from one of the 115 total appeared in the 3D environment, which the user wrote down on the virtual whiteboard.

VI. CLASSIFIER NETWORK CONFIGURATION

The classifier network consisted of two layers. One fully connected layer, a dropout layer with ratio 50% and finally a softmax classifier.

VII. RESULTS EVALUATION

Using the unmodified Alexnet architecture after 50 epochs with augmentation we were able to achieve very good accuracy results equal approximately to 98% which are presented in Table I.

TABLE I. ACCURACY COMPARISON

Classification accuracy		
Dataset type	Accuracy	Loss
Full dataset	95.83%	0.1678
Lower case characters subset	99.22%	0.0486
Upper case characters subset	98.44%	0.0443
Lower case and upper case mean	98.83%	0.0465

A. Misclassified cases analysis

Herein we will present the cases of contours which were misclassified by the predictor trained on the full dataset. The misclassification cases can be broken into a few subcategories.

The first subcategory includes classes which bear heavy resemblance to each other: lowercase letters to their uppercase counterparts, dash to underscore, capital I to apostrophe, the letter Z to the letter Ž. Non-obvious examples such as the capital letter B being confused with the number 8 can also be included in this subcategory. Most of the misclassified cases belong in this subcategory and are presented in Fig. 6 cases 1 to 6.

The second subcategory includes the contours that were incorrectly captured, either because of software malfunction or a human error.

There was a single case which could not be placed into either of those categories (see Fig. 6, case 6).

Case no.	Bitmap image	predicted character	true character
		notes	
1.		u	U
		This is an example from the first subcategory. Miscapitalizations are the most common type of error.	
2.		S	s
		Another example of miscapitalization.	
3.		ž	Ž
		This is another example from the first subcategory. This time the diacritic was misrecognized	
4.		L	l
		In this example the character written resembles a capital L.	
5.		I (uppercase letter)	("pipe" character)
		This is in fact a case from the second subcategory since all pipe characters were to be written as broken bars.	
6.		=	>
		This is the only example which could not be placed into either subcategory.	

Fig. 6. Examples of misclassification.

We predict that implementing a “shift” key to differentiate upper case from lower case letters would greatly benefit the classification accuracy and in turn, writing speed. Some other measures to differentiate similar classes could also be considered, such as requiring serifs for capital letters I, as most of misclassification cases are results of intrinsic similarity between classes.

VIII. CONCLUSIONS

The results presented in the paper show that the proposed by the authors solution of text input for virtual reality for

contextless content is correct and promises satisfactory results. To improve the results, we suggest considering relative sizes of previous characters, or implementing a “shift” key to differentiate upper case from lower case as well as to discern small punctuation characters.

Potentially a hybrid system, which uses common word recognition techniques for natural language and our system for punctuation or more involved code structures, would improve entry speed.

We acknowledge that currently, the system is in the prototype stage of development and other potential factors such as User Experience, handwriting style were not yet considered.

ACKNOWLEDGMENT

This work was supported under grant „Szkoła Orłów na PW” co-financed by the European Union funds under the European Social Fund Operational Programme Knowledge Education Development, Priority Axis III – Higher Education for the Economy and Development, Measure 3.1. Competences in higher education.

REFERENCES

- [1] A. Krizhevsky, I. Sutskever, G.E. Hinton, "ImageNet classification with deep convolutional neural networks." *Communications of the ACM*, vol. 60 no. 6, pp. 84–90.
- [2] N. Tanaka and H. Takagi, "Virtual Reality Environment Design of Managing Both Presence and Virtual Reality Sickness." *J. Physiol. Anthropol. Appl. Hum. Sci.*, no. 23, pp. 313–317, 2004
- [3] J.G. Jimenez and J.P. Schulze, "Continuous-Motion Text Input in Virtual Reality." *Electronic Imaging*, no. 3, pp. 450-1, Jan 2018
- [4] Y. Lee and G. J. Kim, "Vitty: Virtual Touch Typing Interface with Added Finger Buttons. Virtual Augmented and Mixed Reality" in *International Conference on Virtual, Augmented and Mixed Reality*, Springer, Cham, 2017, pp. 111–119
- [5] C. Boletsis and S. Kongsvik, "Text Input in Virtual Reality: A Preliminary Evaluation of the Drum-Like VR Keyboard" *Technologies* 7, no. 2, p.31, Jun 2019
- [6] C. Yu, Y. Gu, Z. Yang, X. Yi, H. Luo and Y. Shi "Tap, Dwell or Gesture?: Exploring Head-Based Text Entry Techniques for HMDs" in *Proceedings of the 2017 CHI Conference on Human Factors in Computing System*, 2017, pp.4479-4488
- [7] G. Lepouras, "Comparing methods for numerical input in immersive virtual environments", *Virtual Reality*, 22.1, pp.63-77, 2018
- [8] J. Dudley, H. Benko, D. Wigdor and P.O. Kristensson, "Performance Envelopes of Virtual Keyboard Text Input Strategies in Virtual Reality" in *2019 IEEE International Symposium on Mixed and Augmented Reality (ISMAR)*, IEEE, 2019, pp. 289-300
- [9] T. J. Dube and A. S. Arif, "Text Entry in Virtual Reality: A Comprehensive Review of the Literature" in *International Conference on Human-Computer Interaction*, Springer, Cham, 2019, pp.419-437
- [10] Epic Games. (2021). *Blueprint Visual Scripting | Unreal Engine Documentation* [Online]. Available: <https://docs.unrealengine.com/4.26/en-US/ProgrammingAndScripting/Blueprints/>
- [11] K. Siwek, S. Osowski, Deep neural networks and classical approach to face recognition – comparative analysis, *Przegląd Elektrotechniczny*, 94(4), 1-4 (2018).

APPENDIX

The source code and examples are made available publicly on the Github repositories under addresses:
<https://github.com/ogoras/CharacterRecognitionUnreal>
<https://github.com/ogoras/CharacterRecognitionPython>

Advanced Paraglider Simulator Control System

Richard Sivera*, Petr Stašek*, Jakub Vorlíček*, Petr Kropík†, Pavel Karban†

*University of West Bohemia, Czech Republic, {rsivera, stasekp, vorlicek}@students.zcu.cz

†University of West Bohemia, Czech Republic, {pkropik, karban}@fel.zcu.cz

Abstract—Control systems for every simulator have to be fast and precise. These are exact properties that are needed when designing a paraglider simulator. With its complex set of controls and complicated aerodynamics physics, paraglider simulator requires a very precise system to mimic its real world counterpart behaviour. From construction to software solution, a team of people with various sets of skills was put together to develop the control system, that is worthy of simulator going into production. This paper will go over how the control system was developed, what parts we're chosen for it and what can we expect from such system.

Index Terms—paraglider simulator, control, servomotor, microcontroller, sensor

I. INTRODUCTION

Paraglider flying is a dangerous and exciting sport [1], [2], [3]. Every preparation of flight is a very tough and time consuming experience. Paraglider novice can have a hard time learning to fly on the paraglider properly. That is why project FlyOnVision was started [4]. Project aim is to develop a simulator (Fig. 1), that provides novice and even experienced pilots an opportunity to train their paraglider skills without actually having to go flying. It is meant to be achieved with motion control system in combination with virtual reality headset.

Advanced control system plays a crucial role in providing a real feeling of a flight. While system has to position harness, in which pilot sits, in a given angle, it also has to provide the pilot with appropriate controls. Controls in FlyOnVision simulator include two brake lines, speed system which attaches to harness and a set of tensometers through which pilot can transform his tilt in the harness to changes in direction [5], [6], [7].

System is split into four main parts: servomotors with drivers, sensors, physical construction and software solutions. Servomotors were chosen for their precision and variety of possible functionalities. Industry grade servomotors Kinco [8], [9] were chosen for their low price and having capabilities for fast movements. System also contains tensometers for indicating pilots tilt in the harness. Pilots tilt also plays a crucial role as it is considered a main way of steering the flight. Physical construction has to stay rigid under high load while at the same time has to be springy in some way. Last but not least, the software has to read pilots inputs to properly control virtual paraglider in the simulation.

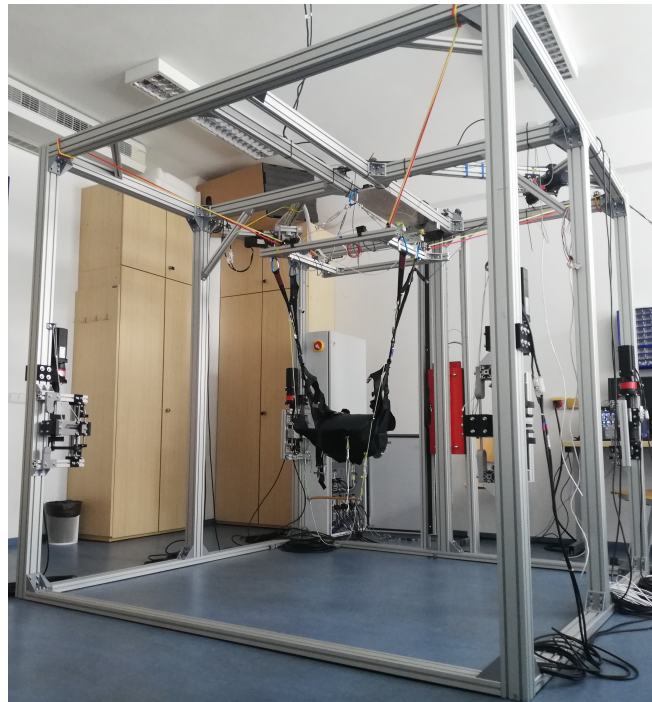


Fig. 1. Simulator design under development.

II. SERVMOTORS AND PHYSICAL CONSTRUCTION

A. Servomotors

Seven servomotors in total were used to assemble the simulator. One three phase 1570 W servomotor positions pilot vertically, four smaller 1000 W servos position the pilot horizontally in all directions (including tilt) and two 400 W servos simulate real brake lines, Fig. 2. Whole system can draw up to 50 A peak. Kinco servomotors have to ability to be positioned very precisely, which is used to position a pilot according to position in simulation. Servos for brake lines operate in torque mode against the pilot. Torque mode was chosen so pilot still has enough force to overcome their pull and because brake lines have a natural tendency to pull upwards.

Every servomotor has its own driver (Fig. 3), which functions as a bridge between controller and motor. As a controller, an Arduino Mega 2560 was used [10]. The controller has the ability to control up to four servomotors at the same time. It is connected to main computer via USB. Controller represents a simpler and cheaper version of PLC, that's why it was chosen

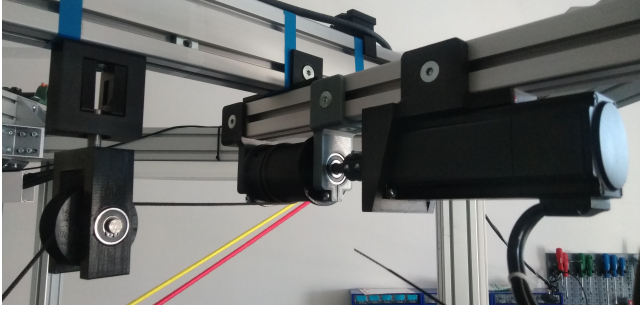


Fig. 2. Servo motor mounting and equipment.

over it. Another reason for using our own controller was ability to program it specifically for our needs. Parts of program are universal and can be rewritten to other controller languages. RS-232 standard communication is used for communication between controller and driver and strictly follows master/slave protocol.



Fig. 3. Motor drivers box.

B. Construction

Control system has to be attached to a solid construction, where simplicity and safety of a pilot are the two priorities. Main material used for construction were aluminium profiles with high degree of modularity, which enabled the team with

rapid prototyping potential. Small moving parts were 3D printed from all sorts of plastics, chosen for their specific application.

Brake servos, for example, use a coil which is connected to motor through a metal shaft. Second coil in front of the first one is used to leading the brake line to the main coil. Many prototypes of coils were made to test out the optimal diameter, which as it turned out was 59 mm. Thanks to 3D printing, a new prototype could be made within hours.

III. SENSORS AND SOFTWARE

Sensors are the main part through which pilot controls the virtual paraglider. Tensometers sense the pilots tilt, whilst position of brake servos encoder tells us how much a brake line has been pulled down. A shield for Arduino Mega was developed to manage two tasks: convert Arduino TTL voltages to RS-232 and convert tensometer signals voltages from analog to digital. 24-bit A/D converters were used to feed the highest demands for precision, while RS-232 converter provides high enough baudrate for fast transfer of commands. A control architecture of the simulator is depicted on Fig. 4.

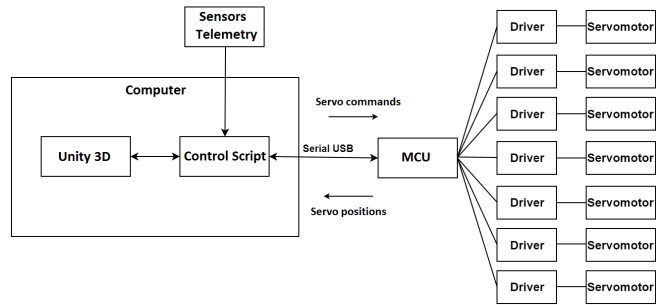


Fig. 4. Control architecture of the simulator.

A. Software

Software for Arduino has to be written in a way so the unit functions as a PLC. It has to be able to communicate with computer running simulation and drivers at the same time. Since Arduino uses 1-core ATmega2560 MCU, all tasks are executed serially. Data packets for communication are sent both ways, while no error detection is used.

An example of sending data packet which enables selected motor driver:

```
void enabled_on(uint8_t adr, serial_port port) {
    uint8_t packet_temp[PL] = {adr, 0x2B, 0x10, 0x20,
                                0x02, 49, 0x00, 0x00, 0x00, 0x00};

    packet_temp[PL-1]= eval_chksum(packet_temp);
    send_packet_to_port(packet_temp, port);
}
```

Still, data correctness is a priority and a faulty packet could mean poor user experience on simulator. For that reason, communication with drivers uses check sum error detection and communication with computer uses odd parity check. Both communication lines should use highest speed possible for

high refresh rate of controls. Computer com is capable up to 1 MBd while Driver currently runs at 115.2 kBd.

Another part of software lies in the computer. This part bridges the communication between Unity 3D game engine that runs the simulation with the controller. Program is based on number of scripts implemented in the simulation itself. Written in C#, code is easily readable, modular and provides enough speed for numerous calculations. A minor part of C# code (one method) example:

```
void Update()
{
    taskController.Update();
    if (Application.targetFrameRate != FPS_TARGET)
        Application.targetFrameRate = FPS_TARGET;

    if (!_gamePaused)
    {
        _gameTimePlayed += Time.deltaTime;

        // Speed and Accel for MotionControl
        if (!Avatar.Body.IsSleeping())
        {
            var velocity = Avatar.Body.velocity;
            Velocity = velocity.magnitude;
            VelocityY = velocity.y;
        }

        Acceleration = (Velocity - _lastVelocity)
            / Time.fixedDeltaTime;
        _lastVelocity = Velocity;
    }
}
```

Calculations include servomotor position commands, torque commands for brake servos and other recalculations regarding nonlinear torque applied by brakes. These more complex calculations are executed strictly on computer for speed purposes, controller executes only small necessary part of them.

Software also has to protect the user from injury and safety measures have to be defined. Right now, software includes system emergency stop and checking for maximum values.

IV. REALISTIC BRAKE CONTROL

Brake lines are controls which pilots interacts with the most. Pilot holds brake lines in his hands and uses them as a control and feedback mechanism, deducting paragliders state of flight from them. That's why brakes have to feel especially realistic.

Their operation is as follows. Motors position is read from its encoder and sent to computer via controller. Script in Unity then calculates for how much percent the brake has been pulled. Right and left percentages are handed over to kernel level driver ViGEM Bus, that internally emulates these percentages to Xbox 360 controls. These controls are then used to steer the paraglider in simulation. The ViGEM Bus (*Virtual Gamepad Emulation Framework* [11]) has been used to transfer data from simulator sensors to the control PC in the intelligible form for the Unity.

Next step in realization of brakes real feel is to dynamically change applied torque on them. To provide pilot with feedback, torque changes with flight conditions. Next important part is torque ramp up with bigger line pull down. That all is realized in Unity scripts, results are sent to controller which commands

these settings to brake servos. We aim at a refresh rate of 90 Hz, which is exact refresh rate of virtual headset displays (Fig. 5). Higher refresh rate doesn't make sense since Unity game engine only recalculates pilots position in simulation with a new frame.



Fig. 5. Virtual reality headset.

V. CONTROLLER CONTROL PROGRAM

As was previously said, controller act as a PLC. It has to have all specific necessary for servo control. MCU waits for computer to connect, then begins communication with servo drivers. After then, it waits for specific commands from computer. Program runs in an endless loop, waiting for control commands from computer, but is not busy waiting. After receiving a command, state machine function is called. We designed specific states to be as simple as possible, leaving higher layer of program abstraction to unity scripts. States are controlled by one byte variable for every servo, so every servo can operate at its own different state. After state machine, MCU reads desired data from drivers and sends it back to computer for next calculations.

VI. CONTROL SYSTEM INITIALIZATION PROCEDURE

After every launch of Unity simulation, MCU automatically connects and homing of servos is proceeded. It is done with the help of limit and homing inductive indicators attached to construction. Another way of homing is with the mechanical method in which servo with a given configured maximal current reaches mechanical limit, current overruns the maximal value and the home is set. After homing is indicated done, program automatically disables drivers so they don't consume energy when pilot is in menu. With launch of a flight, servos are enabled, and again disabled after pilot is back in menu. This provides system with energy saving capabilities. Further energy savings could be done by disabling the MCU or lowering its clock.

VII. PROGRAM SPEED OPTIMISATION

To achieve mentioned 90 Hz refresh rate, program revision and speed up was required. After tests, MCU with driver came out unsurprisingly as the biggest bottlenecks. Particularly, communication with driver showed up to be the problem.

There is a delay of approximately 2 ms when requesting data reading from driver, which in result costs us circa 8ms of time lost when reading position from four drivers. This delay doesn't leave up much headroom for achieving 90Hz refresh rate.

One way to decrease mentioned delay is to increase baudrate between MCU and driver. To increase it, a quality TTL to RS-232 converter with good parameters was needed. Older MAX3232 converter couldn't keep up with high speed demand, as it's output signal at speeds beyond 100kBd showed signs of skew and major deformation. Output speed didn't match input speed also, at speeds of 115.2kBd there was ± 5 kBd baudrate variation in signal. For this reason a MAX3225 converter was chosen, since it has 1MBd and beyond speed capabilities, operates at 3.3V and has energy saving auto shutdown feature, Fig. 6.

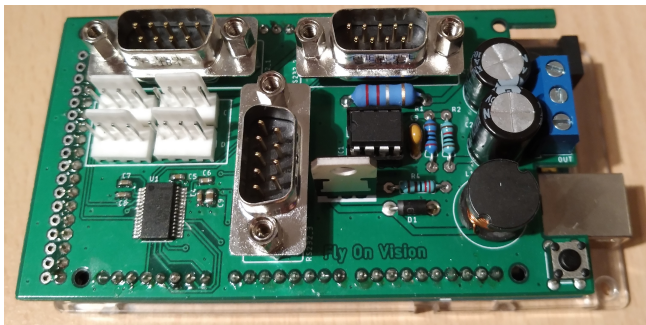


Fig. 6. Serial communication shield.

Another way of optimising speed is checking whether certain commands weren't already sent. Sometimes it can happen that over one refresh a control variable doesn't change its value. That can be easily avoided and can greatly improves refresh rate, where every millisecond spared can improve the rate dramatically.

VIII. RESULTS

Over the course of year and a half, our team managed to assemble the construction after many prototypes, found better materials and improved its 3D printed parts. Complex control programs were developed to fit the needs for control system, speed and precision. MCU is capable of controlling servos position at a 10^{-5} degree with approx 2ms response time. Brake servos provide pilot (Fig. 7) with dynamic torque and are responsive enough for pilot not to realise any delay. Brake line zero position extension is possible for pilots with shorter hands to fit the needs of everyone.

On the other hand, position servos need more work to be done, especially from calculations perspective. MCU is able to position every one of them, but more recalculations are needed for proper use so system is safe to use.

Currently, our team focuses on finishing smaller version of simulator that only uses two brake lines with a harness. This version could be more affordable for smaller flight schools and paraglider enthusiasts. Currently, we're are on the right track,



Fig. 7. Pilot in the harness of a simulator.

with construction parts finished and bugs being repaired. After that all that's left to do is improving the graphics of a game, optimizing the code and adding up to physics of the game.

In addition, control programs can be reused in other project that require such dynamics and precision at a cheap price, from simulators to industry robots.

ACKNOWLEDGMENT

This research has been supported by the project of the Technology Agency of the Czech Republic with number FW01010257: Paragliding Flight Simulator and internal project of UWB and University Students Project SGS-2021-011.

REFERENCES

- [1] J. Obergruber, L. Mehnen, "Development of a Paraglide Control System for Automatic Pitch Stabilization to Increase the Passive Safety", [online], Science Direct, 2016, [cit. 22.3.2021]. ISSN 1877-7058. Available through Science Direct. DOI: <https://doi.org/10.1016/j.proeng.2016.06.184>.
- [2] Aviation Supplies & Academics. "Glider Flying Handbook". Washington: FAA, 2013. ISBN 978-1619541047.
- [3] Flybubble, "Flight Skills" [online], Flybubble Paragliding, [cit. 23.3.2021]. Available on: <https://flybubble.com/blog/flightskills>.
- [4] University of West Bohemia – Fly on Vison team (FEL KEP), "FlyOnVision", [online], UWB, 2020, [cit. 10.8.2021]. Available on <https://flyonvision.com/>.
- [5] P. Stašek: Design of Main Drives of Paraglider Simulator (written in Czech), bachelor thesis, Faculty Electrical Engineering, University of West Bohemia in Pilsen, 2021.
- [6] R. Sivera: Advanced Control of Servomotors for Paraglider Simulator (written in Czech), bachelor thesis, Faculty Electrical Engineering, University of West Bohemia in Pilsen, 2021.
- [7] J. Vorlíček, "Control system design for paraglider simulator" (written in Czech), bachelor thesis, Faculty Electrical Engineering, University of West Bohemia in Pilsen, 2021.
- [8] Kinco automation. "Servo systems" [online], Anaheim Automation Inc., [cit. 26.3.2021]. Available on: <https://www.kincoautomation.com/marketing/servo/>
- [9] Kinco Electric (Shenzhen) Ltd. [online], "Kinco FD Series Servo User Manual" [cit. 20.2.2021]. Available: https://kamelectro.com/pdf/Kinco/Servo/Servo_FD_User_Manual_EN.pdf
- [10] Arduino. "Arduino MEGA 2560 & Genuino MEGA 2560" [online], Arduino, 2021 [cit. 8.4.2021]. Available on: <https://www.Arduino.cc/en/Main/ArduinoBoardMega2560/>
- [11] B. Höglinger-Stelzer et al., "Virtual Gamepad Emulation Framework – ViGEMBus" [online], ViGEMBus, 2021 [cit. 8.4.2021]. Available on: <https://vigem.org/>